Université Fédérale
Toulouse Midi-Pyrénées

THÈSE

En vue de l'obtention du

DOCTORAT DE L'UNIVERSITÉ DE TOULOUSE

Délivré par :

Université Toulouse 3 Paul Sabatier (UT3 Paul Sabatier)

Présentée et soutenue par :
QILIN ZOU

le vendredi 28 janvier 2022

Titre :

Nanoparticules inorganiques luminescentes dopées aux lanthanides :
synthèses, caractérisations
et applications

École doctorale et discipline ou spécialité :
ED SDM : Sciences et génie des matériaux - CO034

Unité de recherche :
CEMES - Centre d'Elaboration de Matériaux et d'Etudes Structurales

Directeur/trice(s) de Thèse :

Robert MAURICOT et Clément ROUX

Jury :
M. Fabien DELPECH, Président
Mme Sophie CARENCO, Rapporteure
Mme Véronique JUBERA, Rapporteure
Mme Montserrat GOMEZ , Examinatrice
Mme Ute RESCH-GENGER, Examinatrice
M. Pierre FAU, Invité
M. Robert MAURICOT, Directeur
M. Clément ROUX, Co-directeur

Acknowledgments

The works in my thesis were mainly completed at M3 group of Centre d'Élaboration de Matériaux et d'Etudes Structurales (CEMES) and group IDeAS of Laboratoire des Interactions Moléculaires et Réactivités Chimiques et Photochimiques (IMRCP), under direction of Dr. Robert Mauricot and Dr. Clément Roux. I would like to thank the group leaders Prof. Marc Verelst from M3 and Dr. Jean-Daniel Marty from IDeAS, the lab directors Prof. Alain Couret and Prof. Christophe Mingotaud for the supports of providing the excellent research conditions and comfortable work atmosphere. I would like to also thank the financial support from French government and Paul Sabatier University.

I would like to gratefully acknowledge my supervisors Dr. Robert Mauricot and Dr. Clément Roux for the opportunity to work on the interesting nanoparticles, for giving me the maximum freedom on the academic exploration during the three years, and for seeking for collaborations to smoothly advance my project. I appreciate that you always show your support and patience when I share you some initial ideas that usually are just came out in embryonic phase. Robert, I must say, I am awed by your diverse expertise in spectroscopy and imaging. As for Clément, you play the roles of colleague, friend, more than a supervisor in my 3 years' life in Toulouse. I still remember that three years ago, you picked up my wife and me in the airport, after that, you helped me to rent an apartment, to buy furniture, to finally build a warm home that has witnessed my first child's coming and so many happy moments during the years. In the three years' academic life, you give me a lot of suggestions, courage and confidence in the research, presentation, and future plans. I am still trying my best to standardly pronounce the key word "yttrium" that you kindly pointed out from my oral presentations. I really enjoy this precious work experience with both of you, thank you!

I would like to thank my colleagues from CEMES for the various technical and administrative support: Cécile M. and Sébastien J. (TEM training and analysis), Nicolas

R.R. (XRD training and analysis), Pierre L. (WAXS measurements), Sébastien M. (spectra measurements), David N. (spectrometers training), Sébastien P. (furnace use), Christine V. (chemical reservation and management), Joël D., Aurore P. and Elodie J.A. (administrations). I must especially acknowledge Prof. Marc Verelst who guided me through some practical experiments, and MRI, CT and photoacoustic imaging analyses. As my project was completed partially at IMRCP, the biological experiments were carried out by Laure and some spectra measurements were done with help of Charles-Louis, many thanks to you. I would like to thank Christophe for the interesting and in-depth discussion about upconversion with you. Many thanks to Jean-Claude who gave me impressive presentations on upconversion luminescence kinetics investigations. Besides, I would like to acknowledge other the permanent and non-permanent staffs who put me in touch with the research fields polymers, stimuli-responsive soft matters…

I would like to thank DAAD and IDeAS support me studying two months in Germany. I specially acknowledge Prof. Ute Resch-Genger for providing me the opportunity and excellent work conditions at BAM. Many thanks to Florian, Christian, Cui, Elina, Arne for the help of photoluminescence spectra, decay, quantum yield and ICP measurements, and organizations of administrative documents.

I would like to thank Ali, Aude, and Michel from LASIRE, University of Lille for the help of spectra and lifetime measurements; Pierre R. from IGC-UPS for the SAXS measurements and analysis; Xiaodong, Jie, Prof. Zheng, Prof. Zhu and Prof. Chen from Fujian Institute of Research on the Structure of Matter, China for the help of temperature-dependent UCL spectra and NIR-II imaging measurements, and fruitful discussion; Delphine from LPCNO-INSA for the measurements of NIR-II emission spectra; Franck from ENI-CREFERE for the measurements of MRI and CT; Pierre and Paiyabhroma from INSERM, University of Montpellier for the measurements of photoacoustic and ultrasound.

In the end, I would like to thank all my friends of Toulouse out of the lab for helping and feeding my family and me, you make our life in Toulouse more colourful. I would like to, of course, thank my families from China for the spiritual support and please forgive us that we have no chance to go back and see you in China in the whole three years. I would like to thank my wife for the always support and encouragement, and my son that “allows” me sometimes “travailler” in the weekend.

"On and on stretched my road, long it was and far, I would go high and go low in this search that I made."

Qu Yuan

Table of contents

General introduction

With the rapid developments of nanotechnology, various nanoparticles (NPs) have been widely explored due to their unique optical, electronic, and magnetic properties. These NPs show great promise in diverse applications, such as bioimaging.

My doctorate is conducted within the project entitled "New optical probes and a new imaging approach for deep in vivo application", which is funded by the ministry of national education of France. The main objectives of this project are to design a new kind of optical probe with efficient photoluminescence and to shift both the excitation and emission wavelength at ~800 nm for in vivo imaging.

Chapter 1 briefly reviews the history of nanoparticles and some of popularly studied inorganic NPs including semiconductor, metal, metallic oxide/sulfide, lanthanide-based, and so on. Among those NPs, we mainly focus on introducing lanthanide (Ln)-based inorganic NPs and their luminescence properties, classifications, synthesis methods, surface modification, and applications. The Ln-based inorganic NPs are emerging NPs that attract huge attention for many applications especially in nanomedicine. In our group, we've investigated Ln-doped Gd_2O_2S NPs for many years and these NPs are good candidates for many bio-applications. However, there are still some obstacles:

1) no general synthesis method reported to prepare small-sized, highly crystalized, well dispersed, and high yield Gd_2O_2S NPs;

2) no further core/shell construction example reported for Gd_2O_2S nanoparticles;

3) no effective surface modification strategy reported to transfer hydrophobic organic ligand coated Gd_2O_2S to hydrophilic.

To overcome the first obstacle, we explore a new general method to synthesize rare-earth oxysulfide (RE_2O_2S) NPs in chapter 2. The reaction parameters of the synthesis are fully explored for obtaining high-quality NPs. Aiming at acquisition of multiple functions (NIR-II luminescence, magnetism, and x-ray attenuation, and photoacoustic performance) from the RE_2O_2S, we further synthesize Nd-doped Gd_2O_2S (Gd_2O_2S:Nd) NPs. The NIR-II luminescence spectra of the NPs are recorded at LPCNO-INSA Toulouse. To render the as-synthesized Gd_2O_2S:Nd NPs hydrophilic, three different

surface modification strategies are discussed and optimized. These hydrophilic PVP-coated Gd_2O_2S:Nd NPs were sent to our collaborators (ENI-CREFRE in Toulouse, Fujian Institute of Research on the Structure of Matter (FJIRSM) in China, and INSERM-CNRS of University of Montpellier) for magnetic resonance, computed tomography, NIR-II luminescence, photoacoustic, and ultrasound imaging experiments.

To overcome the second obstacle, we develop a new core/shell structure where an inert $NaYF_4$ shell of ~4 nm thickness is deposited on the Gd_2O_2S:20%Yb,1%Tm core NPs. The core/shell structure is demonstrated by transmission electron microscopy (TEM) and X-ray diffraction (XRD) analyses. The growth kinetics of RE_2O_2S@$NaREF_4$ core/shell nanoparticles are studied by analysing TEM, XRD, and small-angle X-ray scattering (SAXS) in different reaction phases. Upconversion properties including upconversion luminescence (UCL) intensity, lifetimes, and quantum yields (QYs) of Ln^{3+}-doped Gd_2O_2S@$NaYF_4$ core/shell nanoparticles are systematically investigated. The decay curves and power-dependent QYs are recorded at BAM-Berlin Germany.

In chapter 4, we investigate the potential nanothermometry application of the lanthanide-doped Gd_2O_2S@$NaYF_4$ heterogeneous core/shell UCNPs. Towards that purpose, the temperature-dependent UCL emission spectra are first measured at FJIRSM. Based on the temperature-dependent UCL emission spectra, we notice the thermally enhanced UCL phenomenon in our UCNPs. Moreover, temperature-dependent UCL spectra and in-situ XRD measurements manifest a correlation between selected emission band ratio of Er^{3+} and lattice strain. Finally, we show that Ln^{3+}-doped Gd_2O_2S@$NaREF_4$ core/shell UCNPs have a great potential for nanothermometry application with high relative thermal sensitivities.

To shift both the excitation and emission wavelength at ~800 nm, core/shell/shell $NaYF_4$:40%Gd,20%Yb,1%Tm@$NaYF_4$:10%Yb@$NaYF_4$:10%Yb,20%Nd UCNPs are synthesized through high-temperature co-precipitation method. The classic UCL properties are characterized at CEMES and IMRCP. The time-gated spectra are

measured for the as-prepared core/shell/shell UCNPs at LASIRE, Lille. The emission spectra and decays of Tm^{3+}, Nd^{3+}, and Yb^{3+} in the NIR range of 700~1050 nm, are recorded and carefully analysed. Then, the PVP-coated core/shell/shell UCNPs are further prepared and incubated with HCT-116 cells. Then, via confocal microscope, we obtain images of cells under 980 nm and 405 nm irradiation.

This thesis systematically discusses the synthesis, characterizations, and applications of lanthanide-doped core and core/shell NPs based on RE_2O_2S and $NaREF_4$ hosts. The results demonstrate the versatility of strategies to synthesize RE_2O_2S based core and core/shell NPs and their potential applications such as multimodal imaging, temperature sensing, and time-gated imaging.

Chapter I: Literature investigations and project objectives

"There's Plenty of Room at the Bottom" - Richard P. Feynman.

Since the concept of nanotechnology was first presented by Nobel laureate Richard P. Feynman during his well famous lecture "There's Plenty of Room at the Bottom" at annual American Physical Society meeting in 1959, there have been made various revolutionary developments in the field of nanotechnology.[1] Nanotechnology produced a variety of materials at nanoscale level, so called nanomaterials. Nanoparticles (NPs) are materials within the 1~100 nm size range in one dimension at least, have triggered tremendous interest due to their unique optical, electronic, and magnetic properties which stem from a combination of their intrinsic characteristics such as size, shape, structure, chemical composition, and the types of functionalized molecules on the surface. The comparison of nanoparticles to other objects in a size range is shown in Figure 1, for a better understanding. With decades of development, many kinds of NPs including semiconductor quantum dots (QDs), noble metal, transition metal oxide, and lanthanide-doped NPs have been explored.[2] Semiconductor QDs (e.g., CdSe, CdTe, PbS, and perovskite) are able to be highly luminescent due to their electronic structure. Metallic NPs (especially Au and Ag) can exhibit strong optical absorption and scattering. Transition metal oxide NPs such as Fe_3O_4 exhibits unique superparamagnetism which is not encountered in the corresponding bulk materials. Lanthanide-based NPs have a very wide emissive range from ultraviolet to infrared because of the abundant energy levels of lanthanide ions. These properties have given the NPs great potential for various applications in imaging, therapy, sensing, solar cell, catalysis, anticounterfeiting, optical storage, to name a few.

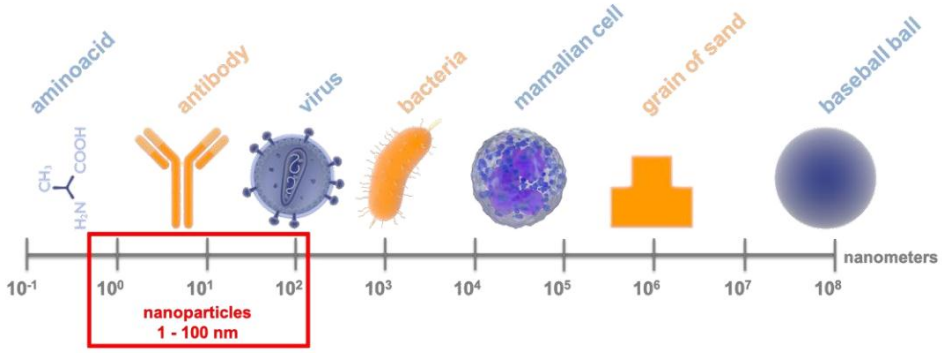

Figure 1.1 Comparison of objects on a logarithmic scale.[3] Reprinted from MDPI.

In this chapter, we first briefly review the history of nanoparticles. Then, inorganic NPs including semiconductor, metal, metallic oxide/sulfide, and lanthanide-based are introduced in the following section. Among those NPs, we mainly focus on introducing lanthanide-based inorganic NPs including their luminescence properties, classifications, synthesis methods, surface modification, and applications. Finally, based on the literature investigation, we conclude with the objectives of the project regarding my PhD study.

1 Definition

About 100 years ago, the German scientist, Paul Ehrlich, Noble laureate for contribution in adaptive and acquired immunity, introduced the concept of targeted therapy as "magic bullet" to generate new therapies that are able to tackle the disadvantages of chemotherapeutic agents.[4, 5] Then the concept of nanoparticles and of drug targeting was born in his mind.[6, 7] Inspired by that idea, in the last twenty years, construction of tiny systems to detect, diagnose, and treat disease has given rise to the most promising advances in the fight against cancer.[5] And currently, nanoparticles are considered viable options in the treatment of different types of cancer. Therefore, about 40 years ago, a definition of nanoparticles for pharmaceutical purposes was made[7]: "Nanoparticles are solid colloidal particles ranging in size from 10 to 1000 nm. They consist of macromolecular materials in which the active principle (drug or biologically active material) is dissolved, entrapped, encapsulated and/or to which the active principle is adsorbed or attached".

In 2008, as well as in the latest version in 2018[8], the International Organization for Standardization (ISO) defined a nanoparticle as an zero-dimensional nano-object where all three external dimensions are less than 100 nm. Similarly, the two-dimensional nano-objects (e.g., nanodiscs and nanoplates) and the one-dimensional nano-objects (e.g., nanofibers and nanotubes) were defined by the ISO. Three years later, the Commission of the European Union (CEU) accepted a more-technical but wider-

ranging definition of nanomaterial which includes nanoparticle[9]: a natural, incidental or manufactured material containing particles, in an unbound state or as an aggregate or as an agglomerate and where, for 50% or more of the particles in the number size distribution, one or more external dimensions is in the size range 1 nm~100 nm. Under that definition, a nano-object needs only one of its characteristic dimensions to be in the range 1~100 nm to be classed as a nanoparticle, even if its other dimensions are outside that range. The main difference between the CEU Recommendation and definitions in non-EU countries is that the EU definition does not include the specific properties of nanomaterials.[10]

2 Inorganic nanoparticles

In terms of classification, NPs can be classified into various categories, according to their morphology, size, and material properties. For example, one classification is depending on whether the NPs are carbon-based, ceramic, semiconducting, or polymeric. From the aspect of physical properties, the NPs can be classified as hard (e.g. TiO_2, SiO_2, and C_{60}) or as soft (e.g. liposomes and nanodroplets); or they can be classified into plasmonic, magnetic, and luminescence NPs. Moreover, the NPs even can be classified regarding their applications such as diagnosis or therapy, or the ways they are produced. In fact, in most of literatures, NPs are distinguished typically between organic and inorganic where the former includes dendrimers, liposomes, and polymeric NPs while the latter converse semiconductor, metal, oxide, carbon-based, and lanthanide-based NPs, and so on. Based on this classification, some of well-known inorganic NPs are given below and discussed briefly.

A variety of inorganic NPs have been developed as nanoprobes for imaging, display, therapy, and optogenetic applications. Their unique optical, electronic, and magnetic properties can be fine-tuned via controlling the chemical composition, size, morphology, surface groups, and structure of the NPs, which adapts to the demanding of various utilizations. In this section, we will briefly introduce representative classes of inorganic NPs excluding lanthanide-base NPs which will be deeply discussed in the following

section.

2.1 Metal nanoparticles

Metal NPs are purely synthesized from the metal precursors and they can possess many kinds of properties that are decided by composition, size, shape, and structure. Two characteristic properties of metal NPs are superparamagnetism and surface plasmon resonance (SPR).[11]

When the ferromagnetic or ferrimagnetic NPs are reduced below to a critical size, typically less than 20 nm, magnetization can randomly flip direction under the influence of ambient thermal energy, resulting in a net magnetization of zero.[12] This phenomenon is called superparamagnetism. Such NPs are not capable of permanent magnetism if there is absence of an external field, however, similarly with a paramagnet, they can quickly respond to an external magnetic field and their magnetic susceptibility is much larger than that of paramagnets. Superparamagnetic NPs, such as single-composition metal NPs[13-15] of Co, Fe, and Ni and alloyed metal NPs[16-18] of FePt, CoPt, $CoPt_3$, and FeCoPt, have been extensively reported. These NPs have demonstrated the potential for magnetic resonance imaging (MRI) and magnetic induction hyperthermia therapy applications.[19]

SPR is a phenomenon whereby free electrons oscillate collectively at the interface of between negative and positive permittivity medium under stimulation of incident light.[20] Metal NPs such as Au and Ag, can resonantly absorb and scatter incident light upon excitation of their surface plasmon oscillations. Their absorption cross-sections are several orders of magnitudes larger than organic molecules.[21] By dark-field optical microscopy[22] or optical coherence tomography (OCT)[23], the metal NPs with SPR effect can be exploited for biological optical imaging. Besides, the metal NPs can be also used for photoacoustic tomography (PA)[24] and X-ray computed tomography (CT)[25] imaging because they have large absorption cross-section for light and large absorption coefficients for X-ray, respectively. Additionally, due to their strong surface-enhanced Raman scattering, the metal NPs can be exploited for diagnosis or imaging

applications[19].

2.2 Metal Oxide nanoparticles

Metal oxide NPs display a wide variety of sizes, shapes, structures and properties, which make them very attractive for various applications.[26, 27] And it is found that the sizes, shapes, and structures can significantly affect the properties of Metal oxide NPs.[11] For example, Cu_2O NPs show facet-dependent catalytic properties that 111 faceted octahedral Cu_2O shows higher reactivity towards the C–N coupling reaction than 100 faceted cubic.[28] However, the low reactivity of the 100 faceted cubic Cu_2O can be improved by the O_2 assisted etching process which provides more active sites on the obtained facet-etched nanocubes.[29]

Magnetic oxide NPs are normally transition oxide such as iron oxide (Fe_2O_3 and Fe_3O_4)[30], cobalt oxide (CoO and Co_3O_4)[31], NiO[32], and MnO[33], showing size dependent magnetic property, as mentioned above. Typically, in the size regime of 10~20 nm, each NP shows superparamagnetic behaviour like a single magnet when the ambient temperature is higher than the so-called blocking temperature. Therefore, the NP shows a fast response against applied magnetic fields with negligible remanence and coercivity. These features enable the superparamagnetic metal oxide NPs promising for bio-applications such as MRI signal-enhancing applications[34] and tumour therapy[35].

2.3 Semiconductor QDs

Semiconductor QDs are small inorganic nanocrystals, which at a size range of 1~10 nm in diameters show quantum confinement effects.[36] Single QD crystal contains several hundreds to thousands of atoms. These QDs are typically composed of III–V, II–VI, IV, and IV–VI semiconductors.[37] They can be synthesized through well-established epitaxial growth technique, such as the metalorganic vapor phase deposition and the molecular beam epitaxy, differently, the colloidal QDs can be obtained through wet chemistry method.[37] Unlike bulk material owing continuous valence and conduction bands, colloidal QDs develop discrete states whose energy and symmetry depend on QD size and shape (Figure 1.2a).[38] The energy gaps between the states increase with

decreasing size of the material, thus relating the energy gap between the highest occupied and lowest unoccupied states to the QD size. Therefore, electronic and optical properties of these QDs can be dramatically tuned through controlling the size, shape, and composition with the existence of quantum effects. Furthermore, surface ligands allow the QDs to assemble into solids from bottom to up in the form of colloids. Then, these QD solids can be engineered and selected with specific electronic and optoelectronic properties to cooperate with other components such as functional polymer substrate and finally to prepare diverse devices, as shown in Figure 1.2b.[38, 39] Besides, semiconductor QDs are emerging a new class of nanoprobes for biological and medical applications like cellular labelling, bioimaging, cancer detection and therapy due to their advantages of tunable emission wavelength, narrow symmetric emission spectra, and extreme photostability.[40-43] Nevertheless, toxicity is the main issue that hinders the larger scale use of QDs because the QDs' basic elements (e.g., Cd, Hg, Pb, As, and Pb) are highly toxic to humans. Developing more biocompatible QDs by coating non-toxic inorganic shell or organic molecules is still the future research direction.[44]

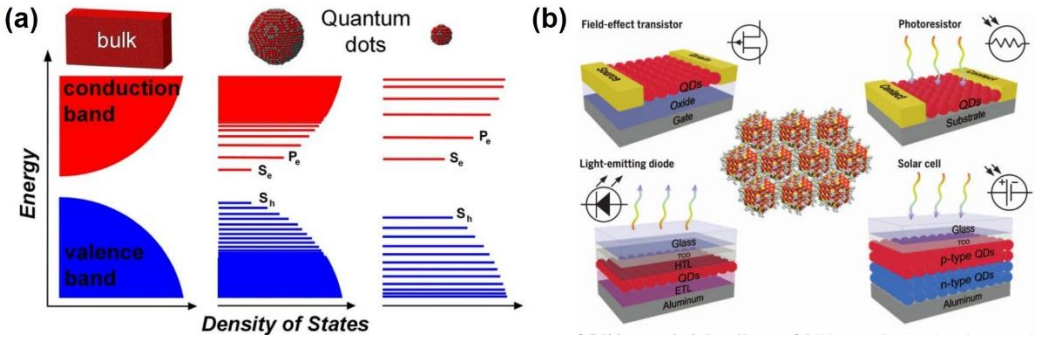

Figure 1.2 (a) Evolution of the electronic structure of inorganic semiconductors with different sizes. (b) Colloidal quantum dot device architectures. Reprinted from American Association for the Advancement of Science.

2.4 Carbon-based nanoparticles

Carbon-based NPs including fullerenes, carbon nanotubes, graphene, graphene oxide, nanodiamonds, and carbon-based quantum dots, have been widely studied due to their

diverse chemical and physical properties such as thermal, mechanical, electrical, optical, and structural performances.[45-47] One of the key features of fullerenes is that they are able to act as sensitizers for the production of singlet oxygen ($^1O_2$) and other reactive oxygen species (ROS) under stimulation of light. Hence, they are utilized for blood sterilization and photodynamic cancer therapy.[48, 49] However, the poor dispersibility of fullerenes in water limits their bio-applications although several methods about surface hydrophilic functionalization of fullerenes have been reported.[50]

Carbon nanotubes (CNTs) are divided into single wall carbon nanotubes (SWCNTs) and multiwall carbon nanotubes (MWCNTs) based on the number of graphene layers in the cylindrical tubes.[46] The diameter of SWCNTs and MWCNTs varies from 0.4 to 2.5 nm and a few nanometres to 100 nm, respectively, and the van der Waals forces interacts between two layers of MWCNTs.[51, 52] Functionalized CNTs have been used in applications in biomedicine such as biosensing, disease diagnosis, and treatment. Nevertheless, worries of the toxicity of CNTs on cell and tissue have been regarded as a practical issue, and a lot of in-depth studies are still ongoing. [53-55]

Carbon quantum dots (CQDs) with sizes less than 10 nm and high fluorescence quantum yield (QY), have been extensively investigated.[47, 56] Many facile and green synthesis methods have been reported. For example, CQDs can be produced from organic materials such as chitosan[57], gelatin[58], watermelon peel[59], and vegetables[60]. Additionally, a variety of easy and economic methods have been developed for the synthesis of CQDs, such as laser ablation[61], combustion/thermal microwave heating[57, 62], chemical oxidation[63], hydrothermal carbonization[64], and pyrolysis[62]. In 2006, Sun et al., reported that PEG_{1500N} passivated CQDs displayed high QYs in water (Figure 1.3) and proved the potential optical bioimaging application.[61]

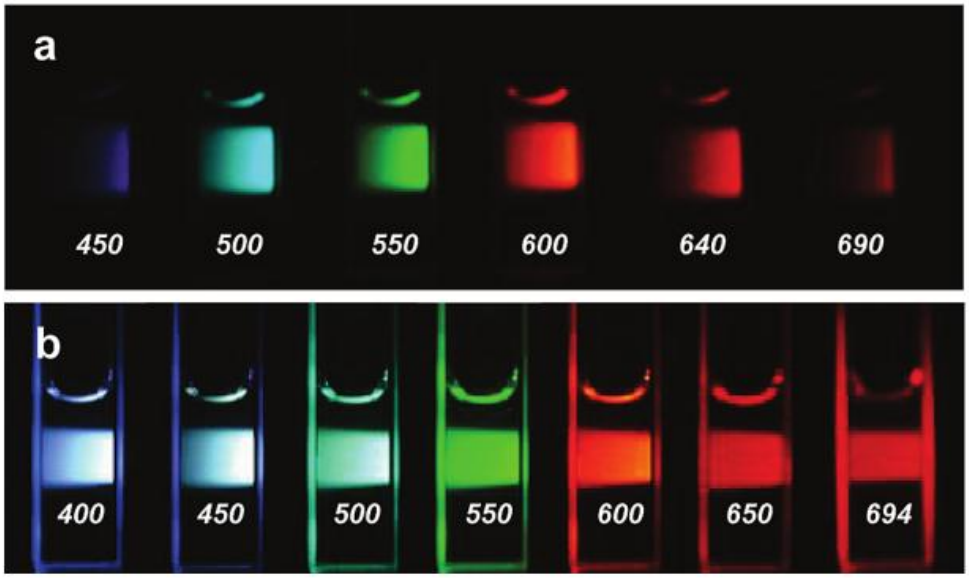

Figure 1.3 PEG_{1500N} functionalized CQDs dispersing in aqueous solution and displaying colourful luminescence under 400 nm excitation with (a) or without (b) filters band-pass. Reprinted from American Chemical Society.[61]

2.5 All-inorganic perovskite nanoparticles

All-inorganic perovskite (AIP) NPs including low-dimensional QDs and nanocrystals (NCs), as an emerging nanomaterials, have recently drawn tremendous attentions because of their excellent optoelectronic properties, high photoluminescence QYs, and facile synthesis,[65-68] showing a great promising in the use of solar cells (SCs)[69-71], light emitting diodes[72], photoelectrochemistry[73], and photodetectors[68]. The general chemical formula of AIP is ABX_3 where A represents a monovalent cation such as Cs^+ or Rb^+, B site represents a divalent metal cation such as Pb^{2+}, Sn^{2+}, or Ge^{2+} and X site represents a monovalent halide anion such as I^-, Br^-, or Cl^-.[74] The crystal structure of ABX_3 is cubic phase (Figure 1.4a) and the compositions of $CsPbI_3$, $CsPbBr_3$, $CsPbI_xBr_{3-x}$, $CsSnI_3$, and $CsSnBr_3$ are typically reported.[75] In 2015, Kovalenko and co-workers reported the first successful preparation of $CsPbX_3$ nanocrystals (NCs) using a hot injection method.[65] The band gap can be tuned by the regulation of halide ion components and size, resulting in absorption and emission peaks in the range of 400~700 nm, as shown in Figure 1.4b. Compared to the organic-inorganic perovskite, solution-processed

colloidal AIP QDs exhibit better thermal stability (stable under 350 °C) because of no unstable organic components.[69, 75] Therefore, AIP QDs possess higher reliability for practical photovoltaic applications. Although, the stability under harsh conditions still cannot meet the requirements for future commercial application. In addition, the toxicity of lead is also in debate. Thus, looking for suitable substitutes is an urgent research direction in the future. In a word, many challenges such as stability, toxicity, and synthesis, should be addressed before AIP NPs can be considered for practical application.[76]

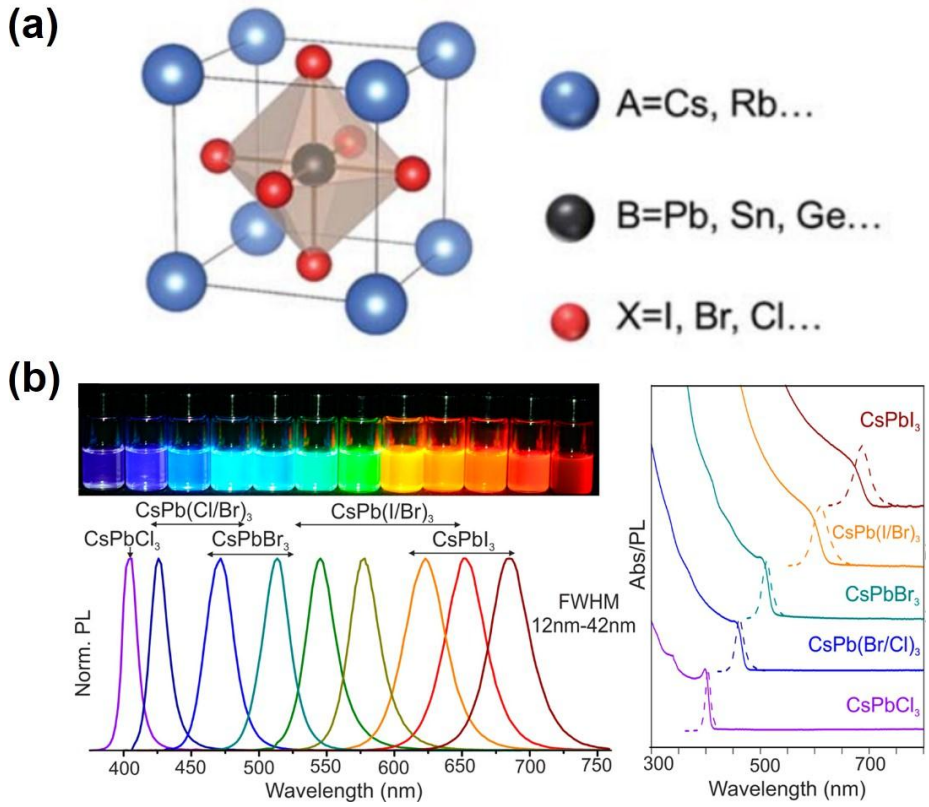

Figure 1.4 (a) Schematic diagram of the AIP cubic structure and sites occupation of the ions in the crystal. Reprinted from The Royal Society of Chemistry.[74] (b) Solution processed colloidal perovskite $CsPbX_3$ nanocrystals (X = Cl, Br, I) exhibit size- and composition-tunable bandgap energies covering the entire visible spectral region with narrow and bright emission. Reprinted from American Chemical Society.[65]

3 Lanthanide-doped nanoparticles

Rare-earth elements (Figure 1.5) including Y and Sc, and 15 types of lanthanides, have

been extensively used in our daily life (cell phone, television, light-emitting diode, etc.) and heavy industry (wind turbine, airplane, etc.) due to their unique optical, electronic, and magnetic properties. Rare-earth elements, in fact, are not really very rare in terms of the abundance on the Earth. They are as common as many common transition metals such as copper, tin, lead and zinc, as shown in Figure 1.5 left. They were named as 'rare earths' as they were first discovered among scarce minerals in the 19th century. The unsaturated 4f orbitals of electron configuration of lanthanides confer them many unique properties of luminescence, magnetism, and electronics, which gives them potential to develop new materials with diverse properties. In recent decades, lanthanide-doped inorganic NPs have attracted much attention due to their advantages of sharp-band emissions, long fluorescence lifetime, large anti-Stokes shifts, high resistance to photobleaching, low toxicity, and wide emission wavelength range, and thus have been applied for a broad range of applications such as background-free bio-detection, light-triggered drug delivery, cancer therapy, multifunctional bioimaging, temperature sensing, solar energy harvesting, and super-resolution microscopy.

In this section, we will discuss the luminescence, host materials, synthesis, surface modification, and applications of lanthanide-doped inorganic NPs.

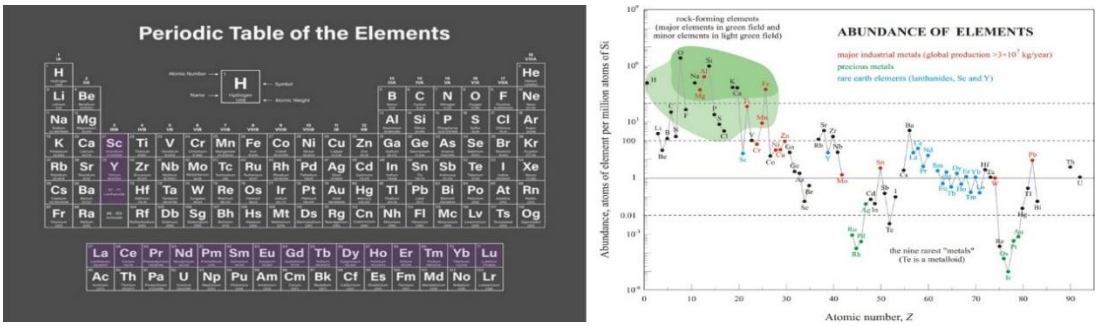

Figure 1.5 Periodic table of elements from the source of Shutterstock, the rare-earth elements are painted in violet. Abundance of main elements on the Earth, source: E. Generalic, https://www.periodni.com/rare_earth_elements.html.

3.1 Electronic structure of lanthanide ions

Trivalent lanthanide (Ln^{3+}) ions doped luminescence materials have been widely

investigated since the early 20th century. The Ln^{3+} ions have a general electronic configuration $[Xe]4f^N$ (N = 0-14) which is key to the chemical and spectroscopic properties of the Ln^{3+} ions.[77] Among the Ln^{3+} ions, La^{3+} has no f electrons, while Lu^{3+} has a filled 4f subshell. It is seen that the valence electrons in the 4f orbitals of the Ln^{3+} ions are shielded, particularly by the filled $5s^2$ and $5p^6$ subshells, which results in weak interactions of the valence electrons with the environment, and minimal electron-phonon coupling interactions.[78] Because of this, inner-shell 4f-4f transitions of Ln^{3+} exhibit sharp peaks and easy identification in the emission spectra. In general, ground states may be comprised of a group of substrates with different values of the total orbital and spin angular momentum quantum number.[77] Term symbols with the format $^{2S+1}L_J$ (S is the total spin angular momentum quantum number, L is the total orbital angular momentum quantum number, J is the spin–orbit coupling or Russell–Saunders quantum number), which summarize the quantum number information, are assigned to describe the individual microstates.[79, 80] A complete diagram, showing the ground and excited states of all Ln^{3+} ions (except for La^{3+} and Lu^{3+}) with corresponding term symbols, is displayed in Figure 1.6.[81] It is displayed that the Ln^{3+} ions have abundant energy levels. The Judd-Ofelt theory has successfully proved the ability to predict oscillator strengths in absorption and emission, luminescence branch ratios, excited-state radiative lifetimes, energy transfer probabilities, and quantum efficiencies for the transitions of Ln^{3+} ions by using only three parameters, $\Omega_{(\lambda)}$ (λ = 2, 4, 6).[82-85] Moreover, the ladder-like structure of the electronic states of Ln^{3+} is very diverse and the lifetimes of excited states are relatively long from microseconds to milliseconds, allowing for a wide emission range covers the UV, visible, and near-infrared (NIR) regions. This versatility allows Ln^{3+} ions in bulk or nanoscale materials for numerous applications of lasers, optical communications, and imaging.[86, 87]

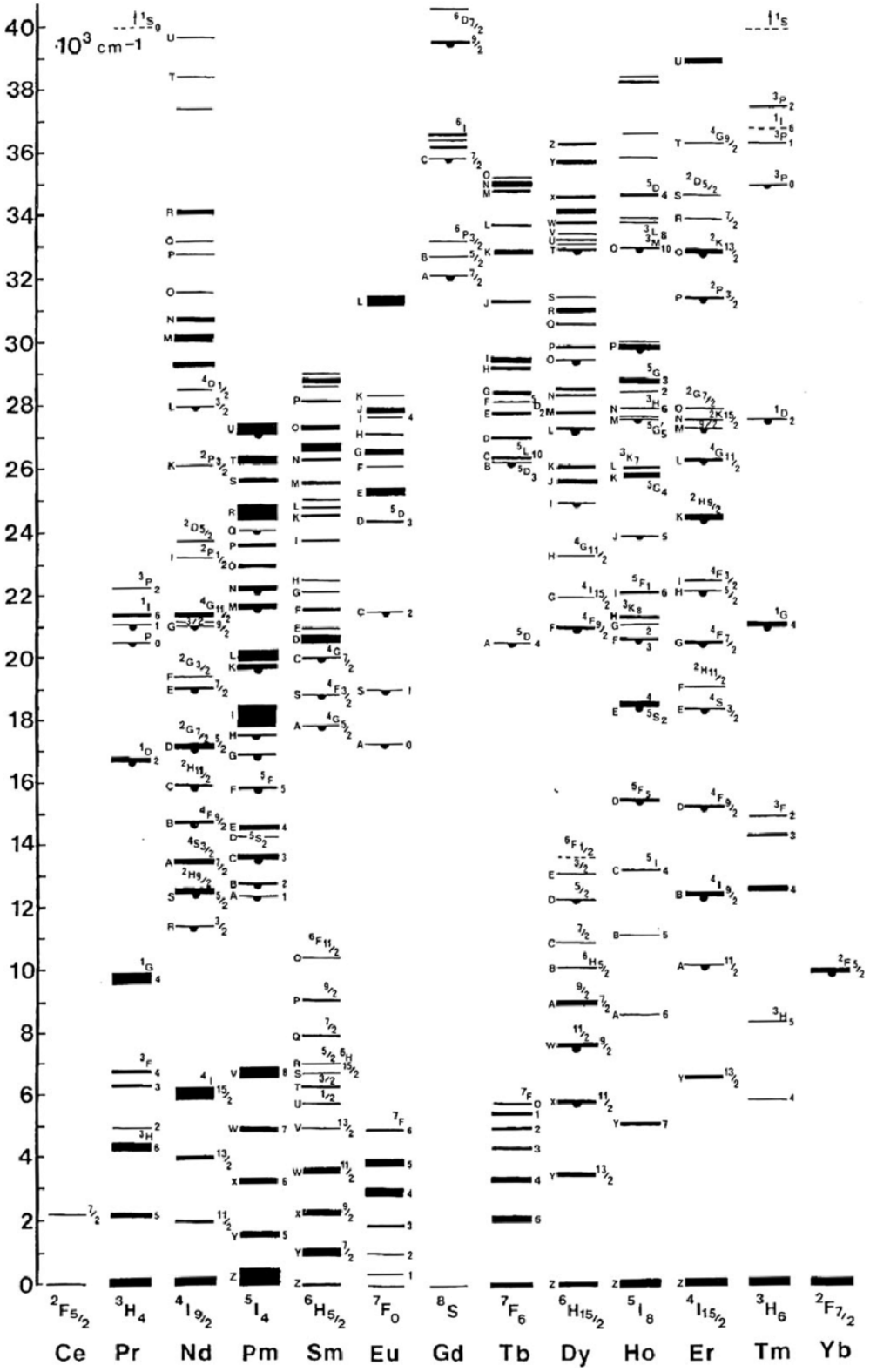

Figure 1.6 Energy levels of Ln^{3+} ions. Reprinted from Optica Publishing Group.[81]

3.2 Luminescence

With regard to the luminescence of Ln^{3+} ions, three types of electronic transitions are

involved.[88-90] The first type is the parity forbidden f-f transition with extremely small absorption coefficients (<1 $M^{-1}cm^{-1}$). The corresponding transitions are very narrow, and the barycentre of the ligand-field split bands is not dependent on the chemical environment. Therefore, these transitions are easily recognizable and become the ideal candidates for optical probes on monitoring the symmetry of the metal-ion environment. All Ln^{3+} ions, except La^{3+} and Lu^{3+} without f-f transitions, are luminescent and their f-f emission profiles cover the entire spectrum, from UV (Gd^{3+}) to visible (e.g., Pr^{3+}, Sm^{3+}, Eu^{3+}, Tb^{3+}, Dy^{3+}, Er^{3+}, Ho^{3+}, Tm^{3+}) and NIR (e.g., Pr^{3+}, Nd^{3+}, Er^{3+}, Ho^{3+}, Tm^{3+}, Yb^{3+}) ranges. Some ions are fluorescent, others are phosphorescent, and some are both. The second type is f-d transition which involves the promotion of a 4f electron into the 5d subshell. The f-d transitions are allowed and broader than f-f transitions. As the 5d orbitals are external and interact directly with the ligand orbitals, these f-d transitions are largely dependent on the metal environment. For instance, Ce^{3+} luminescence can be tuned from about 290 to 400 nm when doping in different matrices. The 4f-5d transitions are commonly observed for Ce^{3+}, Pr^{3+}, and Tb^{3+}. The last type is charge-transfer transition from ligand to metal or from metal to ligand. This transition is allowed by Laporte's selection rule and commonly happens on Eu^{3+} and Yb^{3+} (possibly Sm^{3+} and Tm^{3+}). Unlike widely studied d transition-metal ions, the underlying mechanism of this type of transition is still not so clear for Ln^{3+} ions.

When the Ln^{3+} ions are doped into proper materials, the luminescence can be obtained by using various excitation light sources such as X-ray, lamps, and lasers. When the incident wavelength is shorter than the emission wavelength, the process is called Stokes or down-shifting luminescence (DSL). On the contrary, the anti-Stokes luminescence process requires the incident wavelength to be longer than the emission wavelength, which is known as upconversion luminescence (UCL). The Eu^{3+}, Tb^{3+}, Dy^{3+}, Sm^{3+}, Er^{3+}, Nd^{3+} doped NPs exhibiting intense DSL with sharp peaks and long lifetimes, are extensively used for biodetection *in vitro*, multicolour biolabeling, and time-resolved (TR) PL detection.

Upconversion is a nonlinear optical process that converts two or more low-energy photons (commonly located in the NIR region) into a higher-energy output photon ranging from UV to NIR. This phenomenon was predicted in 1959 by Bloembergen and observed independently by Auzel, Ovsyankin and Feofilov in the mid-1960s. So far, five kinds of popular mechanisms have been proposed to explain the UC process: ground state absorption/excited state absorption (GSA/ESA), energy transfer UC (ETU), photon avalanche (PA), cooperative sensitization upconversion (CSU), and energy migration UC (EMU), as shown in Figure 1.7.

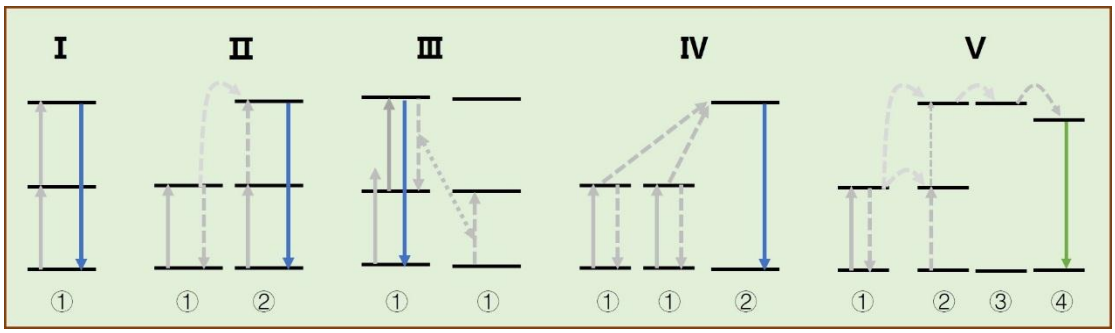

Figure 1.7 Five simplified energy level diagrams describing the reported UC mechanisms. I: GSA/ESA, II: ETU, III: PA, IV: CSU, and V: EMU.

GSA/ESA processes involve two steps of successive photon absorption in only a single ion (Figure 1.7I), which is the simplest UC process. In the GSA step, the ion is excited from the ground state to an intermediate metastable state, whereby a second pump photon promotes the ion from the intermediate state to a higher lying state (ESA step) from which the emission of light occurs.[91, 92] The ETU processes involve two neighbouring ions interaction, for example the sensitizer ion Yb^{3+} and the activator Er^{3+} ion.[93, 94] In the ETU process (Figure 1.7II), the sensitizer ion first absorbs low-energy pump photon and populate to the higher state. Then, the energy is transferred from the excited state of the sensitizer ion to the ground or excited state of activator ion. Finally, the activator ion produces high energy photon. The activator ion can absorb more than 2 photons by this energy transfer process in several steps, resulting in multi emission peaks from just one Ln^{3+} ion. Differing from ESA, the ETU is implemented through an

energy transfer process between two neighbouring ions rather than successive absorption of two photons in a single ion. As a consequence, ETU can be distinguished from ESA by a rising edge in the initial stage of the PL decay curve because the population of the emissive level in the ETU process requires an energy transfer between two ions. Since the ESA process takes place in single Ln^{3+} ions (e.g., Er^{3+}), the very weak absorption by parity-forbidden intra-4f transitions within Ln^{3+} strongly suppresses its UCL efficiency. However, the ETU takes advantage of the larger absorption cross-section of a sensitizer (e.g., Yb^{3+} or Nd^{3+}), and thus is regarded as the most efficient UC process in practical applications.

The PA phenomenon was first discovered by Chivian et al. in Pr^{3+}-based infrared quantum counters.[95] PA process is a positive-feedback system which requires a pump intensity above a certain threshold. In the PA process (Figure 1.7III), the intermediate reservoir level is initially populated by non-resonant weak ground state absorption (GSA), followed by the resonant ESA or energy transfer from another excited ion (i.e., ETU) to populate the emissive level from which UCL occurs.[96] After this initial stage, an efficient cross relaxation (CR) takes place between the excited ion and another adjacent ground-state ion, resulting in the population of the reservoir level of two UC ions. Subsequently, the feedback looping of ESA (or ETU) and CR will exponentially increase the population of the reservoir and emissive levels, thus producing strong UCL. The PA UC is considered to be the most efficient due to the positive optical feedback looping of ESA (or ETU) and CR in UC processes, there are still disadvantages including weak GSA, high pump threshold and much longer rise time (even up to seconds). Despite of the limitations, Lee et al. very recently reported the engineered nanocrystals with high Tm doping concentration ≥ 8% where PA was realized in at room temperature with continuous wave pumping.[97] The PA excitation threshold intensity was fully determined by the $^3F_4$ intermediate-state lifetime of Tm^{3+} at higher concentrations. The Tm^{3+} avalanching behaviour was achieved for excitation in the range 1400-1470 nm in addition to 1064 nm. More importantly, the authors realized

sub-70-nm single-particle super-resolution imaging and <2-nm photon localization with the nonlinear PA emission intensities from those Tm doped nanocrystals, which bring more opportunities for applications in local environmental, optical and chemical reporting and in super-resolution imaging.

CSU mechanism involves the interaction of three ions and takes place with a very low probability.[98] In the CSU process (Figure 1.7IV), the luminescent level is populated through simultaneous energy transfer from two adjacent ions and sometimes phonon assistance is necessary to make up the small energy mismatch between the energy of two sensitizer and that of the luminescent level of the activator. Another similar process is cooperative upconversion (CUC) which happens when the emitters have no real intermediate energy level to match the energy of the donors.[92] CUC usually happens in Yb^{3+} singly-doped and CSU in Yb^{3+}/Tb^{3+} or Yb^{3+}/Eu^{3+} co-doped materials.[99, 100] So far, no practical applications have been displayed for the CSU and CUC because of their low UCL efficiency, for example, an absolute UCQY value of 0.0085% was reported in $LiYbF_4:Tb^{3+}@LiYF_4$ core/shell UCNPs[101].

The EMU process was first proposed by Liu's group in $NaGdF_4:Yb^{3+},Tm^{3+}@NaGdF_4:Ln^{3+}$ (Ln = Tb, Eu, Dy, and Sm) core/shell nanostructures.[102] In this novel UC process, as shown in Figure 1.7V, four types of Ln^{3+} ions are designed for realizing EMU: sensitizers (type ①), accumulators (type ②), migrators (type ③), and activators (type ④). This mechanism is a long-distance energy transfer process involving several steps. Firstly, sensitizer ion (Yb^{3+}) is used to harvest pump photons and subsequently promote a neighbouring accumulator ion (Tm^{3+}) to the excited states. Then, a migrator ion (Gd^{3+}) extracts the excitation energy from high-lying energy levels of the accumulator and the energy is randomly hopped through the migrator ion sublattice. Finally, the trapped energy is migrated to an activator ion (e.g., Tb^{3+}, Eu^{3+}, Dy^{3+}, and Sm^{3+}) producing UCL. To control the energy exchange interaction between the accumulator and the activator, the sensitizer/accumulator and the activator are spatially confined in different layers of the

core/shell structure for eliminating deleterious CR. As a result, multicolour UCL from activators without long-lived intermediate energy levels can be realized. Based on the novel EMU process, a various of core/shell nanostructures have been designed for multicolour luminescence tuning under different modes.[102-105] More importantly, the excitation energy migration dynamics have also been widely investigated, providing a basic understanding for the EMU.[106] It has been believed that this novel UC mechanism is an significant extension of traditional UC processes including ESA, ETU, CSU, and PA, and thus may broaden the applications of Ln^{3+}-doped UCNPs.

Two important parameters characterizing the emission of light from Ln^{3+}-doped NPs are the lifetime of the excited state and the quantum yield (QY). The lifetime of an observed excited state τ_{obs} can be expressed by an equation[77]:

$$\tau_{obs} = 1/k_{obs} \quad (1\text{-}1)$$

where the rate constant k_{obs} is the sum of the rates of the various deactivation processes which can be simply written as:

$$k_{obs} = k^{rad} + \sum_n k_n^{nr} \quad (1\text{-}2)$$

where k^{rad} and k^{nr} are the radiative and nonradiative rate constants, respectively. The simple general expression of QY can be:

$$QY = \frac{number\ of\ emitted\ photons}{number\ of\ absorbed\ photons} \quad (1\text{-}3)$$

The QY is related to the rate at which the excited level is depopulated k_{obs} and to the radiative rate constant k^{rad}. Then the equation can be further expressed as:

$$QY_{int} = \frac{k^{rad}}{k_{obs}} = \frac{\tau_{obs}}{\tau_{rad}} \quad (1\text{-}4)$$

The quantity defined in Eq. (1-4) is called the intrinsic QY which means the QY of the metal-centred luminescence upon direct excitation into the 4f levels. Its value reflects the extent of nonradiative deactivation processes occurring both in the inner- and outer-coordination spheres of the metal ion. In absence of nonradiative deactivation processes, namely $k_{obs} = k^{rad}$ and the QY value would be equal to 1, which is very rare. The intrinsic QY essentially depends on the energy gap ΔE between the emissive state of the metal

ion and the highest sublevel of its ground state. The smaller this gap can easier lead to the nonradiative deactivation processes. Determination of the intrinsic quantum yield with Eq. (1-4) requires evaluation of the radiative lifetime which is related to Einstein's rates of spontaneous emission A from an initial state $|\Psi_J>$ characterized by a quantum number J, to a final state $|\Psi'_{J'}>$:

$$A(\Psi_J, \Psi'_{J'}) = k^{rad} = \frac{1}{\tau_{rad}} = \frac{64\pi^4\tilde{\nu}^3}{3h(2J+1)}\left[\frac{n(n^2+2)^2}{9}D_{ED} + n^3 D_{MD}\right] \quad (1\text{-}5)$$

where $\tilde{\nu}$ is the mean energy of the transition, n is the refractive index, h is Planck's constant, D_{ED} is dipole strength of an induced electric dipole (ED) f–f transition, and D_{MD} is dipole strength of an induced magnetic dipole (MD) f-f transition.

In fact, those calculations may result in large errors because they are pertaining to the hypotheses made within J-O theory. In some cased, up to 20% errors even larger could be obtained for Ln^{3+} ions.[77, 107] Bünzli et al. addressed two important points to correct the errors.[77] The first one is the radiative lifetime features one emitting state. Secondly, the radiative lifetime is not a constant for a given ion and a given electronic level.

In recent years, as instruments such as integrating sphere setups are increasingly becoming more available, several groups have described a technique for measuring the absolute upconversion quantum yield (UCQY) of Ln^{3+}-doped UCNPs based on the use of a commercial fluorimeter and an integrating sphere (Figure 1.8).[108-112] The absolute UCQY is defined as:

$$\Phi_{UC} = \frac{Photons\ emitted}{Photons\ absorbed} = \frac{L_{sample}}{E_{reference} - E_{sample}} \quad (1\text{-}6)$$

where L_{sample} is the emission intensity, $E_{reference}$ and E_{sample} are the intensities of the excitation light not absorbed by the sample and the reference sample, respectively.[113] This technique allows for direct acquiring of the UCQY values in a single measurement through measuring the emission spectra and absorbance of the samples. However, there are still lack of a standard guide of optical corrections for the systems and consolidated reference sample for the corrections, which could lead to unknown errors from lab to

lab for one same sample.

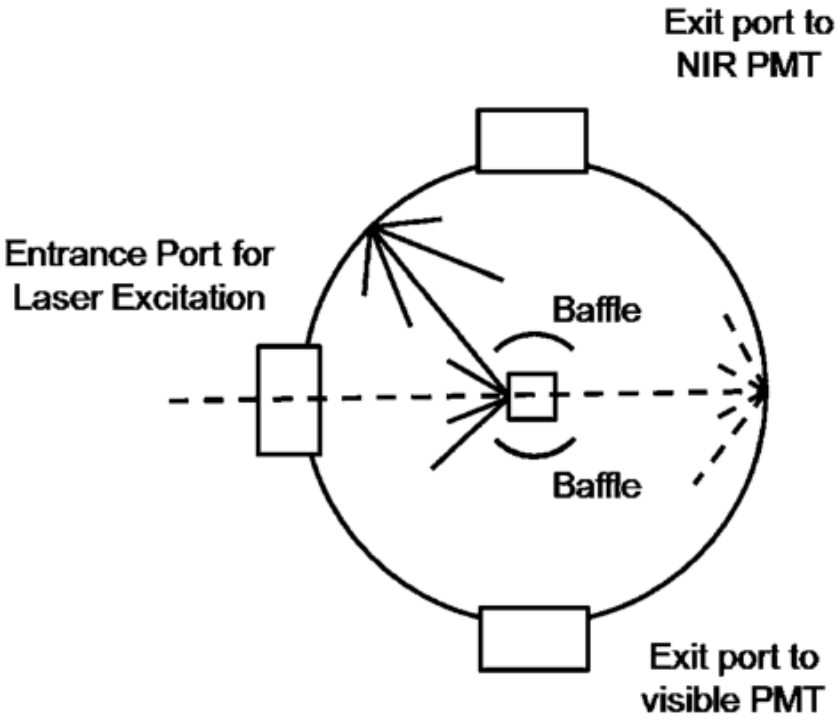

Figure 1.7 Illustration of the integrating sphere setup for luminescence measurements. Dashed line: excitation light. Solid line: sample emission. Reprinted of The Royal Society of Chemistry.[109]

Although Ln^{3+}-doped UCNPs have been used for various applications in reported literatures, the major bottleneck for the further practical applications of Ln^{3+}-doped UCNPs is their low UCQYs. So far, a number of absolute UCQY values have been obtained, for example, some of the high UCQY values of Yb^{3+}/Er^{3+}-based systems are 7.8% for a μm-sized $NaYF_4:Yb^{3+},Er^{3+}$ at a power density of 22 W cm^{-2}, and 5% for 40 nm-sized core/shell $LiLuF_4:Yb^{3+}$, Er^{3+}@$LiLuF_4$ NPs dispersed in hexane at a power density of 127 W cm^{-2}.[108, 114] Recently, the highest values of 9% and 10% have been reported at a similar power density of 20 W/cm^2 for 45 nm $NaYF_4:Yb^{3+},Er^{3+}$@$NaYF_4$ core/shell NPs[115] and 3 μm $NaYF_4:Yb^{3+},Er^{3+}$ bulk material[116]. However, these values are still low especially comparted with the conventional downshifting luminescence nanomaterials like organic dyes or QDs. The brightness of Ln^{3+}-doped UCNPs is further decreased when combined with mediums such as biological tissue, which

strongly restricts their commercial biomedical applications. Therefore, it is very essential to enhance the UCQY of UCNPs, enabling them with high UCL output and more suitable for commercial applications. For that reason, a variety of methods have been proposed to improve UCL, which can be summarized into the following six categories[100]:

(1) selection of the host materials

(2) optimization of the dopant concentrations

(3) intentional cation incorporation

(4) surface passivation

(5) plasmonic enhancement

(6) excitation manipulation

Fortunately, great progress has been made in the field of UCL enhancement and there are many reviews that summarize numerous examples for each single category.[117-126] Hence, we are not going to address all these strategies in this section but we will rather introduce the host materials for UCL in the following section.

3.3 Host materials

Since the emissive peak positions of Ln^{3+} ions are largely unaffected by the external environment, they can be incorporated into a wide variety of inorganic matrices while still exhibiting their characteristic transition properties. The UC efficiency of Ln^{3+} is typically dependent on the structure, local site symmetry, crystal field (CF) strength, and phonon energy of the host materials.[100] Therefore, it is essential to carefully select the host materials for achieving efficient UCL.

Generally, the host materials are desired to be transparent within the wavelength range and the additional merits such as low phonon energy, high optical damage threshold, and close lattice matches to Ln^{3+} dopants are critically expected as well. To date, a large number of suitable matrices doped with Ln^{3+} ions showing upconversion properties have been reported, such as oxides, oxysulfides, fluorides, phosphates, vanadates, molybdates, titanates, zirconates, silicates, and hydroxides.[127-134] Table 1.1

lists some of the above-mentioned host materials with the parameters of interest.

Table 1.1 Site symmetry of dopant, CF strength, and phonon energy of some host materials with different compositions.

Host	Site symmetry	CF strength (cm^{-1})	Highest phonon energy (cm^{-1})	Ref.
Gd_2O_3	C_2	554	600	135, 136
Y_2O_3	C_2	570	380	137, 138
YVO_4	C_{2v}	408	890	139, 140
Gd_2O_2S	C_{3v}	364	520	141, 142
LaF_3	C_2	277	300	143, 144
$LaCl_3$	C_{3h}	116	240	144, 145
$LiYF_4$	S_4	176	330	146, 147
$NaYF_4$	C_2 (or C_s)	385	350	148-150

Phonon energy of the host matrix has a profound effect on UC efficiency. Low phonon energies of host materials are favourable for Ln^{3+} doping to achieve intense UCL, as it allows for low multiphonon relaxation rates and minimal nonradiative energy losses. However, sometimes phonon-assistance is essential for compensation of the energy levels mismatch in some UCL processes like CSU and ETU. Hence, there is a balance between phonon energies and UCL efficiency. Among the listed host materials, fluorides such as $NaYF_4$, owing to the low phonon energy (350 cm^{-1}) and high chemical stability, are considered to be the most efficient UCL host materials for many applications.[151, 152]

Except for the phonon energy, the crystal structure of the host matrix also significantly affects the UC efficiency, for instance, the local site symmetry and CF strength around Ln^{3+} dopants determine their intrinsic electronic transitions. In principle, low-symmetry is more desirable than high-symmetry for the UCL hosts due to the higher 4f-4f transition probabilities of low-symmetry hosts.[153-155] According to the most reports, hexagonal-phase $NaYF_4$ has a higher UCL efficiency than the cubic

$NaYF_4$; for instance, the UC efficiency of the green emission in hexagonal-phase $NaYF_4$:Yb^{3+}/Er^{3+} is approximately 10 times stronger than that in cubic $NaYF_4$:Yb^{3+}/Er^{3+}.[156] By taking advantage of site selective spectroscopy, it was shown that the superior UCL emission originates from the interaction of the dopants located on two different lattice sites.[157] Moreover, Tu et al. revealed of local site symmetry breakdown in this $NaYF_4$ family of disordered crystals by using Eu^{3+} as optical probe in the crystal (Figure 1.8).[148] Still, there is much debate about the spectroscopic site symmetry of Ln^{3+} ions doped in $NaYF_4$, particularly in hexagonal $NaYF_4$, which therefore needs more deep investigations.

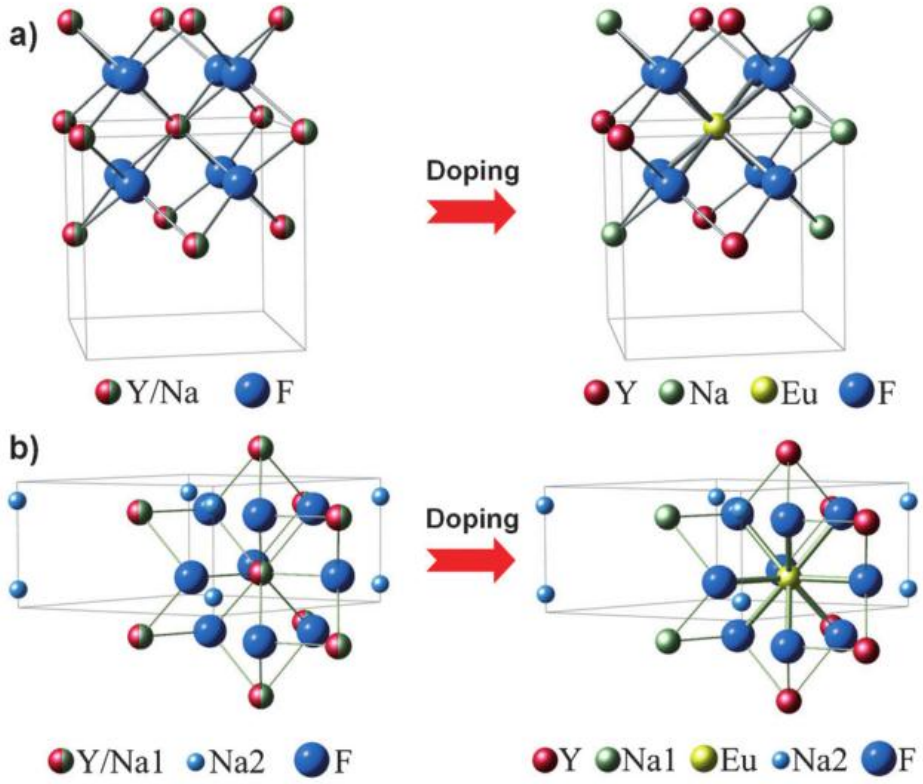

Figure 1.8 Illustration showing the breakdown of crystallographic site symmetry of Eu^{3+} in $NaYF_4$ nanocrystals. (a) α-$NaYF_4$ and (b) β-$NaYF_4$. Reprinted from Wiley-VCH Verlag GmbH & Co. KGaA.[148]

Besides, the lattice parameters and the localized structure of the host matrix could significantly influence the energy transfer between Ln^{3+} dopants thus leading to novel photophysical processes. For example, as the doped Ln^{3+} ions are distributed in the

tetrad clusters in the lattice, the excitation energy within the Yb^{3+} sublattice was preserved and the migration of excitation energy to the defects was minimized, thus leading to an unusual four-photon violet UC emission from Er^{3+} that was observed in orthorhombic KYb_2F_7:Er NPs. The UCL intensity of KYb_2F_7:Er NPs was over 8 times higher than the previously reported value of $NaYF_4$:Yb,Er NPs (Figure 1.9).[158]

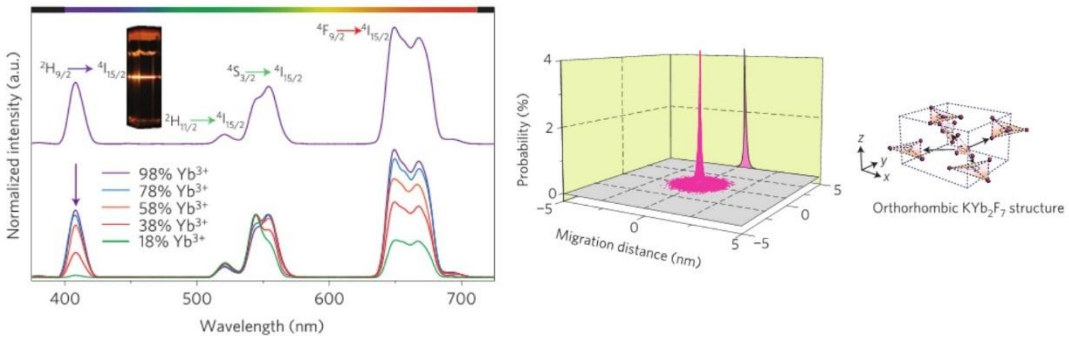

Figure 1.9 UCL spectra of KYb_2F_7:Er (2 mol%) (top) and KYb_2F_7:Er/Lu (2/0-80 mol%; bottom) nanocrystals. The probability of finding the excitation energy plotted against migration distance using Monte Carlo simulations for a KYb_2F_7 crystal. Reprinted from Macmillan Publishers Limited.[158]

Among the host materials, the RE_2O_2S hosts e.g. the hexagonal-phase Gd_2O_2S with a trigonal structure (*P-3m1* space group) have been extensively studied for UCL for years due to their low phonon energy (Gd_2O_2S, 520 cm^{-1}). In 2013, Martín-Rodríguez et al. reported the UCQY values of 12 ± 1% and 8.9 ± 0.7% for optimized Gd_2O_2S:10%Er and β-$NaYF_4$:25%Er, respectively, showing the higher UCL efficiency of Gd_2O_2S:10%Er than β-$NaYF_4$:25%Er under monochromatic excitation around 1500 nm at a power of 700 W/m^2.[159] In the same year, Pokhrel et al. found that the UCQY in the M_2O_2S:Yb^{3+}/Er^{3+} (M = Gd, Y, La) phosphors are 3~4 times higher than that of β-$NaYF_4$:20%Yb^{3+}/2%Er^{3+} at lower excitation power densities (Figure 1.10).[160]

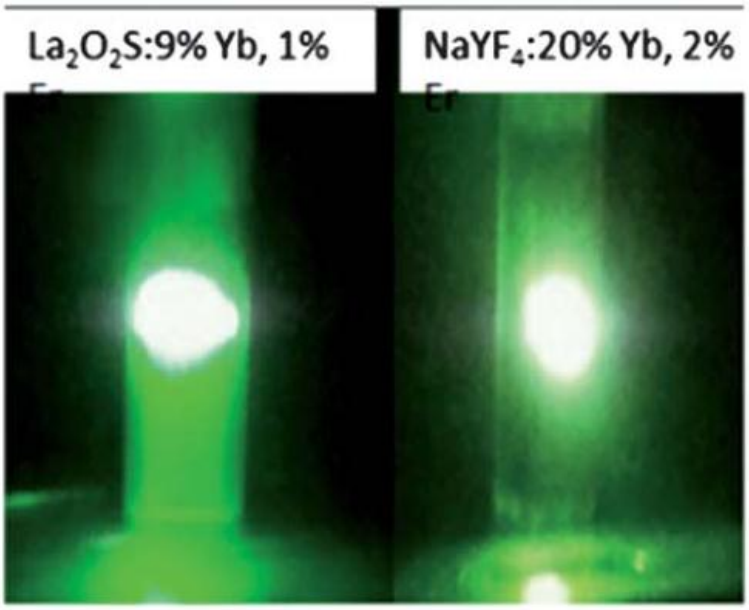

Figure 1.10 Digital image showing the difference in intensity of the green (550 nm) emissions of $La_2O_2S:Yb^{3+}/Er^{3+}$ and β-$NaYF_4$:20%Yb^{3+}/2%Er^{3+} NPs to the naked eye at 100 mW under 980 nm excitation. Reprinted from The Royal Society of Chemistry.[160]

In 2014, our group proposed to use gadolinium oxysulfide ($Gd_2O_2S:Eu^{3+}$ and $Gd_2O_2S:Er^{3+},Yb^{3+}$) based NPs for trimodal imaging.[161] Then, this type of lanthanide doped Gd_2O_2S NPs has been used for mesenchymal stem cell labelling, tracking, and UC bioimaging[162-164], showing great promise for bio-applications (Figure 1.11). However, the NPs were synthesized through a complicated solid state sintering method, causing a large size (>80 nm) and agglomerations which led to the NPs being metabolized and eliminated by the hepatobiliary system in several months in our recent study[164]. Small (≤20 nm) or even ultrasmall sized NPs (≤10 nm) with a good water dispersity can overcome those drawbacks. Therefore, a new method for synthesizing uniform and small RE_2O_2S must be explored. Meanwhile, as mentioned by Zhang et al. in their review paper[165], no core/shell synthesis strategy for RE_2O_2S NPs has not yet been formulated. Besides, no further investigation of surface modification of those as-prepared RE_2O_2S NPs limit their applications in the field of nanomedicine.

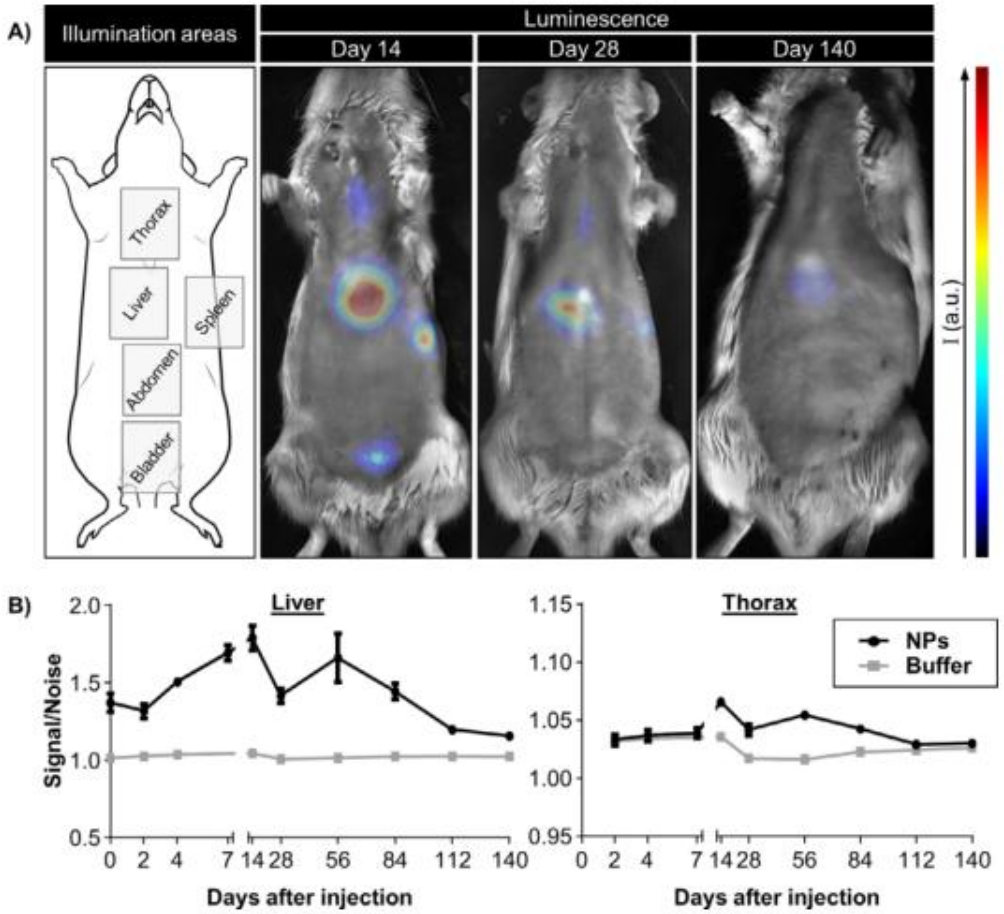

Figure 1.11 Bioimaging illustration of Gd_2O_2S: Yb^{3+},Tm^{3+} NPs carried out in our group. Reprinted from Elsevier Ltd.[164]

3.4 Controlled synthesis of Ln^{3+} doped nanoparticles

Suitable crystalline phases, narrow size distribution, and uniform shapes are prerequisites for lanthanide-doped luminescent NPs to be used as optical probes for bioapplications. Up to now, a variety of chemical synthetic strategies have been developed to synthesize high-quality lanthanide-doped luminescent NPs featuring controlled morphology, good dispersibility, high crystallinity, and desirable optical properties. Hitherto, three popular strategies including hydro(solvo)thermal synthesis, thermal decomposition, and high-temperature coprecipitation have been demonstrated to synthesize high-quality core NPs. To further manipulate the optical properties, the core/shell structures are designed and open new opportunities for various applications. Several strategies including seed-mediated heat-up, Ostwald ripening, successive layer-

by-layer, cation exchange, and non-epitaxial growth have been adopted to construct the core/shell structures. In this section, we would like to highlight the most representative synthetic approaches reported in the past decade to prepare high-quality core and core/shell Ln^{3+} doped NPs.

Routes to the Synthesis of Core Nanoparticles

1) Hydro(solvo)thermal Synthesis

The hydro(solvo)thermal synthesis method usually needs specialized reaction vessels such as autoclaves that provide a high-pressure and sealed environment and thus to promote reactions between solid precursors. As a consequence, this strategy produces high crystalline nanomaterials while under relatively mild conditions (<300 °C, no need of protective atmosphere) when compared to other synthetic routes. In a typical synthesis, some organic additives like oleic acid, polyethylenimine, ethylenediaminetetraacetic acid, and cetyltrimethylammonium bromide are generally added.[166-169] These organics in the reaction can simultaneously control over the crystalline phases, sizes, and morphologies and the resulting nanomaterials are coated with functional groups with specific purpose. For example, Zhang et al. adopted a facile hydrothermal approach (130~230 °C) in which oleic acid was utilized as a stabilizing agent to prepare uniform Ln^{3+}-doped both cubic and hexagonal $NaYF_4$ arrays with controlled nanorods, nanotubes, and flower-patterned nanodisks (Figure 1.12).[170] These nanoarrays offer great potential as light sources for miniaturized solid-state lasers applications.

By using the hydro(solvo)thermal syntheses, a variety of Ln^{3+}-doped inorganic NPs with different matrices such as fluorides ($NaYF_4$, $NaLuF_4$, $BaGdF_5$, YF_3, LaF_3, GdF_3, CaF_2, and $KMnF_4$), oxyfluorides (LaOF), and oxides (ZrO_2, ZnO, Y_2O_3, Gd_2O_3, and TiO_2), featuring high crystallinity, dispersity, and well-controlled crystal phases, sizes, and shapes have been synthesized.[171-178]

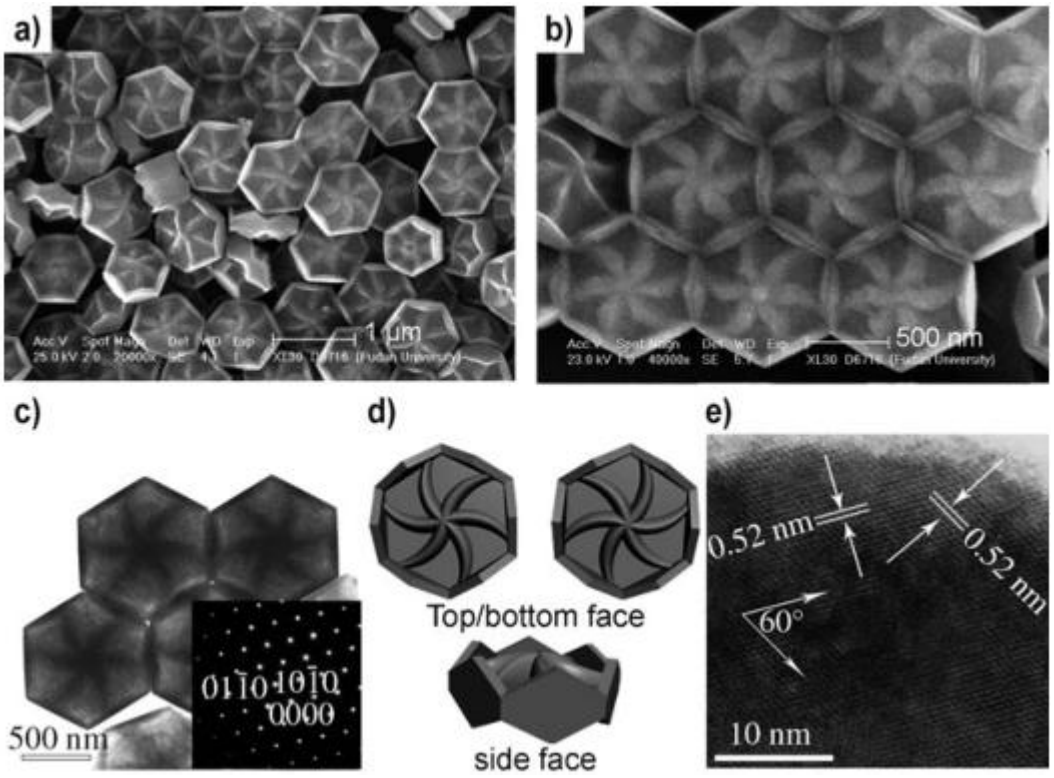

Figure 1.12 SEM and TEM images of arrays of flower-patterned hexagonal disks of β-$NaYF_4$. Reprinted from Wiley-VCH Verlag GmbH & Co. KGaA.[170]

2) Thermal Decomposition

Thermal decomposition method generally utilizes organometallic compounds such as metal trifluoroacetate as precursors which decompose at an elevated temperature in the high-boiling point organic solvent mixtures such as oleic acid, oleylamine, tri-n-octylphosphine oxide, and 1-octadecene. In 2005, one of the earliest reports of this approach was published by Zhang et al.[179] who synthesized highly monodisperse LaF_3 triangular nanoplates via the thermal decomposition of the single-source precursor $La(CF_3COO)_3$) in the presence of oleic acid/octadecene mixture solution under high temperature of 315 °C. This method was then extended as the most commonly used route to prepare high-quality Ln^{3+}-doped NPs of various compositions, especially when adding one of alkali metal trifluoroacetates (for instance, CF_3COOLi, CF_3COONa, and CF_3COOK) in the above mixture can further form alkali metal rare-earth fluorides. For example, Murray's group reported uniform hexagonal $NaYF_4$:Yb/Er NPs with a diverse family of morphologies (spheres, rods, hexagonal prisms, and plates) by using the

thermal decomposition method.[180] More importantly, these as-prepared $NaYF_4$ NPs can be assembled into monolayer and double-layer with different shapes of the $NaYF_4$ NPs (Figure 1.13).

So far, a series of monodisperse Ln^{3+}-doped fluoride NPs based on diverse host materials such as $LiYF_4$, $LiLuF_4$, $NaYF_4$, $NaGdF_4$, $NaLuF_4$, $BaYF_5$, KY_3F_{10}, CaF_2, SrF_2, YOF, LaOF, and GdOF have been achieved through this method.[181-187]

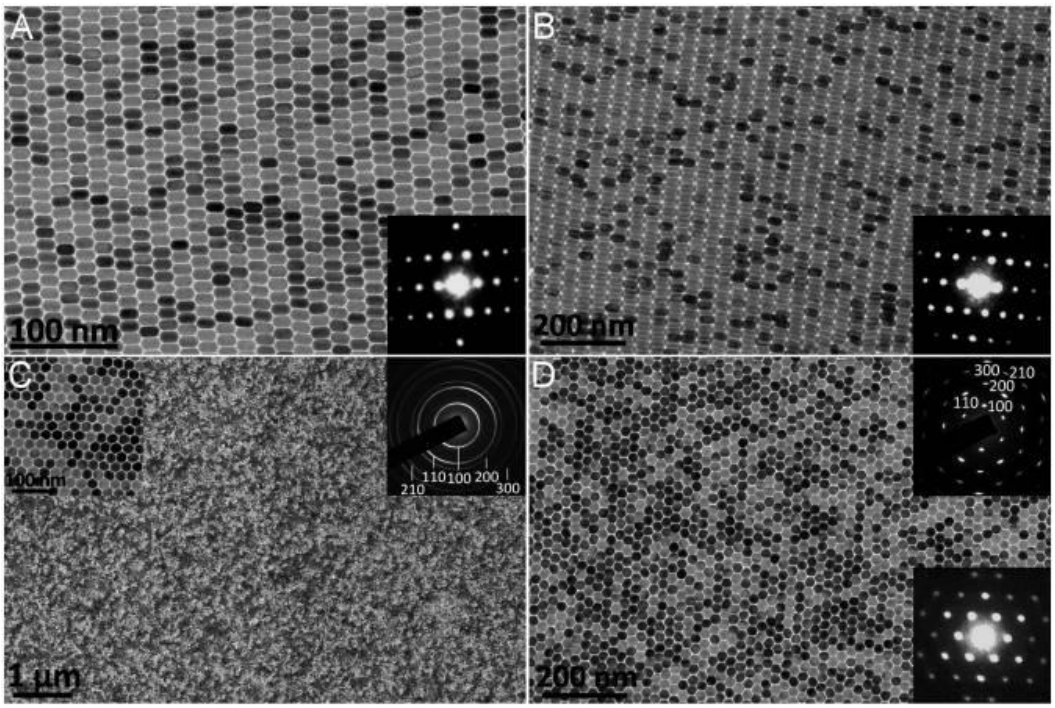

Figure 1.13 Shape-directed assembly monolayer and double-layer superlattices of as-prepared $NaYF_4$ NPs. Reprinted from National Academy of Sciences.[180]

3) High-temperature Coprecipitation

Compared to the two methods described above, high-temperature coprecipitation approach is expected to be more convenient and favourable because of its low cost for required equipment, simple protocols, and short reaction time.[188] By using oleic acid as surfactant and 1-octadecene as solvent, Li and co-workers first reported the high-temperature coprecipitation for the synthesis of highly uniform β-$NaYF_4$:Yb/Er/Tm UCNPs (Figure 1.14) with controllable shapes, sizes, and intense UCL.[189] This protocol was based on the formation of small amorphous $NaYF_4$ coprecipitates at room

temperature followed by the growth of NPs at elevated temperatures (300 °C). Since then, this method has been extensively adopted to prepare monodisperse Ln^{3+}-doped fluorides.[100, 188] Specifically, this method can be used for synthesis of monodisperse and uniform NPs with ultrasmall size (<10 nm).

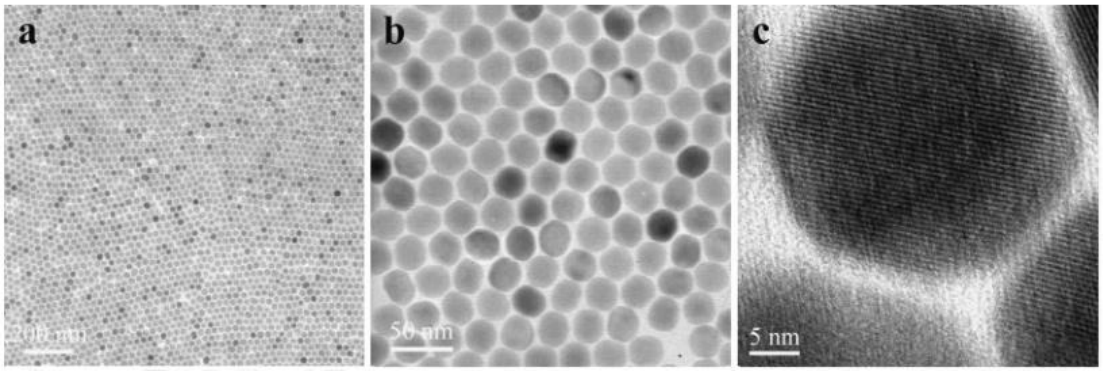

Figure 1.14 TEM images of Ln^{3+}-doped $NaYF_4$ UCNPs synthesized by high-temperature coprecipitation approach. Reprinted from WILEY-VCH Verlag GmbH & Co. KGaA.[189]

Routes to the Synthesis of Core/shell Nanoparticles

1) Seed-mediated shell growth

Seed-mediated shell growth is one of the most frequently used methods to prepare core/shell UCNPs with a uniform morphology and size. Generally, the core of UCNPs is first synthesized and washed, then the purified core is utilized as seed nuclei for the epitaxial growth of the outer shell layer, as shown in Figure 1.15a. In particular, the concentration of shell precursor needs to be carefully controlled for avoiding homogeneous nucleation of the shell instead of formation of core/shell structure. Then the shell thickness can be tuned by adjusting the mole ratio of core to shell precursor and multi layers addition to the core can be carried out by simply repeating the core/shell synthesis procedure. However, the lattice match between the host of core and that of shell is strictly required for the successful epitaxial growth of shell. In spite of the universality of this strategy for many core/shell UCNPs like EuF_3@GdF_3, $NaYF_4$@$NaYF_4$, $NaYbF_4$@CaF_2, and $NaGdF_4$@$NaGdF_4$, it is somehow time-consuming and laborious especially for the synthesis of core/multi-shell UCNPs.[187, 190-

192

2) Ostwald Ripening

Ostwald ripening method was first utilized for the synthesis of $NaYF_4$ based core/shell UCNPs by van Veggel's group.[193] The process is that the smaller α-phase is added as sacrificial nanoparticle in the solution where the larger β-phase exists, driving by Ostwald ripening, the free monomers tend to deposit on the larger stable core NPs and finally the core/shell structure forms (Figure 1.15b). The shell thickness and multiple shells of the core/shell NPs can be precisely controlled by simply repeating the defocusing and self-focusing cycle by adding the smaller α-phase. This method can be easily extended to prepare other high-quality core/shell NPs with different compositions.

3) Successive Layer-by-layer

Successive layer-by-layer (SLBL) shell deposition is a more facile protocol to prepare core/shell UCNPs especially with multishells (Figure 1.15c) compared to above two approaches. In this strategy, the shell precursors are added at the reaction temperature and the shell thickness can be well controlled from 0.36 nm to more than 8 nm by tuning the amounts of shell precursors.[194] More importantly, the shell morphologies can be also controlled by changing the injection rate of shell precursors while the other conditions keep constant. This method has been extensively adopted for others like $LiLuF_4$@$LiLuF_4$.[108] With this method, core/mutishell UCNPs with multifunctions can be easily constructed.

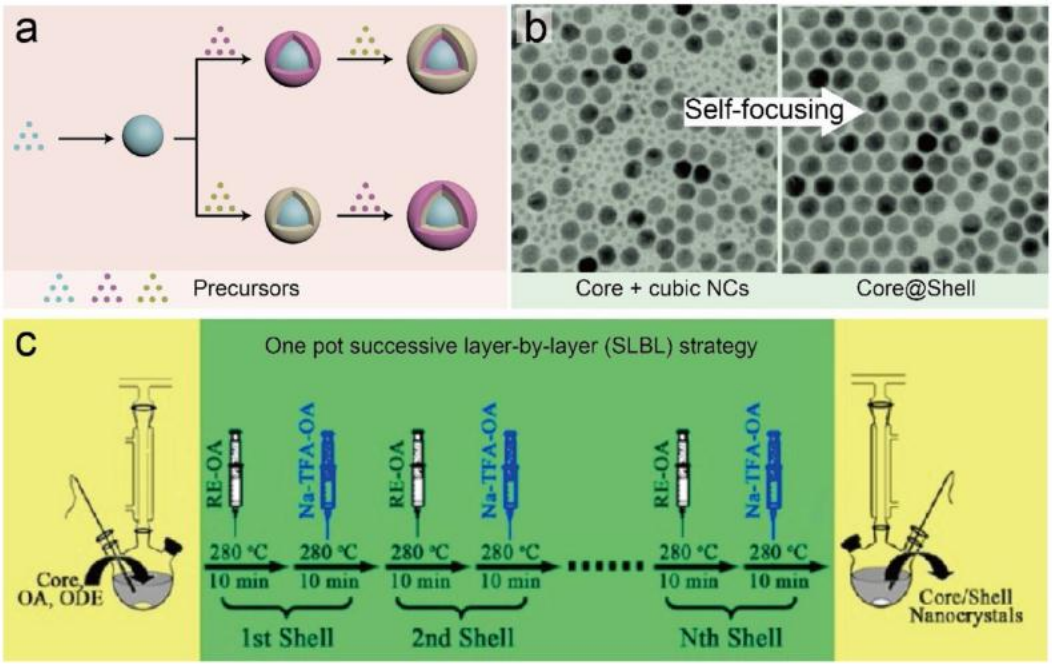

Figure 1.15 (a) Seed mediated shell growth method. (b) TEM images showing the self-focusing process of the NPs driven by Ostwald Ripening. (c) One pot successive layer-by-layer synthetic procedure for the core/shell UCNPs. Reprinted from American Chemical Society. [193-195]

4) Other Approaches

Besides the three above-mentioned methods, others like cation exchange (GdF_3@LnF_3[196]) in water solution and non-epitaxial growth between two very different hosts ($NaYF_4$:Yb/Er@CdSe[197], UCNP@SiO_2@mSiO_2[198]) have been demonstrated successfully for the synthesis of core/shell UCNPs as well.

Examining the integrity of core/shell UCNPs is necessary before using these NPs for further applications. The characterization techniques include direct observation of the NPs by high-resolution transmission electron microscopy (HRTEM), high-angle annular dark field scanning TEM (HAADF-STEM), energy dispersive X-ray spectroscopy (EDS), electron energy-loss spectroscopy (EELS), X-ray photoelectron spectroscopy (XPS), and X-ray powder diffraction (XRD), and indirect ways like photoluminescence (PL), photoluminescence lifetime, and dynamic light scattering (DLS).

Routes to the Synthesis of RE_2O_2S Nanoparticles

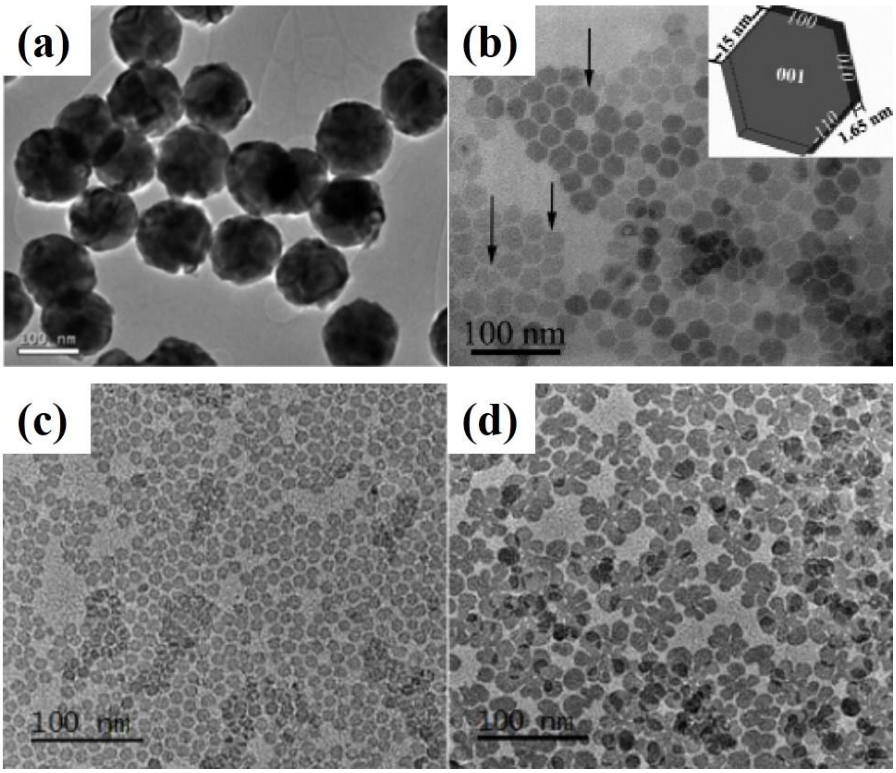

Figure 1.16 Gd_2O_2S NPs synthesized through different methods (a) high temperature sintering under Ar/H_2S atmosphere[161], reprinted from Royal Society of Chemistry; (b) thermal decomposition using the single precursor[199], reprinted from American Chemical Society; (c, d) thermal decomposition using elemental S_8 as sulfur source[141], reprinted from Royal Society of Chemistry.

Conventionally, the bulk RE_2O_2S can be synthesized by partial sulfidation of oxides, oxidation of sulfides or reduction of sulfates under high temperature and specific atmosphere.[200] The produced large particles limit their applications towards biomedicine. Several strategies for synthesizing RE_2O_2S NPs have been demonstrated as well. For example, our group reported a novel strategy for the synthesis of Gd_2O_2S:Eu NPs.[201] In this strategy, the rare-earth nitrates and urea were added in a water/ethanol mixture, following a dissolution, the rare-earth hydroxycarbonate precursor was formed. After purification, the obtained powder was first sulfurized by Ar/H_2S at 750 °C for 90 min and then maintained in an argon atmosphere only at 850 °C for 4 h. The final products were crystalline and spherical Gd_2O_2S NPs by determination

of XRD and TEM (Figure 1.16a). Importantly, the diameter of NPs can be tuned by adjusting the water/ethanol ratio and reaction time. In the following years, we demonstrated that the Ln^{3+} doped Gd_2O_2S NPs synthesized by this method or with slight modification were successfully utilized for various applications such as biolabeling, fluorescence, magnetic resonance (MR), and computed tomography (CT) bioimaging.[161-164] However, there are disadvantages like sophisticated synthesis procedure, rigorous reaction conditions, evitable aggregations and resulted large size of NPs, which still limit the extensive bioapplications of the Gd_2O_2S NPs.

Some other organic medium based strategies for the synthesis of RE_2O_2S including Gd_2O_2S NPs were reported in recent years. The obtained NPs are organic ligand coated, monodisperse, small-sized (ranging from 5 to 40 nm), and multiple shapes available (nanoplates, nanorods, and nanospheres, Figure 1.16b, c, and d). So far, to our best knowledge, there is no further core/shell construction example reported for Gd_2O_2S NPs. Additionally, the as-prepared organic ligand coated Gd_2O_2S NPs need an effective surface modification strategy to be hydrophilic for various bio-applications.

3.5 Surface modification

Ln^{3+}-doped inorganic NPs are of great potential as fluorescence nanoprobes for various bio-applications which require the nanoprobes possessing chemical stability, biocompatibility, water solubility and low toxicity. In order to assess these properties of the Ln^{3+}-doped inorganic NPs, one of the prerequisites is to functionalize them via surface modification. Much effort has been devoted into surface modification of Ln^{3+}-doped inorganic NPs and many strategies like surface salinization, ligand free, ligand oxidation, ligand exchange, ligand attraction, and layer-by-layer assembly (Figure 1.17).[202] In this section, we will focus on 3 most common strategies reported in the recent literature to synthesize hydrophilic NPs for versatile applications.

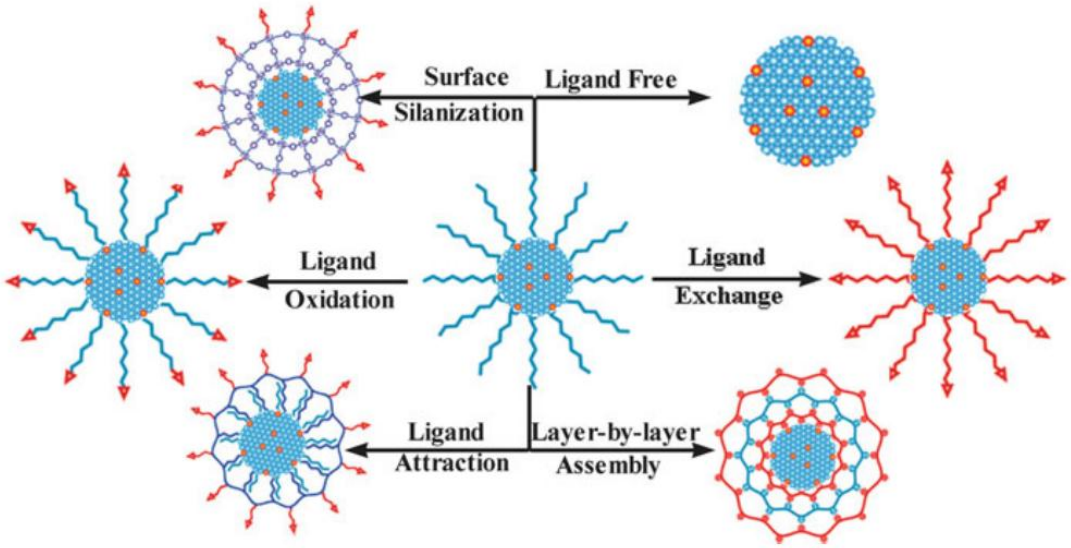

Figure 1.17 Typical surface modification strategies for synthesizing hydrophilic Ln^{3+}-doped inorganic NPs.[202] Reprinted from Royal Society of Chemistry.

1) Ligand Free

Ligand-free method is carried out by first mixing the oleic acid coated Ln^{3+}-doped NPs with acidic ethanol or water solution, then sonicating the mixture to yield water soluble NPs with bare Ln^{3+}. The surface Ln^{3+} ions of NPs can be directly conjugated of hydrophilic and biocompatible molecules with electronegative groups such as –COOH, $–NH_2$, and –OH since the Ln^{3+} ions have a strong coordination capability. Capobianco's group[203, 204] developed this facile approach to modify oleic acid capped $NaYF_4$:Yb/Er and $NaGdF_4$:Yb/Er UCNPs. In a typical acid treatment procedure, the oleic acid capped UCNPs were added in a HCl solution at pH 4 and then the oleate ligands were protonated by sonication, and the ligand-free NPs were obtained by several washing with water. This method yields a positive charged ligand-free nanoparticle which can be further conjugated with electronegative groups of biological molecules like heparin in an aqueous medium. Similarly, Liu et al.[205] adopted this acid washing strategy for the synthesis of PEG-coated $NaYF_4$:Yb/Er@$NaGdF_4$ core/shell UCNPs for bioimaging and drug delivery applications.

Since this method requires acid environment it is not well suitable for surface ligand removal for some oxides such as Gd_2O_3 and other acid-sensitive hosts because of the

high risk of dissolution.

2) Ligand Exchange

Ligand exchange is currently the most popular strategy to modify the surface of hydrophobic NPs since it does not affect their shapes, compositions, and morphologies. In a typical synthesis, the surface hydrophobic ligands such as oleic acid and oleylamine can be replaced with other organic molecules or polymers thereby rendering the NPs water soluble. These organic molecules or polymers should have one functional group which can be anchored on the nanoparticle surface tightly and another hydrophilic functional group outside of the nanoparticle to make nanoparticle capable of dispersing in the water or being further functionalized with other biocompatible molecules. In 2007, Zhang et al.[206] first demonstrated a robust and general ligand exchange strategy to transfer hydrophobic oleic acid capped inorganic NPs into water by using poly(acrylic acid) (PAA) as a new capping ligand at an elevated temperature (240 °C) in the polar solvent diethylene glycol (DEG). In this study, the authors found that the PAA-coated CdSe nanocrystals show ~54% higher quantum yield than the sample without ligand exchange. In 2011, Murray's group[207] proposed a more generalized ligand exchange strategy that enables sequential surface functionalization of NPs. Briefly, nitrosonium tetrafluoroborate ($NOBF_4$) was used to replace the surface attached molecules of NPs, thereby stabilizing the NPs in various polar media such as N,N-dimethylformamide (DMF), dimethylsulf-oxide (DMSO), or acetonitrile without aggregation or precipitation for a very long time. Those prepared hydrophilic NPs can be further functionalized by employing different capping organic molecules. Importantly, this approach proves applicable to the synthesis of various types of NPs such as metal oxides, metals, semiconductors, and dielectrics, without affecting their compositions and morphologies.

3) Ligand Attraction

The approach of ligand attraction mainly makes use of amphiphilic molecules whose hydrophobic group can interact between the surface hydrophobic molecules of NPs

through van der Waals force and the hydrophilic group can be exposed to the water environment making NPs water soluble. Since the coating amphiphilic molecules do not directly interact with the nanoparticle surface, this method is expected to produce water-soluble NPs with preserved optical properties. So far, the most commonly used amphiphilic polymers in this approach include DEPE-PEG, poly(maleic anhydride-alt-1-octadecene), poly(ethylene glycol)-block-poly(caprolactone), and tocopherol PEG.[191, 208-212]

3.6 Applications

Ln^{3+}-doped luminescent inorganic NPs possessing excellent physical and chemical properties such as large Stokes shift, long luminescence lifetimes, sharp emission bands, good chemical stability, and low toxicity have been widely used for various applications including light harvesting, display, optical security, nanomedicine, imaging, nanomedicine, optogenetics, and sensors. In this section, we would like to focus on two commonly mentioned applications of Ln^{3+}-doped luminescent inorganic NPs, imaging and temperature sensing.

Imaging

Ln^{3+}-doped inorganic NPs as biomedical nanoprobes play an important role in nanomedicine because of their unique electric, optical, and magnetic properties, and high stability, low toxicity, and resistance of photobleaching. Bioimaging particularly fluorescence, magnetic resonance (MR), computed X-ray tomography (CT), and photoacoustic imaging based on Ln^{3+}-doped nanoprobes offers a versatile strategy for visualizing morphological information in tissue and thus has become a powerful non-invasive tool for visualizing biological tissue. The Ln^{3+}-doped NPs not only can be used for just sole imaging mode but also multimode imaging when the they exhibit multifunction.

1) Fluorescence imaging

Downshifting Luminescence (DSL) Imaging. DSL exhibits distinguished optical properties such as narrow bandwidth, long-lived emission, high quantum yield, and

large Stokes shifts.[213] Most investigations of the DSL bioimaging are based on Eu^{3+}, Tb^{3+}, and Dy^{3+} doped NPs that can produce visible light under UV excitation.[214, 215] However, the UV light can irradiate both the NPs and the endogenous molecules to produce strong tissue autofluorescence, thus generating high background noise. Finally, excitation light, auto-fluorescence, and fluorescence generated by NPs can be further absorbed (Figure 1.18b) and scattered by biological tissues, thus reducing the intensity and penetration depth of fluorescence signal.[216] Compared with visible fluorescence imaging, photon scattering of biological tissue is smaller in near infrared (NIR) window, especially in the range NIR-II (1000–1700 nm) the background noise of strong auto-fluorescence tissues is greatly reduced (Figure 1.18c and d).[217] Therefore, fluorescence imaging using Ln^{3+}-doped NPs with NIR-II emission profiles has obvious advantages in superior imaging depth and contrast.

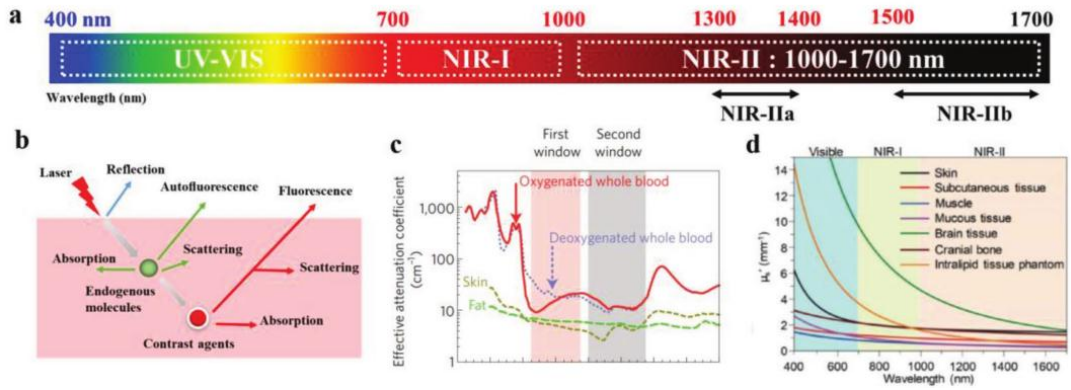

Figure 1.18 (a) Fluorescence imaging in different wavelengths. (b) Schematic interaction of between light and tissue. (c) Attenuation coefficient of skin, fat, and blood at different light wavelength. (d) Scattering coefficients (μ_s') of various tissues under different wavelength. Reprinted from WILEY-VCH Verlag GmbH & Co. KGaA.[216]

Some Ln^{3+} ions[218] such as Nd^{3+}, Er^{3+}, and Yb^{3+} listed in the Figure 1.19 can be excited directly or indirectly by NIR laser, and generate characteristic NIR-II emissions, which further decrease the background noise and provide great advantage in bioimaging. So far, the NIR luminescence efficiency of Ln^{3+}-doped NPs is still low compared to organic dyes. Sensitizer doping, matrix sensitization, organic dye sensitization, and

passivation shell are the main strategies to improve QYs.[219]

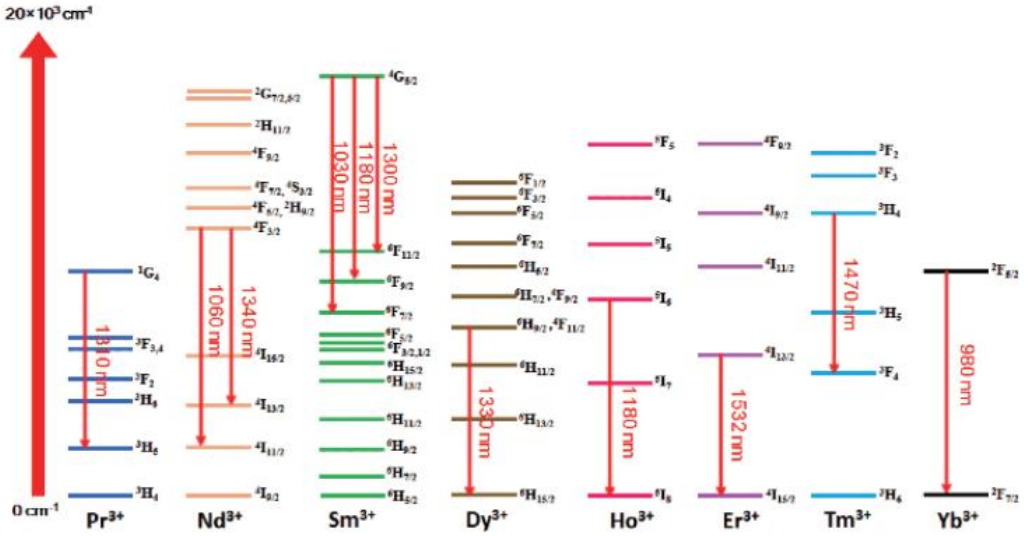

Figure 1.19 Energy level diagrams of Ln^{3+} ions with typical emissions within the NIR-II region. Reprinted from China Press and Springer-Verlag GmbH Germany.[218]

Upconversion Luminescence Imaging

In comparison with DSL imaging using UV light excitation, UCL imaging by using NIR laser as the excitation source have many advantages such as no autofluorescence, low phototoxicity, and large tissue penetration depth.[220-222] As a result, Er^{3+}, Tm^{3+}, and Ho^{3+} Ln^{3+}-doped materials with desirable UCL have been developed as a new class of luminescent probes.[223] In 1999, Zijlmans et al.[224] for the first time reported the UCL bioimaging based on 0.2-0.4 μm Y_2O_2S:Yb/Tm particles which were labelled with antibodies in order to bind specifically to antigens on intact cells or in tissue sections. Upon 980 nm laser excitation, these particles performed strong visible UCL which can be visualized and recorded by an epifluorescence microscope. After that, small-sized and highly-efficient Ln^{3+}-doped UCNPs based on fluorides, oxides, and other hosts have been well established for in vitro cellular and in vivo animal imaging.[225-227]

Time-Gated luminescence Imaging

Time-Gated luminescence (TGL) methodology can largely eliminate autofluorescence of tissue and light scattering interference, and collect the luminescence signal of a long-lived probe. Ln^{3+}-doped NPs with long luminescence

lifetimes, are widely used for high-contrast bioimaging via the TGL methodology.[228, 229] In principle, under pulsed excitation, the short-lived signals and long-lived luminescence signal start to decay (Figure 1.20a). After the short-lived background signal decays beyond the detection limit of the detector, the chopper turns open and allows the light to pass through it. In this case, the excitation and short-lived background signals are blocked, only the desirable long-lived luminescence signal is collected. Based on this TGL technique, signal-to-noise ratio can be remarkably enhanced through eliminating the deleterious short-lived background noise.

In 2016, Jin's group developed a time-gated UCL imaging system to realize high-contrast imaging of mice with long-lived UCNPs (Figure 1.20b). This system contained a pulsed 980 nm laser, a camera lens, an optical chopper, a microscope eyepiece, and an EMCCD camera. In their work, hydrophilic $NaLuF_4$:Yb,Tm UCNPs that are excited at 980 nm and emit at 800 nm, were used as the long-lived probe, and a pulsed laser was used to reduce the overall thermal accumulation to the mice as compared to the continuous-wave laser. The resulting time-gated image for a mouse was clear without any autofluorescence or scattered light interference, demonstrating that UCNPs have promise for background-free NIR imaging with a time-gated imaging system.

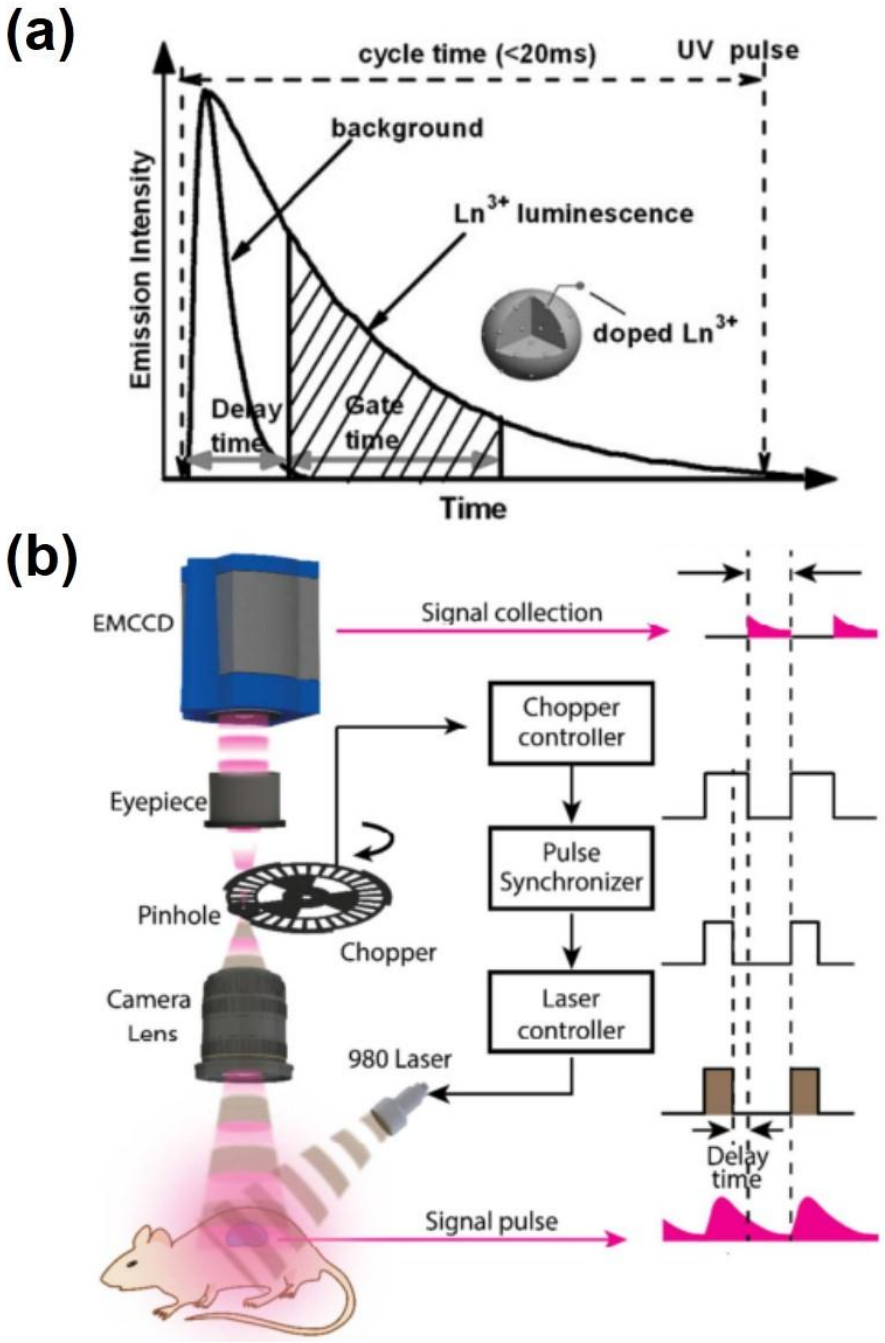

Figure 1.20 (a) Principle of time-gated luminescence technique. Reprinted from John Wiley and Sons.[213] (b) Schematic illustration of the time-gated luminescence system for in vivo NIR imaging. Reprinted from American Chemical Society.[230]

2) Magnetic Resonance Imaging

As one of the most powerful clinically medical imaging techniques, magnetic resonance imaging (MRI) has many advantages such as non-invasiveness, free outer

photon radiation, high spatial resolution, good contrast in soft tissues, and the ability to provide information related to blood circulation and blood vessels.[231, 232] MRI contrast agents play a vital role in improving the image quality by enhancing the image contrast between normal and diseased tissues. The contrast agents are generally classified as T_1 and T_2 contrast agents in terms of the magnetic properties and relaxation mechanisms.

The longitudinal T_1 relaxation rate describes the time after excitation for the magnetization to return to the equilibrium ground state. This return to energy equilibrium is accomplished by transferring the excess energy of the magnetic spins of the excited ^{1}H nuclei (protons) to the surrounding lattice, thereby giving the T_1 relaxation rate. The transverse T_2 relaxation rate is associated with the dephasing process of coherent, detectable net magnetization in a plane that is transverse to the direction of the main field of the MRI spectrometer magnet.[233, 234]

Contrast agents based on Gadolinium ion are commonly used as T_1 contrast agents, generating a positive image contrast. Currently, Gd complexes such as Gd-DTPA are typical MRI contrast agents for imaging blood vessels, and Gd^{3+}-based inorganic NPs have been widely investigated as potential T_1 MRI contrast agents in recent years.[235] For example, a very high relaxivity (r_1) value (r_1 = 28.39 $mM^{-1}s^{-1}$) was achieved for Gd^{3+} surface-doped $NaYF_4$:Yb,Er UCNPs, where the UCNPs were synthesized by cation exchange with Y^{3+} ions on the surface of $NaYF_4$:Yb,Er (Figure 1.21a). The MR images in Figures 1.21c, d, e, and f revealed a significant contrast enhancement in the liver area by injecting the NPs into the liver and spleen areas of mouse.

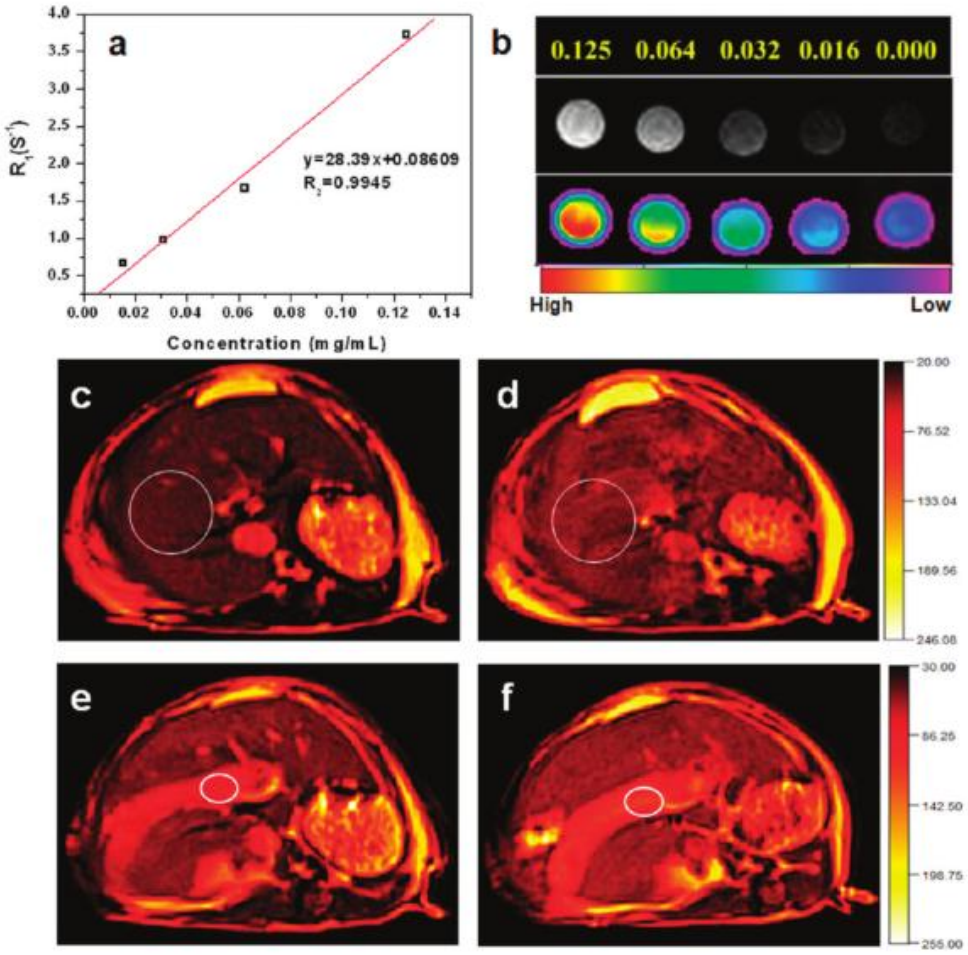

Figure 1.21 (a) Relaxation rate r_1 ($1/T_1$) versus various concentration. and (b) T_1-weight and colour-mapped MR images. MR images of the liver (c, d) and spleen (e, f) of mouse at pre-injection and at10 min post-injection of the as-prepared NPs by the authors. Reprinted from American Chemical Society.[236]

3) Computed Tomography Imaging

Computed tomography (CT) imaging is very common in clinical use to diagnose disease and monitor treatment because of its low cost and deep tissue penetration capability. Ln elements can be used as CT contrast agents due to their high X-ray attenuation. Therefore, various Ln-based host materials with high atomic numbers have been designed for CT contrast enhancement.[232] For example, Liu et al. reported that $NaYbF_4:Er^{3+}$ UCNPs showed a higher contrast effect than a clinical contrast agent.[237] Lu based NPs have been recently investigated as the Lu^{3+} ions have the highest atomic

number among Ln elements. Zhu et al.[238] found the Fe_3O_4@$NaLuF_4$:Yb,Er/Tm core/shell multifunctional NPs exhibiting almost five-fold higher contrast effects than the commercial iodinated agent. The longer circulation time and lower toxicity of the inorganic NPs compared to commercial agents make them a highly promising.

4) Photoacoustic Imaging

Photoacoustic imaging (PAI) is a technique that can overcome the high degree of scattering of optical photons in biological tissue by taking advantage of the photoacoustic effect. In principle, upon pulsed laser irradiation, the optical energy can be absorbed by endogenous biomolecules or exogenous contrast agents, which will be subsequently converted to localized heat, and then followed by the generation of a pressure rise through thermoelastic expansion. Such pressure rise will be propagated as an acoustic wave, and can thus be captured by ultrasonic transducers.[239] NIR organic dyes as photoacoustic contrast agents, which may provide functional imaging, are suffering from low chemical stability.[240] Ln^{3+}-doped inorganic NPs are candidates for PAI because of their chemical stability and ability of absorption in NIR region. Kumar Maji et al. proposed a unique PA signal enhancement strategy by making use of the heating capacity and luminescence quenching-induced non-radiative relaxation of UCNPs, thereby generating enhanced PA signal in water for in vivo PAI of the mouse kidney under 980 nm excitation (Figure 1.22).[241]

PAI performances of Ln-based inorganic NPs for deep tissue diagnosis are still limited by the low photoacoustic conversion efficiency as well as nonspecific background interferences, which would be the future direction of effort.[239, 242]

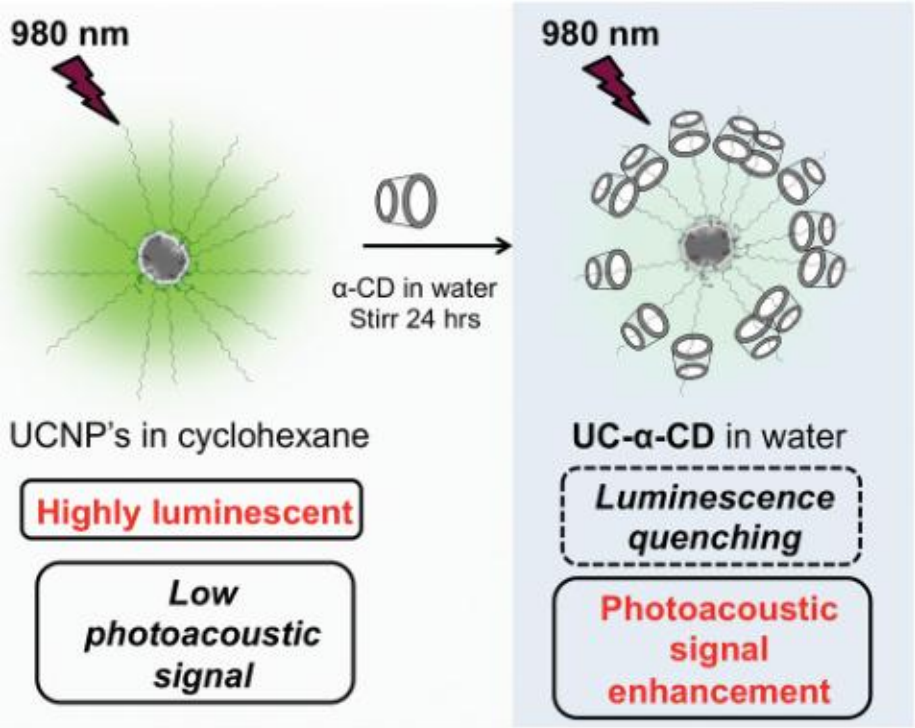

Figure 1.22 Schematic illustration of luminescence quenching effect and subsequent photoacoustic signal enhancement from UC-α-CD (α-CD = α-cyclodextrin) in water. Reprinted from WILEY-VCH Verlag GmbH & Co. KGaA.[241]

5) Temperature Sensing

Fluorescent nanothermometers can monitor local temperature changes in living cells and reveal fundamental insights into biological properties. In all fluorescence-based temperature sensing strategies, temperature is calculated from the measurement of various indicators, such as intensity, intensity ratio, peak position, polarization and lifetime.[243] When the value of these fluorescence indicators is quantified as Q, the rate of the change of Q related with temperature T is defined as the absolute sensitivity:

$$S_a = \left|\frac{\partial Q}{\partial T}\right| \tag{1-7}$$

To compare the fluorescent nanothermometers with different indicators, the relative sensitivity is used:

$$S_r = \left|\frac{1}{Q}\frac{\partial Q}{\partial T}\right| \tag{1-8}$$

The uncertainty (δ) reflects random variations in replicated independent measurements

and systematic effects in the measurement process. Temperature resolution (T_{min}) represents the smallest change in a temperature that causes a perceptible change in the fluorescence indicator, which is expressed:

$$\Delta T_{min} = \frac{\sigma}{S_a} \tag{1-9}$$

where σ is the standard deviation of the parameter used for temperature determination.

Nanothermometry has attracted many efforts in developing both temperature-responsive materials and detection procedures to achieve high temperature resolution in biosystems. Since $^3F_{2,3} \rightarrow {}^3H_6$ and $^3H_4 \rightarrow {}^3H_6$ of Tm^{3+}, $^2H_{11/2} \rightarrow {}^4I_{15/2}$ and $^4S_{3/2} \rightarrow {}^4I_{15/2}$ of Er^{3+} arising from their respective thermally coupled energy levels comply with Boltzmann distribution theory[244, 245], therefore the Er^{3+} and Tm^{3+} -doped UCNPs good candidates for fluorescence intensity ratio nanothermometer. For instance, Vetrone et al. first reported $NaYF_4:Er^{3+},Yb^{3+}$ NPs as the nanothermometer measuring the internal temperature of the living HeLa cell from 25°C to its thermally induced death at 45 °C (Figure 1.23).

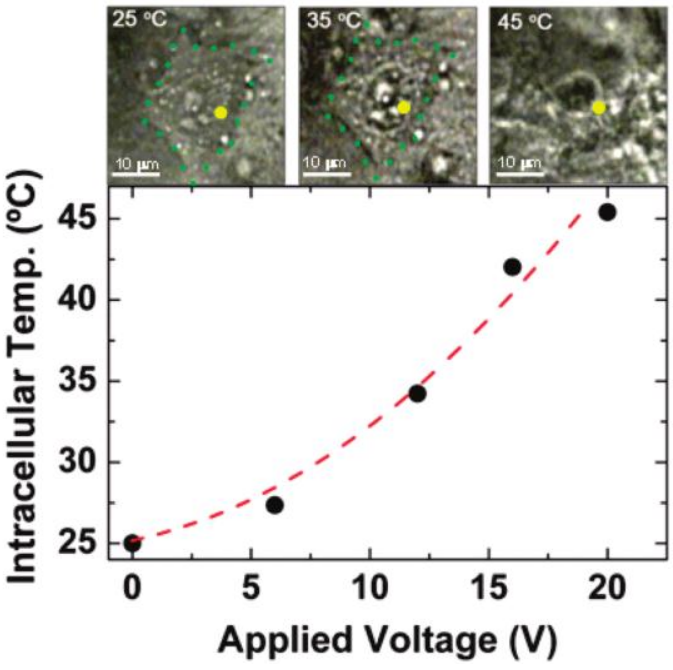

Figure 1.23 Temperature of the HeLa cell determined by the Er^{3+} ion fluorescence in the $NaYF_4:Er^{3+},Yb^{3+}$ NPs as a function of the applied voltage.[246]

4 Objectives of the manuscript

My PhD project entitled "New optical probes and a new imaging approach for deep in vivo application" is funded by the ministry of national education of France. Hence, the aim of the project is at first to synthesize new NPs with proper size, good biocompatibility and sufficient luminescence. Then these NPs will be further used for in vivo bioimaging applications. Regarding the chemical composition of the NPs, we focus on the Gd_2O_2S host material because it has been reported as good candidate for luminescence because of its intrinsic features. Besides, lanthanide-doped Gd_2O_2S NPs have been studied for years in our lab, showing great attractions for many applications especially for imaging.

This thesis will describe how we prepare the lanthanide-doped NPs with small size, good water stability, and efficient luminescence towards not only imaging but also nanothermometry applications.

Chapter 2 discusses a general method to synthesize rare-earth oxysulfide NPs. The Nd-doped Gd_2O_2S NPs were selected and deeply investigated as a new kind of multimodal imaging nanoplatform where the multiple techniques include NIR-II fluorescence, magnetic resonance, computed tomography, and ultrasound.

Chapter 3 discusses the synthesis and optical properties of core/shell NPs based on the lanthanide-doped Gd_2O_2S cores. A heterogeneous lanthanide-doped Gd_2O_2S@$NaREF_4$ core/shell structure and a homogeneous lanthanide-doped Gd_2O_2S@Gd_2O_2S core/shell structure were explored with a purpose of enhancing the optical properties of lanthanide-doped Gd_2O_2S core NPs. Then optical properties of both core and core/shell UCNPs have been comprehensively studied.

Chapter 4 discusses the temperature-dependent UCL properties of several types of lanthanide-doped Gd_2O_2S@$NaREF_4$ core/shell UCNPs towards temperature sensing application.

Chapter 5 discusses the potential of time-gated imaging at ~800 nm excitation and detection by using typically designed core/multi-shell UCNPs.

In order to achieve the goals, we seek for diverse technical supports from our collaborators including labs of LPCNO-INSA Toulouse, FJIRSM-CAS (China), INSERM-CNRS of University of Montpellier, BAM (Germany), LGC-UPS, and LASIRE-Université de Lille.

Chapter II: Ultrasmall rare earth oxysulfide for multimodal bioimaging

1 Introduction

In recent decades, biomedical imaging technologies have been exploited for early disease detection and diagnosis. Several imaging modes such as, computed tomography (CT), magnetic resonance imaging (MRI), photoacoustic imaging (PAI), positron-emission tomography (PET), single-photon-emission computed tomography (SPECT), and optical imaging (OI) have played important roles in observation of the structures and functions of biological systems, and providing important information concerning the pathogenesis, progression and treatment of diseases such as cancer.[247, 248] Using monomodal imaging technique usually cannot meet the requirements for high sensitivity and spatial resolution because of their respective drawbacks. Consequently, combination of two or more than two imaging modalities, so called dual- or multi-modal imaging, is a popular way to overcome those limitations.[249, 250] Nowadays, combining various components into one platform is the most commonly used strategy to take advantage of their respective functions. This strategy is impeded by the complicated composition and synthetic procedure, inevitable interference, poor reproducibility and uncertain pharmacokinetics, hence less accessible for clinical use. Alternatively, one component with multiple contrasting capacities remains more desirable due to the lower interference, simpler fabrication, defined structure, and far better reproducibility than the composite agents.

Recently, due to the development of instruments, OI in the second near-infrared (NIR-II) biological window (1000-1700 nm) has attracted much attention because of the deep tissue penetration, low light scattering and autofluorescence interference.[251-254] At present, many probes, such as small organic molecule dyes, inorganic quantum dots (QDs), and single-walled carbon nanotubes (SWCNTs), which are able to generate NIR-II fluorescence. Among them, rare-earth (RE) doped nanoparticles (NPs) have demonstrated great contrasting powers for NIR-II bioimaging because of their excellent optical performance such as large anti-Stokes or Stokes shift, sharp emission profiles, long lifetime, low biotoxicity, and low background autofluorescence.[250, 255] Generally,

Yb^{3+} or Nd^{3+} ions are single- or co-doped in RENPs to absorb 980 nm or 800 nm NIR excitation photons ($^2F_{7/2} \rightarrow {}^2F_{5/2}$ transition of Yb^{3+} ions, $^4I_{9/2} \rightarrow {}^4F_{5/2}$ transition of Nd^{3+} ions), where commercial diode lasers with low-cost, high-power are available which makes RENPs more suitable for bioimaging. Compared to fluorescence produced by radiative transitions, PA signal is produced by nonradiative decay pathways from the excited state to the ground state, after absorbing NIR photons. PAI is an emerging noninvasive imaging tool that can provide large penetration depth beyond the optical diffusion limit meanwhile maintaining high spatial resolution yet the sensitivity is not that satisfied. In the same way, ultrasound imaging (USI), also called echography, often coupled with PAI devices, allow also the visualization of deep body structure by recording echoes reflection of pulses ultrasonic waves. Single nanoparticle combined with NIR-II fluorescence, MR, CT, PA, and US functions can provide abundant imaging information to meet high requirements of modern medicine.

For complimentary but non-optical imaging, Gd^{3+} cation is particularly indicated. Indeed, gadolinium present important paramagnetic properties highly valuable for MRI as well as X-ray absorption capacities useful for CT in relation to its important atomic number (Z = 64).[256] In 2014, we proposed to use gadolinium oxysulfide ($Gd_2O_2S:Eu^{3+}$ and $Gd_2O_2S:Er^{3+}$; Yb^{3+}) based NPs for trimodal imaging using T_2-weighted MRI, CT and OI.[161] Then, this type of lanthanide doped Gd_2O_2S NPs has been used for mesenchymal stem cell labelling, tracking, and UC bioimaging[162-164], showing great promise for bio-applications. However, the NPs were synthesized through a complicated solid state sintering method, causing a large size (>80 nm) which led to the NPs being metabolized and eliminated by the hepatobiliary system in several months in our recent study[164]. Small (≤20 nm) or even ultrasmall sized NPs (≤10 nm) with a good water dispersity can overcome those drawbacks. Thanks to pioneer works[199, 257] on synthesis of rare earth oxysulfide (RE_2O_2S) in presence of high boiling temperature organic solvents, smaller (5~40 nm) NPs have been prepared. However, it still needs a reproducible and general synthesis route for RE_2O_2S NPs with good dispersity, uniform

size, and steady reaction yield.[127, 258] Besides, no further investigation of surface modification of those as-prepared RE_2O_2S NPs limit their applications in the field of nanomedicine.

In this chapter, we present a versatile strategy to synthesize 15 kinds of RE_2O_2S NPs with excellent monodispersity and small sizes. Further, a series of Nd-doped Gd_2O_2S NPs are successfully prepared by optimizations. Based on transmission electron microscopy (TEM), X-ray diffraction (XRD) and spectroscopy characterizations, we investigate the effects of size and doping concentration on the NIR-II downshifting luminescence intensity of Nd-doped Gd_2O_2S NPs. 3 surface modification methods are used to enable the Gd_2O_2S:Nd NPs from hydrophobic to hydrophilic. These PVP-coated Gd_2O_2S:Nd NPs display extremely low cytotoxicity. Finally, we demonstrate that PVP-coated Gd_2O_2S:Nd NPs are capable of four types of imaging configurations: NIR-II luminescence, PA, US, MR, and CT.

2 Experimental

2.1 Materials

N, N'-Diphenylthiourea (DPTU), $LiOH \cdot H_2O$, acetic acid, hydrochloric acid (HCl), Nitrosonium tetrafluoroborate ($NOBF_4$), *N*,*N*-Dimethylformamide (DMF), ethanol, methanol, chloroform, cyclohexane, KBr powder, and PVP (MW= 10000) were purchased from Sigma-Aldrich. Oleic acid (OA), oleylamine (OM) and tri-n-octylamine (TOA) were purchased from TCI. Milli Q water (18.2 MΩ.cm, 25 °C) was produced with by the purification system. All rare earth oxides (RE_2O_3, RE = Y, La, Ce, Pr, Nd, Sm, Eu, Gd, Tb, Dy, Ho, Er, Tm, Yb, and Lu) were purchased from Rhône Poulenc. $RE(CH_3COO)_3 \cdot 4H_2O$ were prepared by firstly dissolving moderate amount of the RE_2O_3 in excess acetic acid solution at 90 °C, then filtering and evaporating the solution, finally drying the resultant slurry in the oven at 70 °C. All chemicals were used as received without further purification.

2.2 Synthesis of ultrasmall RE_2O_2S NPs

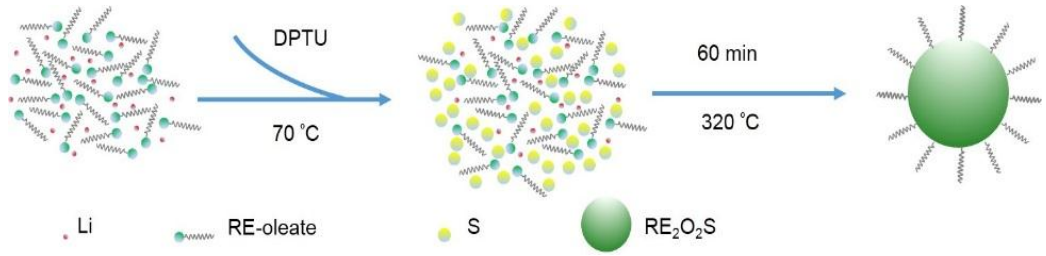

Figure 2.1 Schematic illustration of synthesis of RE_2O_2S NPs.

The RE_2O_2S NPs were prepared through a thermal decomposition method, as shown in Figure 2.1. In a typical synthesis, 1 mmol of $RE(CH_3COO)_3 \cdot 4H_2O$, 1 mmol of $LiOH \cdot H_2O$, 3 mL of OA, 7 mL of OM and 10 mL of TOA were mixed in a 100 mL three-necked round-bottom flask and heated to 160 °C under an argon flow with constant stirring for 30 min to form a clear solution, after that, the solution was cooled down to room temperature. Then, an ethanol solution (10 mL) of DPTU (3 mmol) was added dropwise and stirred for 30 min. The reaction mixture was then heated to 70 °C and maintained for 60 min to remove the ethanol. After ethanol was evaporated, the resulting solution was heated to 320 °C under an argon flow with vigorous stirring for 60 min, and then cooled down to room temperature (RT). The resulting NPs were collected by centrifugation (5000 rpm, 10 min) by mixing with ethanol, and washed for 3 times with both cyclohexane and ethanol. Note all RE_2O_2S (RE = Y, La, Ce, Pr, Nd, Sm, Eu, Gd, Tb, Dy, Ho, Er, Tm, Yb, and Lu) including Nd-doped Gd_2O_2S NPs were synthesized through above optimized conditions. For optimizing the reaction conditions, solvent ratio, amount of DPTU, reaction temperatures and times were varied.

2.3 Acid treatment

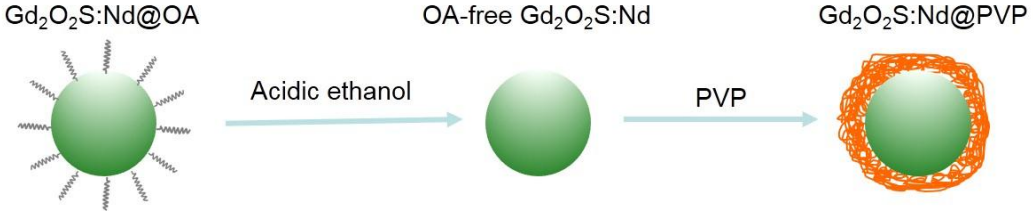

Figure 2.2 Schematic illustration diagram of acid treatment method.

Acid treatment method for removing oleic acid of NPs, especially for sodium rare-earth fluoride matrixes, has been reported in many publications. Briefly, as shown in Figure 2.2, the OA coated NPs were first added in the acidic ethanal solution, then OA layer can be washed out by the hydrochloric acid. The OA-free NPs can be further coated with hydrophilic polymers, such as PVP, to render NPs water soluble. In our typical treatment, 1 mL cyclohexane solution of Gd_2O_2S:60%Nd NPs (20 mg/mL) was mixed with 30 mL acidic ethanol solution (pH = 4). The mixture solution was sonicated for 2 h, then 0.02 mL of HCl was added in the above solution. After a few minutes, the solution became transparent, transferred into the tubes for centrifugation. The NPs were washed with ethanol three times, finally dispersed in 2 mL Milli-Q water. After that, 0.2 g of PVP was added in the dispersion of the OA-free NPs, and the mixture solution was stirred for 1 h. The PVP-coated NPs were collected by centrifugation, washed with water three times and dispersed in the Milli-Q water again for future use.

2.4 Ligand exchange with $NOBF_4$

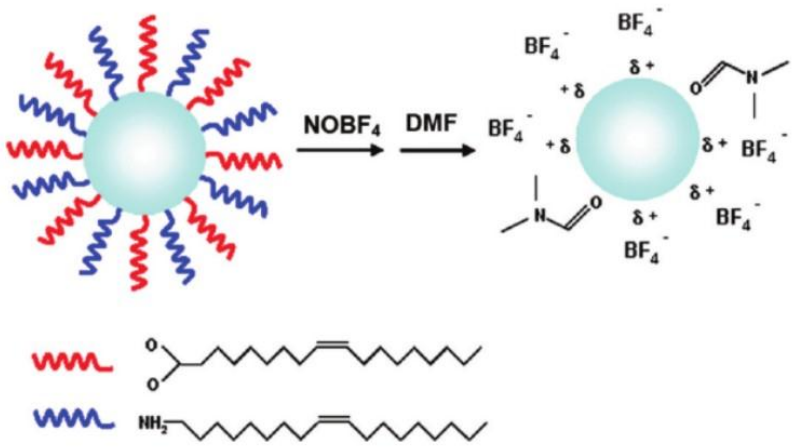

Figure 2.3 Illustration diagram of ligand exchange with $NOBF_4$.[207] Reprinted from American Chemical Society.

Ligand exchange with $NOBF_4$ method (Figure 2.3) has been commonly used for many kinds of NPs. In our case, 3 mL of nanocrystal dispersion in cyclohexane (~10 mg/mL) mixed with 3 mL of DMF solution of $NOBF_4$ (30 mg) to form a two-phase mixture at room temperature. The resulting mixture was stirred gently for 10 min. After removing

the supernatant, 20 mL of chloroform were added to precipitate the nanocrystals, then centrifuging and washing the nanocrystals with DMF and chloroform for 3 times. The final hydrophilic NPs were re-dispersed in polar media, for instance, DMF.

2.5 Ligand exchange with PVP

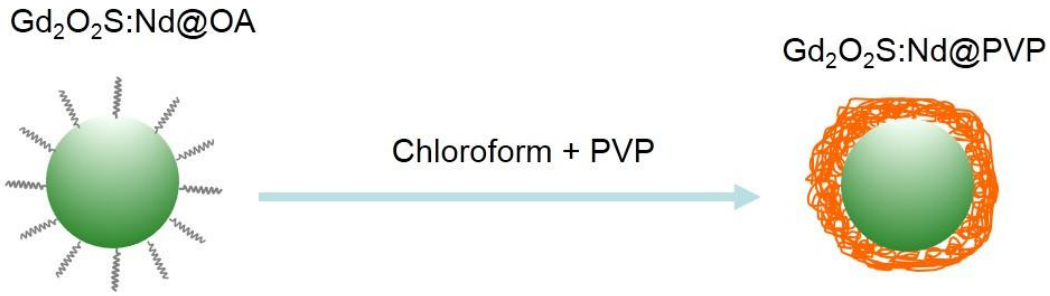

Figure 2.4 Schematic illustration diagram of ligand exchange with PVP.

As shown in Figure 2.4, the ligand exchange method was adapted from a previous reported protocol[259] with a slight modification. Firstly, 10 mg of NPs were first dispersed in 20 mL of chloroform. After 5 min sonication (forming a transparent suspension), 10 mL of chloroform containing 0.25 g PVP were added. Then the mixture was stirred for 72 h at room temperature. PVP-coated NCs were precipitated by addition of 30 mL of cyclohexane and collected by centrifugation at 5000 rpm for 15 min. The obtained powder was washed by chloroform and cyclohexane mixture (1:1, V/V) solution twice, after centrifugation, the resulted powder was further washed by water twice. The purified powder was re-dispersed in water. After that, the suspension was sonicated for another 30 min to obtain transparent solution, finally stored at ~4 °C in refrigerator.

2.6 Cytotoxicity assay

Human HCT-116 colorectal cancer cells (CCL-247) were purchased from ATCC and grown in DMEM containing 4.5 gL^{-1} glucose, GLUTAMax, and supplemented with 10% of heat-inactivated fetal bovine serum, 100 U/mL penicillin, and 100 $\mu g \cdot mL^{-1}$ streptomycin. Cells were maintained at 37 °C in a humidified atmosphere containing 5% CO_2. Throughout the experiments, cells were tested negative for mycoplasma (MycoAlert mycoplasma detection kit, Lonza). The day before the experiments, 20,000

HCT-116 cells were seeded in 96-well plates. The day of the experiment, the cells were incubated for 48 h at 37 °C with increasing concentration of PVP-coated Gd_2O_2S:Nd NPs, from 0.0001mg/ml to 1mg/ml. Cell viability was then assessed using PrestoBlue reagent (Invitrogen) according to the manufacturer's instructions. In brief, after 48 h of incubation, the cell culture medium was removed and cells were incubated for 30 min at 37 °C with 100 µL of 1X PrestoBlue reagent diluted in PBS before reading absorbance at 570 and 600 nm on a plate reader (Synergy H1, Biotek, Winooski, VT, USA). Eight biological replicates were produced and analysed for each condition. A positive control, namely incubation with 75µg/ml saponin known to induce cell death, was added in the experiment. Data analysis was performed using GraphPad Prism 8 (GraphPad Software, Inc., La Jolla, CA, USA), and data were expressed as mean ± SEM. Statistical comparisons were performed using one-way analysis of variance (ANOVA), followed by Dunnett's post-test in comparison to the control condition (0 mg/ml). *$p < 0.05$, **$p < 0.01$, ***$p < 0.001$, and ****$p < 0.0001$. These experiments were carried out at IMRCP.

2.7 Characterizations of morphology and structure

Nanocrystal size and shape characterizations of the RE_2O_2S NPs were characterized *via* Transmission Electron Microscope (TEM, Phillips CM20 200 kV). The power X-ray diffraction (XRD) patterns were recorded on a Bruker D8 Advance X-ray diffractometer (Cu Kα radiation, $\lambda = 1.5418$ Å) with a 2θ range from 20° to 80° at a scanning rate of 1° per minute.

2.8 NIR-II luminescence spectra measurements

NIR-II luminescence spectra were recorded by a spectrometer (Princeton Instruments SpectraPro HRS 500) and a N_2-cooled InGaAs infrared detector (Princeton Instruments PyLoN-JR-1.7) using a continuous-wave 808 nm laser excitation at a power density 16 W/cm^2 (SpectraPysics Tsunami Ti:Sapphire oscillator). All samples were dispersed in cyclohexane with a concentration of 20 mg/mL. These measurements were carried out with collaboration from LPCNO, INSA, Toulouse.

2.9 UV-Vis-Near infrared (UV/Vis/NIR) absorption spectra measurements

UV/Vis/NIR absorption spectra were recorded on a Cary 5000 spectrometer. All the samples were dispersed in cyclohexane.

2.10 Determination of hydrodynamic size

Dynamic light scattering (DLS) was performed on a Malvern Zetasizer to determine the hydrodynamic sizes and size distributions. NPs were dispersed in water with a very low concentration of about 0.01 mg/mL.

2.11 Fourier transform infrared (FTIR) spectra measurements

FTIR spectra were recorded on a Perkin Elmer Spectrum 100 FTIR spectrometer and the samples were prepared by mixing with KBr fine powder in a pellet with a mass ratio of 1% (NPs : KBr).

2.12 Procedure of MR relaxivity measurements

Longitudinal (T_1) and transverse (T_2) relaxation times of different Gd concentration were measured on an NMR relaxometer (Bruker Minispec 20 MHz, 37 °C) at a magnetic field 0.47 T (Figure 2.5). Every sample had been placed in the chamber to reach thermal equilibrium before measuring.

Figure 2.5 Photo of Bruker Minispec relaxometer.

2.13 MR and CT imaging

Magnetic Resonance Imaging (MRI) experiments were performed using a 7 T imager for small animals. We prepared a stock solution of PVP-coated Gd_2O_2S:60%Nd NPs dispersed in water with a high concentration. Then x mL of stock solution and (0.5-x) mL of water were mixed with 0.5 mL of 20 wt% gelatin phantom to form a series of 10 wt% gelatin phantom with NPs concentrations 0, 0.2, 0.4, 0.6, 0.8, 1, 1.5 mg/mL. These 7 samples with concentrations from low to high were added in a 15 mL centrifugal tube in sequence. The centrifugal tube was used for T_1 and T_2 MRI experiments, as shown in Figure 2.6.

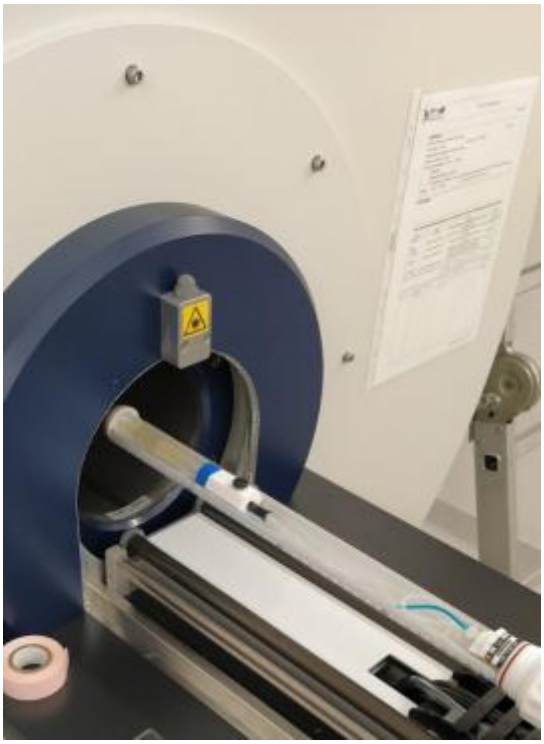

Figure 2.6 Photo of the set-up for MRI experiments.

X-ray tomography scan was carried out on a GERT16 and set from 80 to 140 kV. Since the technique of X-ray tomography has lower sensitivity compared to MRI, high concentrations of the contrast agents are required. Similarly, 10 samples of 10 wt% gelatin with NPs concentrations 0, 0.3, 0.5, 1.0, 2.0, 5.0, 7.0, 10.0, 20.0, 27.0 mg/mL were prepared for CT scans. Both MR and CT imaging experiments were carried out at

ENI-CREFERE.

2.14 NIR-II imaging

NIR-II imaging experiments were carried out on a small animal imaging system (Series III 900/1700, NIROPTICS) equipped with a cooled InGaAs camera (900–1700 nm), with collaboration of Professor Zhu's group in Xiamen Institute of Rare Earth Materials, Xiamen, China. The excitation source is a diode continuous wavelength laser with wavelength of 808 nm. NPs were covered with 1% Intralipid medium with varied depth. Power density was also tuned from 0 to 100 mW/cm^2. Exposure time for all images was 75 ms.

2.15 Photoacoustic and ultrasound imaging

PA and US experiments were carried out at INSERM, University of Montpellier, the data was provided by Dr. Pierre Sicard.

3 Results and discussion

3.1 Synthesis and characterizations of ultrasmall RE_2O_2S NPs

To optimize the conditions for synthesis of RE_2O_2S, in this section, we firstly investigated how the parameters such as amount of DPTU, solvent composition, reaction temperature and time affect the sizes, morphologies, and phases of RE_2O_2S NPs. Then, using the optimized conditions, we synthesized a series of RE_2O_2S NPs.

1) Influence of the amount of DPTU

In previous synthesis of RE_2O_2S NPs based on thermal decomposition of precursors in organic medium, S_8 powder is reported to be the common sulphur source whereas some other sulphur containing molecules like $Ln[(phen)(ddtc)_3]$ (phen = 1,10-phenanthroline; ddtc = diethyldithiocarbamate) are less used because of their sophisticated preparations. Despite that, it still remains challenging to synthesize nanoscaled RE_2O_2S NPs with heavy lanthanides[127] and steady reaction yield[258]. DPTU, reported in other syntheses of metal sulfides[261], has been used in our synthesis and can in-situ release H_2S at elevated temperature. To achieve the monodispersed Gd_2O_2S NPs,

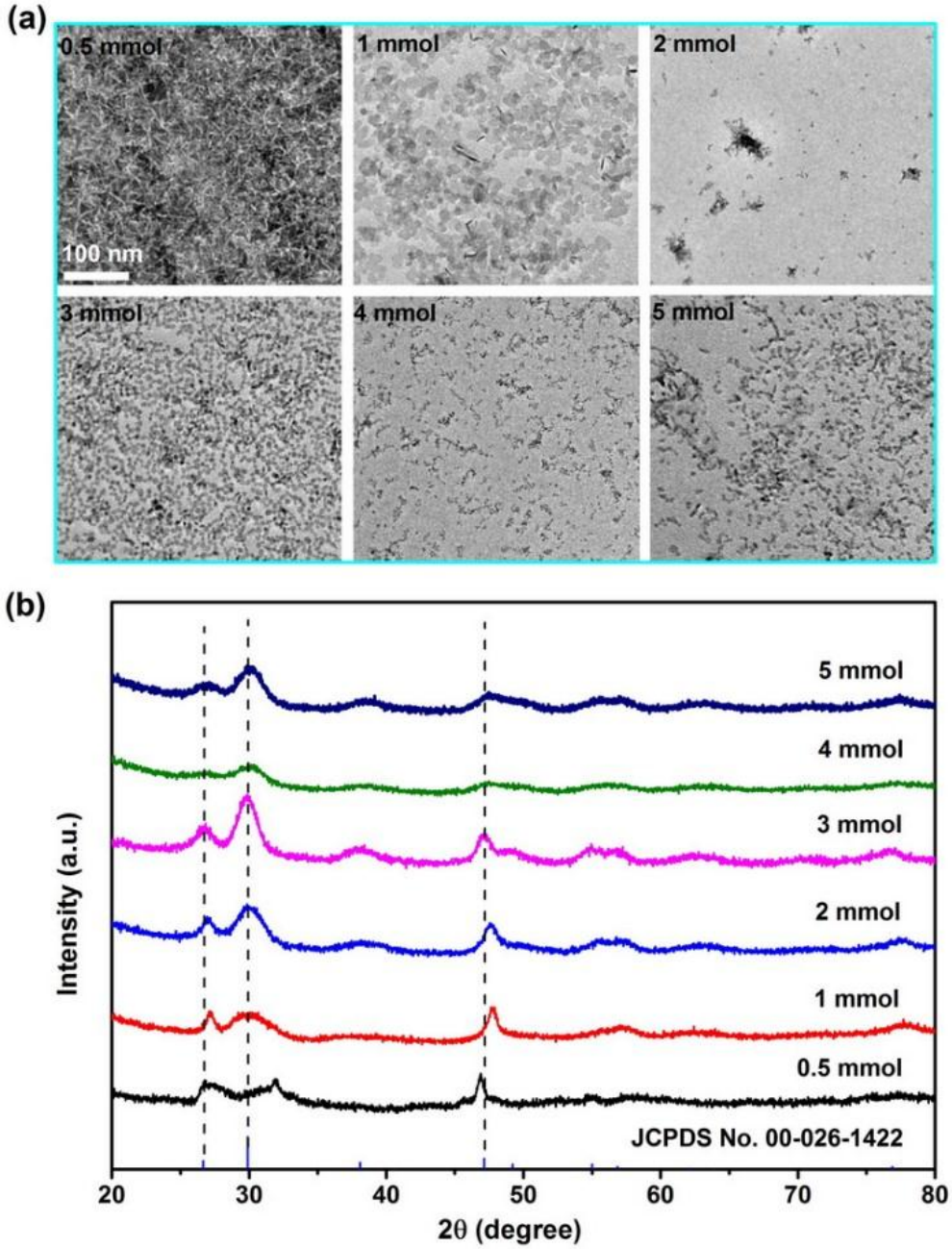

Figure 2.7 (a) TEM images and (b) X-ray diffraction (XRD) patterns of Gd_2O_2S nanocrystals synthesized at different amount of DPTU.

a variety of synthesis parameters were optimized. TEM images in Figures 2.7a and XRD patterns in Figure 2.7b show the influence of DPTU on the change of size, morphology, and phase in the syntheses. It is found that Gd_2O_3 impurities or mixtures are present due to low substitution of sulphur for oxygen, however, higher concentration (more than 3 mmol) of DPTU cause smaller size and poor dispersity maybe because of

higher concentration released from DPTU. Besides, when more than 3 mmol are added, the NPs show smaller sizes and weaker diffraction intensities. This is because large excess DPTU addition leads to the formation of a large amount of extremely small NPs due to explosive nucleation at the beginning of reaction, whereas no more Gd precursors are available for growth of the small NPs. This leads us to conclude that in our hands, 3 mmol of DPTU is optimal.

2) Influence of solvent composition

It is known that solvents have dramatic effects on the dispersity, morphology and crystallinity of NPs, particularly when at least one of the solvents also acts as a surface-active agent, which is the case for the trio OA/OM/TOA. As shown in Figure 2.8, the influence of various volume ratios of solvents was studied. The rule is to fix the total volume of the organic solvents at 20 mL and vary ratios of OA/OM/TOA from 2:8:10 to 7:3:10. We observed severe aggregation with 2 mL of OA, which is attributed to strong interaction between oleates. The distances of the oleates are closer when less OA molecules are present in the solution. Then the volume of OA was fixed to 3 mL and the volume of OM was gradually increased from 3 to 7 mL, it is clear that the uniformity and dispersity of the NPs are both improved. And the size of the NPs cannot be tuned by the strategy of adjusting solvent ratios even if the volume of OA was varied from 2 to 5 mL. Unfortunately, no crystalline phase was obtained when 7 mL of OA applied, which could be ascribed to weaker interaction between the oleates when more OA molecules added in the solution. As a result, the ratios of solvents can slightly affect the morphology and size of the NPs. The ratio is finally optimized at 3:7:10 of OA/OM/TOA.

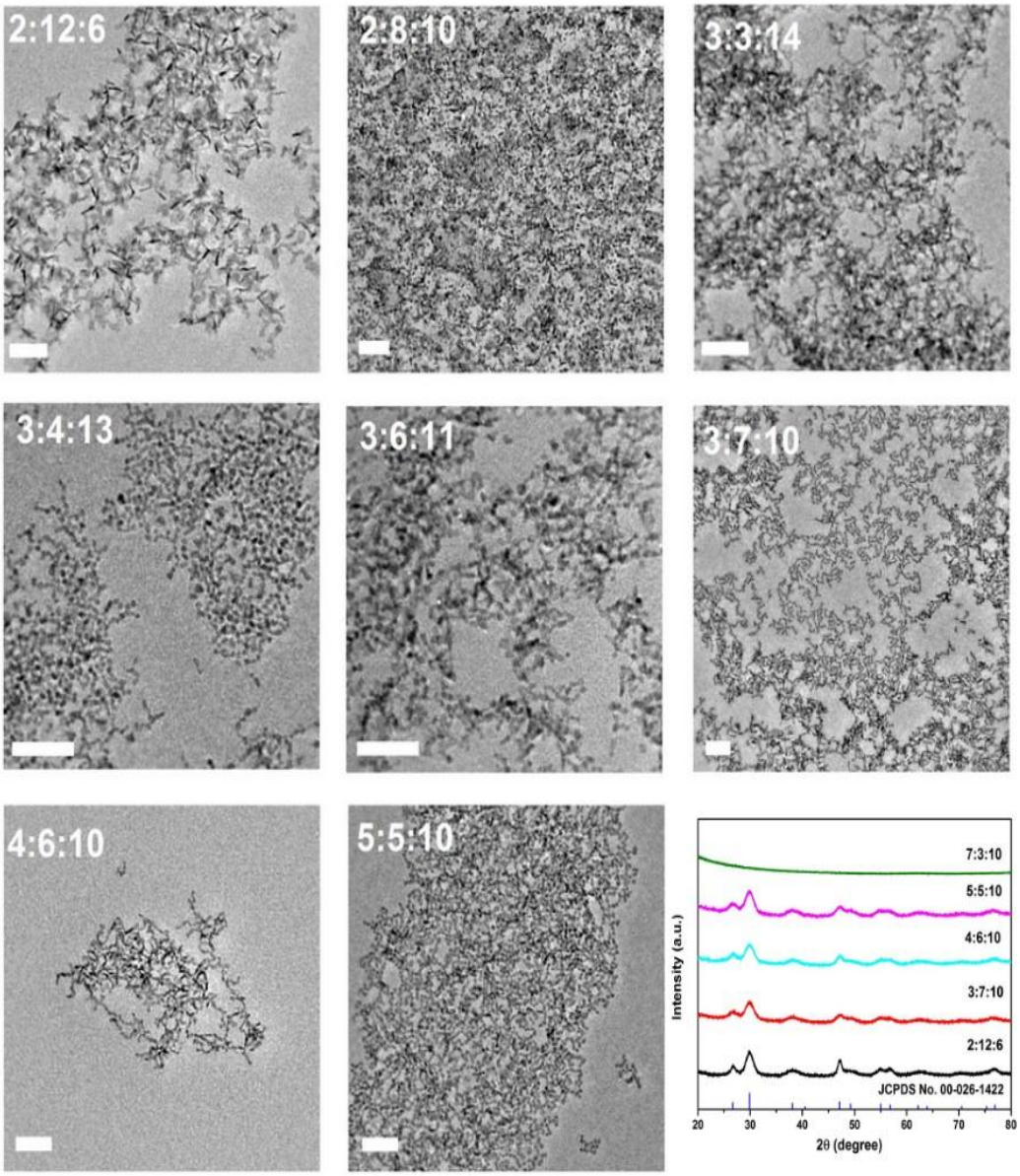

Figure 2.8 Low-resolution TEM images (scale bars: 50 nm) and XRD patterns of Gd_2O_2S nanocrystals synthesized at different volume ratios of OA/OM/TOA.

3) Influence of reaction temperature and time

Reaction time and temperature are the other important parameters that can generally influence the size or morphology of the NPs. In Figure 2.9, the Gd_2O_2S NPs were prepared under the same conditions (3 mmol DPTU, 3:7:10 of OA/OM/TOA), except for varied reaction times and temperatures. As we can see, the temperature was varied from 310 °C to 330 °C and the time was fixed at 1 or 2 h. However, in our cases, it seems that prolonged time and elevated temperature cannot cause the increase of the

size of the NPs. While measuring the sizes of the NPs obtained, we obtained a narrow size distribution of Gd_2O_2S NPs from approximately 5 to 7 nm. The larger size distribution could be obtained by further investigations of other conditions such as the amount of Gd precursors, other ions doping, and even new methods for instance flow reaction conditions where the precursors are passed through a tube in a furnace.

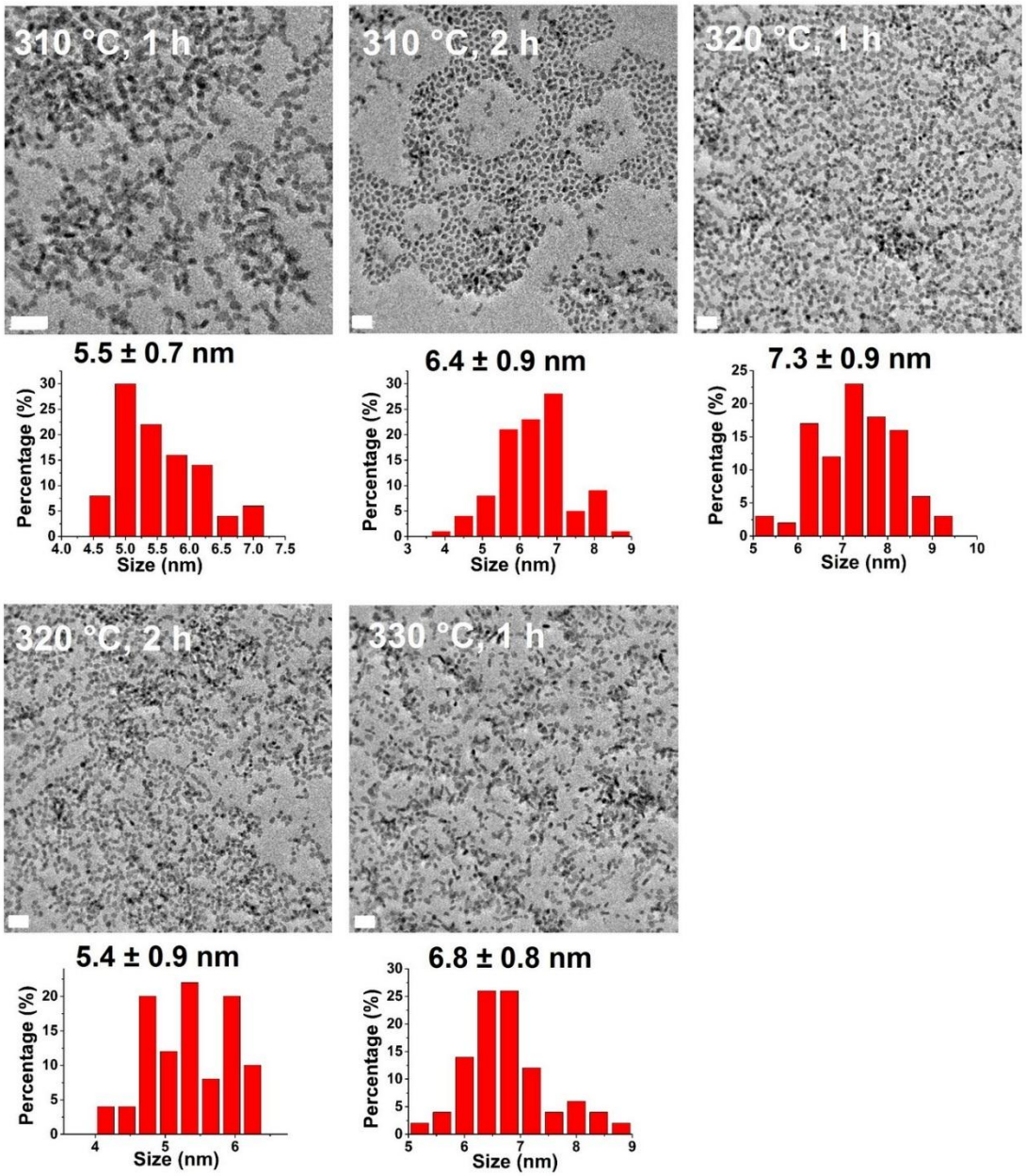

Figure 2.9 Low-resolution TEM images of Gd_2O_2S NPs synthesized at different reaction times and temperatures. Scale bars: 20 nm.

4) Influence of LiOH

Besides, it is found that LiOH plays a significant role in the synthesis. For example, in our case, nothing can be obtained without addition of LiOH or replacing by NaOH can cause unknown phases and serious aggregations. Observation of essential addition of alkaline ions is consistent with previous works[141, 257, 258, 262], however, there are controversial points on the effects of alkaline. For instance, Carenco's group recently has demonstrated that an alkali-oleate mesophase serves as a template for NPs nucleation and growth, rather than the substitution modal where it was believed that alkali ions can replace rare-earth ions in crystal sites. Hence, further investigation is still needed.

5) Synthesis and characterizations of Gd_2O_2S NPs

The Gd_2O_2S crystal has a trigonal structure (*P-3m1* space group) with Gd^{3+} ions surrounded by four O^{2-} ions and three S^{2-} ions that form a seven coordinated geometry (Figure 2.10a).[260] All Gd^{3+} ions occupy a 2d site with a symmetry of C_{3v}. Ultrasmall Gd_2O_2S NPs were synthesized through an improved high-temperature decomposition method with presence of OA, OM and TOA as surfactant, DPTU as sulphur source and LiOH as mineralizer. All reaction conditions used here are optimized, the details about the optimization will be discussed in subsequent sections. The as-synthesized NPs are hydrophobic and can be stably dispersed in various nonpolar organic solvents, for instance, cyclohexane. The powder XRD pattern (Figure 2.10b) shows a set of indexed diffraction peaks of hexagonal phase Gd_2O_2S (JCPDS No. 00-026-1422) without impurity observed. The intense and broad peaks are evidence of good crystallinity and small size of the NPs. The typical TEM image (Figure 2.10c) shows the NPs are spherical with a mean size of 5.9 ± 0.8 nm by randomly counting 100 NPs. The high crystallinity of the NPs was further confirmed by measuring the d-spacings 0.311 nm, 0.295 nm, 0.198 nm and 0.185 nm of high-resolution TEM (HRTEM) images (Figure 2.10d and f) which are related to (100), (101), (110) and (111) planes of Gd_2O_2S, respectively. The corresponding fast Fourier transform (FFT) which exhibits a series of

clear diffraction rings which can be indexed to (101), (111) and (202) planes (Figure 2.10e).

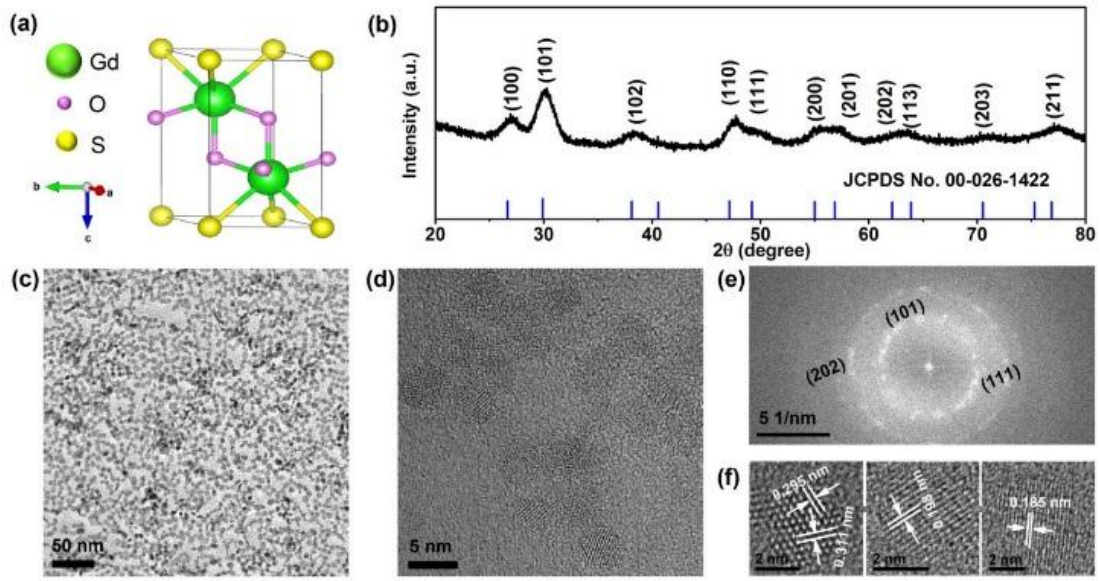

Figure 2.10 (a) VESTA presentation of crystal structure of hexagonal Gd_2O_2S. (b-f) XRD patterns, typical TEM image, HRTEM image, FFT diffraction, and identical planes of Gd_2O_2S NPs, respectively.

6) Towards the synthesis of other RE_2O_2S NPs

Furthermore, it is essential to investigate the syntheses of other rare earth oxysulfide NPs because of their high performance as luminescent materials for many promising applications. Therefore, the optimal conditions for synthesis of Gd_2O_2S were simply applied for that of other RE_2O_2S NPs. Strikingly, we obtained other 14 kinds of RE_2O_2S (RE = Y, La, Ce, Pr, Nd, Sm, Eu, Tb, Dy, Ho, Er, Tm, Yb, and Lu) NPs (Figure 2.11) with good dispersity and the mean sizes range from ~3 to ~10 nm (Table 2.1). All the corresponding XRD patterns of the RE_2O_2S NPs can be well indexed to their standard diffraction data although some of them (La_2O_2S, Pr_2O_2S) seem have poor crystallinity due to non-optimized protocols for specific RE_2O_2S. It is worth emphasizing that not only were heavy lanthanide oxysulfides (crystallized and nanoscaled Tm_2O_2S synthesized for the first time, to the best of our knowledge) readily prepared but also a high and steady reaction yield (over 70%) for all RE_2O_2S NPs was roughly estimated

(considering 30% oleates of final products, according to previous thermogravimetric analysis of Ln_2O_2S by Carenco's group[263]). These results demonstrate a versatile strategy for syntheses of ultrasmall RE_2O_2S NPs, which may lead to more investigations of their optical and magnetic properties at such nanoscale.

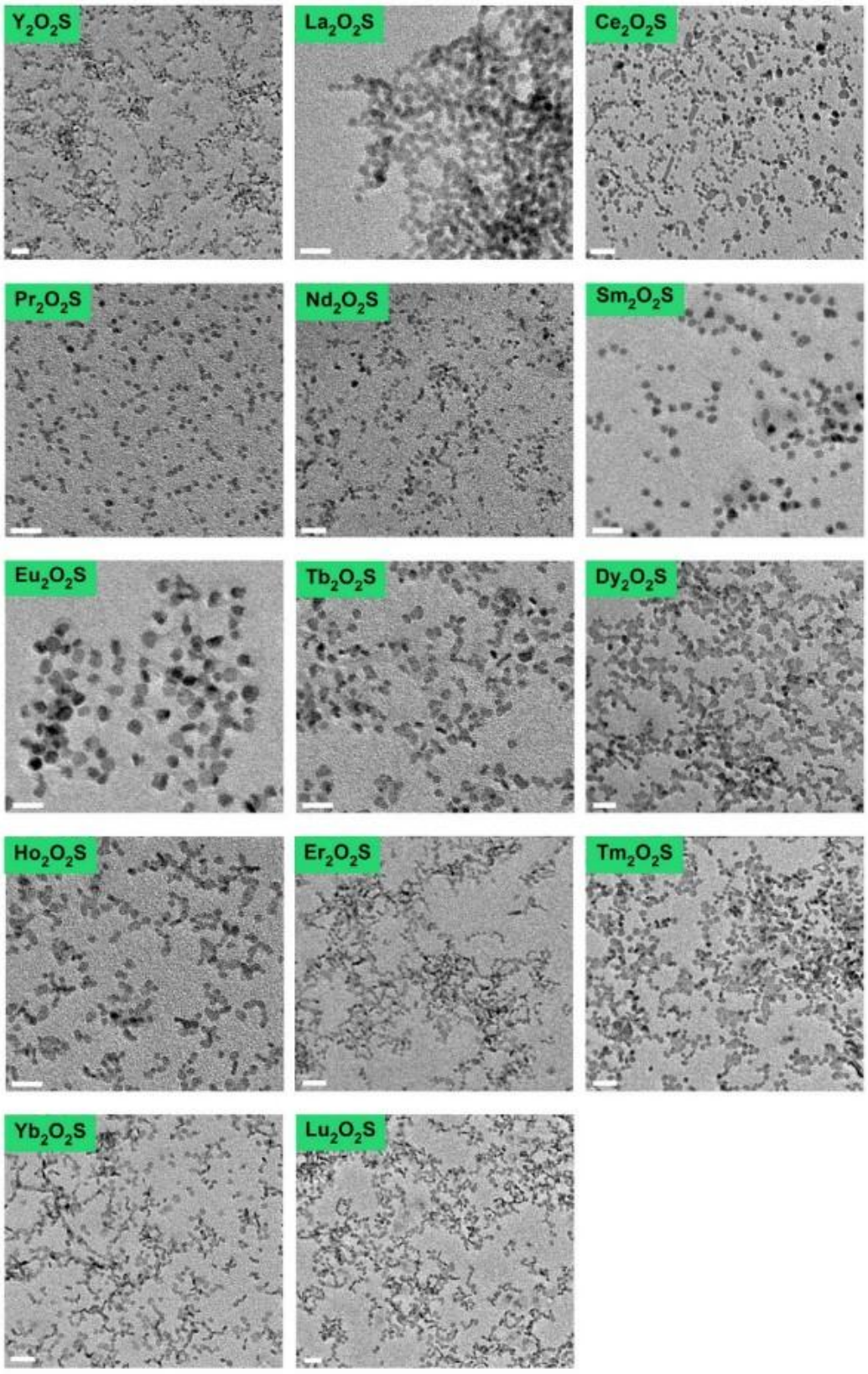
Y_2O_2S
La_2O_2S
Ce_2O_2S
Pr_2O_2S
Nd_2O_2S
Sm_2O_2S
Eu_2O_2S
Tb_2O_2S
Dy_2O_2S
Ho_2O_2S
Er_2O_2S
Tm_2O_2S
Yb_2O_2S
Lu_2O_2S

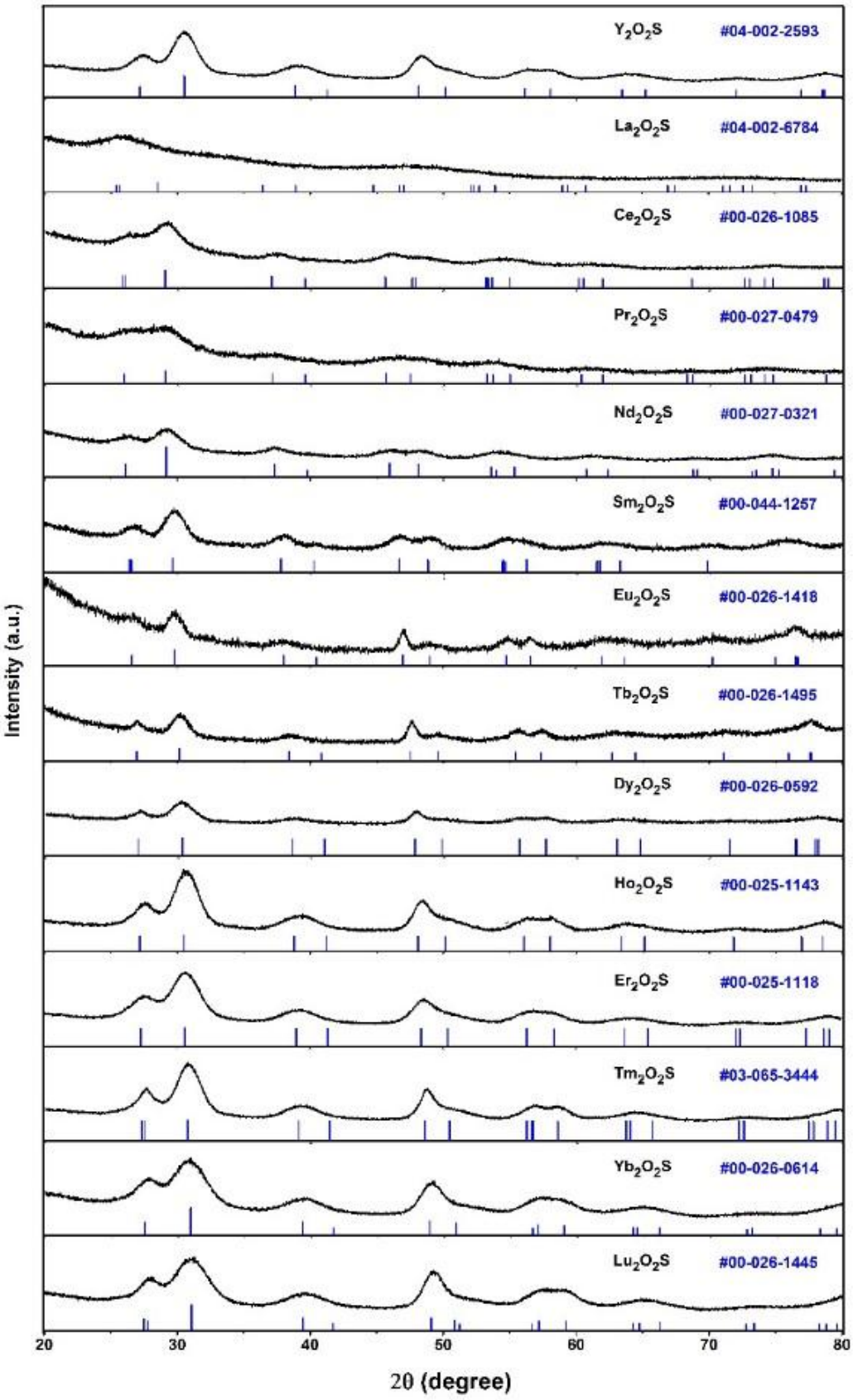

Figure 2.11 Low-resolution TEM images (first) and corresponding XRD patterns

(second) of RE_2O_2S NPs (RE = Y, La, Ce, Pr, Nd, Sm, Eu, Tb, Dy, Ho, Er, Tm, Yb, and Lu). Scale bars: 20 nm.

Table 2.1 Summary of statistic sizes of RE_2O_2S NPs.

NPs	Size (nm)
La_2O_2S	7.3 ± 1.1
Ce_2O_2S	8.4 ± 1.0
Pr_2O_2S	3.9 ± 0.7
Nd_2O_2S	3.5 ± 0.5
Sm_2O_2S	5.7 ± 0.8
Eu_2O_2S	9.7 ± 0.9
Tb_2O_2S	6.6 ± 1.1
Dy_2O_2S	7.6 ± 1.1
Ho_2O_2S	6.4 ± 0.9
Er_2O_2S	5.6 ± 0.9
Tm_2O_2S	7.1 ± 0.9
Yb_2O_2S	6.0 ± 0.7
Lu_2O_2S	5.8 ± 0.9

3.2 Synthesis and optical properties of Nd-doped Gd_2O_2S NPs

In this section, we will present the characterizations of Nd-doped Gd_2O_2S NPs, and their optical properties and ability of multimodal imaging.

1) TEM and XRD characterizations

To acquire ultrasmall RE_2O_2S NPs with efficient NIR-II emission and magnetic properties, we synthesized a series of NIR-II luminescent Gd_2O_2S:Nd NPs with different Nd concentration by the optimized synthesis method. As shown in Figure 2.12, the TEM images verify that the Gd_2O_2S:Nd NPs have good dispersity and small size, only a little change of the size and morphology with different Nd concentration. The

mean sizes of the Gd_2O_2S:Nd NPs were calculated in the range of 3~6 nm. XRD patterns in Figure 2.12 confirm the corresponding crystal structures of the NPs. The diffraction peaks of NPs shift to lower diffraction angles with increase of Nd concentration due to larger ion radius of Nd^{3+} than Gd^{3+}. All diffraction peaks of every kind of NPs can be indexed to Gd_2O_2S (JCPDS No. 00-026-1422) or Nd_2O_2S (JCPDS No. 00-027-0321) without impurity.

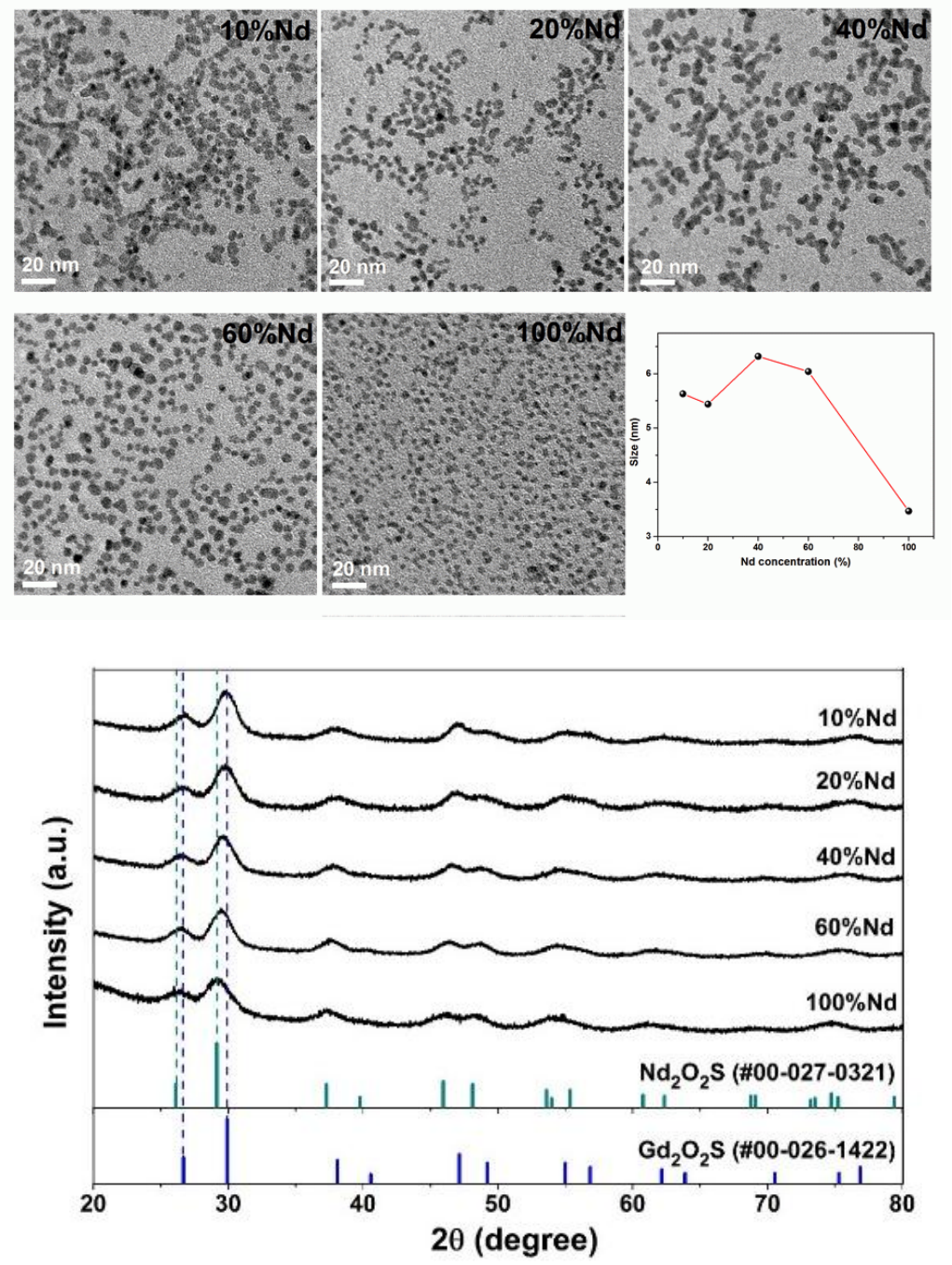

Figure 2.12 TEM images (top) and XRD patterns (bottom) of Gd_2O_2S:x%Nd (x=10,

20, 40, 60, 100) NPs.

2) Absorption

To study the optical properties of the Gd_2O_2S:Nd NPs, we first measured UV-vis-NIR absorption spectra on the absorption spectrometer. In the UV-vis-NIR absorption spectra of Figure 2.13, all the peaks can be identified to the transitions of Nd^{3+}. The absorption intensity of Nd gradually elevates with Nd concentration rises (Figure 2.14), which is consistent with the ideal doping trend.

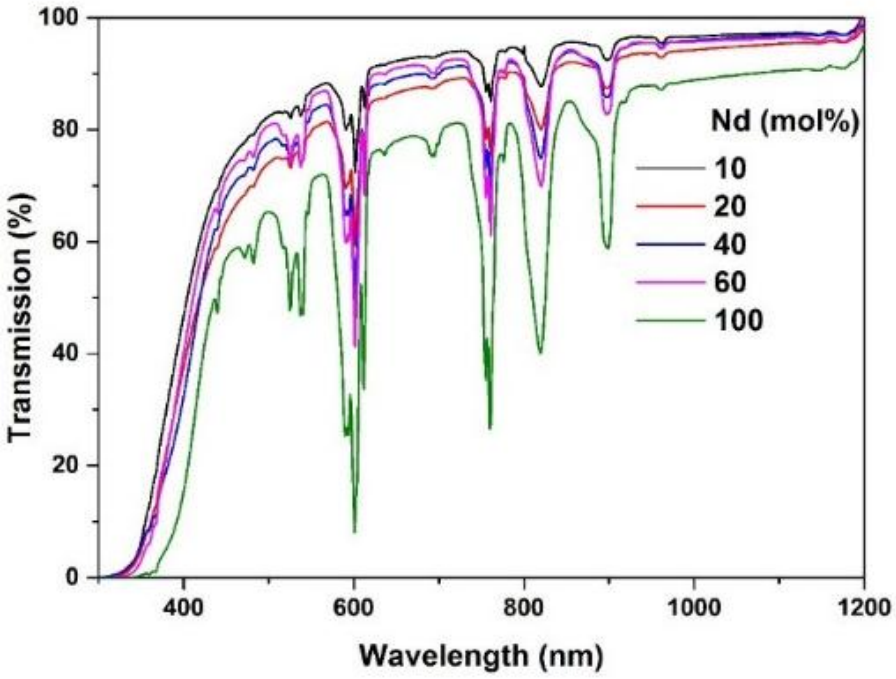

Figure 2.13 UV/vis/NIR absorption spectra of Gd_2O_2S:x%Nd (x = 10, 20, 40, 60, and 100) NPs with the concentration of 20 mg/mL.

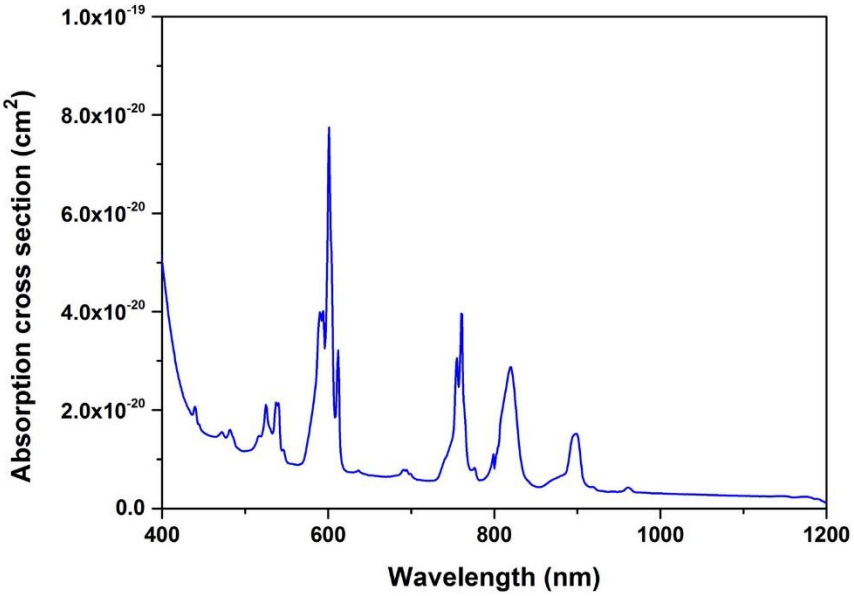

Figure 2.14 Absorption cross section for Nd in Nd_2O_2S nanoparticle at room temperature.

Based on the UV/vis/NIR absorption spectrum, we can determine absorption cross section through the Beer–Lambert Law:

$$A = -log\frac{I}{I_0} = -\log(T) = \varepsilon \times C \times L \quad (2\text{-}1)$$

where I is the transmitted intensity; I_0 is the incident intensity; T is the transmittance in %; A is the absorbance; ε is the molar attenuation coefficient in $L \cdot mol^{-1} \cdot cm^{-1}$; C is the sample concentration in $mol \cdot L^{-1}$; L is the optical path length in cm. Further, the absorption cross section σ can be written as:

$$\sigma = \frac{2303\varepsilon}{N_A} \quad (2\text{-}2)$$

where N_A is the Avogadro's number. Therefore, according to the 2 equations above, we determined the absorption cross section of Nd atoms as shown in Figure 2.13. The σ value at 808 nm is 1.91×10^{-20} cm^2. This value is close to the value of 2.10×10^{-20} cm^2 that was previously reported in Nd doped LiYF4 crystal.[264]

3) Judd-Ofelt parameters

In this section, the Judd–Ofelt (J-O) theory will be applied to the absorption spectrum of Nd_2O_2S NPs to derive the J-O intensity parameters (Ω_λ, $\lambda = 2, 4, 6$).

Based on the absorption spectrum in Figure 2.14, the absorption bands of Nd^{3+} in Nd_2O_2S NPs at 438, 481, 538, 601, 692, 762, 762, 818, and 897 nm are ascribed to the transitions from $^4I_{9/2}$ to $^2P_{1/2}$, $^2G_{9/2} + {}^4G_{11/2} + {}^2K_{15/2} + {}^2D_{3/2}$, $^4G_{7/2} + {}^4G_{9/2} + {}^2K_{13/2}$, $^4G_{5/2} + {}^2G_{7/2}$, $^4F_{9/2}$, $^4F_{7/2} + {}^4S_{3/2}$, $^4F_{5/2} + {}^2H_{9/2}$, and $^4F_{3/2}$, respectively. From the absorption spectrum of Nd_2O_2S NPs, the experimental oscillator strengths (f_{exp}) of absorption bands are determined by the equation[265]:

$$f_{exp} = 4.318 \times 10^{-9} \int \varepsilon(v) dv \quad (2\text{-}3)$$

where $\varepsilon(v)$ is the molar absorptivity of a band at wavenumber (v) in cm^{-1}. According to the Judd–Ofelt (J-O) theory[83, 85], the calculated oscillator strengths (f_{cal}) for the absorption bands corresponding to the electronic transitions from an initial state ΨJ to a final state $\Psi' J'$ can be estimated by the following equation:

$$f_{cal}(\Psi J \rightarrow \Psi' J') = \frac{8\pi^2 mcv}{3h(2J+1)} \frac{(n^2+2)^2}{9n} \sum_{\lambda=2,4,6} \Omega_\lambda \left(\Psi J \middle\| U^\lambda \middle\| \Psi' J'\right)^2 \quad (2\text{-}4)$$

where m is the mass of the electron, c is the velocity of light in vacuum, h is the Planck's constant, n is refractive index, $(n^2 + 2)^2/9n$ is the Lorentz local field correction for the absorption band, Ω_λ (λ = 2, 4, 6) are the host dependent J-O intensity parameters and $||U^\lambda||$ are the doubly reduced matrix elements of the unit tensor operator which are considered to be the independent of the host.

The values of experimental oscillator strengths f_{exp} along with the calculated oscillator strengths f_{cal} of corresponding absorption bands were calculated from the absorbance spectrum and the known concentration of Nd^{3+} in the solution (0.113 $mmol/cm^3$), and presented in Table 2.2. The small root-mean-square deviation (d_{rms}) of 0.88×10^{-6} was obtained for the calculations, indicating the good fit between the f_{exp} and f_{cal} oscillator strengths. Then, the measured oscillator strengths give the J-O intensity parameters:

$\Omega_2 = 3.015 \times 10^{-20}$ cm^2,

$\Omega_4 = 5.271 \times 10^{-20}$ cm^2,

$\Omega_6 = 8.964 \times 10^{-20}$ cm^2.

In general, the magnitude of Ω_2 parameter depends on the site symmetry and the

covalent nature between rare-earth ions and ligand anions, whereas the values of Ω_4 and Ω_6 are related to the rigidity of the host medium.[266] The determined J-O parameters can be in turn used to calculate the radiative properties of Nd^{3+} ions luminescent levels.[266, 267]

Table 2.2 Transitions from $^4I_{9/2}$ other energy levels, peak positions λ (nm), experimental (f_{exp}), and calculated (f_{cal}) oscillator strengths in Nd_2O_2S NPs.

Transitions ($^4I_{9/2}$ →)	λ (nm)	f_{exp} (10^{-7})	f_{cal} (10^{-7})
$^2P_{1/2}$	438	3.17	0.23
$^2G_{9/2} + {}^4G_{11/2} + {}^2K_{15/2} + {}^2D_{3/2}$	481	8.13	0.06
$^4G_{7/2} + {}^4G_{9/2} + {}^2K_{13/2}$	538	21.88	4.49
$^4G_{5/2} + {}^2G_{7/2}$	601	80.48	80.28
$^4F_{9/2}$	692	1.61	0.33
$^4F_{7/2} + {}^4S_{3/2}$	762	23.07	9.45
$^4F_{5/2} + {}^2H_{9/2}$	818	23.8	30.24
$^4F_{3/2}$	897	7.90	4.92

4) NIR emission of Nd^{3+}

To examine the photoluminescence of Nd^{3+} in Gd_2O_2S, we measured emission spectra for Gd_2O_2S:x%Nd (x = 10, 20, 40, 60, and 100) NPs, as shown in Figure 2.15. Upon 808 nm continuous-wave (CW) laser irradiation, the typical downshifting emission bands of Nd^{3+} at 900, 1078, and 1365 nm were observed. The three main emission peaks can be exclusively assigned to the transitions of $^4F_{3/2} \rightarrow {}^4I_{9/2}$, $^4F_{3/2} \rightarrow {}^4I_{11/2}$, and $^4F_{3/2} \rightarrow {}^4I_{13/2}$ of Nd^{3+}. The integrated downshifting luminescence intensity of Nd^{3+} first decreases and then increases with Nd concentration varying from 10% to 100%. As it is known that the luminescence intensity of NPs can be affected by many factors, such as size, doping level, absorption, and quenching. The decrease at the beginning from 10% to 20%Nd doping, can be explained by the concentration quenching between Nd^{3+} ions, as these two samples have similar size but different Nd

doping levels. However, with further increase of Nd doping, absorption is improved massively, on the other hand, the size of NPs also slightly increases compared to the first two samples, so, in this case, concentration quenching is not dominant and luminescence intensity increases. Note the size of Nd_2O_2S is smallest, whereas the intensity of Nd_2O_2S slightly decrease even if it has the strongest absorption. Therefore, by overall consideration of absorption, quenching, and size variation, we select the most intense Gd_2O_2S:60%Nd as the optimal one.

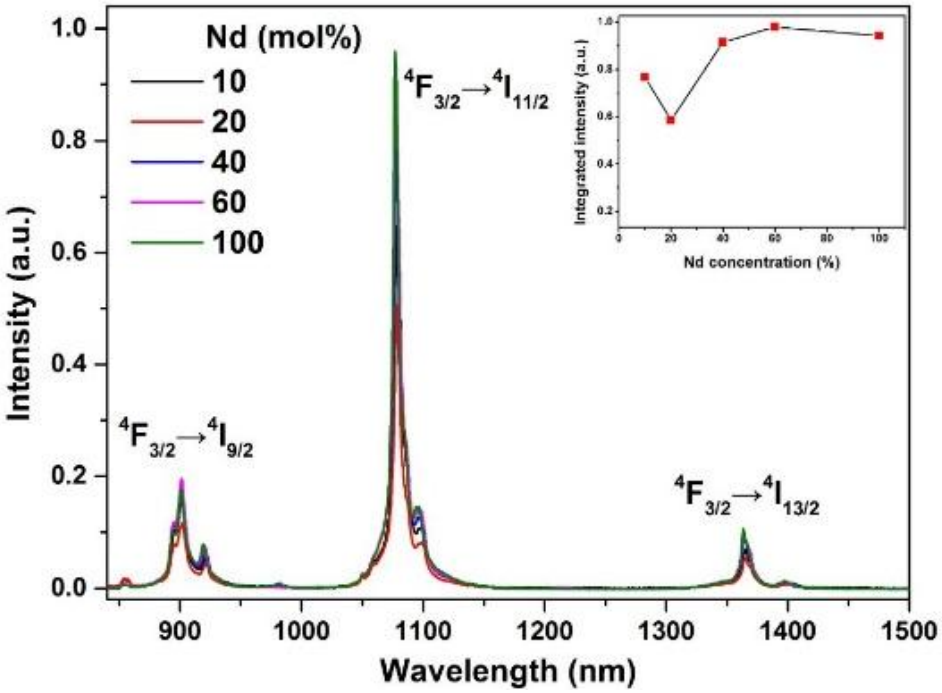

Figure 2.15 NIR-II luminescence spectra of Gd_2O_2S:x%Nd (x = 10, 20, 40, 60, and 100) NPs with the concentration of 20 mg/mL, power density of 16 W/cm^2.

3.3 Surface modification and cytotoxicity assessment

This section will present you 3 surface modification methods of Gd_2O_2S:60%Nd NPs. By comparing and optimizing the results of these methods, we select the best one for the surface modification of Gd_2O_2S:60%Nd NPs.

To utilize our as-synthesized OA-coated Gd_2O_2S:60%Nd for further bio-application such as bioimaging, we need confer hydrophilicity to our NPs. In this chapter, we select 3 strategies for investigations: acid treatment, ligand exchange with $NOBF_4$, and ligand

exchange with PVP. Acidic ethanol solution washing to remove OA has been demonstrated efficient for most kinds of NPs. For NPs of metals, metal oxides, or metal oxysulfides, it is rarely reported, probably because of their sensitivity to inorganic acid. But we believe that because of its simplicity, the possibility of using acid washing for removing the OA layer of our NPs is still worthy of a study; some parameter like pH value, should be carefully controlled. Based on the motivation, we carried out the acid washing process for the Gd_2O_2S:60%Nd NPs.

1) Acid treatment

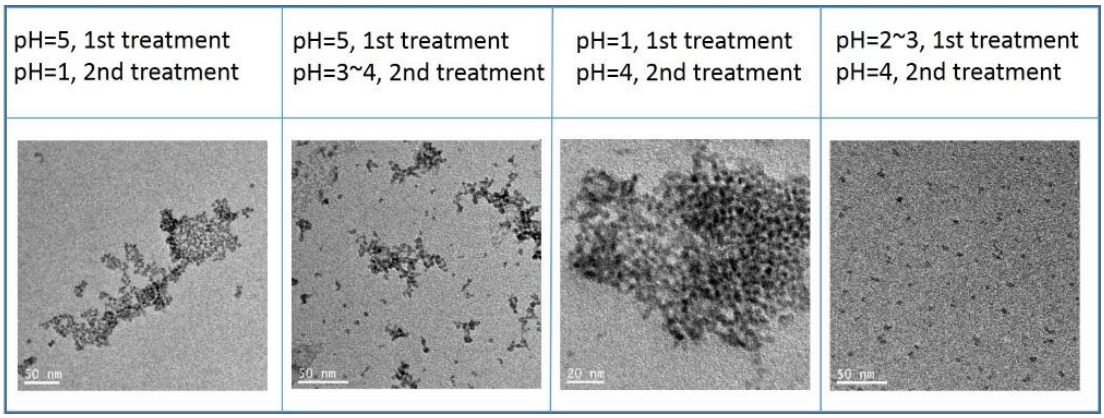

Figure 2.16 TEM images for different samples prepared under different conditions.

As shown in Figure 2.16, the NPs were treated under different conditions to completely remove surface OA layer of NPs. As a result, we found that the NPs could be dissolved quickly when pH value was too low (pH = 1). On the contrary, the OA cannot be removed if the pH was too high (such as pH = 6). So, pH value plays an important role in this case. Then we washed the NPs two times with acidic ethanol solution with proper pH value to be sure the OA can be removed while NPs cannot be dissolved. In Figure 2.16, with this "two-time" wash, NPs can be collected with good dispersity. But this method is time-consuming and takes several hours. Another problem is poor repeatability for this strategy. Therefore, we made a little modification where after sonication of first washing, the concentrated HCl was added directly into the solution. The solution became transparent very fast (in a few minutes), then NPs were collected and centrifugated quickly. The advantage of this method is that we can use of

the heating energy produced by long time sonication to accelerate the process of removing OA. The obtained OA-free NPs are displayed in Figure 2.17a, TEM images show the NPs morphology and size, DLS results show the size distributions of NPs dispersed in pure water or culture medium. OA-free NPs were easily dispersed in pure water (the inset photo in Figure 2.17a1), the hydrodynamic size of the NPs was measured to be 1.2 nm by DLS, when dispersed in culture medium, the DLS size was measured to be 1.6 nm. Both the two DLS sizes are smaller than that of OA-coated Gd_2O_2S:60%Nd NPs (~6 nm), which means that the sizes were reduced after the acid treatment. After PVP coating, the mean sizes of NPs slightly increase to 3.4 nm and 2.8 nm, for dispersion in pure water and culture medium, respectively (Figure 2.17b).

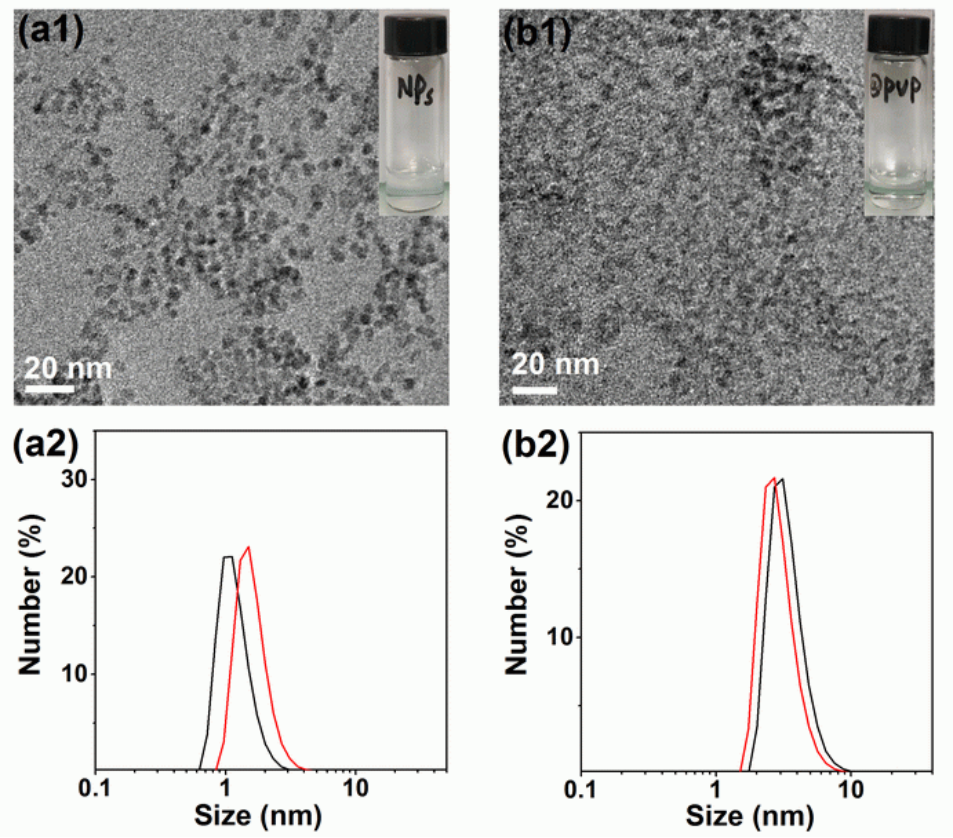

Figure 2.17 TEM images and DLS (black colour: water; red colour: culture medium) of OA-free (a1 and a2) and PVP-coated (b1 and b2) Gd_2O_2S:60%Nd NPs.

For the purpose of evaluation of acid treatment method, we carried out FTIR absorption spectra for these 3 types of Gd_2O_2S:60%Nd NPs (OA-coated, OA-free, and

PVP-coated). As shown in Figure 2.18, two typical the peaks at 1509 cm^{-1} and 1427 cm^{-1} were ascribed to the asymmetric and symmetric stretching vibration of COO^{-1} group of OA molecule for the OA-coated NPs. After acid treatment, the two peaks were massively diminished that means the OA layer was successfully washed out. When further PVP coating, two other peaks at 1648 cm^{-1} and 1394 cm^{-1} appeared, corresponding to the stretching vibration of C=O and C–N from the PVP, respectively. These results unambiguously demonstrate the effectiveness of the acid treatment method.

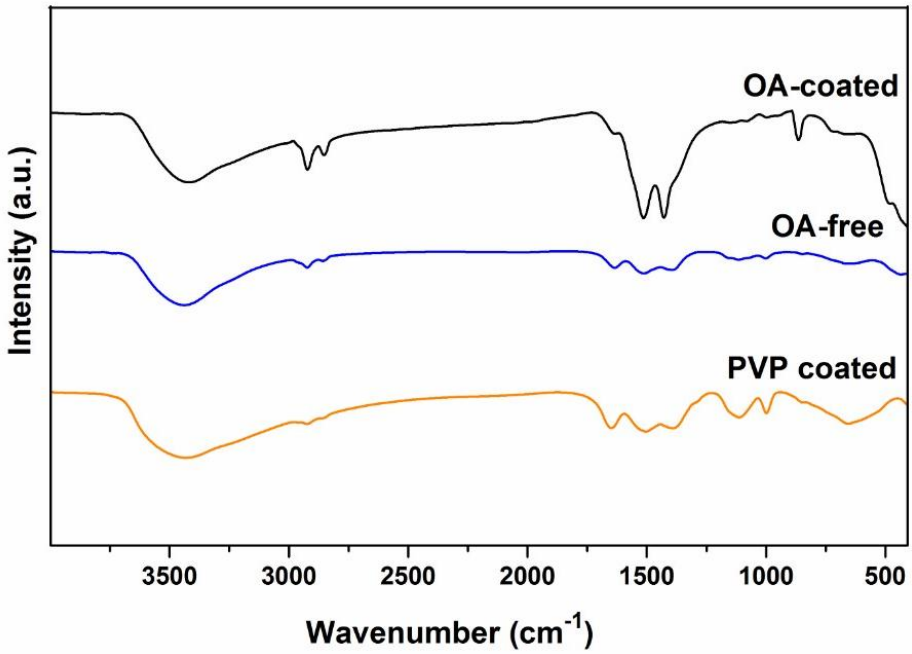

Figure 2.18 FTIR absorption spectra of 3 types of Gd_2O_2S:60%Nd NPs (OA-coated, OA-free, and PVP-coated).

To study the potential for bio-application, we first assessed the cytotoxicity of OA-free NPs *in vitro* on human HCT-116 colorectal cancer cells using Prestoblue assay. As shown in Figure 2.19, the cell viability remains almost 100% after incubation with the NPs for 48 h in the concentration range of 0.0001-1 mg/mL. This result obviously exhibits an extremely low toxicity of the NPs within our experimental concentration range, showing promising bio-applications for the NPs. Moreover, it is still worthy to continue assessing the cytotoxicity of the NPs within a wider concentration range

compared to that of our current study in the future.

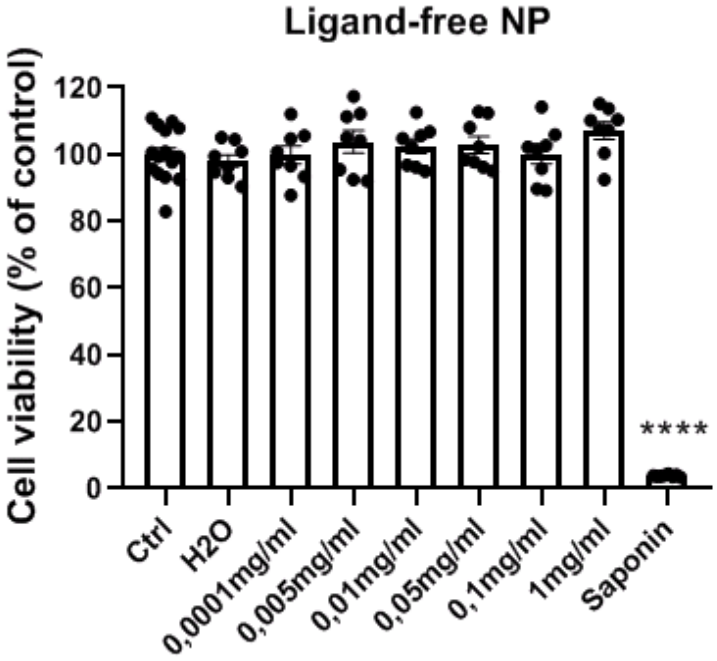

Figure 2.19 Cell viability of OA-free Gd_2O_2S:60%Nd NPs.

By using acid treatment, we obtained OA-free NPs, and PVP was also successfully coated on the surface of OA-free NPs. However, there are some disadvantages with acid treatment method, for instance, low yield (~1%, 1 mg OA-free NPs obtained after treatment with 100 mg of OA-coated NPs), time consumption, and easy dissolution. Overall, a more efficient strategy for Gd_2O_2S NPs surface modification should be further explored.

2) Ligand exchange with $NOBF_4$

Ligand exchange with $NOBF_4$ method has been demonstrated feasible for Fe_3O_4, TiO_2, FePt, Bi_2S_3, and rare-earth based fluorides.[207] In a typical protocol, cyclohexane solution containing OA-coated NPs is mixed with DMF solution containing $NOBF_4$ to form two-phase mixture. The ligand exchange process can be completely accomplished in 10 min with gentle shaking or stirring. The purified NPs are able to disperse in hydrophilic media. Following this procedure, we treated OA-coated Gd_2O_2S:60%Nd NPs and the TEM image was obtained as shown in Figure 2.20. Unfortunately, no

individual NPs were observed according to TEM. Although we tried to optimize the mole ratio of NPs and $NOBF_4$ molecules, the ways and time of ligand exchange process, agglomerates cannot be avoided. It seems that there are some key factors we need to know and improve.

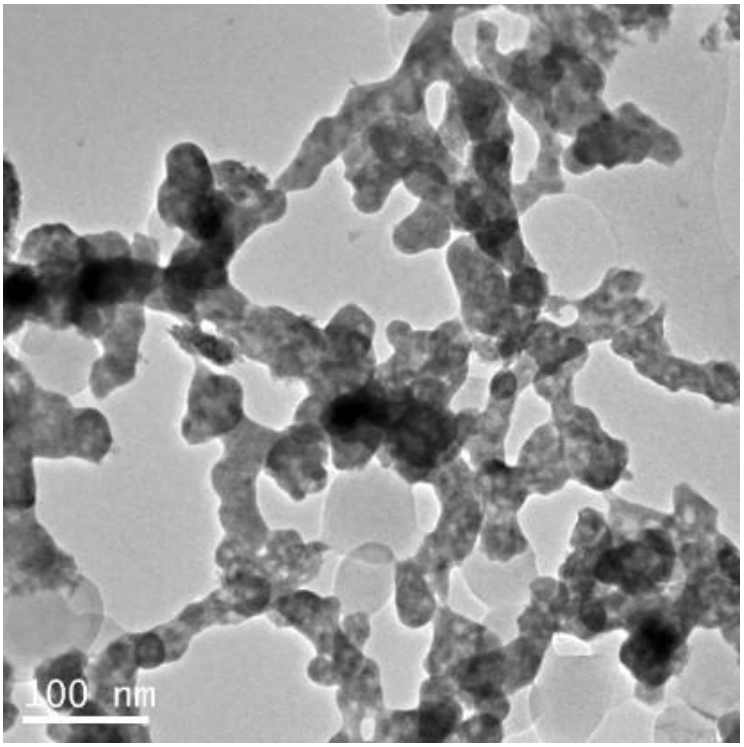

Figure 2.20 TEM image of Gd_2O_2S:60%Nd NPs after $NOBF_4$ treatment.

3) Ligand exchange with PVP

Apart from the ligand exchange with $NOBF_4$, researchers also report a strategy where PVP can displace OA molecule in chloroform solution, then PVP-coated NPs can be achieved in just one step synthesis. We prepared PVP-coated Gd_2O_2S:60%Nd via the reported ligand exchange method with slight modification. The TEM images in Figure 2.21 show the morphology and size of the NPs before and after ligand exchange. The mean sizes were measured to be 6.0 nm and 5.9 nm for OA-coated and PVP-coated Gd_2O_2S:60%Nd NPs, respectively (Figure 2.22). By DLS measurements, the hydrodynamic diameter of PVP-coated Gd_2O_2S:60%Nd NPs was determined as 25 nm which is larger than the size determined by TEM (Figure 2.23). This is because water molecule layer on the surface of NPs and possible small aggregations can cause a larger

size. It is obvious that NPs are individual without any change of morphology and size after ligand exchange. When dispersed in water with a concentration of 10 mg/mL, the PVP-coated Gd_2O_2S:60%Nd NPs displayed excellent dispersity in water and no visible agglomerates were observed (Figure 2.20, right one in the inset photo). These hydrophilic NPs can be stably dispersed in aqueous for several months at ~4 °C in refrigerator.

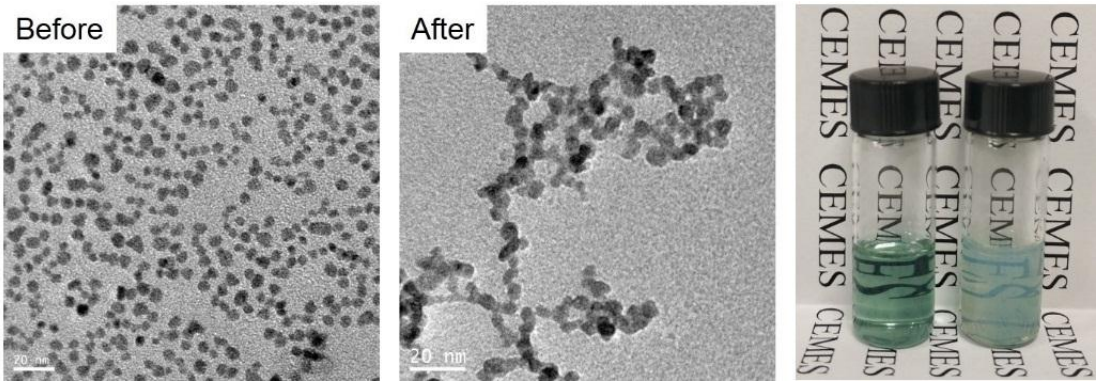

Figure 2.21 TEM images of before and after PVP ligand exchange process. The inset photo showing NPs dispersed in chloroform (left one) or water (right one) with same concentration of 10 mg/mL.

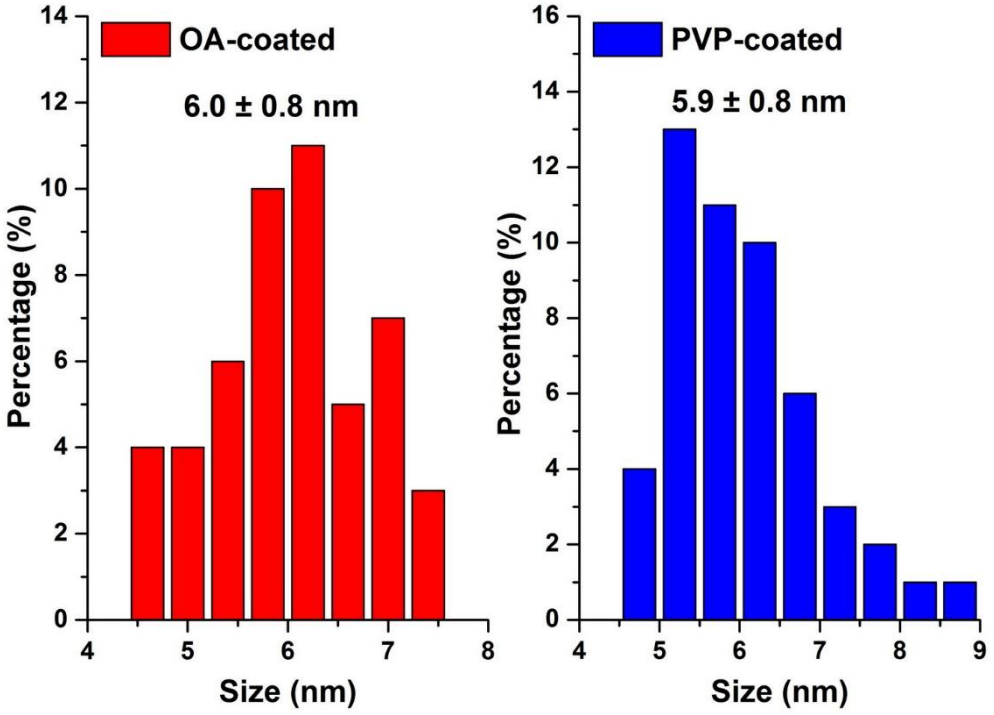

Figure 2.22 Size distributions of OA-coated and PVP-coated Gd_2O_2S:60%Nd NPs.

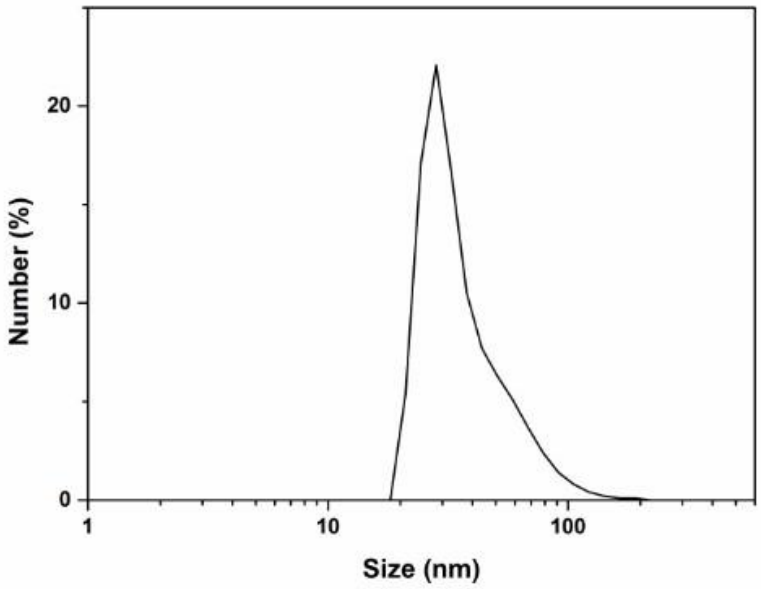

Figure 2.23 DLS of PVP-coated Gd_2O_2S:60%Nd NPs.

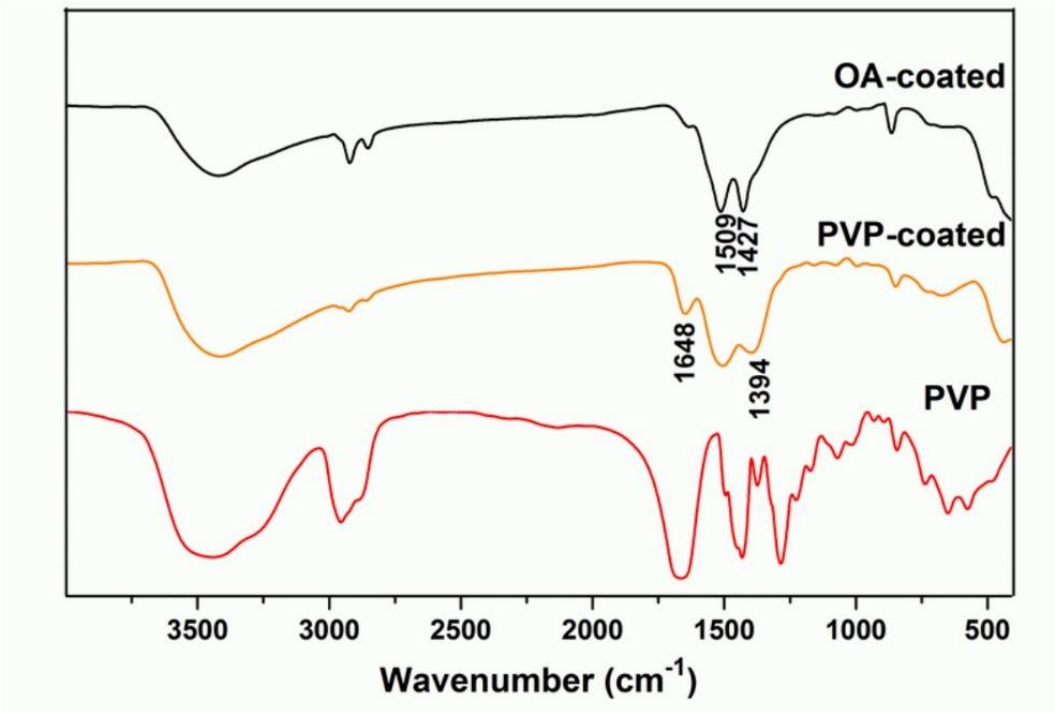

Figure 2.24 FTIR absorption spectra of OA-coated and PVP-coated Gd_2O_2S:60%Nd NPs, and PVP.

We carried out the FTIR absorption spectra to qualitatively investigate effectiveness of the ligand exchange strategy. Then, the FTIR absorption spectra of OA-coated and PVP-coated Gd_2O_2S:60%Nd NPs, and PVP were first recorded on the

spectrometer (Figure 2.24). For the spectrum of OA-coated Gd_2O_2S:60%Nd NPs, the peaks at 1509 cm^{-1} and 1427 cm^{-1} were ascribed to the asymmetric and symmetric stretching vibration of COO^{-1} group. After PVP exchanging, two peaks at 1648 cm^{-1} and 1394 cm^{-1} appeared, corresponding to the stretching vibration of C=O and C–N from the PVP, respectively. The results seem to demonstrate the successful coating of PVP by the ligand exchange method, however, to fully confirm the successful exchange process, we need to do more analyses such as nuclear magnetic resonance, thermogravimetry, etc.

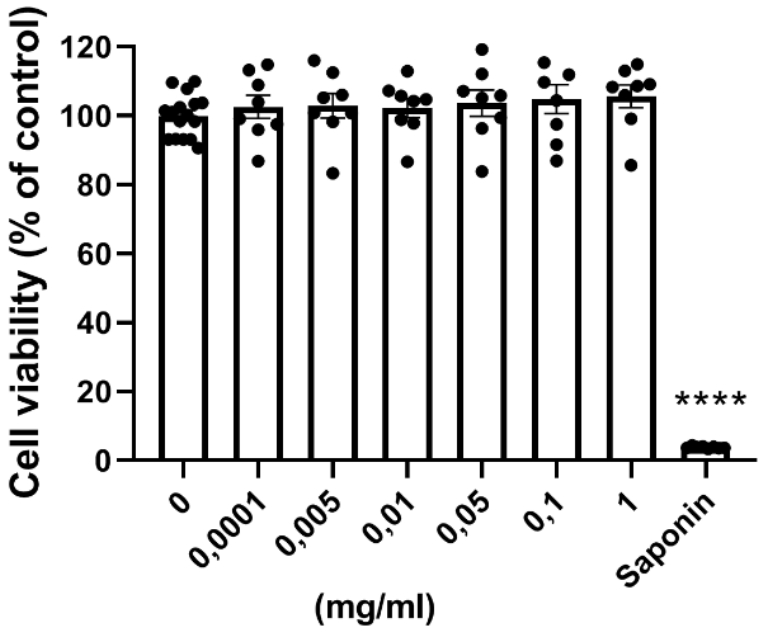

Figure 2.25 Viability of human HCT-116 colorectal cancer cells after 48 h incubation with PVP-coated Gd_2O_2S:Nd NPs in the concentration range of 0~1 mg/mL. 75µg/ml saponin inducing high cytotoxicity was used as positive control.

The as-prepared PVP-coated Gd_2O_2S:60%Nd NPs were incubated with human HCT-116 colorectal cancer cells for 48 h for cytotoxicity assessment. As shown in Figure 2.25, the cell viability keeps at very high levels (almost 100%) but with larger deviations in the higher concentration range after incubation with PVP-coated Gd_2O_2S:60%Nd NPs for 48 h. This result obviously exhibits an extremely low toxicity of PVP-coated Gd_2O_2S:60%Nd NPs within our experimental concentration range,

showing promising bio-applications for our NPs.

Compared to other 2 surface modification methods, ligand exchange with PVP proves more beneficial. For example, firstly, the synthesis procedure is simple as obtaining PVP-coated NPs needs only one step; secondly, the size of nanoparticle is nearly not changed with replacing OA molecule by PVP; thirdly, the yield of hydrophilic NPs is improved to about 10% compared to less than 1% from acid treatment. In a word, in our opinion, we demonstrate that ligand exchange with PVP is very suitable for preparing water-soluble ultrasmall RE_2O_2S NPs.

3.4 Magnetic resonance property evaluation

To validate the usability of PVP-coated Gd_2O_2S:60%Nd NPs as potential contrast agents, the T_1 and T_2 relaxation times of different Gd concentration were measured on a relaxometer. It is obvious that both the T_1 and T_2 relaxation times display very linear dependence on the Gd concentration, as shown in Figure 2.26. The longitudinal (r_1) and transversal relaxivity (r_2) values were determined from the slope of the relaxation rate ($1/T$) as a function of Gd^{3+} concentration. As the r_1 is related to the change in the relaxation rates of the protons of water in the presence of contrast agents, it requires high amount of Gd^{3+} ions on the surface and close distance between water molecules and exterior Gd^{3+} ions to produce high r_1 value. Luckily, the PVP-coated ultrasmall Gd_2O_2S:60%Nd NPs own large surface to volume ratio and excellent water solubility, exhibiting a high r_1 longitudinal relaxivity of 2.42 $(mM)^{-1}\cdot S^{-1}$ at a magnetic field of 0.47 T, 37 °C. This value is comparable to the r_1 of the gadolinium-based clinical agents such as gadopentetate dimeglumine (Gd-DTPA), gadoterate (Gd-DOTA) and gadodiamide (Gd(DTPA-BMA)) with a range of 3.5-3.8 $(mM)^{-1}\cdot S^{-1}$ (0.47 T, 37 °C)[268]. However, a quite low r_2 transversal relaxivity was obtained at 2.83 $(mM)^{-1}\cdot S^{-1}$. MR contrast agents can be classified according to their T_1 or T_2 enhancement capability based on the ratio of r_2/r_1. When the r_2/r_1 value is close to 1, application as a positive contrast agent is favoured. On the other hand, when this ratio is larger, the contrast agents are viewed as negative contrast agents. In our study, the r_2/r_1 ratio is calculated

to be 1.17, indicating the promising use of the NPs a positive contrast agent is favoured at the low magnetic field.

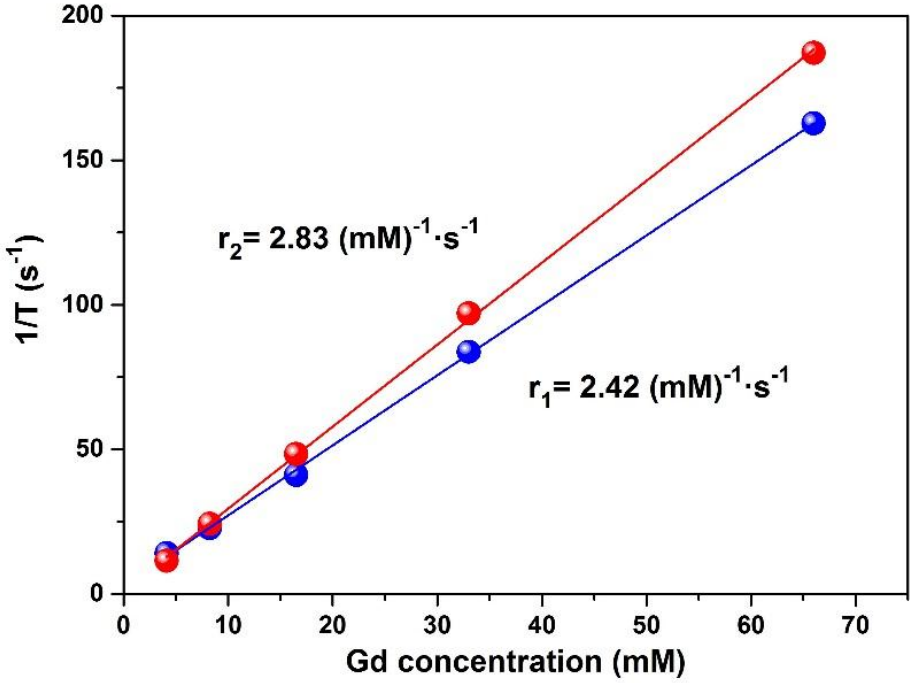

Figure 2.26 T_1 and T_2 relaxivity plot of aqueous suspension of PVP-coated Gd_2O_2S:60%Nd NPs.

3.5 Multimodal imaging

In this section, the Nd doped Gd_2O_2S NPs will be used for multimodal (NIR-II luminescence, PA, US, MR, and CT) imaging. Among these experiments, the NIR-II luminescence imaging experiments were carried out at Xiamen Institute of Rare-earth Materials, Xiamen, China; the MR and CT imaging experiments were carried out at CREFRE, Toulouse; PA and US imaging experiments were carried out at INSERM-CNRS, University of Montpellier.

1) NIR-II luminescence imaging

To explore the potential of imaging at the NIR-II biological window, we carried out imaging experiments for Gd_2O_2S:60%Nd NPs using a small animal imaging system, as shown in Figure 2.27a. The as-prepared NPs were covered by a petri dish containing Intralipid medium (1%) with varied thicknesses from 0 to 11 mm and excited at variable

power densities from 0 to 100 mW/cm^2. In Figure 2.27b, it is observed that although the luminescence intensity drastically decreases with increased thickness of Intralipid medium, the fluorescence signals still can be collected. Optical penetration length can be estimated by the following equation:[269, 270]

$$I = I_0 exp(-d/L_p) \quad (2\text{-}3)$$

where I is the intensity, I_0 is a constant, d is the depth and L_p is the optical penetration length. The resulted fitting curve matches well with our experimental data and the fitted value of L_p is 2.4 mm. The penetration length is comparable with that of LaF_3:Nd NPs[271] but much lower than that of $LiLuF_4$:Nd@$LiLuF_4$ NPs (20 mm penetration length reported)[272]. Considering the very small size and the absence of inert shell protection of Gd_2O_2S:60%Nd NPs, it undoubtably shows promise for NIR-II bioimaging application. We further investigated the power-dependent imaging behaviour of Gd_2O_2S:60%Nd NPs with a fixed depth (2 mm) of Intralipid medium, as shown in Figure 2.27c. The inset photo shows that the luminescence intensity gradually increases with increasing excitation power, while the signals can be detected with power density as low as 5 mW/cm^2. Apparently, the fitting curve shows linear relationship of intensity and power density.

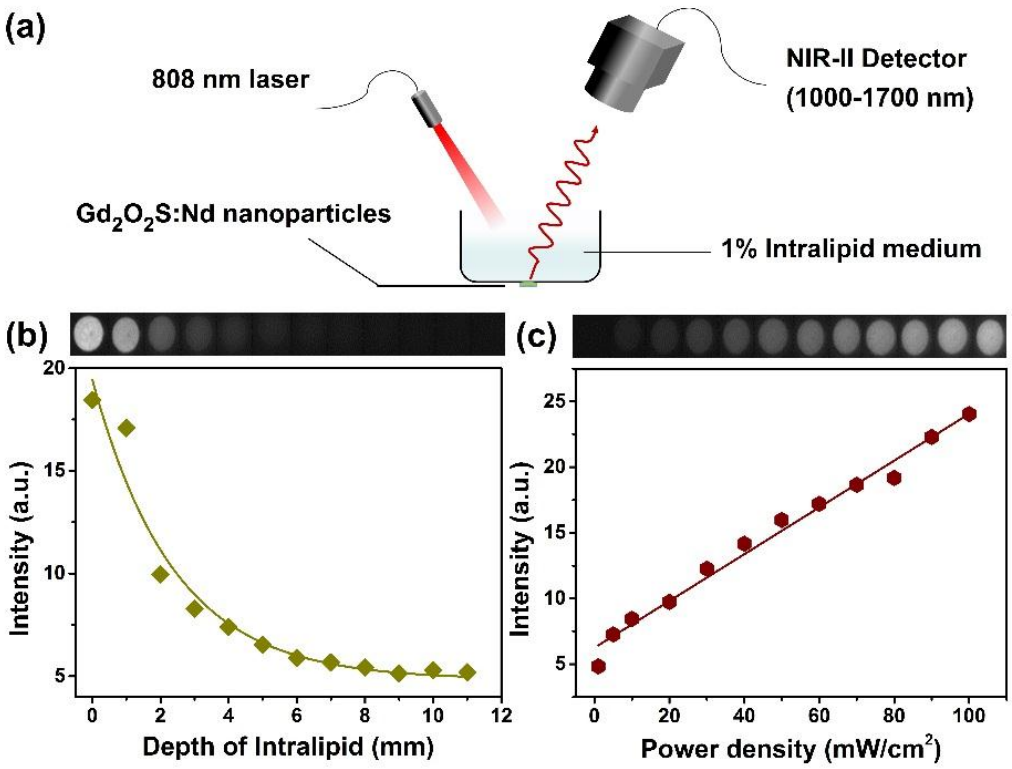

Figure 2.27 (a) Schematic illustration for NIR-II luminescence imaging of Gd_2O_2S:60%Nd NPs covered with 1% Intralipid medium. (b) NIR-II luminescence intensities obtained for Gd_2O_2S:60%Nd NPs with respect to immersion depth of the Intralipid medium under 808 nm laser excitation with power density of 50 mW/cm^2. (c) Plot of intensity as a function of the laser excitation power density with Intralipid depth of 2 mm. Inset photos show the variations with increase of Intralipid depth or power density. Exposure time for all images is 75 ms.

2) Magnetic resonance imaging

T_1- and T_2-weighted MR studies were performed at 7 T. The obtained T_1- and T_2-weighted MRI pictures for T_1- and T_2-weighted MRI are shown in Figure 2.28a. As we can see, with the concentration increases from left to right, the MR signal increases as well. By extracting the data from the MR images, we acquired T_1 and T_2 relaxivity times at each respective NPs concentration. Then the plot of $1/T$ vs. Gd concentration was drawn in Figure 2.28b. r_1 value of 25 $(mM)^{-1}s^{-1}$ and r_2 value of 65 $(mM)^{-1}s^{-1}$ were obtained by linearly fitting the plot. The r_2 value is relatively close to the transversal relaxivity observed for commercial T_2 contrast agents such as RESOVIST or

FERRIDEX (between 100 to 200 $(mM)^{-1}\cdot S^{-1}$ depending on conditions). More interestingly, we obtained a high r_1 value for our NPs, exhibiting the promise for T_1/T_2 dual contrast agents imaging. However, these results are still preliminary that we need to devote more efforts to reproducibility study of Gd_2O_2S:60%Nd NPs.

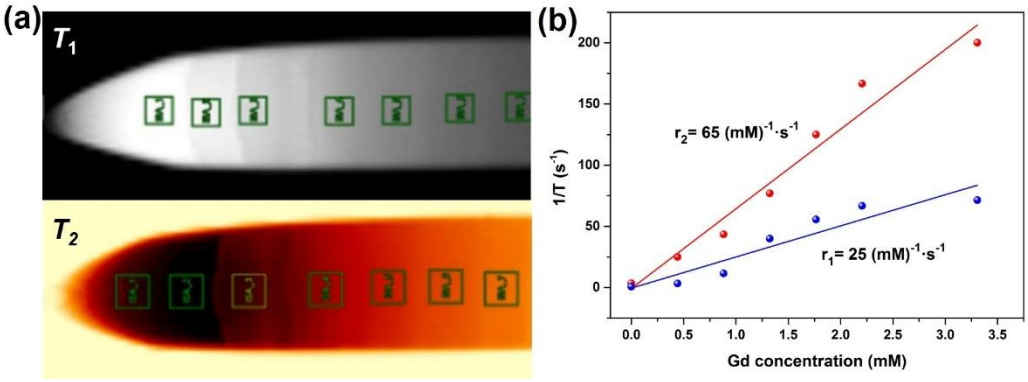

Figure 2.28 (a) T_1- and T_2- weighted MR images of Gd_2O_2S:60%Nd NPs with concentrations (0, 0.2, 0.4, 0.6, 0.8, 1, 1.5 mg/mL) increasing from left to right. T_1 and T_2 relaxivity times as a function of Gd concentration of Gd_2O_2S:60%Nd NPs.

3) X-ray computed tomography imaging

In order to investigate the CT imaging of Gd_2O_2S:60%Nd NPs, 10 samples were prepared in the centrifugal tubes, the upper layer contained NPs and pure gelatin solution was on the bottom layer as a control. Under X-ray irradiation, the Gd_2O_2S:60%Nd NPs can produce radiation–matter interactions such as absorption and Compton scattering, resulting contrast imaging. Figure 2.29a shows the CT images with different concentrations and Figure 2.29b shows the intensity of CT value as a function of concentrations. As we can see, X-ray absorption increases with NPs concentration increasing and the contrast starts on the image from the concentration of 2 mg/mL. The obtained scattering data show a linear relationship between the CT value and the NPs concentration.

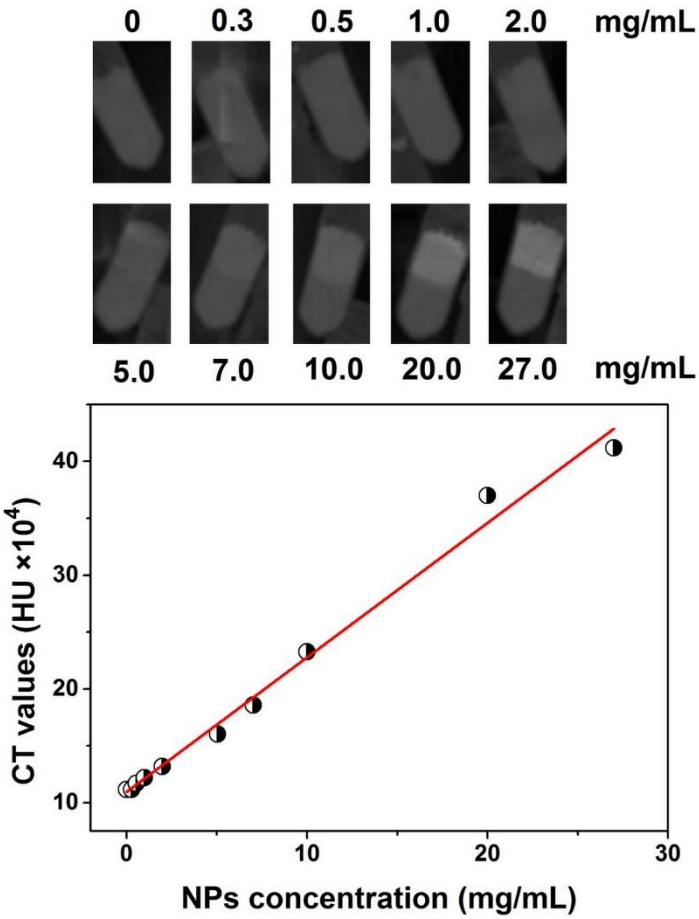

Figure 2.29 (a) CT images and (b) plot of HU vs. concentrations of Gd_2O_2S:60%Nd NPs.

4) Photoacoustic and ultrasound imaging

PA and US imaging are presented together because they were performed on the same device from the same batches of samples. The linearity curves of the PA and US intensity as a function of the concentration are presented in Figures 2.30a and b. According to the fitting curves, it seems that the sensitivities of these two imaging techniques are substantially equivalent and at the same order of magnitude for the tomodensitometry. The contrast starts from a concentration of around 5 mg/mL. Figure 2.30c shows the PA, US, and their merged images with NPs concentrations of 0 and 30 mg/mL. It shows good contrasts for both PA and US imaging at a concentration of 30 mg/mL.

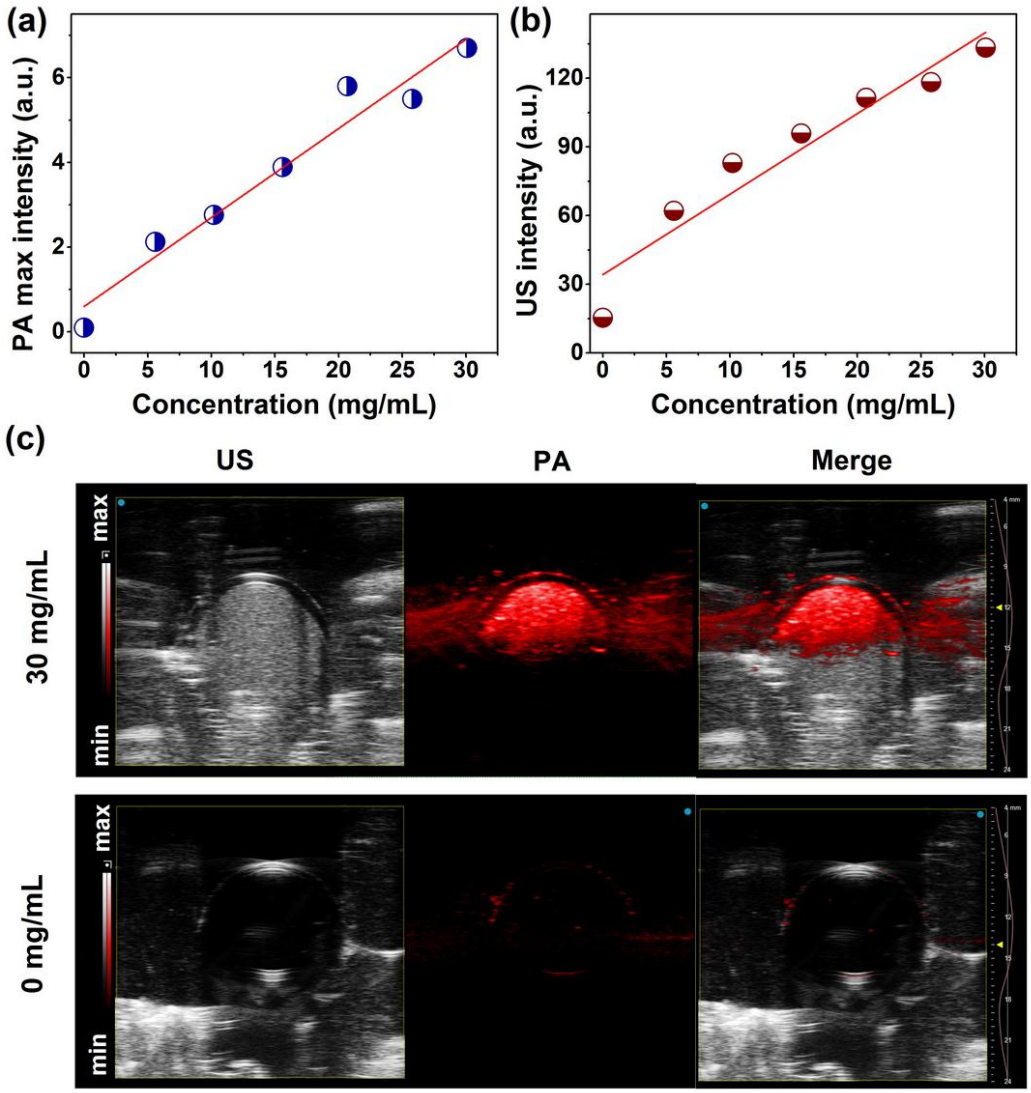

Figure 2.30 (a) PA and (b) US signal as a function of concentration of Gd_2O_2S:60%Nd NPs. (c) PA, US, and merge images of tubes filled with Gd_2O_2S:60%Nd NPs at concentration 0 and 30 mg/ml mixed with 10% gelatin.

4 Conclusions

In summary, we demonstrate a versatile strategy for synthesizing 15 kinds of ultrasmall RE_2O_2S NPs with size from 3 to 11 nm. Various reaction conditions including solvent ratio, amount of DPTU, reaction temperature and time, are carefully optimized to synthesize monodisperse Gd_2O_2S NPs. XRD and TEM are used for size and morphology characterizations.

To acquire multi modalities (NIR-II luminescence, photoacoustic, ultrasound,

magnetic, and CT performances), we further synthesize a series of Nd-doped Gd_2O_2S NPs with varying concentration. XRD and TEM are utilized to study the variation of size and morphology with varying Nd concentration. UV-vis-NIR absorption spectra also show the Nd concentration dependent absorption. With acquired absorption spectra, we calculate the absorption cross section of Nd in Nd_2O_2S small crystal. Under 808 nm laser irradiation, photoluminescence emission spectra of Gd_2O_2S:x%Nd (x=10, 20, 40, 60, and 100) NPs are recorded, following, Nd concentration is optimized to be 60% in Gd_2O_2S.

To render NPs hydrophilic, we investigate 3 surface modification strategies for Gd_2O_2S:60%Nd NPs. The acid treatment gives extremely low yield and reduced size of nanoparticle. Ligand exchange with $NOBF_4$ method gives severe aggregation, although different conditions are applied in the preparation. Further investigation on the interaction between surface ions of nanoparticle and BF- function group should be made for better understanding of aggregations. Finally, a ligand exchange with PVP method is proposed, where PVP molecules displace hydrophobic oleic acid layer of the surface of Gd_2O_2S:60%Nd NPs. FTIR spectra confirm the successful ligand exchange process. This method provides simple preparation procedure, high yield, and excellent water solubility and can be extended for other RE_2O_2S NPs obtained by thermal decomposition method with presence of OA. Cytotoxicity study of as-prepared PVP-coated Gd_2O_2S:60%Nd NPs show very low toxicity of our NPs.

Using those PVP-coated Gd_2O_2S:60%Nd NPs, we perform the multimodal imaging experiments. NIR-II luminescence imaging experiments demonstrate that an optical penetration of 2.4 mm is determined for the NPs. Besides, the NPs show ability of both T_1 and T_2 weighted imaging, which is for the first time reported for Gd_2O_2S NPs. CT-imaging experiments show the NPs have effective absorption ability of X-ray, which confirms the promising application of CT contrast agents. And the clear contrast can be detected beyond 2 mg/mL. PA and US imaging results show good linearity between the PA or US signals and concentrations of the NPs. The contrast starts on the image from

a concentration around 5 mg/ml. These findings pave an avenue for the bio-applications of ultrasmall RE_2O_2S NPs. The future work will focus on in vivo multimodal bioimaging on cells or small animals with RE_2O_2S NPs.

Chapter III: Exploration of core/shell nanoparticles

1 Introduction

Core/shell heterostructure engineering plays a vital role in the development of nanoparticles (NPs). For example, heterostructured NPs such as $CoPt_3$/Au, Pt/Au and FePt/Au have been synthesized and have shown boosted catalytic properties as compared to their individual components.[273] For traditional semiconductor quantum dots (QDs), CdSe/CdTe, CdSe/CdS/ZnS, and InP/ZnS heterostructures with combined advantages have exhibited significantly improved electrical and optical properties.[274] Unlike the traditional Stokes fluorescence displayed by QDs, photon upconversion is a nonlinear process which can convert low-energy infrared photons into high-energy ultraviolet (UV) or visible ones.[275] It is now widely accepted that in the construction of rare-earth (RE) based upconversion NPs (UCNPs), the addition of an inert shell can drastically reduce quenching of upconverted luminescence from the core by surface processes.[276] Depositing two or more dedicated layers onto the core to form a core/multi-shell nanostructure where the various dopant lanthanide ions (sensitizers and activators) are distributed into separate layers can provide precise control over excitation and emission profiles.[277] QDs/UCNPs heterostructures such as InP/$Ln_xY_{1-x}F_3$/REF_3 (Ln = Yb, Nd; RE = Lu, Y) core/shell/shell and $CsPbBr_3$/$NaYF_4$:Yb,Tm core/shell NPs have been successfully synthesized and opened new opportunities for tunability of excitation wavelength of QDs from ultraviolet (UV) to near infrared (NIR).[278, 279]

However, much effort is devoted to studying upconversion on the well-known materials family of sodium rare-earth fluoride ($NaREF_4$) because it allows for high upconversion quantum yields (QY); for example, values of 9% and 10% were reported at a same power density of 20 W/cm^2 for 45 nm $NaYF_4$:Yb^{3+},Er^{3+}@$NaYF_4$ core/shell NPs[115] and 3 μm $NaYF_4$:Yb^{3+},Er^{3+} bulk material[116], respectively. Another hexagonal matrix, Gd_2O_2S, is also one of the best candidates for upconversion because of its high efficiency as a host[159, 160], but less widely studied than $NaYF_4$, even though it has been demonstrated promising for many bio-applications such as bioimaging and

biolabeling[162-164]. The reason is that there is lack of a more universal synthesis method to prepare small-sized and uniform NPs although several methods have been reported.[141, 159, 258] Luckily, in chapter II, we have demonstrated a versatile strategy for synthesis of ultrasmall (< 10 nm) RE_2O_2S NPs. With doping proper lanthanide ions, we may obtain upconversion luminescence but at a very low efficiency due to surface quenching originated from so called small size effect. Further, the challenge of looking for a strategy to enhance the upconversion luminescence (UCL) efficiency of the ultrasmall UCNPs must be undertaken.

In this chapter, we first prepare 4 mmol of Gd_2O_2S:20%Yb,1%Tm UCNPs through an amplification synthesis approach. Then we successfully deposit an inert $NaYF_4$ shell of ~4 nm thickness on the Gd_2O_2S:20%Yb,1%Tm core NPs. The core/shell structure is demonstrated by transmission electron microscopy (TEM) and X-ray diffraction (XRD) analyses. The growth kinetics of RE_2O_2S@$NaREF_4$ core/shell NPs are studied by minutely analysing TEM, XRD, and small-angle X-ray scattering (SAXS) in different reaction phases. Upconversion properties including UCL intensity, lifetime, and QY of Ln^{3+}-doped Gd_2O_2S@$NaYF_4$ core/shell NPs are systematically investigated. Finally, we also characterize the diverse chemical and physical properties of 20%Yb/x%Er doped Gd_2O_2S@$NaYF_4$ UCNPs to gain deep insights into the UCNPs.

2 Experimental section

2.1 Materials

N, N'-Diphenylthiourea (DPTU), $LiOH{\cdot}H_2O$, NaOH, ammonium fluoride (NH_4F), polyvinylpyrrolidone (PVP, MW= 10000), alendronate, acetic acid, ethanol, methanol, and cyclohexane were purchased from Sigma-Aldrich. Oleic acid (OA), 1-Octadecene (ODE), Oleylamine (OM), and tri-n-octylamine (TOA) were purchased from TCI. All rare earth oxides (RE_2O_3, RE = Y, La, Ce, Pr, Nd, Sm, Eu, Gd, Tb, Dy, Ho, Er, Tm, Yb, and Lu) were purchased from Rone Poulenc. The $RE(CH_3COO)_3{\cdot}4H_2O$ were prepared by firstly dissolving moderate amount of the RE_2O_3 in excess acetic acid solution at 90 °C, then filtering and evaporating the solution, finally drying the resultant slurry in

the oven at 70 °C. All chemicals were used as received without further purification.

2.2 Large-scale synthesis of Gd_2O_2S:Yb,Tm UCNPs

Briefly, 8 mmol of $Ln(Ac)_3 \cdot 4H_2O$ (Ln=Gd, Yb, Tm at a ratio of 79/20/1), 8 mmol LiOH, 24 mL of OA, 56 mL of OM and 80 mL of TOA were mixed in a 500 mL flask and then heated up to 160 °C and maintained for 1 h under argon atmosphere. An ethanol solution containing 24 mmol of DPTU was added in the above solution when it was cooled down to RT. Where after, the resulting mixture solution was heated to 70 °C and maintained for 3 h to remove the ethanol and then further heated to 320 °C and maintained for 1 h, and then cooled down to room temperature. The nanocrystals were precipitated by addition of 290 mL of ethanol and then further purified with a mixture solution of ethanol and cyclohexane. The resulting nanocrystals were re-dispersed in 320 mL of cyclohexane and stored in refrigerator at ~4 °C for future use.

2.3 Synthesis of Gd_2O_2S:20%Yb,1%Tm@Gd_2O_2S core/shell UCNPs

The Gd_2O_2S:20%Yb,1%Tm@Gd_2O_2S core/shell nanocrystals were prepared by using a hot injection of shell precursors method. The shell precursor solution was first prepared by heating a mixture of 0.5 mmol of $Gd(CH_3COO)_3 \cdot 4H_2O$, 0.5 mmol of LiOH, 1.5 mL of OA, 3.5 mL of OM and 5 mL of TOA at 160 °C under an argon flow with constant stirring for 30 min. After cooling down, an ethanol solution (5 mL) of DPTU (1.5 mmol) was added dropwise and stirred for 30 min. Meanwhile, 5 ml of cyclohexane containing 0.25 mmol of Gd_2O_2S:20%Yb,1%Tm core nanocrystals, 1.5 mL of OA, 3.5 mL of OM and 5 mL of TOA were mixed in a 100 mL three-necked flask and heated to 80 °C under an Argon flow with constant stirring for 30 min to remove cyclohexane. Then the mixture solution was heated to 320 °C, subsequently, the shell precursors solution was added into the above solution by a syringe pump at a rate of 0.55 mL/min. To ensure the added shell precursor can be equably attached on the surface of the core seeds, a time interval 20 min was adopted after a single injection of 1 mL shell precursor solution. After adding all the shell precursors solution, the mixture solution was heated at 320 °C for another 40 min, and then cooled down to room temperature. The resulting

products were centrifuged and washed 3 times with ethanol and finally re-dispersed in 10 mL of cyclohexane.

2.4 Synthesis of lanthanide-doped RE_2O_2S@$NaREF_4$ UCNPs

Gd_2O_2S:20%Yb,1%Tm@$NaYF_4$ UCNPs were synthesized by a similar procedure which is normally used for the synthesis of pure fluoride core/shell nanocrystals according to the previous literature. In a typical synthesis, a mixture of 0.5 mmol of $Y(CH_3COO)_3 \cdot 4H_2O$, 6 mL of OA and 15 mL of ODE was heated at 160 °C for 30 min. After cooling down, 10 ml cyclohexane dispersion of 0.125 mmol Gd_2O_2S:20%Yb,1%Tm core NPs were added, followed with addition of 5 mL methanol solution containing 2 mmol of NH_4F and 1.25 mmol of NaOH. After moderate stirring for 60 min at 60 °C to remove cyclohexane and methanol, the solution was heated to 300 °C for 1 h, and then cooled down to room temperature naturally. The products were precipitated, purified and re-dispersed cyclohexane. For the synthesis of Gd_2O_2S:20%Yb,1%Tm@$NaYREF_4$ (RE = La, Ce, Pr, Nd, Sm, Eu, Gd, Tb, Dy, Ho, Er, Tm, Yb, and Lu) nanocrystals, the same procedure was applied only $Y(CH_3COO)_3 \cdot 4H_2O$ was replaced by corresponding $RE(CH_3COO)_3 \cdot 4H_2O$ (RE = La, Ce, Pr, Nd, Sm, Eu, Gd, Tb, Dy, Ho, Er, Tm, Yb, and Lu).

2.5 Preparation of hydrophilic Gd_2O_2S:Yb,Er@$NaYF_4$ UCNPs

The OA-free NPs were prepared through a ligand exchange method as reported previously[207]. Typical, 4 mL of nanocrystal dispersion in cyclohexane (~10 mg/mL) mixed with 4 mL of DMF solution of $NOBF_4$ (40 mg) to form a two-phase mixture at room temperature. The resulting mixture was gently shaken for 10 min. After removing the upper supernatant, 20 mL of chloroform was added to precipitate the nanocrystals, then centrifuging and washing the nanocrystals with DMF and chloroform for 3 times. The final OA-free NPs were re-dispersed in DMF.

To further coat PVP or alendronate on the OA-free NPs, 1.2 g of PVP or alendronate was added in 3 mL of DMF dispersion (5 mg/mL). The mixture was stirred for 6 hours, then, 20 mL of acetone was added to precipitate the NPs. The obtained NPs were

washed several times with DMF and acetone and finally dispersed in 1 mL of water. The solution was stored in fridge under 4 °C for further use.

2.6 XRD and TEM measurements

Power XRD patterns of samples were recorded on a Bruker D8 Advance X-ray diffractometer (Cu Kα radiation, λ = 1.542 Å). Size, morphology, structure, and composition analyses of NPs were carried out *via* TEM. Low-resolution TEM images were recorded on Phillips CM20, 200 kV; high-resolution (HR) TEM images were recorded on Hitachi I2TEM, 200 kV; annular bright field (ABF), high angle annular dark field scanning TEM (HAADF-STEM), element mapping, and electron energy loss spectroscopy (EELS) were measured on JEOL ARM-200F FEG.

2.7 Determination of hydrodynamic size

Dynamic light scattering (DLS) was performed on a Malvern Zetasizer to determine the hydrodynamic sizes and size distributions under a temperature of 25 °C. NPs were dispersed in DMF or water with a very low concentration of about 0.01 mg/mL.

2.8 SAXS measurements

The SAXS analyses were performed on XEUSS 2.0 (Xenocs Company) composed of X-ray micro-source delivering at 8 keV with a spot sized beam equal to 0.5 mm and the intensity close to 30×10^6 photons·s^{-1}. The samples were placed on sample loader dedicated to capillaries with 1216.5mm of distance from the detector, providing a range of scattering vector starting from 0.005 Å^{-1} to 0.5 Å^{-1}. The samples were exposed during 600 s under vacuum and the scattered beam was collected on the 1M Pilatus detector (1 million counts/pixel). Data integration and reduction were performed with the software FOXTROT. All of data are normalized by the transmission, the optical path and the acquisition time.

2.9 UCL spectra measurements

Room-temperature UCL spectra were recorded on a Jobin-Yvon Model Fluorolog FL3-22 spectrometer that was combined with a 980 nm diode laser (MDL-III-980-5W,

Changchun New Industries Optoelectronics Tech Co., Ltd) as excitation source, at CEMES, Toulouse, France. The NPs were dispersed in cyclohexane with the same concentration of 10 mg/mL.

2.10 UCL decay measurements

Time resolved luminescence measurements of Gd_2O_2S:20%Yb,1%Tm core and Gd_2O_2S:20%Yb,1%Tm@$NaYF_4$ UCNPs were performed using a nanosecond 976 nm excitation (fwhm 7-8 ns, 2.5 mJ, 2 Hz) provided by a 10-Hz Nd:YAG laser (Continuum Surelite II) coupled to an OPO (Continuum Panther EX OPO). Samples were introduced in a quartz cell (4 × 10 mm) and the emitted light was collected at 90°, dispersed by a monochromator (Horiba Jobin-Yvon, iHR320, bandpass 10 nm) and analyzed with a gated intensified CCD camera (1024 x 256 pixels, PI-MAX 4, Princeton Instruments) triggered by a photodiode. Time-resolved spectra between 400 and 900 nm were recorded with constant gate width of 500 ns for core Gd_2O_2S:20%Yb,1%Tm UCNPs. The first time gate was set to start at 26 ns (insertion delay of the camera) and 100 gates were recorded (26 ns to 50 µs). Time-resolved spectra of core-shell Gd_2O_2S:20%Yb,1%Tm@$NaYF_4$ UCNPs were recorded with constant gate width of 50 µs (100 gates, 26 ns to 5 ms). These measurements were carried out at LASIR, Université de Lille, France.

UCL decays of Gd_2O_2S:20%Yb,x%Er@$NaYF_4$ UCNPs were recorded on an Edinburgh Instruments Model FLS980-xD2-stm spectrofluorometer equipped with an electrically pulsed, 978 nm laser diode under 20 °C, at BAM, Berlin, Germany. The UCNPs were dispersed in cyclohexane.

2.11 UC quantum yield (UCQY) measurements

Power-dependent UC quantum yield measurements were performed on a purposely designed set up which includes a high stability 8 W 976 nm diode laser, a calibrated integrating sphere, a set of neutral density filters, and a detector with spectral response of UV/vis/NIR luminescence. All the calibration of integrating sphere, beam profiles, and detector calibration can be found in the previous reports.[280, 281] The NPs were

dispersed in cyclohexane and a pure cyclohexane solution was used as the blank reference. The absolute UCQYs were calculated by[281]

$$\Phi_{UC} = \frac{N_{em}}{N_{ab}} \quad (3\text{-}1)$$

where Φ_{UC}, N_{em}, and N_{ab} represent UCQY values, emitted photons, and absorbed photons, respectively. All the UCQYs measurements were done at BAM.

2.12 ICP-OES measurements

Quantification of the composition of the UCNPs was carried out by ICP-OES using a Model: FHX, 76004553, spectrometer from SPECTRO Across-EOP at BAM, Berlin, Germany. The UCNPs were dissolved in HNO_3 solution.

2.13 UV-vis-NIR absorption measurements

Absorption spectra were recorded on a Cary 5000 spectrophotometer from Varian Inc.

3 Results and discussion

3.1 Characterizations of RE_2O_2S@$NaREF_4$ heterogeneous structure

Lanthanide-doped NPs have been widely used in many applications due to their unique properties and various mature synthesis methods. However, the size of NPs may differ from batch to batch, which may bring troubles for researchers especially when comparing a series of core/shell NPs synthesized with the same core composition. Large-scale synthesis seems to be a good solution that has attracted much attention, yet, it still remains challenging. In the previous chapter, we have demonstrated the high-temperature decomposition for the synthesis of RE_2O_2S NPs. Here, we first synthesized a big batch (4 mmol) of Gd_2O_2S:20%Yb,1%Tm NPs through the large-scale synthesis method. As shown in Figure 3.1a, the TEM image displays the morphology and mono-dispersity of the NPs. The mean size of the NPs was measured to be 5.2 ± 0.9 nm (Figure 3.1c). The high-resolution (HR) TEM image (Figure 3.1b) shows several sets of clear lattice fringes, indicating the fine crystallinity of the NPs. The d-spacing was measured to be 0.308 nm which can be indexed to (101) lattice plane of Gd_2O_2S. The inset photo in Figure 3.1 shows that the obtained NPs are well dispersed in 320 mL of

cyclohexane to form a concentration of 0.0125 M for the use of core/shell synthesis.

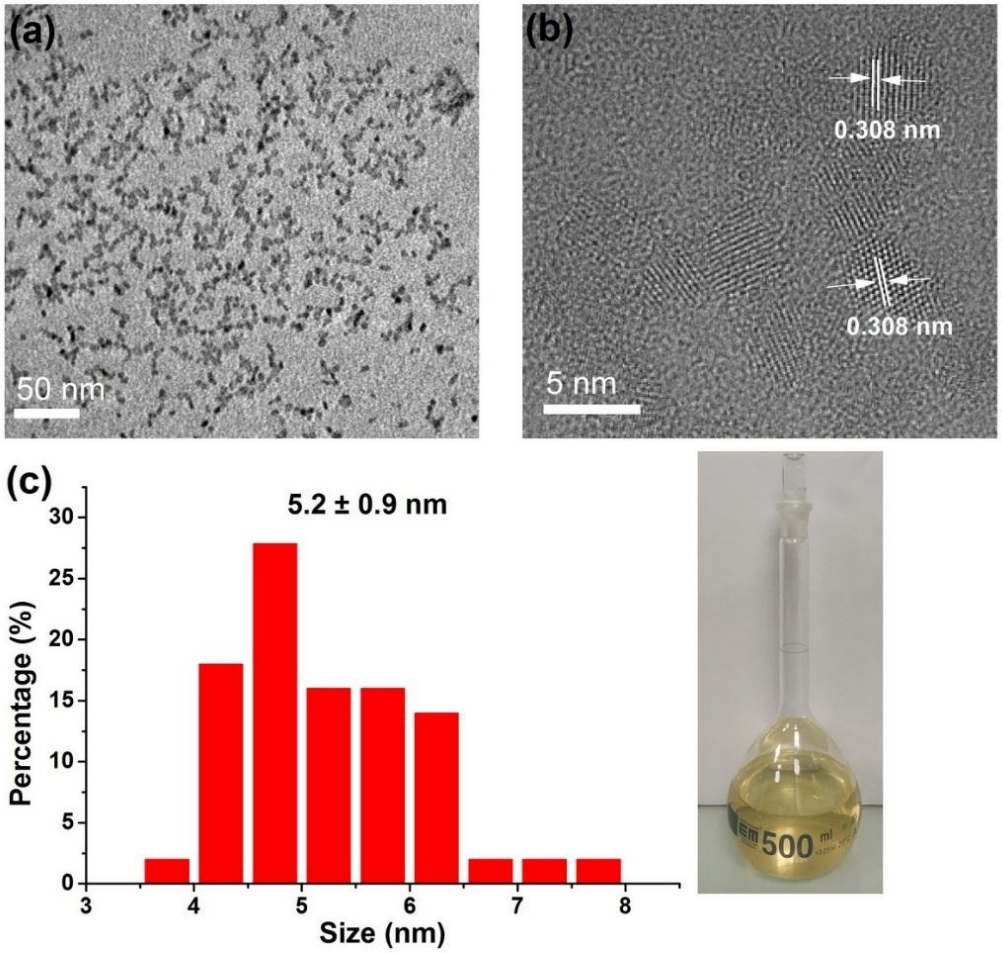

Figure 3.1 (a) Low- and (b) high-resolution (HR) TEM images of Gd_2O_2S:20%Yb,1%Tm core UCNPs. (c) Size distribution histogram of the NPs. The lattice d-spacing of 0.308 nm was determined by analysing the HRTEM images, which corresponds to (101) plane of Gd_2O_2S. The mean size was measured to be 5.2 ± 0.9 nm by counting 100 NPs from (a). Inset photo shows all the purified core NPs were dispersed in 320 mL cyclohexane solution, forming a concentration of 0.0125 mmol/mL.

Then, two types of core/shell NPs were explored based on the Gd_2O_2S:20%Yb,1%Tm core NPs. To coat a shell on the core NPs, we first thought about the homogeneous composition Gd_2O_2S due to the smallest lattice mismatch. Then, the homogeneous Gd_2O_2S:20%Yb,1%Tm@Gd_2O_2S core/shell NPs were prepared by a hot injection method where the shell thickness can be controlled by the amount of

addition of shell precursors. Figure 3.2a exhibits the TEM image and size distribution of Gd_2O_2S:20%Yb,1%Tm@Gd_2O_2S core/shell NPs synthesized with addition of 0.25 mmol shell precursors. The core/shell NPs had good dispersity and polygonal shape, and the size was determined to be 12.3 ± 1.5 nm. When further increasing the amount of the shell precursors up to 0.5 mmol, the size of NPs enlarged as well with a mean size of 14.0 ± 1.4 nm (Figure 3.2b) but the NPs were irregularly shaped.

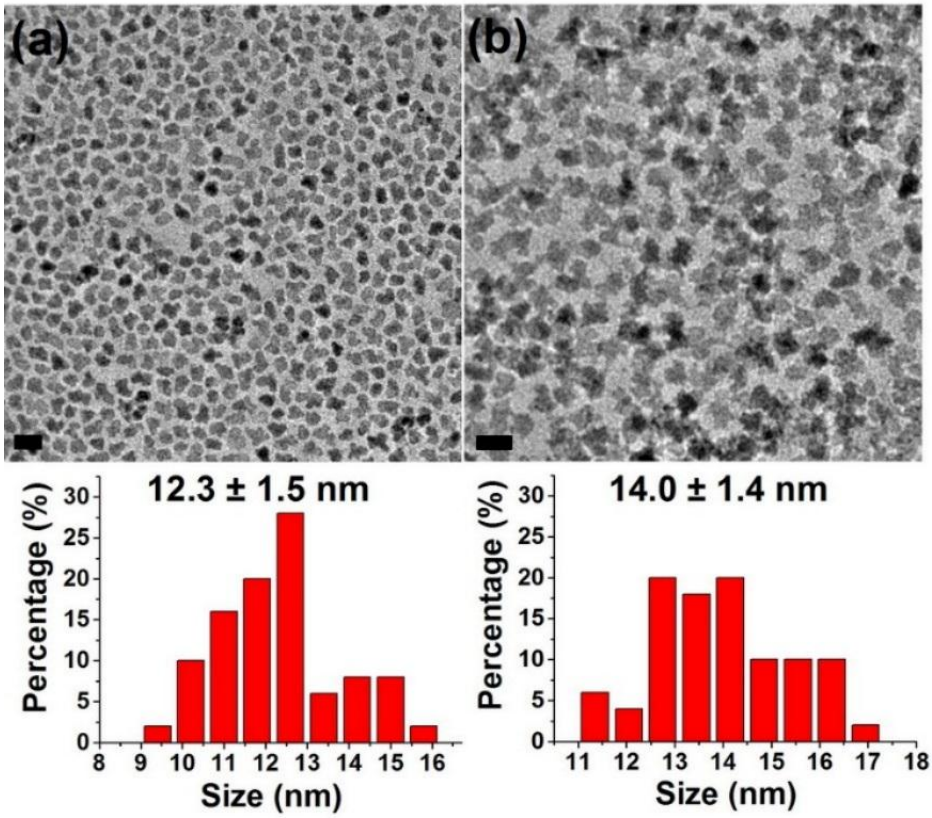

Figure 3.2 TEM images and size distributions of Gd_2O_2S:20%Yb,1%Tm@Gd_2O_2S core/shell NPs synthesized with different amount of addition of shell precursors (a: 0.25 mmol; b: 0.5 mmol). Scale bar: 20 nm.

On the other hand, both Gd_2O_2S and $NaYF_4$ are known to have their thermodynamically stable products in a hexagonal lattice, which inspires us to construct a new heterogeneous structure. For the synthesis of heterogeneous nano-architecture, lattice mismatch is normally one of the key factors. In general, when the lattice mismatch of two materials is less than 5%, the theoretical possibility of heterogeneous structure formed by epitaxial growth exists.[282, 283] Hence, it is necessary to first calculate

the lattice mismatches of RE_2O_2S and $NaREF_4$ and provide a prediction.

As it can be seen in Table 3.1, majority lattice planes and corresponding d-spacings of RE_2O_2S and $NaREF_4$ were extracted from the ICDD. The selected lattice plane (101) or (011) of RE_2O_2S present the highest diffraction intensity according to the ICDD files. Accordingly, the (110) or (101) plane of $NaREF_4$ was selected for comparison.

Table 3.1 List of selected d-spacings for RE_2O_2S and $NaREF_4$ of hexagonal phase.

Core	hkl	d-spacing (Å)	Shell	hkl	d-pacing (Å)
Y_2O_2S	(011)	2.929	$NaYF_4$	(110)	2.97
La_2O_2S	(101)	3.128	$NaLaF_4$	(110)	3.09
Ce_2O_2S	(101)	3.07	$NaCeF_4$	(101)	3.082
Pr_2O_2S	(101)	3.07	$NaPrF_4$	(101)	3.001
Nd_2O_2S	(101)	3.06	$NaNdF_4$	(110)	3.05
Sm_2O_2S	(101)	3.009	$NaSmF_4$	(110)	3.03
Eu_2O_2S	(101)	2.995	$NaEuF_4$	(110)	3.034
Gd_2O_2S	(101)	2.985	$NaGdF_4$	(110)	3.01
Tb_2O_2S	(101)	2.962	$NaTbF_4$	(110)	2.995
Dy_2O_2S	(101)	2.945	$NaDyF_4$	(110)	2.99
Ho_2O_2S	(101)	2.929	$NaHoF_4$	(110)	2.998
Er_2O_2S	(101)	2.92	$NaErF_4$	(110)	2.97
Tm_2O_2S	(011)	2.906	$NaTmF_4$	(110)	2.98
Yb_2O_2S	(101)	2.887	$NaYbF_4$	(110)	2.96
Lu_2O_2S	(101)	2.876	$NaLuF_4$	(110)	2.94

*Powder diffraction files (PDF) of hexagonal phase RE_2O_2S and $NaREF_4$ are collected from the international center for diffraction data (ICDD). Y_2O_2S: #04-002-2593; La_2O_2S: #04-002-6784; Ce_2O_2S: #00-026-1085; Pr_2O_2S: #00-027-0479; Nd_2O_2S: #00-027-0321; Sm_2O_2S: #00-044-1257; Eu_2O_2S: #00-026-1418; Gd_2O_2S: #00-026-1422; Tb_2O_2S: #00-026-1495; Dy_2O_2S: #00-026-0592; Ho_2O_2S: #00-025-1143; Er_2O_2S: #00-025-1118; Tm_2O_2S: #03-065-3444; Yb_2O_2S: #00-026-0614; Lu_2O_2S: #00-026-1445;

$NaYF_4$: #00-016-0334; $NaLaF_4$: #01-082-4237; $NaCeF_4$: #00-050-0154; $NaPrF_4$: #04-018-8799; $NaNdF_4$: #00-035-1367; $NaSmF_4$: #00-027-0779; $NaEuF_4$: #00-049-1897; $NaGdF_4$: #00-027-0699; $NaTbF_4$: #00-027-0809; $NaDyF_4$: #00-027-0687; $NaHoF_4$: #00-049-1896; $NaErF_4$: #00-027-0689; $NaTmF_4$: #00-027-0814; $NaYbF_4$: #00-027-1427; $NaLuF_4$: #00-027-0726.

Then, the lattice mismatches were calculated by the conventional definition given by the equation[284]:

$$\frac{Shell\ Lattice\ Parameter - Core\ Lattice\ Parameter}{Core\ Lattice\ Parameter} \quad (3\text{-}2)$$

where the core and shell lattice parameters are corresponding to RE_2O_2S and $NaREF_4$ d-spacing values respectively from the Table 3.1.

Table 3.2 Summary of lattice mismatch values of RE_2O_2S and $NaREF_4$.

	$NaYF_4$	$NaLaF_4$	$NaCeF_4$	$NaPrF_4$	$NaNdF_4$	$NaSmF_4$	$NaEuF_4$	$NaGdF_4$	$NaTbF_4$	$NaDyF_4$	$NaHoF_4$	$NaErF_4$	$NaTmF_4$	$NaYbF_4$	$NaLuF_4$
Y_2O_2S	1.40%	5.50%	5.22%	2.46%	4.13%	3.45%	3.59%	2.77%	2.25%	2.08%	2.36%	1.40%	1.74%	1.06%	0.38%
La_2O_2S	-5.05%	-1.21%	-1.47%	-4.06%	-2.49%	-3.13%	-3.00%	-3.77%	-4.25%	-4.41%	-4.16%	-5.05%	-4.73%	-5.37%	-6.01%
Ce_2O_2S	-3.26%	0.65%	0.39%	-2.25%	-0.65%	-1.30%	-1.17%	-1.95%	-2.44%	-2.61%	-2.35%	-3.26%	-2.93%	-3.58%	-4.23%
Pr_2O_2S	-3.26%	0.65%	0.39%	-2.25%	-0.65%	-1.30%	-1.17%	-1.95%	-2.44%	-2.61%	-2.35%	-3.26%	-2.93%	-3.58%	-4.23%
Nd_2O_2S	-2.94%	0.98%	0.72%	-1.93%	-0.33%	-0.98%	-0.84%	-1.63%	-2.12%	-2.29%	-2.03%	-2.94%	-2.61%	-3.27%	-3.92%
Sm_2O_2S	-1.30%	2.69%	2.43%	-0.27%	1.36%	0.70%	0.84%	0.03%	-0.47%	-0.63%	-0.37%	-1.30%	-0.96%	-1.63%	-2.29%
Eu_2O_2S	-0.83%	3.17%	2.90%	0.20%	1.84%	1.17%	1.31%	0.50%	0.00%	-0.17%	0.10%	-0.83%	-0.50%	-1.17%	-1.84%
Gd_2O_2S	-0.50%	3.52%	3.25%	0.54%	2.18%	1.51%	1.65%	0.84%	0.34%	0.17%	0.44%	-0.50%	-0.17%	-0.84%	-1.51%
Tb_2O_2S	0.27%	4.32%	4.05%	1.32%	2.97%	2.30%	2.44%	1.62%	1.11%	0.95%	1.22%	0.27%	0.61%	-0.07%	-0.74%
Dy_2O_2S	0.85%	4.92%	4.65%	1.90%	3.57%	2.89%	3.03%	2.21%	1.70%	1.53%	1.80%	0.85%	1.19%	0.51%	-0.17%
Ho_2O_2S	1.40%	5.50%	5.22%	2.46%	4.13%	3.45%	3.59%	2.77%	2.25%	2.08%	2.36%	1.40%	1.74%	1.06%	0.38%
Er_2O_2S	1.71%	5.82%	5.55%	2.77%	4.45%	3.77%	3.91%	3.08%	2.57%	2.40%	2.67%	1.71%	2.05%	1.37%	0.68%
Tm_2O_2S	2.20%	6.33%	6.06%	3.27%	4.96%	4.27%	4.41%	3.58%	3.06%	2.89%	3.17%	2.20%	2.55%	1.86%	1.17%
Yb_2O_2S	2.87%	7.03%	6.75%	3.95%	5.65%	4.95%	5.10%	4.26%	3.74%	3.57%	3.84%	2.87%	3.22%	2.53%	1.84%
Lu_2O_2S	3.27%	7.44%	7.16%	4.35%	6.05%	5.35%	5.50%	4.66%	4.14%	3.96%	4.24%	3.27%	3.62%	2.92%	2.23%

The results of the calculation are listed in the Table 3.2. Note that the “positive” or “negative” signs before the lattice mismatch values can be explained by “tensile” or “pressure” stress between the core and shell components. According to the analysis of lattice mismatch, the value “-0.5%” can be easily found for Gd_2O_2S core and $NaYF_4$ shell in Table 3.2. It apparently indicates that there is theoretical possibility for coating a $NaYF_4$ shell on Gd_2O_2S.

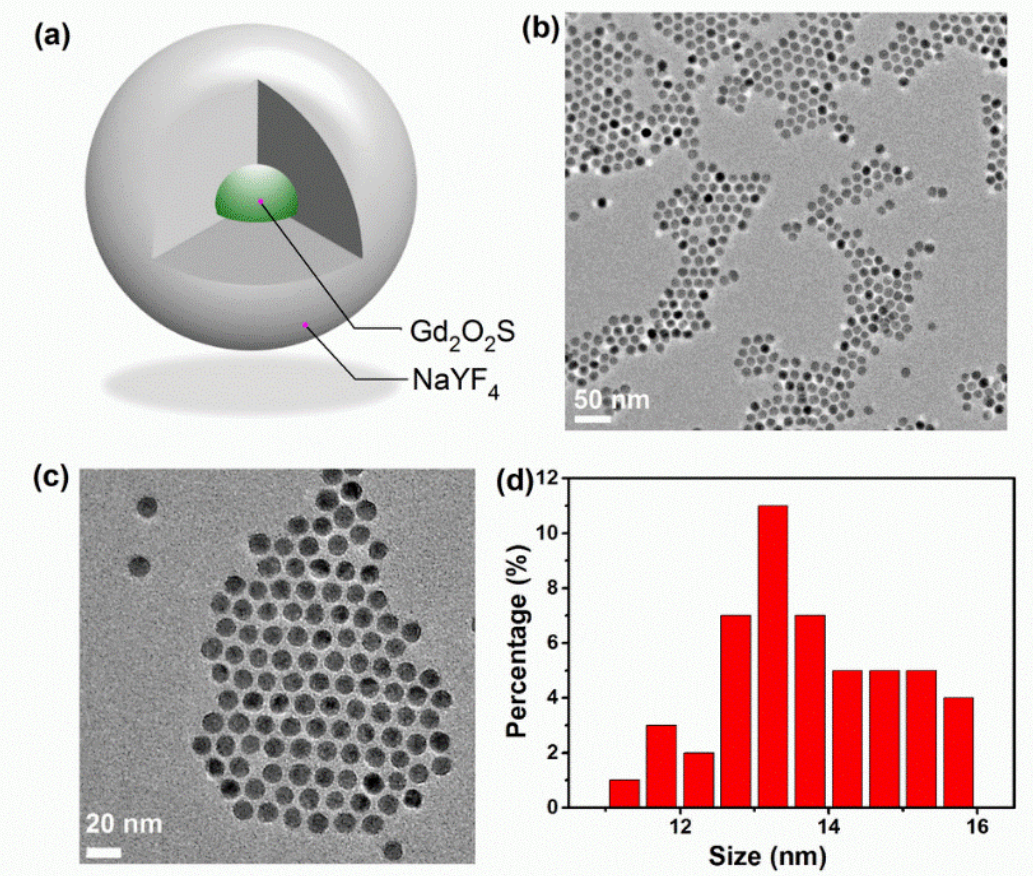

Figure 3.3 (a) Concept of Gd_2O_2S@$NaYF_4$ heterogeneous nanoarchitecture. (b, c) Typical TEM images of Gd_2O_2S:20%Yb,1%Tm@$NaYF_4$ heterogeneous NPs. (d) Size distribution histogram plotted by counting the NPs in TEM image of (c).

To carry out our concept of Gd_2O_2S@$NaYF_4$ as shown in Figure 3.3a, we added the as-prepared Gd_2O_2S:20%Yb,1%Tm core NPs as the seeds in a mixture solution in the presence of OA and ODE, for subsequent growth of hexagonal $NaYF_4$ shells. The details of synthesis have been already given in the corresponding synthesis section. The final products were collected for the further characterizations. As seen from the TEM images of the Figures 3.3b and 3.3c, high quality, monodispersed, uniform, and spherical NPs were obtained. No independent nucleation particles were observed. The mean size (Figure 3.3c) was determined to be 13.7 ± 0.8 nm in diameter nm by counting 100 NPs from the TEM image of Figure 3.3b. Due to the size enlargement of NPs, compared to the small size of Gd_2O_2S:20%Yb,1%Tm core NPs (~5 nm), we suggest that $NaYF_4$ shell is coated on the core NPs successfully. Further confirmations were

implemented by a series of qualitative analyses detailed below.

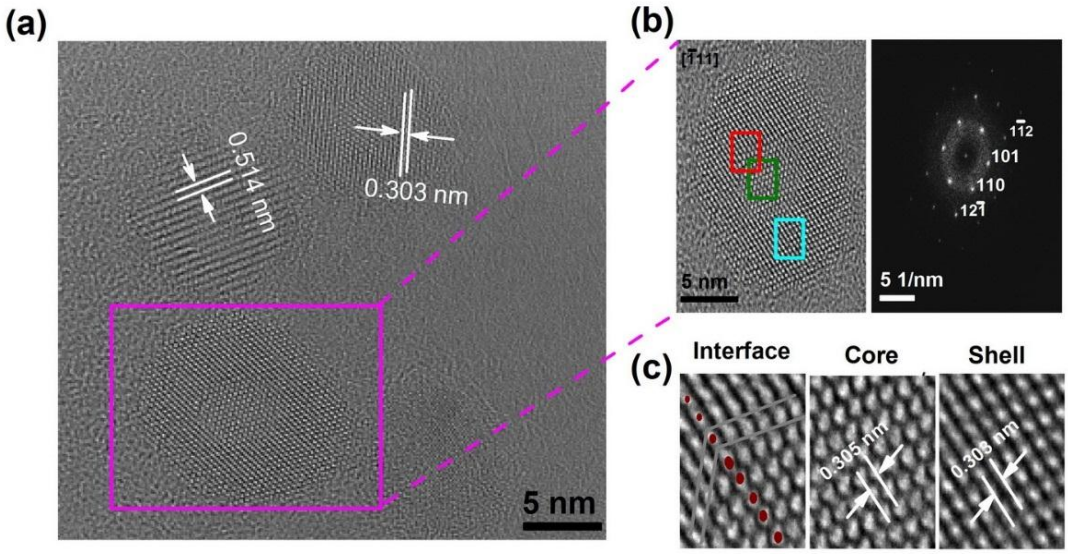

Figure 3.4 (a) High-resolution TEM (HRTEM) image, (b) HRTEM image of single NP extracted from (a) and its FFT pattern. (c) Magnification of selected red, olive, and cyan regions in HRTEM image of (g) show interface, core, and shell domains, respectively, of the single NP.

From the high-resolution TEM (HRTEM) image in Figure 3.4a, we can see clear lattice fringes of NPs. The d-spacings were measured to be 0.303 nm and 0.514 nm which can be assigned to (110) and (100) planes of hexagonal $NaYF_4$. A single NP was extracted from HRTEM image for further analysis (Figure 3.4b left). As shown in Figure 3.4b right, the corresponding FFT pattern can be indexed to the reflections of $NaYF_4$. Figure 3.4c displays three magnification areas of the single NP. The three different domains clearly show the coherent lattice fringes across the NP with obvious contrast between the Gd_2O_2S seed and the grown $NaYF_4$ shell. And the interface also can be observed. The d-spacings were determined to be 0.305 and 0.303 nm corresponding to (110) of Gd_2O_2S and (110) of $NaYF_4$ respectively. Based on these d-spacing values, we calculated the real lattice mismatch value as -0.66% which is very close to the theoretical value in Table 3.2.

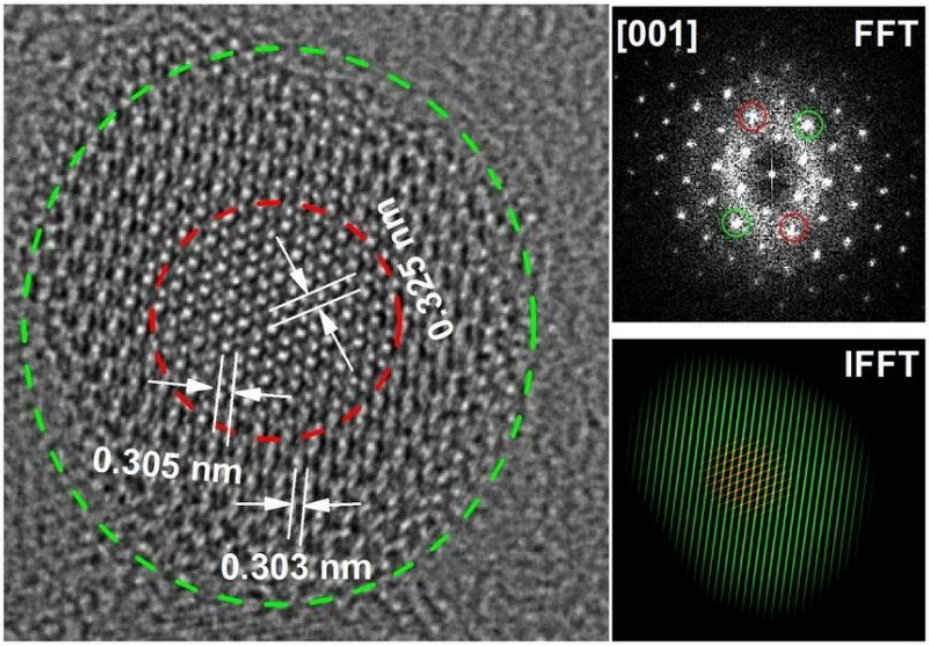

Figure 3.5 HRTEM image and its FFT pattern of single Gd_2O_2S:20%Yb,1%Tm@$NaYF_4$.

Furthermore, this arrangement difference between core and shell can be also unambiguously proved by another single NP in Figure 3.5. The lattice d-spacings in the center (in the red circle) were determined to be 0.325 nm and 0.305 nm, which respectively correspond to (100) and (101) plane of Gd_2O_2S; and the d-spacing in the out layer (between red and green circles) was determined to be 0.303 nm which corresponds to (110) of $NaYF_4$. These results imply that the (110) plane of $NaYF_4$ epitaxially grows along (101) plane of Gd_2O_2S. To further confirm it, we performed fast Fourier transform (FFT) and inverse FFT (IFFT) analysis (Figure 3.5 right). Two sets of filtered spots (marked as red and green circles) in the FFT pattern were chosen and applied for IFFT respectively. The acquired overlaid IFFT image displays that the red fringes are only from the core region and the green fringes are from shell region matched to core without line defects at the interface.

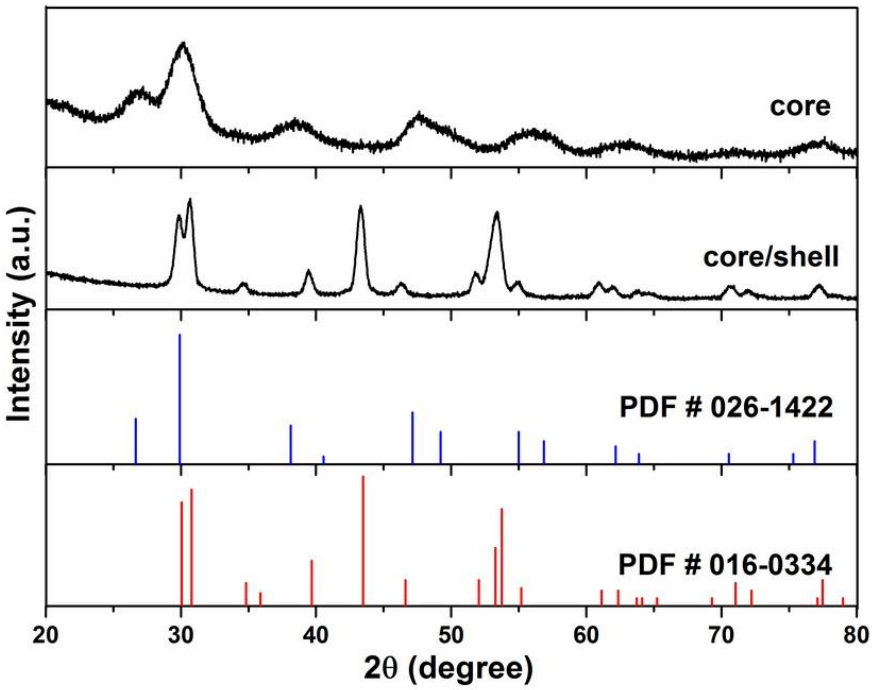

Figure 3.6 XRD patterns of Gd_2O_2S:20%Yb,1%Tm core and Gd_2O_2S:20%Yb,1%Tm@$NaYF_4$ heterogeneous core/shell NPs.

By using X-ray irradiation for Gd_2O_2S:20%Yb,1%Tm core and Gd_2O_2S:20%Yb,1%Tm@$NaYF_4$ core/shell NPs, we obtained diffraction patterns that allow us to acquire the structure information. Figure 3.6 shows the XRD patterns of both core and core/shell NPs. The peaks of core NPs are well matched with standard PDF card #026-1422 of hexagonal Gd_2O_2S, and the peaks are broad because of small size. All the diffraction peaks of core/shell NPs can be indexed to hexagonal $NaYF_4$ with slight shift to small angles, which means that there is existence of the lattice expansion after shell coating; this is consistent with the results of HRTEM analyses. Note that no obvious Gd_2O_2S diffraction patterns appearing among the XRD patterns of Gd_2O_2S:20%Yb,1%Tm@$NaYF_4$ core/shell NPs, which could be explained by very weak diffractions from Gd_2O_2S. We suggest the vanishing of Gd_2O_2S diffraction patterns is because very weak diffraction signals of the ultrasmall core crystallites are covered by the strong diffraction of the bigger shell. A similar phenomenon has been reported in other heterogenous α-$NaREF_4$@β-$NaREF_4$ core/shell NPs.[285, 286]

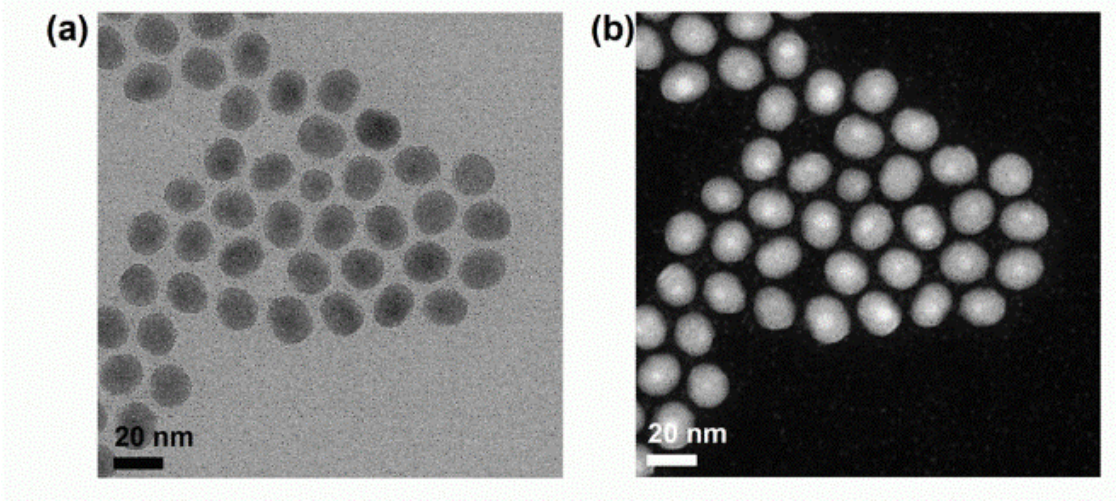

Figure 3.7 (a) Bright field and (b) high-angle annual dark field scanning TEM (HAADF-STEM) images of Gd_2O_2S:20%Yb,1%Tm@$NaYF_4$ core/shell NPs.

High-angle annular dark field scanning TEM (HAADF-STEM) is a STEM technique which produces an annular dark field image formed by very high angle, incoherently scattered electrons from the nucleus of atoms (Rutherford scattering). This technique is highly sensitive to variations in the atomic number (Z) of atoms in the sample, which is also named as Z-contrast imaging. In principle, more electrons are scattered at high angles for elements with a higher Z where a brighter image is caused by the HAADF detector. On the contrary, a lower Z produces a darker image. With this technique, HAADF is commonly used in heterogeneous structure research for distinguishing two or more than two elements in different layers. In purpose of confirmation of Gd_2O_2S:20%Yb,1%Tm@$NaYF_4$ core/shell NPs, we acquired bright field (BF) and HAADF-STEM images as shown in Figure 3.7. As the atomic number of Gd is larger than that of Y, thus the brighter dots present the heavier Gd element and the darker layers present the lighter Y element (Figure 3.7b). Inversely, in the BF-TEM image of Figure 3.7a, heavier Gd atoms present black areas in the centre of NPs and lighter Y atoms present grey areas of the NPs. In a word, BF and HAADF-STEM analyses help us to know that the Gd element is mainly located in the centre of the NP and Y element in the out layer.

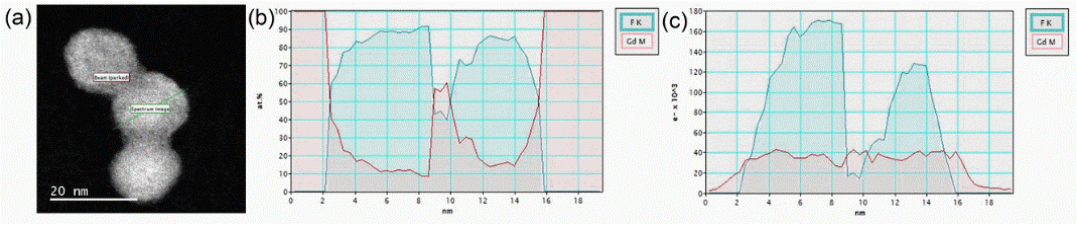

Figure 3.8 (a) HAADF-STEM image, electron energy loss spectra (EELS) presented by (b) atomic percentage and (c) peak intensity function as distance.

Simultaneously, electron energy loss spectra (EELS) were recorded for the Gd_2O_2S:20%Yb,1%Tm@$NaYF_4$ by detecting a single NP with a line scanning at a distance 5 Å between two points, as shown in Figure 3.8a. The atomic percentage (Figure 3.8b) and intensity (Figure 3.8c) of Gd and F element were respectively collected along the scanning line. As we can see, both the atomic percentage and intensity of F sharply decrease when it goes across the centre position of the NP. Oppositely, the atomic percentage of Gd massively increases compared to that of F, and the intensity slightly increases due to the low Gd content accounted for entire NP and ion immigration to the shell. Results of the EELS clearly manifest that the Gd atoms are located in the centre of the NP and F atoms have decreased portion in the centre, confirming the main element distribution of the Gd_2O_2S:20%Yb,1%Tm@$NaYF_4$ core/shell structure.

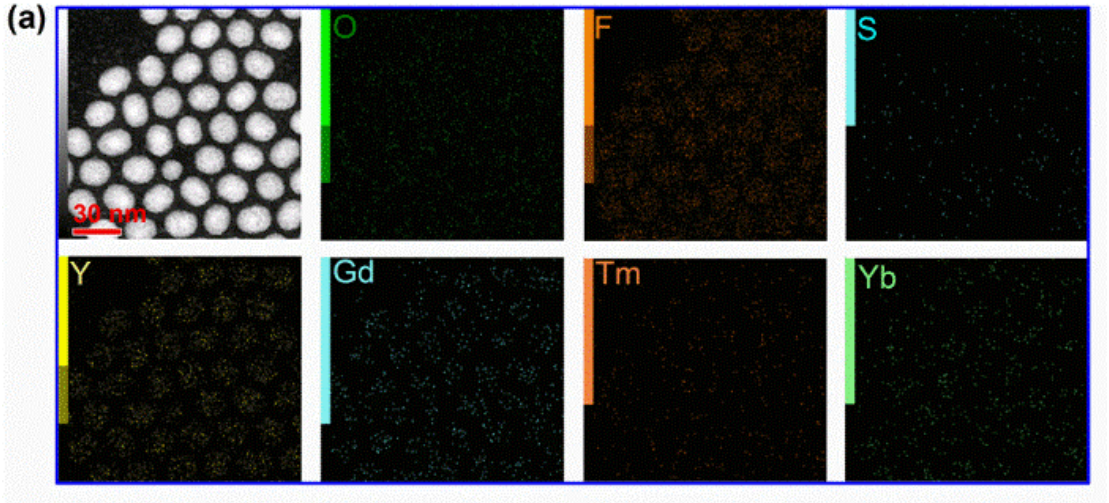

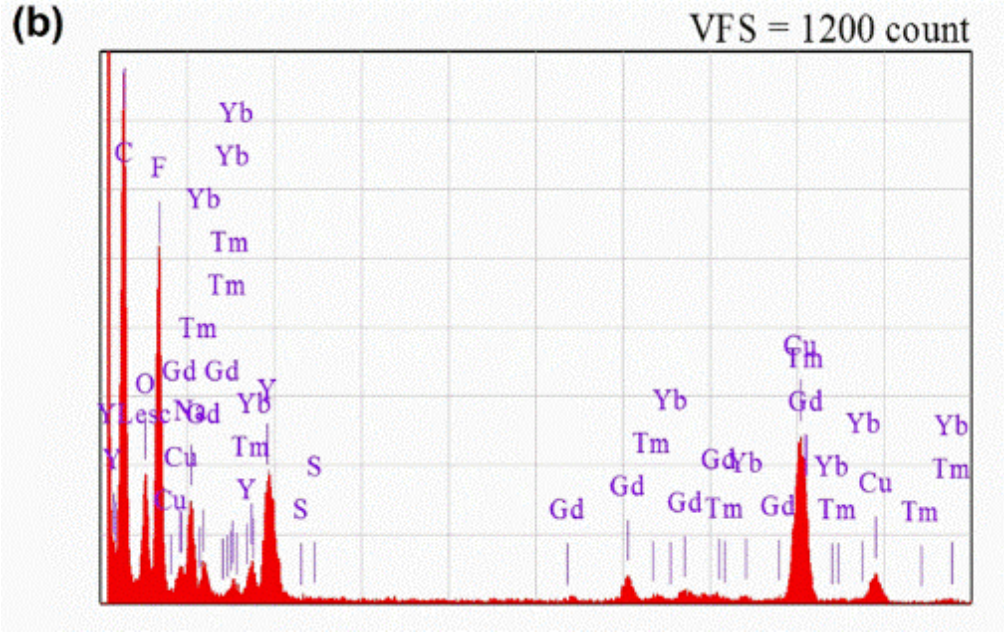

Figure 3.9 (a) Element mapping images and (b) energy dispersive X-ray spectroscopy (EDS) of Gd_2O_2S:20%Yb,1%Tm@$NaYF_4$ NPs.

Element mapping images in Figure 3.9a show the distributions of elements O, F, S, Y, Gd, Tm, and Yb. It is clear that the elements Gd, S, Yb, and Tm are gathered in the core locations while Y and F are gathered as shells. Note O distributions are from both core and surface organic compounds. Besides, energy dispersive X-ray spectroscopy (EDS) of Gd_2O_2S:20%Yb,1%Tm@$NaYF_4$ NPs shows the existence of all elements from both core (Gd, O, S, Yb, and Tm) and shell (Na, Y, and F) components, in Figure 3.9b.

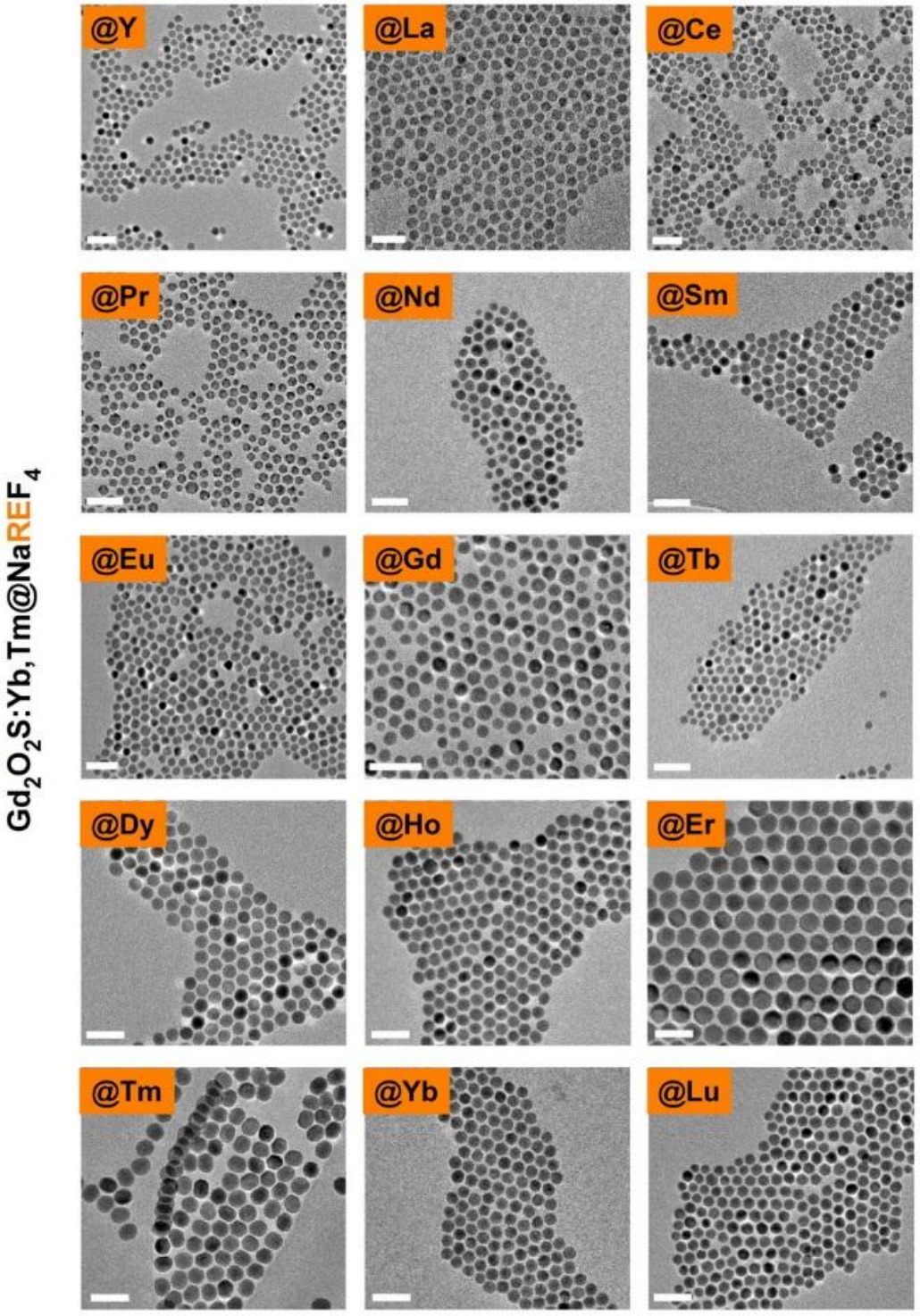

Figure 3.10 TEM images of Gd_2O_2S:20%Yb,1%Tm@$NaREF_4$ NPs (RE= Y, La, Ce, Pr, Nd, Sm, Eu, Gd, Tb, Dy, Ho, Er, Tm, Yb, Lu). Scale bars: 50 nm.

In terms of the small lattice mismatches (absolute value ranging from 0.17% to 3.52%, smaller than 5%) of Gd_2O_2S and $NaREF_4$, Gd_2O_2S:20%Yb,1%Tm@$NaREF_4$

(RE = Y, La, Ce, Pr, Nd, Sm, Eu, Gd, Tb, Dy, Ho, Er, Tm, Yb, and Lu) own the theoretical possibility of formations. Importantly, we have demonstrated the formation of Gd_2O_2S:20%Yb,1%Tm@$NaYF_4$ heterogeneous core/shell structure. Then, on the base of large-scale synthesized Gd_2O_2S:20%Yb,1%Tm core NPs as seeds, we synthesized other 14 types of Gd_2O_2S:20%Yb,1%Tm@$NaREF_4$ core/shell NPs by the coprecipitation method. All as-prepared core/shell NPs were able to be well dispersed in cyclohexane without aggregation. As their TEM images displayed in Figure 3.10, all Gd_2O_2S:20%Yb,1%Tm@$NaREF_4$ core/shell NPs are spherical with different sizes and good dispersity. By counting at least 50 NPs from the TEM images, the mean sizes of Gd_2O_2S:20%Yb,1%Tm@$NaREF_4$ core/shell NPs were determined and collected in Table 3.3. The sizes of these core/shell NPs range from about 11 to 27 nm.

Table 3.3 Composition and mean sizes of RE_2O_2S@$NaYF_4$ NPs.

RE_2O_2S@$NaREF_4$	Size (nm)
Gd_2O_2S:20%Yb,1%Tm@$NaYF_4$	13.7 ± 0.8
Gd_2O_2S:20%Yb,1%Tm@$NaLaF_4$	14.1 ± 1.0
Gd_2O_2S:20%Yb,1%Tm@$NaCeF_4$	14.6 ± 1.4
Gd_2O_2S:20%Yb,1%Tm@$NaPrF_4$	12.0 ± 1.3
Gd_2O_2S:20%Yb,1%Tm@$NaNdF_4$	13.8 ± 1.7
Gd_2O_2S:20%Yb,1%Tm@$NaSmF_4$	14.6 ± 0.8
Gd_2O_2S:20%Yb,1%Tm@$NaEuF_4$	15.9 ± 1.3
Gd_2O_2S:20%Yb,1%Tm@$NaGdF_4$	13.5 ± 1.3
Gd_2O_2S:20%Yb,1%Tm@$NaTbF_4$	11.3 ± 1.4
Gd_2O_2S:20%Yb,1%Tm@$NaDyF_4$	18.5 ± 1.1
Gd_2O_2S:20%Yb,1%Tm@$NaHoF_4$	16.7 ± 1.0
Gd_2O_2S:20%Yb,1%Tm@$NaErF_4$	26.6 ± 1.1
Gd_2O_2S:20%Yb,1%Tm@$NaTmF_4$	24.1 ± 1.2
Gd_2O_2S:20%Yb,1%Tm@$NaYbF_4$	17.0 ± 0.9
Gd_2O_2S:20%Yb,1%Tm@$NaLuF_4$	15.1 ± 1.0

As we are able to synthesize 15 types of ultrasmall RE_2O_2S NPs as discussed in chapter II, ideally, we can ideally synthesize 225 types of RE_2O_2S@$NaYF_4$ NPs based on those RE_2O_2S cores, while ignoring the lattice mismatch of RE_2O_2S and $NaREF_4$. The findings provide a fundamental investigation for RE_2O_2S@$NaREF_4$ core/shell NPs.

3.2 Growth kinetics investigation

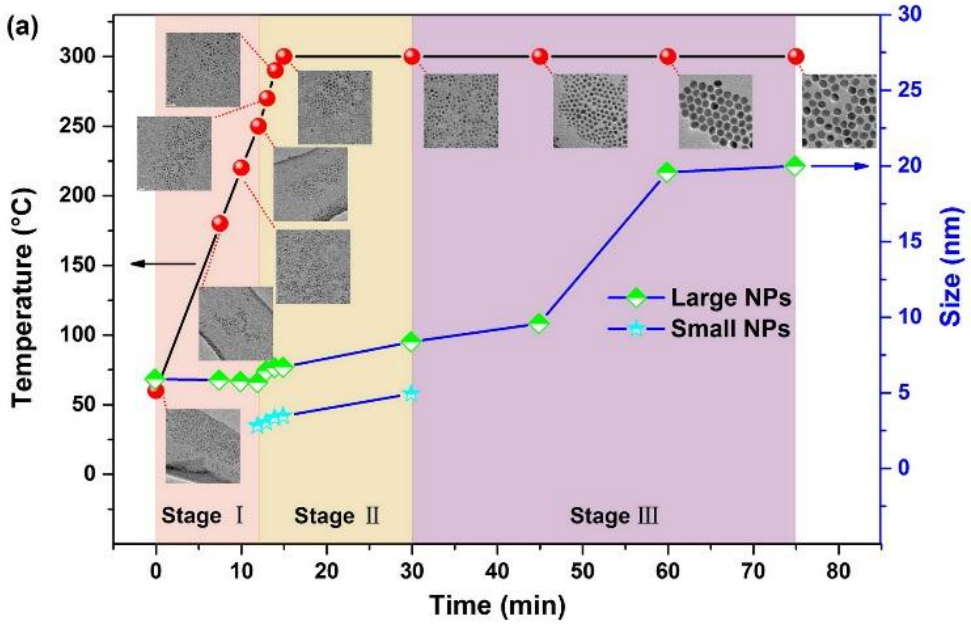

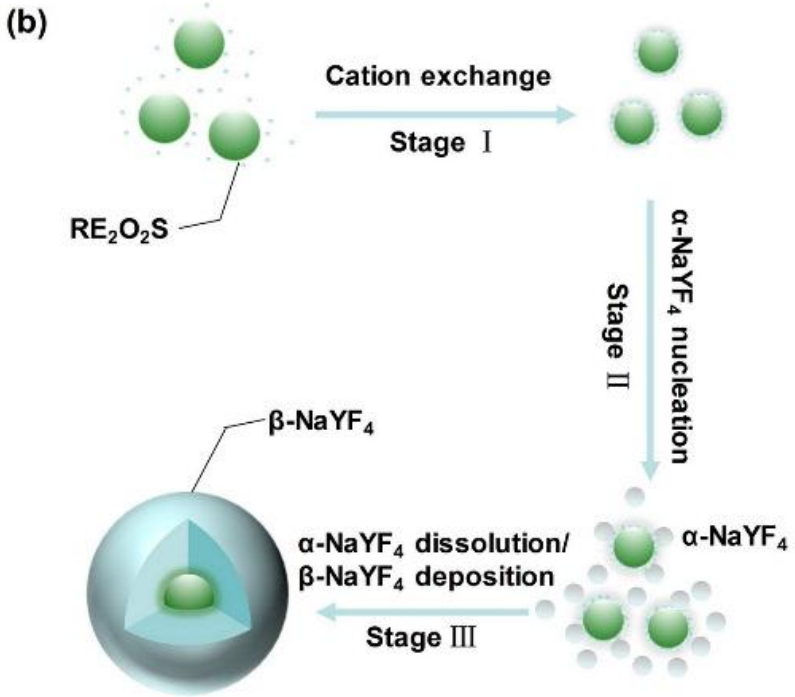

Figure 3.11 (a) TEM images showing status of NPs at different stages, and sizes evolution during the synthesis. (b) Proposed growth mechanism for RE_2O_2S@$NaYF_4$ core/shell heterostructure.

To gain insights into the growth kinetic process of Gd_2O_2S:20%Yb,1%Tm@$NaYF_4$ core/shell heterostructure, we performed size and phase evolution investigation based on TEM, XRD, and SAXS characterizations. During the core/shell synthesis, the core NPs were first added as seeds into the solution which contains yttrium precursors and organic solvents, then NaOH/NH_4F methanol solution was added. The samples were collected from the reaction solution after different heating times.

The TEM images in Figures 3.11a and 3.12 show the size and morphology evolution during the reaction process. The sizes were statistically determined by counting at least 50 particles. From 60 °C to 220 °C (Stage I), we observed one population of well crystallized and uniform NPs with size slightly decreasing with temperature increasing. These NPs were supposedly core NPs, maybe some poorly crystallized and small sized α-$NaYF_4$ had been removed during washing process since it is claimed that α-$NaYF_4$ can be obtained below 220 °C.[287] Apart from the core NPs, as temperature raised, a second population of smaller NPs with size of 2.8 nm were first observed at 250 °C. These small NPs slowly grew with temperature rising and manifestly disappeared before the point 300 °C, 30 min (end of Stage II). Meanwhile, the size of large NPs increased a little as well. We assume that the small NPs may be α-$NaYF_4$ as reported previously[288-290], and the large NPs may be the core NPs with size enlargement by surface attachments of ultrasmall α-$NaYF_4$. Then, the large NPs continued to grow and small NPs disappeared as the reaction progressed (Stage III).

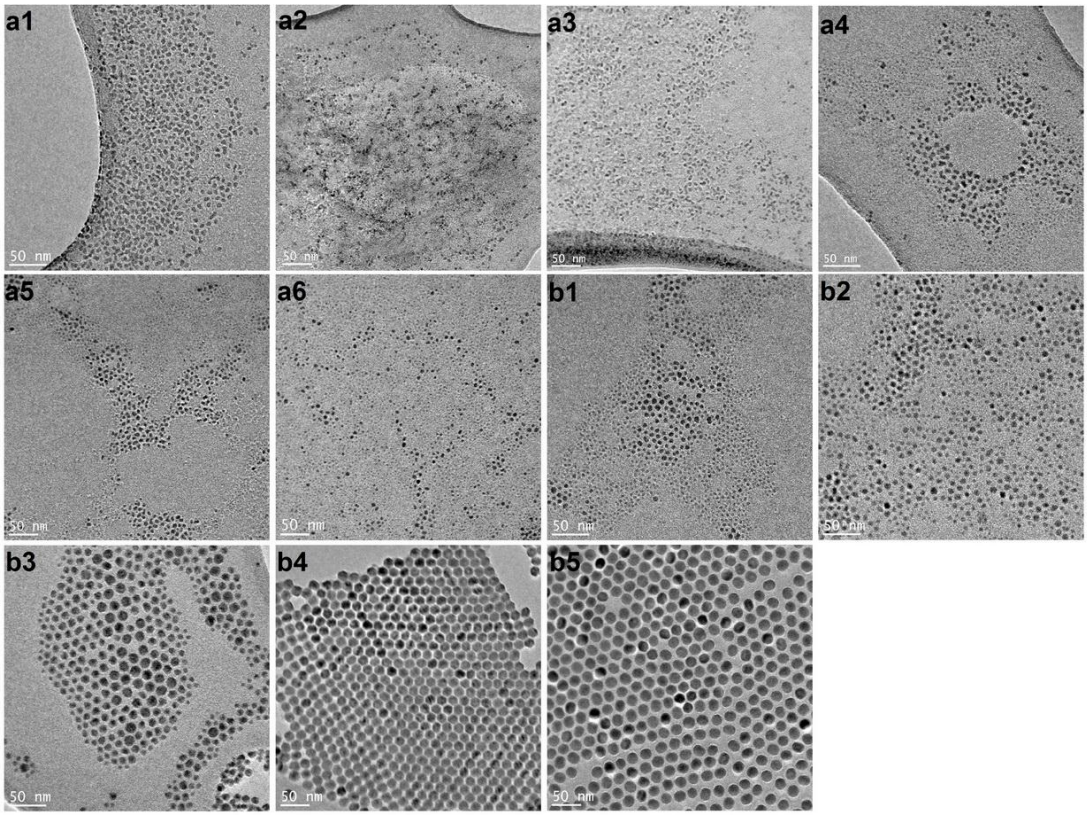

Figure 3.12 TEM images of NPs obtained at different reaction stages. Images from (a1) to (a6) correspond to reaction temperatures 60 °C, 180 °C, 220 °C, 250 °C, 270 °C, 290 °C, respectively; from b1 to b5 correspond to reaction times 0 min, 15 min, 30 min, 45 min, 60 min at 300 °C, respectively.

XRD measurements further confirm the phases evolution of the NPs. As seen in Figure 3.13, only Gd_2O_2S phase was observed before 220 °C but the peaks become a little broader with temperature increases. It is possibly because rare earth-cation exchange process between core and precursor solution leads to smaller size by forming a very thin amorphous layer on the surface. This phenomenon is often observed in the synthesis of heterogeneous nanostructures.[291] Subsequently, intense XRD signals of α-$NaYF_4$ phase appeared at 250 °C and overshadow the intensity of Gd_2O_2S, indicating plenty of α-$NaYF_4$ produced by burst nucleation. With the disappearance of α-$NaYF_4$, the peaks of β-$NaYF_4$ phase became dominant (Figure 3.13b). The XRD results are consistent with the size and morphology analysis of TEM images. To conclude, we proposed a tentative growth mechanism for the Gd_2O_2S:20%Yb,1%Tm@$NaYF_4$

core/shell heterostructure, as shown in Figure 3.11b. Firstly, cation exchange at the solid-liquid interface is able to contribute to lower the interfacial energy of the system, which may form an amorphous layer. Then, α-$NaYF_4$ nucleation happens with temperature increases (Stage II). In this stage, ultrasmall α-$NaYF_4$ could be attached on the core particles by electrostatic attraction effect[292], or even forming a thin α-$NaYF_4$ layer as some NPs were observed to be more round than before. As the α-$NaYF_4$ is the kinetic product, it dissolves quickly at the elevated temperature and nucleates into thermodynamic β-$NaYF_4$ phase which then deposits on the larger RE_2O_2S (Stage III). Note that this dissolution/deposition process is very rapid. Driven by Ostwald ripening, the larger nanoparticles grow bigger and bigger.

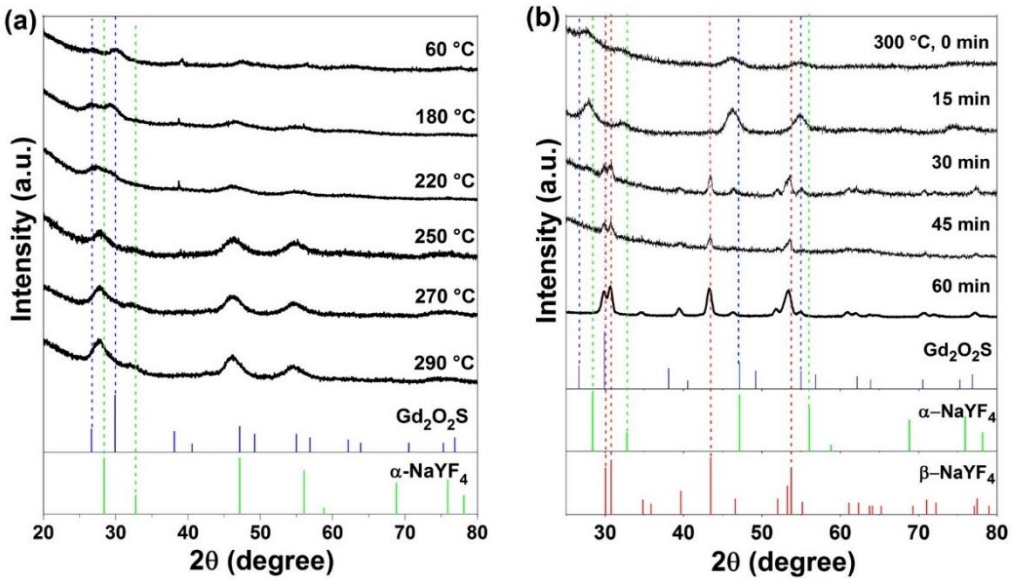

Figure 3.13 XRD patterns of NPs obtained at different reaction stages: (a) reaction temperature rising from 60 °C to 290 °C; (b) reaction time counting from 0 min to 60 min at 300 °C.

Additionally, SAXS measurements were carried out to investigate global dimensions of the NPs in different reaction phases. As shown in Figure 3.14a, the superimposition of the SAXS curves shows an evolution of the increased signal during the temperature rise phase (60 °C *vs.* 300°C, 0 min), suggesting the formation of high concentration of α-$NaYF_4$ NPs. Then, the decrease of the intensity from 0 to 30 min at 300°C is due to

gradually lowered concentration of α-$NaYF_4$. Apparently, β-$NaYF_4$ occurs and grows by observation of forming new shapes and higher peaks of SAXS curves from 45 to 60 min at 300°C. By extracting the data from the SAXS curves, the gyration radius (Rg) and the Porod volume of particle are determined to follow the particle growth (Figure 3.14b). It can be seen that the size increases a little during the temperature rise phase, which is consistent with observation by TEM. The variations of Rg and volume of particle during the synthesis are in a good agreement with observations by TEM, as well.

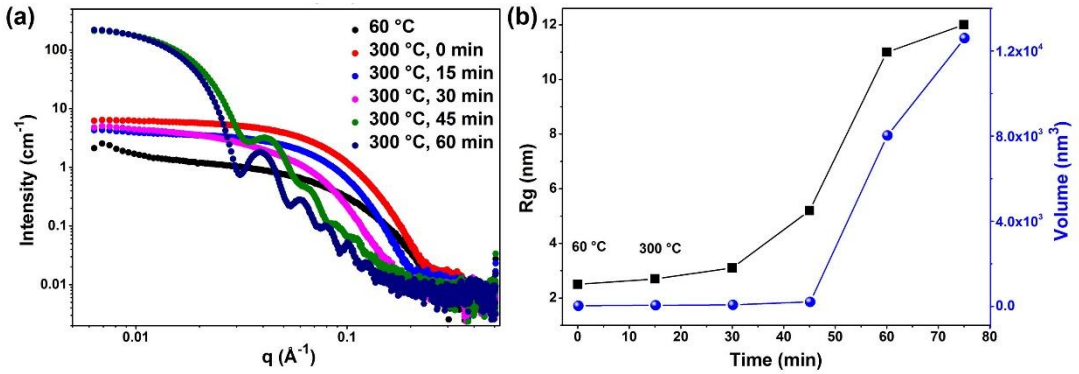

Figure 3.14 (a) SAXS curves for NPs at 60 °C and 300 °C with soaking times from 0 to 60 min. (b) Rg and Porod volume extracted from the SAXS data of (a). The data were plotted as a function of I(q) *vs.* q, where I(q) is expressed in cm^{-1} and q the scattering vector ($q = 4\pi\sin\theta/\lambda$) in $Å^{-1}$.

Immediately, we fitted the curve (T = 300°C, 0 min) with a simple model of flat cylinder. Then we obtained particle with a diameter of 4.3 nm and a length of 3.5 nm, as shown in Figure 3.15 (the blue particle). During the temperature stabilization phase, we observed a drastic change of the formation factor where the initial particle described above became a bigger 3D object with a shape close to an ellipsoid. With remarkable modulations, it indicated a good monodispersity of the particle in solution. By applying a model of ellipsoid object, we extracted the global dimensions from the curve (T = 300°C, 60 min) and obtained an ellipsoid of an equatorial diameter of 31 nm and a polar diameter of 25.8 nm (red particle in Figure 3.15).

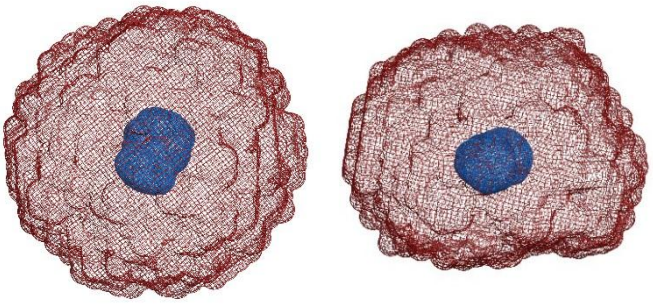

Figure 3.15 3D objects obtained from the modulations of SAXS curves of T = 300°C, 0 min and T = 300°C, 60 min.

3.3 Upconversion properties of lanthanide-doped Gd_2O_2S@$NaYF_4$

Because of severe surface quenching, ultrasmall lanthanide (Ln) -doped Gd_2O_2S upconversion NPs (UCNPs) must have very low photoluminescence efficiency. Generally, coating with an inert shell, for instance, Gd_2O_2S or $NaYF_4$ could improve the optical properties. In this section, upconversion photoluminescence (UCL) intensity, lifetimes, and quantum yield (QY) of Ln-doped Gd_2O_2S core and Gd_2O_2S@$NaYF_4$ (or Gd_2O_2S@Gd_2O_2S) core/shell UCNPs will be measured and discussed.

We first characterized the UCL spectra of both Gd_2O_2S:20%Yb,1%Tm core and as-prepared ~14 nm irregular Gd_2O_2S:20%Yb,1%Tm@Gd_2O_2S core/shell UCNPs (Figure 3.16a). However, only 1.2-fold enhancement was obtained for Gd_2O_2S:20%Yb,1%Tm@Gd_2O_2S core/shell UCNPs under 980 nm excitation (Figure 3.16b).

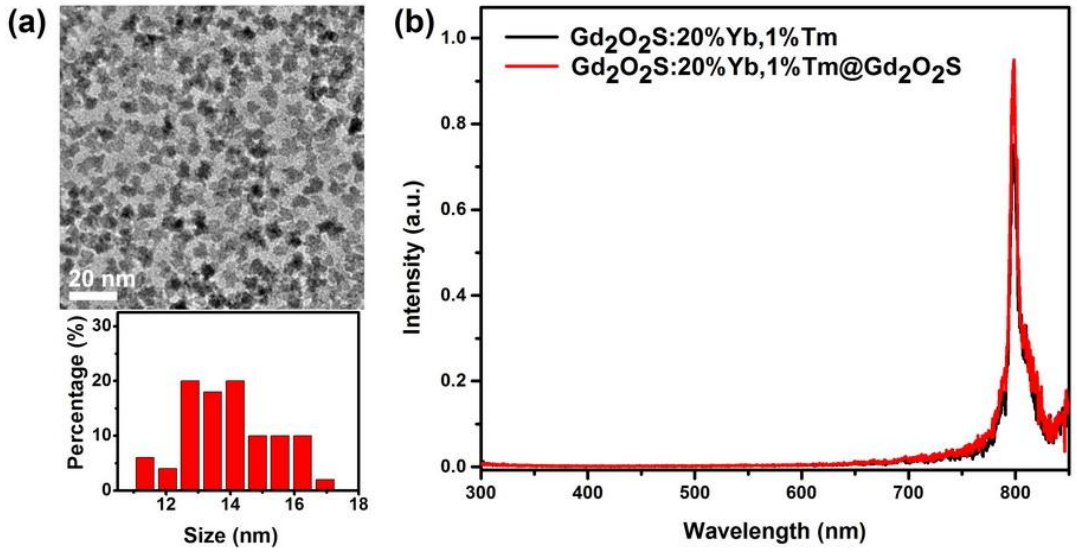

Figure 3.16 (a) TEM image and size distribution histogram of Gd_2O_2S:20%Yb,1%Tm@Gd_2O_2S core/shell UCNPs. (b) UCL spectra of Gd_2O_2S:20%Yb,1%Tm core and Gd_2O_2S:20%Yb,1%Tm@Gd_2O_2S core/shell UCNPs.

On the contrary, the inert $NaYF_4$ shell is able to protect lanthanide ions (Ln^{3+}) doped Gd_2O_2S cores from surface quenching, thus significantly boosting the UCL properties. As shown in Figure 3.17, under irradiation by CW 980 nm laser, both Gd_2O_2S:20%Yb,1%Tm core and Gd_2O_2S:20%Yb,1%Tm@$NaYF_4$ core/shell UCNPs exhibit three identical emission bands at 469 nm, 640 nm, and 803 nm which are ascribed to $^1G_4 \rightarrow {}^3H_6$, $^1G_4 \rightarrow {}^3F_4$, and $^3H_4 \rightarrow {}^3H_6$ transitions of Tm^{3+}, respectively. Spectacularly, we observed 836-fold enhancement in overall emission for Tm-doped UCNPs after coating $NaYF_4$, which shows the effective protection from surface quenching. It is obviously proving the greater advantage of heterogeneous coating of the $NaYF_4$ shell for RE_2O_2S compared to Gd_2O_2S:20%Yb,1%Tm@Gd_2O_2S homogeneous core/shell UCNPs which displays imperfect protections by partial coating, irregular shapes, and wide size distribution.

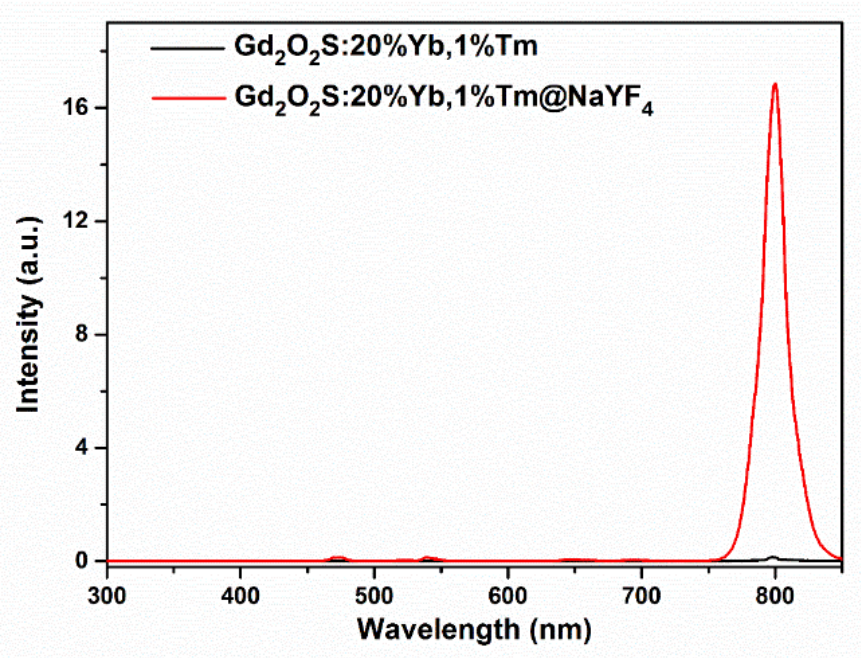

Figure 3.17 UCL spectra of Gd_2O_2S:20%Yb,1%Tm core and Gd_2O_2S:20%Yb,1%Tm@$NaYF_4$ core/shell UCNPs under 980 nm laser excitation.

Meanwhile, we synthesized Gd_2O_2S:20%Yb,2%Er core and Gd_2O_2S:20%Yb,2%Er@$NaYF_4$ core/shell UCNPs. Upon 980 nm laser excitation, typical emission bands at 520 nm ($^2H_{11/2} \rightarrow {}^4I_{15/2}$), 540 nm ($^4S_{3/2} \rightarrow {}^4I_{15/2}$), and 652nm ($^4F_{9/2} \rightarrow {}^4I_{15/2}$) are observed in Figure 3.18. 4922-fold enhancement of UCL intensity was obtained for Gd_2O_2S:20%Yb,2%Er@$NaYF_4$ core/shell UCNPs compared to that of Gd_2O_2S:20%Yb,2%Er core UCNPs.

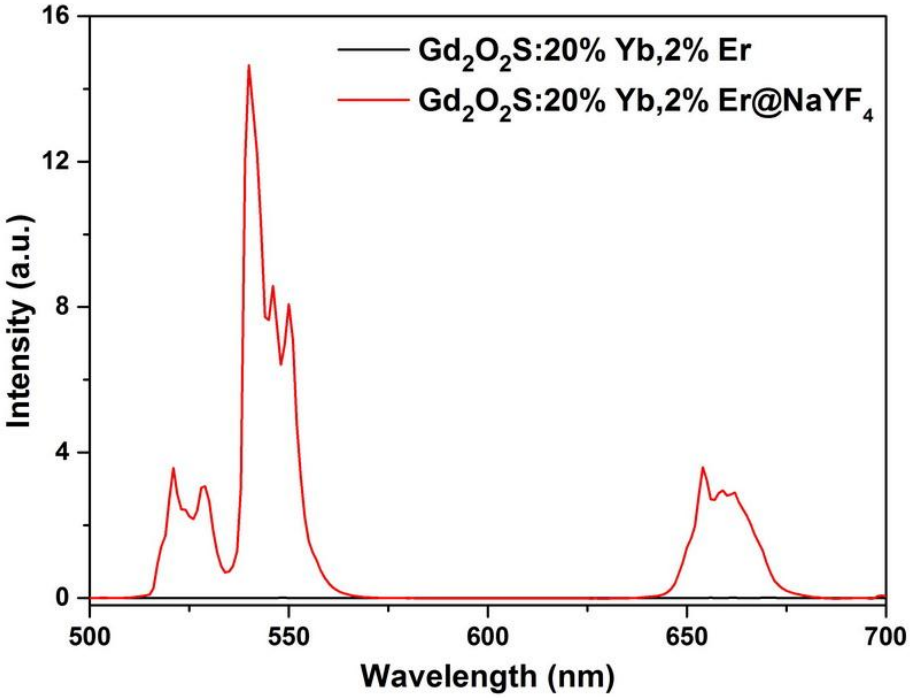

Figure 3.18 UCL spectra of Gd_2O_2S:20%Yb,2%Er core and Gd_2O_2S:20%Yb,2%Er@$NaYF_4$ core/shell UCNPs under 980 nm laser excitation. The UCNPs were dispersed in cyclohexane with concentration of 10 mg/mL.

We further recorded decays for those Yb^{3+}/Tm^{3+} and Yb^{3+}/Er^{3+} doped UCNPs. In Figure 3.19, it shows the decays for Gd_2O_2S:20%Yb,1%Tm core (Figure 3.19a) and Gd_2O_2S:20%Yb,1%Tm@$NaYF_4$ core/shell (Figure 3.19b) UCNPs under 980 nm laser excitation. The lifetimes obtained by monoexponential fitting of the 469 nm and 803 nm emission decays were prolonged from 8 μs and 5 μs for the core to 919 μs and 997 μs for the core/shell sample, respectively, that are approximately 100- to 200-fold longer lifetimes. Meanwhile, we recorded the decay curves of 520 nm, 540 nm, and 652 nm of Gd_2O_2S:20%Yb,2%Er@$NaYF_4$ core/shell UCNPs through a longer pulse laser excitation (180 μs), as shown in Figure 3.20. The decay curves were fitted and lifetimes were calculated to be 305 μs, 316 μs, and 351 μs correspond to 520 nm, 540 nm, and 652 nm, respectively. Note that the lifetimes cannot be obtained for the Gd_2O_2S:20%Yb,2%Er core UCNPs by the longer pulse laser excitation due to the very weak luminescence of the core UCNPs.

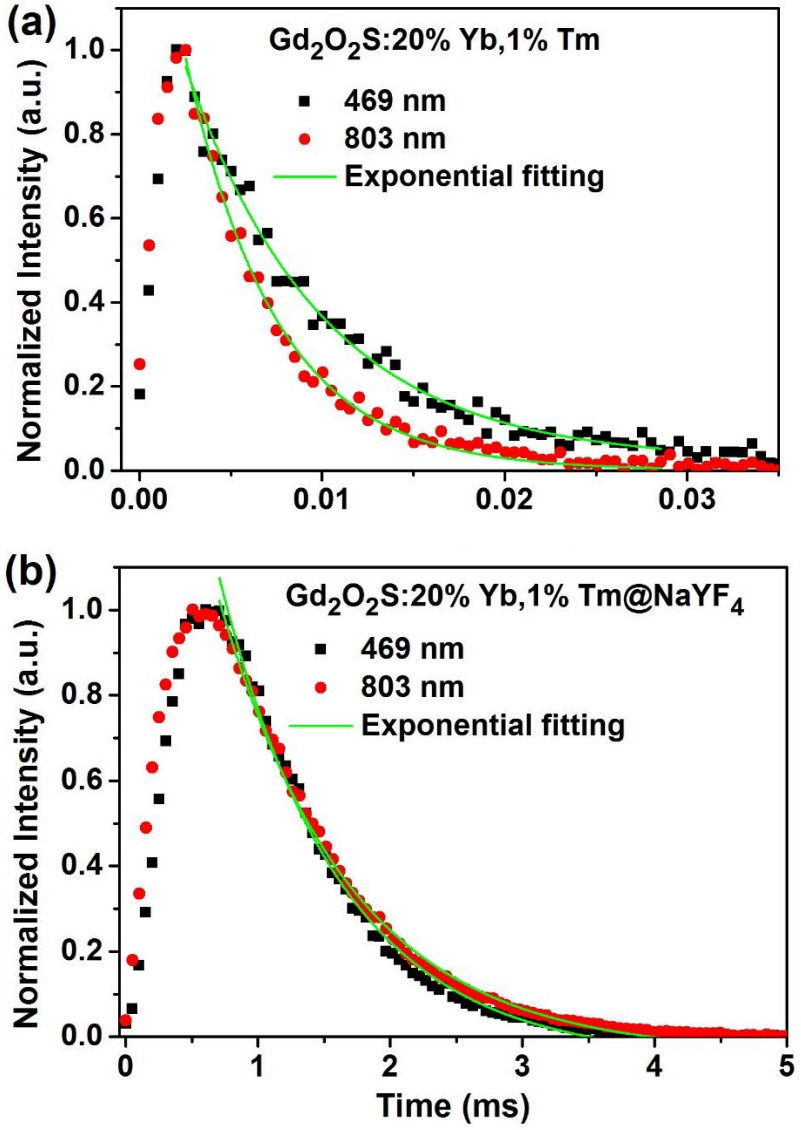

Figure 3.19 Decays of (a) Gd_2O_2S:20%Yb,1%Tm core and (b) Gd_2O_2S:20%Yb,1%Tm@$NaYF_4$ core/shell UCNPs under 980 nm laser excitation.

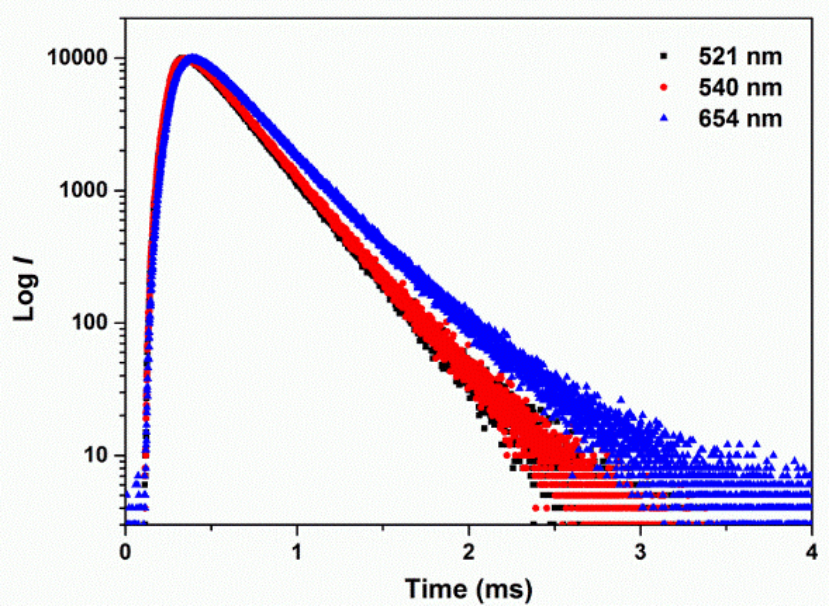

Figure 3.20 Decays of Gd_2O_2S:20%Yb,2%Er@$NaYF_4$ core/shell UCNPs under 980 nm laser excitation.

To quantify the UCL efficiency of the Ln^{3+} doped RE_2O_2S@$NaREF_4$ core/shell NPs, the power-dependent upconversion absolute quantum yields (UCQYs) of three samples with different doping ions and shell substrates were measured, as shown in Figure 3.21. With increasing of power density, the UCQYs increase gradually from the minimum UCQY values of approximately 0.06%, 0.04%, and 0.04% at a power density of 7 W/cm^2 to the maximum values of 0.76%, 0.61%, and 0.68% at the power density of 155 W/cm^2 for Gd_2O_2S:20%Yb,1%Tm@$NaYF_4$, Gd_2O_2S:20%Yb,2%Er@$NaYF_4$, and Gd_2O_2S:20%Yb,2%Er@$NaGdF_4$, respectively. These UCQYs values are moderate but remarkable considering the very small size of the emitting cores of these UCNPs. In the future, preparing large core NPs or screening proper shell matrix can be attempted to improve the UCQYs.

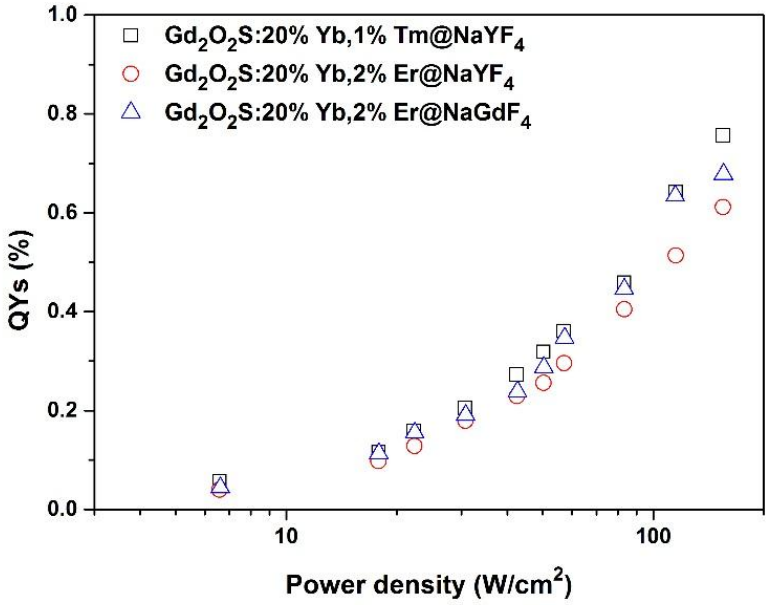

Figure 3.21 Power-dependent UCQYs of Gd_2O_2S:20%Yb,1%Tm@$NaYF_4$, Gd_2O_2S:20%Yb,2%Er@$NaYF_4$, and Gd_2O_2S:20%Yb,2%Er@$NaGdF_4$.

3.4 Optical properties of Gd_2O_2S:20%Yb/x%Er@$NaYF_4$

In this section, we will systematically compare the optical properties of a series of Gd_2O_2S:Yb/Er@$NaYF_4$ samples with different Er doping level with different sizes by investigating their UCL intensity, absorption, size, shell thickness, and chemical composition.

We first synthesized Yb/Er doped Gd_2O_2S core UCNPs with Er doping concentrations of 1%, 2%, 5%, 10%, and 15%. As we can see the from TEM images, the size and shapes changed with variable concentration. The sizes of the core UCNPs were determined in the Table 3.4, in a range of approximately 7~10 nm. Then, the Gd_2O_2S:20%Yb/x%Er@$NaYF_4$ core/shell UCNPs were synthesized through the co-precipitation approach in the same conditions. As shown in Figure 3.23, we obtained the core/shell UCNPs with large size and different morphologies. Apparently, the different sizes and shapes of core UCNPs lead to the difference of sizes and morphologies of core/shell UCNPs. Likewise, the sizes were determined and assembled in the Table 3.4 where you can find the sizes range from ~15 nm to ~22 nm. We further

calculated the shell thickness of core/shell UCNPs according to the sizes of core and core/shell UCNPs. Comparing the sizes in the Table 3.4 and Figure 3.24, it is observed that the sample of 1% Er has the smallest core (7.5 nm) but thickest shell (7.2 nm) and the sample of 2% Er has the thinnest shell. The variation of the sizes and morphologies make it difficult for comparison of optical properties of the samples.

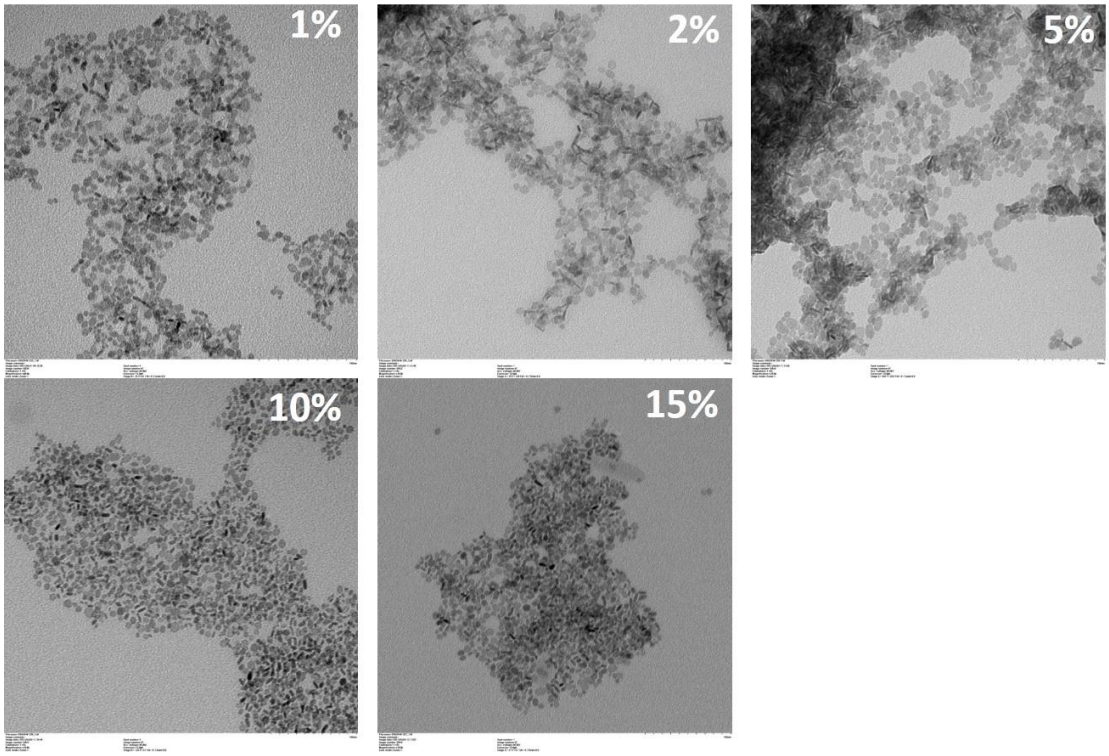

Figure 3.22 TEM images of Gd_2O_2S:20%Yb,x%Er (x = 1, 2, 5, 10, and 15) core UCNPs.

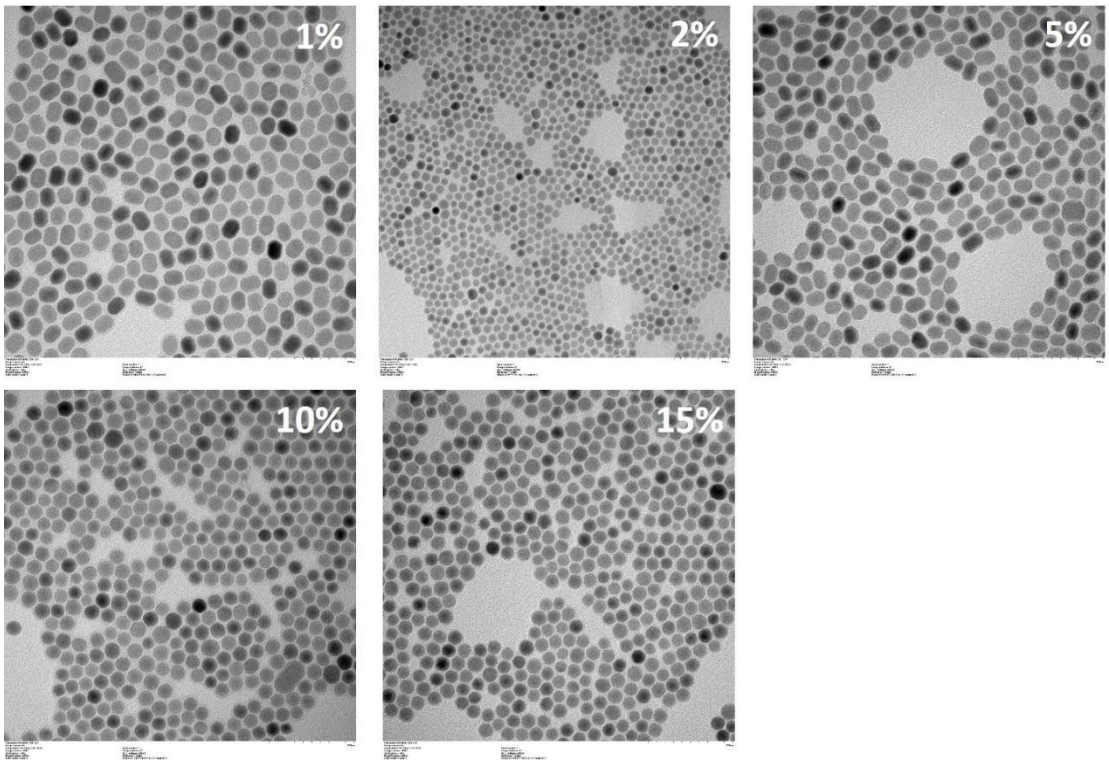

Figure 3.23 TEM images of Gd_2O_2S:20%Yb,x%Er@$NaYF_4$ (x = 1, 2, 5, 10, and 15) core/shell UCNPs.

Table 3.4 Summary of sizes of core, core/shell, and shell thickness of samples at different Er concentrations.

Er doping level	**1%**	**2%**	**5%**	**10%**	**15%**
Core (nm)	7.5	9.1	10.4	8.9	8.3
Core/shell (nm)	21.9	14.6	21.6	17.5	16.4
Shell thickness (nm)	7.2	2.8	5.6	4.3	4.1

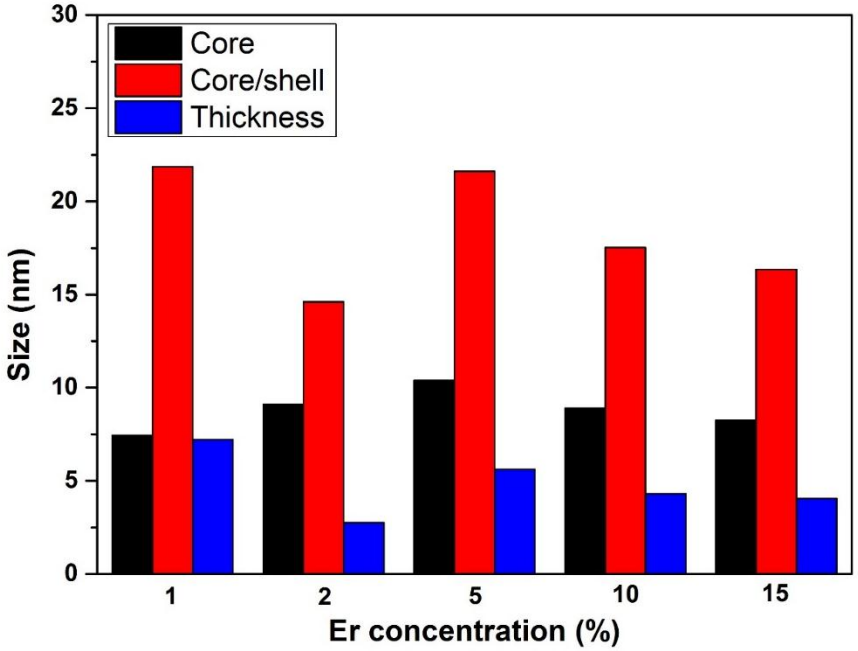

Figure 3.24 Sizes comparison of core, core/shell, and shell thickness of samples at different Er concentrations.

To know the precise concentration of all the rare earth elements, we further carried out ICP-OES measurements for the core/shell samples. As it can be seen in Table 3.5, we first calculated the composition based on the rare earth elements of Gd_2O_2S:20%Yb,x%Er core UCNPs. Generally, the Er concentrations are little smaller than the theoretical values; for Yb concentration, all the samples have about 11% mol which is quite stable although it is smaller than the theoretical value of 20%. The low substitution of Yb for Gd is possible due to moisture absorption of Yb related raw material. Then, we analysed the composition including all are earth elements based on the core/shell UCNPs, as displayed in Table 3.6. It is found that the concentration of Y varies from 67.54% to 71.71% with the maximum difference of 4.17%. These ICP-OES results confirm the composition of core/shell UCNPs.

Table 3.5 ICP-OES for Gd_2O_2S:Yb,Er@$NaYF_4$ with different Er concentrations. The values calculated based on only rare earth elements of core (Er, Yb, and Gd) in the core/shell nanoparticle.

Theoretical concentration of Er (mol)	**1%**	**2%**	**5%**	**10%**	**15%**
ICP-Er (mol)	0.90%	1.58%	3.92%	7.73%	12.31%
ICP-Yb (mol)	11.17%	11.13%	11.61%	11.06%	11.77%
ICP-Gd (mol)	87.93%	87.29%	84.48%	81.21%	75.92%

Table 3.6 ICP-OES for Gd_2O_2S:Yb,Er@$NaYF_4$ with different Er concentrations. The values calculated based on the all rare earth elements (Er, Yb, Gd, and Y) in the core/shell nanoparticle.

Theoretical concentration of Er (mol)	**1%**	**2%**	**5%**	**10%**	**15%**
ICP-Er (mol)	0.29%	0.51%	1.20%	2.19%	3.80%
ICP-Yb (mol)	3.63%	3.60%	3.55%	3.13%	3.64%
ICP-Gd (mol)	28.54%	28.23%	25.84%	22.97%	23.45%
ICP-Y (mol)	67.54%	67.66%	69.41%	71.71%	69.12%

Following, we recorded UCL spectra for those Gd_2O_2S:20%Yb,x%Er@$NaYF_4$ (x = 1, 2, 5, 10, and 15) core/shell UCNPs. The UCNPs were dispersed in cyclohexane with concentration of 10 mg/mL. Upon 2 W, 980 nm laser irradiation, the UCNPs displayed mostly green emission. The identical emission bands at 520 nm, 540 nm, and 652 nm can be found in Figure 3.25. As concentration increases, the UCL intensity increases from 1% to 2% due to reduced distance of Yb^{3+} and Er^{3+}, then decreases from 2% to 15% because of concentration quenching effect.

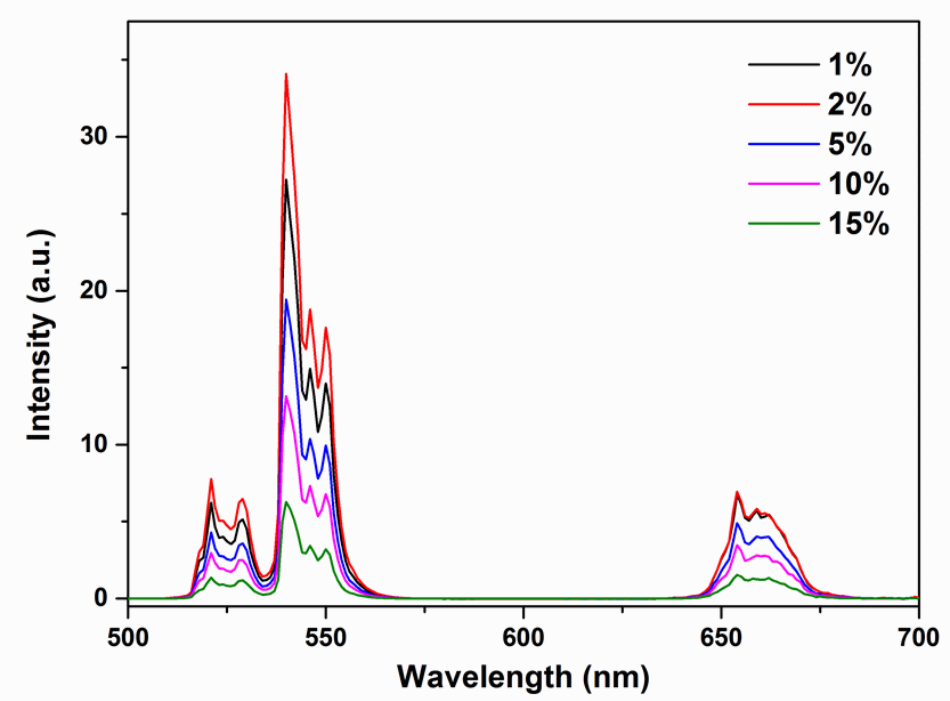

Figure 3.25 UCL intensity of Gd_2O_2S:20%Yb,x%Er@$NaYF_4$ (x = 1, 2, 5, 10, and 15) core/shell UCNPs under 980 nm laser excitation.

The UCL decay times of 540 nm emission band of all samples were also recorded by 980 nm pulse laser irradiation with pulse width of 180 μs. As shown in Figure 3.26, the decay times were determined to be 509 μs, 316 μs, 238 μs, 197 μs, and 105 μs, and the rise times were determined to be 162 μs, 107 μs, 104 μs, 89 μs, and 67 μs, for the 1%, 2%, 5%, 10%, and 15% Er core/shell samples. As we can see, both decay time and rise time decreases with increasing of Er concentration.

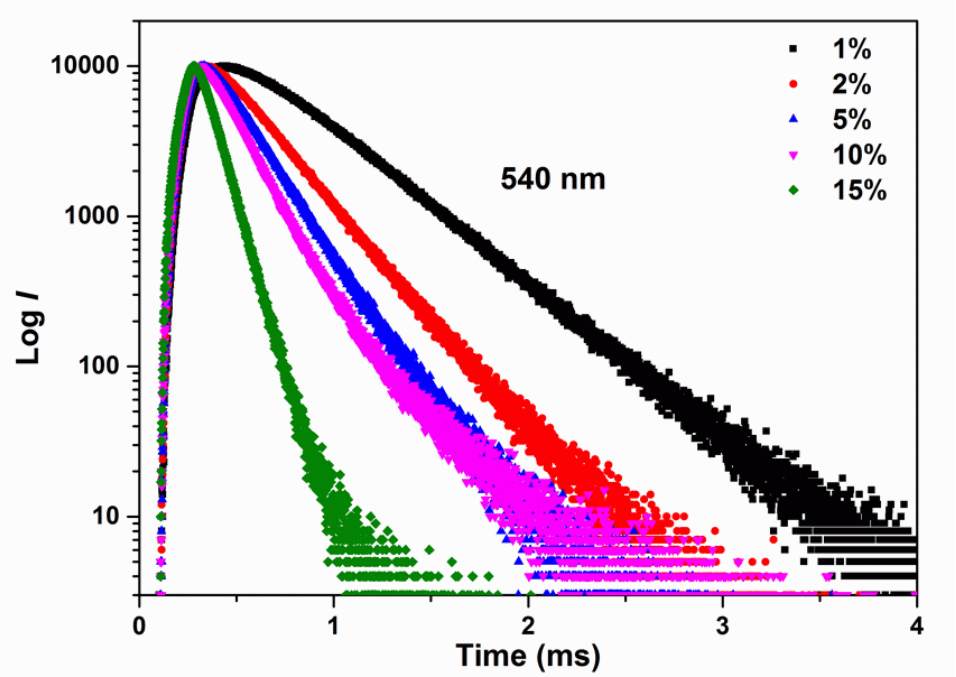

Figure 3.26 UCL decay times of 540 nm of Gd_2O_2S:20%Yb,x%Er@$NaYF_4$ (x = 1, 2, 5, 10, and 15) core/shell UCNPs under 980 nm pulse laser excitation.

To comprehensively evaluate the optical properties, we measured the absorbance of the UCNPs, as shown in Figure 3.27. The broad absorption peak centred at 960 nm is from the transition of $^2F_{7/2} \rightarrow {}^2F_{5/2}$ of Yb^{3+}. It is observed that the maximum absorbance is 0.011 for the 5% Er sample and the minimum absorbance is 0.004 for the 15% Er sample at 976 nm. It is clear that there is small difference of absorbance for the samples. Note: the negative absorbance could be due to the different purities of the cyclohexane we used for reference and sample.

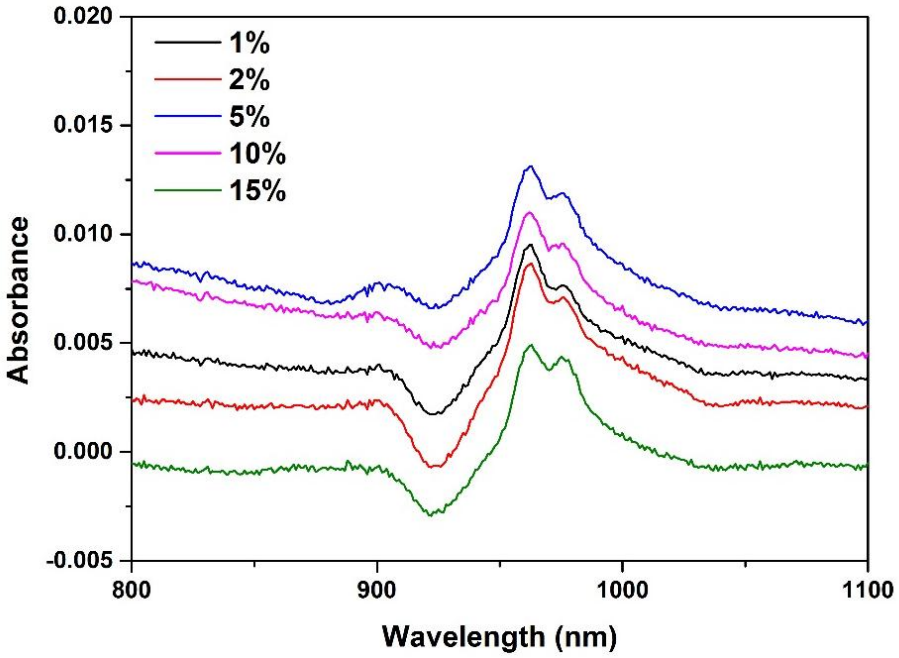

Figure 3.27 Absorbance of Gd_2O_2S:20%Yb,x%Er@$NaYF_4$ (x = 1, 2, 5, 10, and 15) core/shell UCNPs in the wavelength range of 800~1100 nm.

For the purpose of quantifying the UCL efficiency of Gd_2O_2S:20%Yb,x%Er@$NaYF_4$ (x = 1, 2, 5, 10, and 15) core/shell UCNPs, the UCQYs were recorded on the home-made quantum yield measurement system at BAM. In Figure 3.28, it is observed that the UCQYs values of all 5 samples gradually increase with increasing of power density of 980 nm continuous wavelength. The values are in the range from 0.01% to 0.61%. Typically, the UCQYs of 15% Er sample are the lowest at the same power density; the 1% Er sample has the highest UCQYs values when the power density is below 57 W/cm^2, whereas, in the range of 83~155 W/cm^2, it has lower UCQYs values than the 2% Er sample at the same power density. This could be because more Er^{3+} ions of 2%Er sample were excited through GSA/ESA processes at high power densities. It should be noted that we haven't reached saturation yet, and therefore the QY could be even higher at higher incident powers.

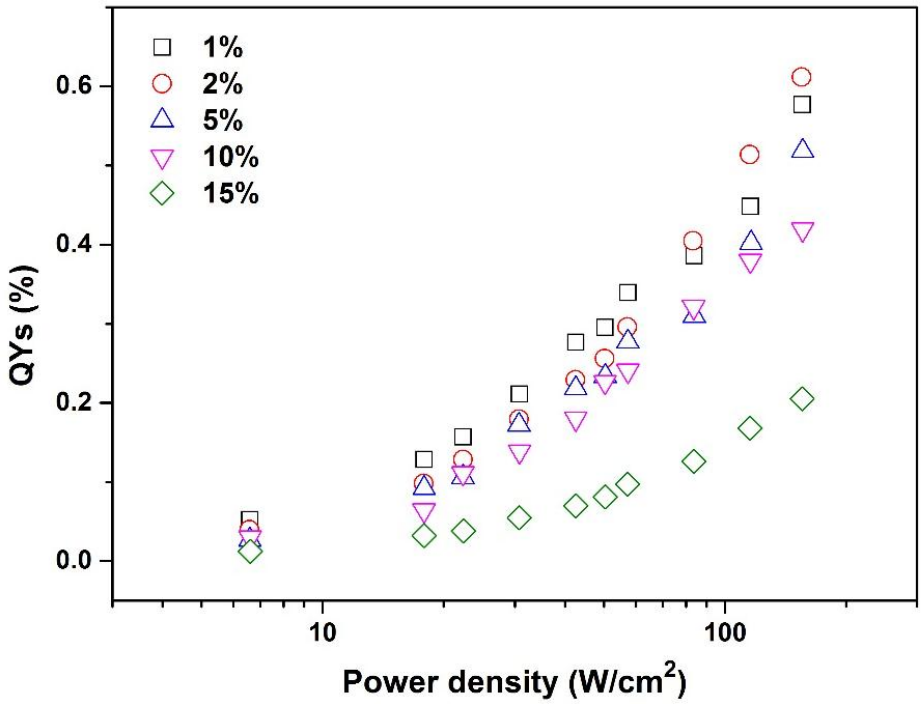

Figure 3.28 UCQYs study of Gd_2O_2S:20%Yb,x%Er@$NaYF_4$ (x = 1, 2, 5, 10, and 15) core/shell UCNPs.

3.5 Surface modification

In this section, we further functionalized Gd_2O_2S:20%Yb,2%Er@$NaYF_4$ UCNPs for future use. To prepare hydrophilic NPs, we first removed the surface oleic acid molecules through ligand exchange with $NOBF_4$ molecules. Then the OA-free NPs were coated with PVP and alendronate. Figure 3.29 shows the TEM images and DLS results of the NPs before and after coating with the molecules. It is obvious that the OA-free NPs can be well dispersed in DMF after ligand exchange process and without any aggregations observed. The DLS shows the size of 57.7 ± 14.9 nm for OA-free NPs, which is bigger that the size of OA-coated NPs (~15 nm) due to the absorbed surface molecules of OA-free NPs. Then two kinds of compounds PVP and alendronate were coated on the OA-free NPs. TEM images show that both PVP and alendronate -coated NPs display aggregations and especially larger aggregations are observed for alendronate-coated NPs. DLS results exhibits mean size of 73.6 ± 14.8 nm and 103.9 ± 40.1 nm for PVP and alendronate -coated NPs, respectively. As we can see, on the one

hand, both of those two samples display larger hydrodynamic sizes than the size of OA-free NPs, confirming the successful molecule coating process; on the other hand, the big deviation values implies that there are some aggregations after further functionalization. Further work will be required to achieve individualized nanoparticle suspension by tuning the concentration of ligand during the resuspension and the simultaneous sonication time.

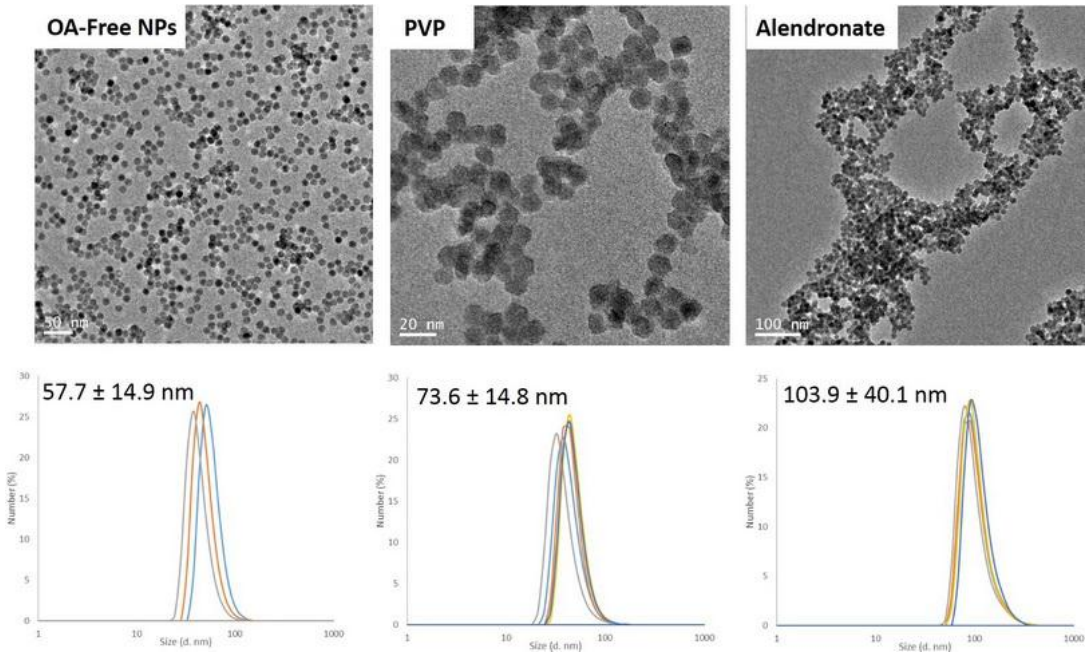

Figure 3.29 TEM images and DLS results of OA-free, PVP-coated, and alendronate-coated Gd_2O_2S:20%Yb,2%Er@$NaYF_4$ UCNPs.

4 Conclusions

In summary, we successfully construct a new class of heterogeneous RE_2O_2S@$NaREF_4$ core/shell nanoparticle. We fist synthesize a large batch of Gd_2O_2S:20%Yb,1%Tm core NPs. Then, ~4 nm $NaYF_4$ shell is deposited on the ~6 nm Gd_2O_2S:20%Yb,1%Tm core nanoparticle. By HRTEM, HAADF, EELS, and element mapping analyses, we confirm the core/shell structure of Gd_2O_2S:20%Yb,1%Tm@$NaYF_4$. Importantly, other 14 kinds of Gd_2O_2S:20%Yb,1%Tm@$NaREF_4$ (RE = La, Ce, Pr, Nd, Sm, Eu, Gd, Tb, Dy, Ho, Er, Tm, Yb, and Lu) with size ranging from 11 nm to 27 nm are prepared by the same synthesis approach.

Then, we further investigate the growth kinetics of Gd_2O_2S:20%Yb,1%Tm@$NaYF_4$ core/shell NPs. By monitoring the size and phase evolution during the whole synthesis, we propose the growth mechanism which include 3 stages: in the first stage, cation exchange process leads to the migration of rare earth elements between the solid core NPs and liquid solution, forming an amorphous layer on the core NPs; in the second stage, with rising temperature, α-$NaYF_4$ phase appears at 250 °C; finally, the α-$NaYF_4$ phase quickly disappears and β-$NaYF_4$ phase occurs, consequently, β-$NaYF_4$ deposits on the core NPs due to small lattice mismatch. Besides, the SAXS results verify the size evolution during the synthesis.

In the section 3.3, we systematically evaluate the optical properties for the lanthanide doped core and core/shell UCNPs. We obtain 836 and 4922 -fold enhancement for Gd_2O_2S:20%Yb,1%Tm@$NaYF_4$ and Gd_2O_2S:20%Yb,2%Er@$NaYF_4$, respectively, compared to their corresponding cores. It is recorded that the lifetimes of 469 nm and 803 nm are increased from 8 μs and 5 μs of Gd_2O_2S:20%Yb,1%Tm core to 919 μs and 997 μs of Gd_2O_2S:20%Yb,1%Tm@$NaYF_4$ core/shell, respectively. The lifetimes of 520 nm, 540 nm, and 652 nm of Gd_2O_2S:20%Yb,2%Er@$NaYF_4$ are determined to be 305 μs, 316 μs, and 351 μs, respectively. All the lifetime values of Yb/Tm and Yb/Er doped Gd_2O_2S@$NaYF_4$ core/shell UCNPs are comparable with other corresponding systems with similar sizes but shorter than microcrystals and bulk materials (lifetimes varying from 1 ms to over 10 ms). Finally, the power dependent UCQYs are measured for Gd_2O_2S:20%Yb,1%Tm@$NaYF_4$, Gd_2O_2S:20%Yb,2%Er@$NaYF_4$, and Gd_2O_2S:20%Yb,2%Er@$NaGdF_4$. The maximum UCQYs value is ~0.76% for Gd_2O_2S:20%Yb,1%Tm@$NaYF_4$ at power density of 155 W/cm^2.

In the section 3.4, we systematically investigate the UCL properties of Gd_2O_2S:20%Yb,x%Er@$NaYF_4$ (x = 1, 2, 5, 10, and 15) UCNPs. By analysing TEM images of Gd_2O_2S:20%Yb,x%Er core and Gd_2O_2S:20%Yb,x%Er@$NaYF_4$ core/shell UCNPs, we compare the size and the shell thickness of core/shell UCNPs. ICP-OES measurements reveal the composition of the core/shell UCNPs. The UCL spectra show

the 2% Er sample has the most intense luminescence. The lifetimes of the core/shell UCNPs at 540 nm display that the lifetime declines as the Er concentration increases. UCQYs show that the 1% Er sample has the highest UCQYs values when the power density is below 57 W/cm^2, whereas, in the range of 83~155 W/cm^2, it has lower UCQYs values than the 2% Er sample at the same power density.

In section 3.5, a two-step surface modification is applied for Gd_2O_2S:20%Yb,2%Er@$NaYF_4$ core/shell UCNPs. Then, we prepare PVP and alendronate -coated UCNPs. TEM images and DLS results show the good dispersity and size. These results are still preliminary, on the one hand, we will optimize the parameters in the process to obtain monodisperse hydrophilic NPs; on the other hand, we will characterize the optical properties for these hydrophilic NPs. And most importantly, we will use the NPs for future application, such as bioimaging.

Chapter IV: Temperature-dependent upconversion luminescence investigation

1 Introduction

Thermal quenching is well known to be able to lead the dramatical decrease of luminescence intensity due to the enhanced non-radiative processes at higher temperatures.[293-295] However, the abnormal thermal enhancement of upconversion luminescence (UCL) has been found in the upconversion nanoparticles (UCNPs) and the possible mechanisms have been warmly discussed as well in recent years.[296] The early observation of thermal enhancement of UCL was reported back in 2005. It was found that the Er^{3+} emissions in β-$NaYF_4$:Yb^{3+}/Er^{3+} powder increased as temperature increased from 10 to 100 K and kept almost constant when temperature further increased to 200 K.[297] Based on high-resolution excitation spectra, the authors suggested that a preferable population of the slightly higher energy $^2F_{5/2}|1>$ multiplet of Yb^{3+} at high temperatures resulted in a more efficient Yb^{3+}-Er^{3+} energy transfer. Years later, Shao's group reported the above-room-temperature thermally enhanced UCL in small-sized β-$NaYF_4$:Yb^{3+}/Er^{3+} NPs for the first time.[298] A phonon confinement effect was proposed to account for the thermally enhanced upconversion emissions. The phonon density of states in small UCNPs are discrete and low-energy acoustic phonon modes were cut off at low temperatures.[299] In this regard, the phonon confinement effect was weakened with increasing temperature and thus more phonons can make up the energy mismatch between Yb^{3+} and Er^{3+}. Up to now, several other mechanisms of thermal enhancement of UCL have been proposed during a few years. Wang and colleagues found that negative thermal expansion material $Yb_2W_2O_{12}$:Yb^{3+}/Er^{3+} exhibited UCL thermal enhancement behaviour.[300] They demonstrated that the thermally enhanced upconversion came from lattice contraction and distortion with increasing temperature. Several groups believe that the thermally enhanced emissions in UCNPs are caused by the alleviation of surface quenching. The mechanism by the desorption of water molecules on the nanoparticle surface at elevated temperatures has been demonstrated by such as the thermogravimetric analysis.[301] This enhancement behaviour is strongly related to the size of core and shell thickness of core/shell NPs.[302,

[303] Another explanation is lattice expansion that suppresses energy transfer from the interior of NPs to surface quenching sites.[304] In 2018, Zhou et al. provided a new explanation about the thermally enhanced UCL in UCNPs, which is called surface phonon-assisted energy transfer.[305] They suggested that more surface phonons are created by the [Yb···O] complexes as temperature rises, and can immediately be coupled with Yb^{3+}, then the trapped energy is transferred to the Tm^{3+} excited state generating brighter UCL.

The availability of improved UCL emission at high temperatures provides appealing opportunities for luminescence thermometry applications. NIR excited UCNPs have many merits such as low toxicity, high penetration depth, long lifetime, high chemical stability and resistance to photo bleaching, being good candidates for contactless, non-invasive temperature measurements.[306-308] For the Boltzmann governed nanothermometry, the absolute and relative thermal sensitivities are normally provided to evaluate the capacity of temperature sensing of the materials.[243] Furthermore, the lattice strain induced thermal sensing enhancement has been demonstrated for heterostructured UCNPs.[309, 310] As described in the previous chapter, we have demonstrated a new class of lanthanide-doped Gd_2O_2S@$NaYF_4$ heterogeneous core/shell UCNPs with improved UCL efficiency.

Herein, in this chapter, we will continue to investigate the potential nanothermometry application of the lanthanide-doped Gd_2O_2S@$NaYF_4$ heterogeneous core/shell UCNPs. Based on the temperature-dependent UCL emission spectra, we find a thermal enhancement of the UCL phenomenon in our UCNPs. Moreover, temperature-dependent UCL spectra and in-situ XRD measurements manifest a correlation between selected emission bands ratio of Er^{3+} and lattice strain. Finally, we show that Ln^{3+}-doped Gd_2O_2S@$NaREF_4$ core/shell UCNPs have a great potential for nanothermometry application with high relative thermal sensitivities.

2 Experimental

2.1 Sample preparation

The samples used in this chapter are prepared as described in last chapter.

2.2 In-situ XRD measurements

In-situ temperature-dependent XRD patterns were recorded on a diffractometer (Panalytical Empyrean, Co Kα radiation, λ = 1.789 Å) equipped with a furnace (Anton Paar HTK1200), with a step size of 0.03°. To avoid burn the surface ligands, the core/shell NPs were washed with acid to yield ligand-free surface and the referential Gd_2O_2S NPs without surface ligands were synthesized by a solid state sintering method reported previously[162]. The lattice parameters of the samples were determined by TOPAS software.

2.3 Temperature-dependent UCL measurements

Temperature-dependent UCL spectra were recorded on an Edinburgh Instruments FLS980 spectrometer equipped with a thermal stage (77-873 K, THMS600, Linkam Scientific Instruments) and a fibre (QE 65000, Ocean Optics) for collecting luminescence. The power density of 980 nm diode laser was fixed at 25 W/cm^2. To avoid the effects of the surface ligands of samples, the as-synthesized core/shell NPs were washed with acid to yield ligand-free NPs.

3 Results and discussion

3.1 Thermally enhanced UCL

As mentioned above, lattice strain at the core-shell interface can tune the optical behaviours upon changes in external parameters, for instance, heating. To verify it, we first implemented temperature-dependent UCL spectra measurements for Yb^{3+}/Tm^{3+} doped Gd_2O_2S@$NaYF_4$ UCNPs. As shown in Figure 4.1, the UCNPs show abnormal temperature-dependent UCL behaviour. It shows that the UCL intensity of the UCNPs under 980 nm laser irradiation increases continuously with temperature increasing from 293 K to 473 K.

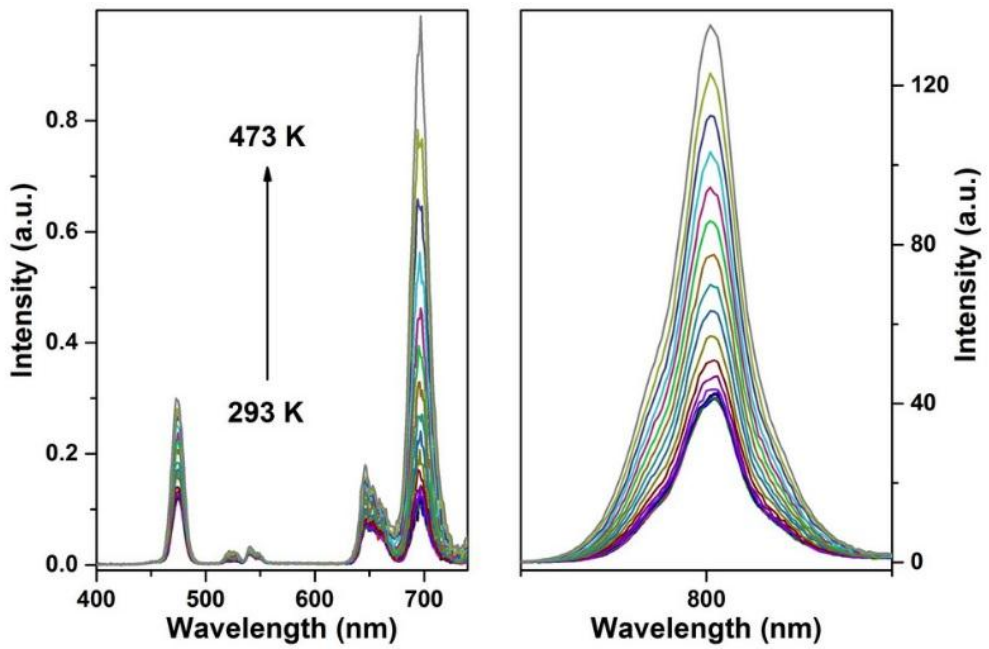

Figure 4.1 Temperature-dependent UCL spectra of Gd_2O_2S:20%Yb,1%Tm@$NaYF_4$ core/shell UCNPs, under 980 nm laser excitation at a power density of 25 W/cm^2.

In Figure 4.2a, the peaks at 469 nm, 640 nm, 690 nm, and 803 nm can be ascribed to transitions of $^1G_4 \rightarrow {}^3H_6$, $^1G_4 \rightarrow {}^3F_4$, $^3F_{2,3} \rightarrow {}^3H_6$, and $^3H_4 \rightarrow {}^3H_6$, respectively. When we compared the intensities at low temperature (293 K) and high temperature (473 K), it was clear that the UCL intensity is enhanced at high temperature. Figure 4.2b shows the integrated intensity of each peak as a function of temperature. It was calculated that the intensities of all the peaks at 469 nm, 640 nm, 690 nm ($^3F_{2,3} \rightarrow {}^3H_6$), and 803 nm of Tm^{3+} are apparently 3, 2,10, and 3 times higher at 473 K than that at 293 K, respectively. Notably, the reason of greater enhancement at 690 nm is that the energy levels of $^3H_4$ and $^3F_{2,3}$ are thermally-coupled, thus leading to a favourable population at the higher level of $^3F_{2,3}$ at an elevated temperature. This indicates that the UCNPs have a good temperature sensing capacity hence can be good candidates for thermometry.

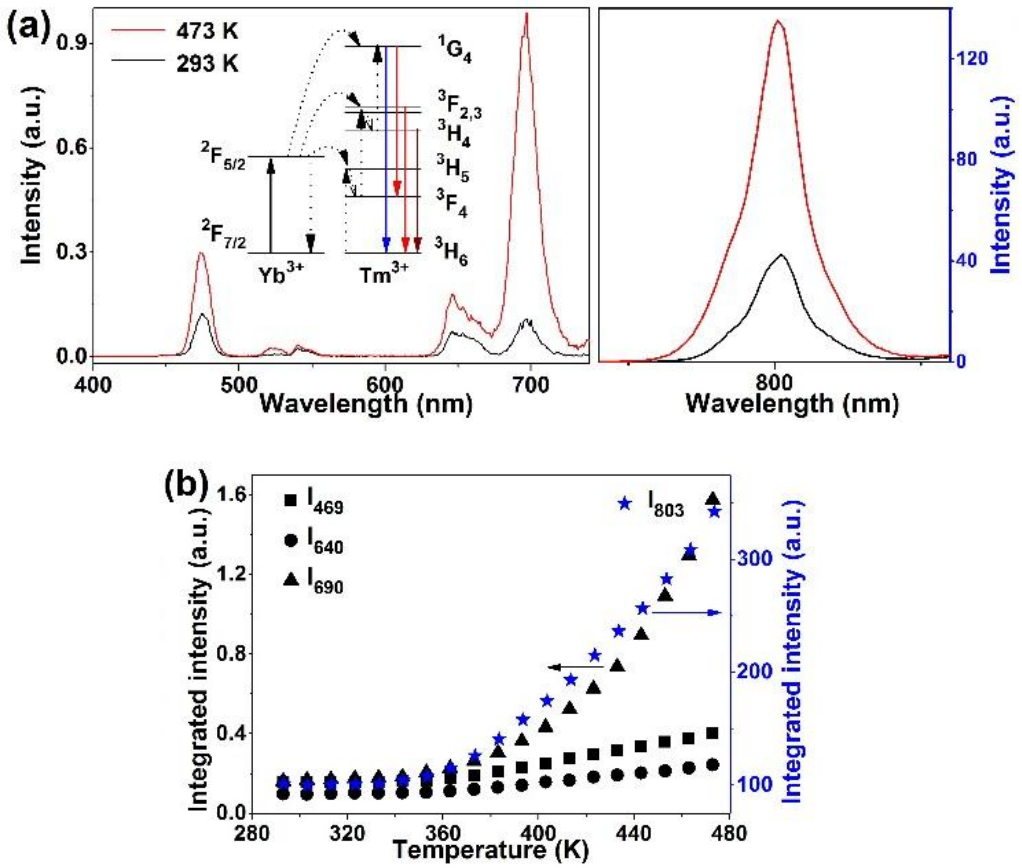

Figure 4.2 (a) Variation of UCL spectra and (b) integrated intensities of the peaks of Tm^{3+}, respectively, of Gd_2O_2S:20%Yb,1%Tm@$NaYF_4$ core/shell UCNPs with increasing temperature. Inset energy level diagram shows the upconversion mechanism of Yb^{3+}/Tm^{3+} ions.

The similar thermal enhancement behaviour was observed for Yb^{3+}/Er^{3+} doped Gd_2O_2S@$NaYF_4$ UCNPs, as well, shown in Figures 4.3. As temperature increases, the intensities of all 3 peaks rise gradually.

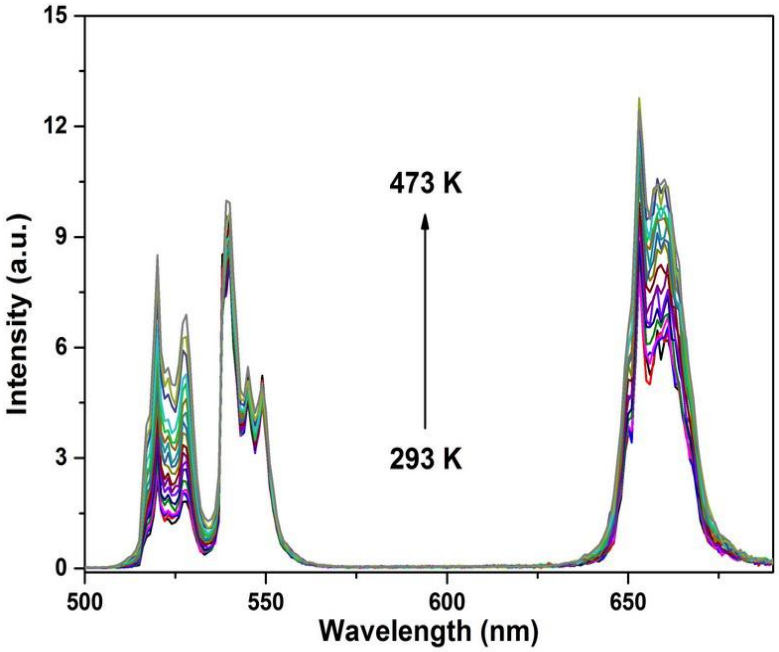

Figure 4.3 Temperature-dependent UCL spectra of Gd_2O_2S:20%Yb,2%Er@$NaYF_4$ core/shell UCNPs under 980 nm excitation at a power density of 25 W/cm^2.

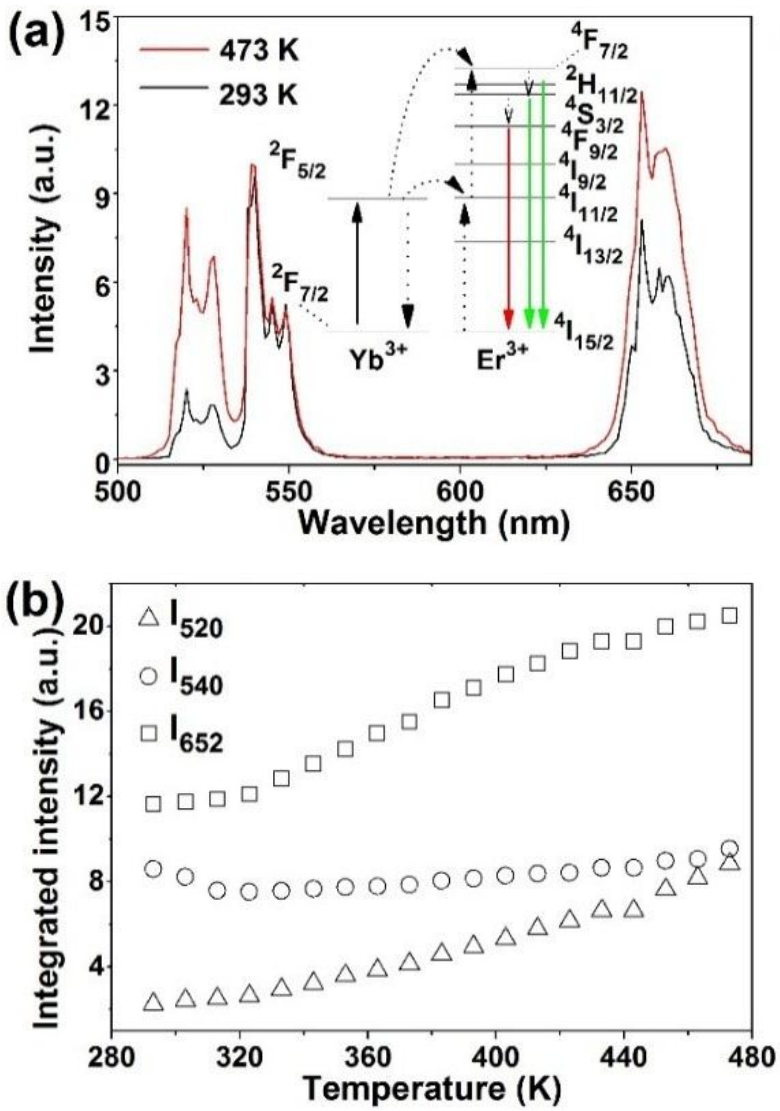

Figure 4.4 (a) Variation of UCL spectra and (b) integrated intensities of the peaks of Er^{3+}, respectively, of Gd_2O_2S:20%Yb,2%Er@$NaYF_4$ core/shell UCNPs with increasing temperature. Inset energy level diagram shows the upconversion mechanism of Er^{3+} ions.

Figure 4.4a shows the intensities of Gd_2O_2S:20%Yb,2%Er@$NaYF_4$ core/shell UCNPs at 293 K and 473 K, and the energy transfer process from Yb^{3+} to Er^{3+}. The identical peaks at 520 nm, 540 nm, and 652nm are due to transitions of $^2H_{11/2} \rightarrow {}^4I_{15/2}$, $^4S_{3/2} \rightarrow {}^4I_{15/2}$, and $^4F_{9/2} \rightarrow {}^4I_{15/2}$, respectively. Furthermore, the integrated intensities of peaks at 520 nm ($^2H_{11/2} \rightarrow {}^4I_{15/2}$), 540 nm ($^4S_{3/2} \rightarrow {}^4I_{15/2}$), and 652nm ($^4F_{9/2} \rightarrow {}^4I_{15/2}$) increase by factors of 3.9, 1.1, and 2.8 at 473 K compared to that at 293 K (Figure 4.4b).

In recent years, thermally enhanced UCL has attracted a lot of attention and several hypotheses such as surface phonon assistance[305], surface molecule desorption[301], and energy transfer suppression induced by lattice expansion[304] have been proposed under different circumstances. In our case, the shell thickness of small (< 30 nm) Gd_2O_2S@$NaYF_4$ core/shell UCNPs is only about 4 nm which cannot completely prevent surface quenching by water molecules, hence causing the UCL enhancement with increasing temperature by water desorption. To verify that, we carried out heating-cooling cycle experiments for Gd_2O_2S:20%Yb,2%Er@$NaYF_4$ core/shell UCNPs, intensities of all emission bands were integrated at specific temperature. As shown in Figure 4.5, in the first cycle, thermal UCL enhancement was observed; following, the UCL intensity kept increasing even if the temperature was declined to 293 K, and as temperature increased again, the intensity still continued to increase. However, for last 3 cycles, the intensity at 473 K was nearly stable, and the UCL intensity at 473 K was always higher than that at 293 K. We assume that in the first 2 heating-cooling cycles, attached surface water molecules of UCNPs were slowly removed, thus leading to enhanced UCL; in the last 3 cycles, the water molecules were almost completely removed, therefore, thermal quenching effect was dominant. The similar results of heating-cooling cycles were obtained for Gd_2O_2S:20%Yb,1%Tm@$NaYF_4$ UCNPs. To further examine the surface water molecules "absorption-desorption effect", we measured the temperature-dependent UCL spectra of Gd_2O_2S:20%Yb,1%Tm@$NaYF_4$ core/shell UCNPs when the sample had been placed in air for 48 days after heating-cooling process. As shown in Figure 4.6, we still observed thermal UCL enhancement behaviour for the UCNPs after standing 48 days in air. In a word, these results are quite consistent with the model of surface water molecules desorption.[301]

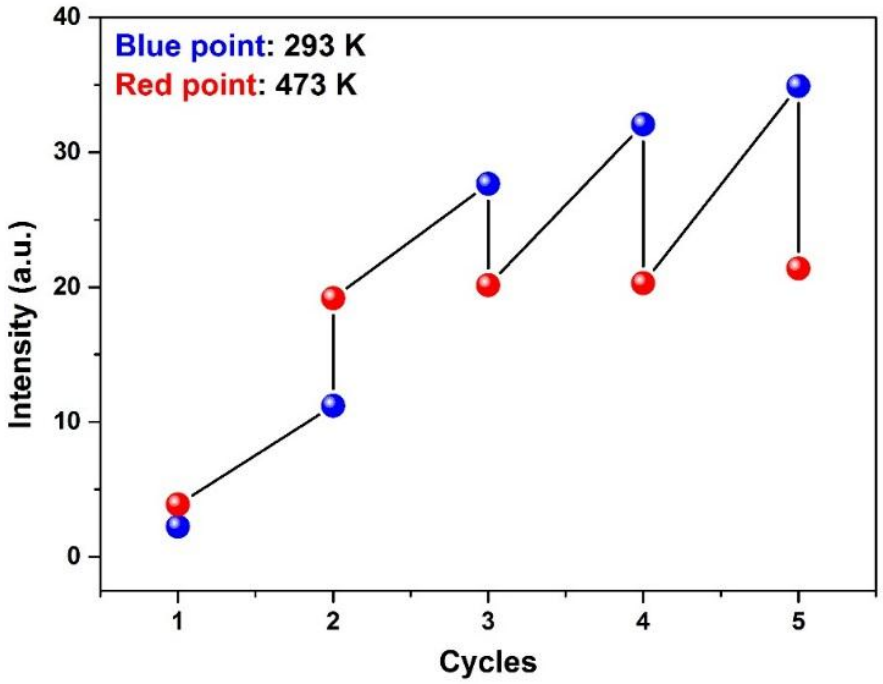

Figure 4.5 Heating-cooling cycles for absolute UCL intensities of Gd_2O_2S:20%Yb,2%Er@$NaYF_4$ core/shell UCNPs at 293 K and 473 K.

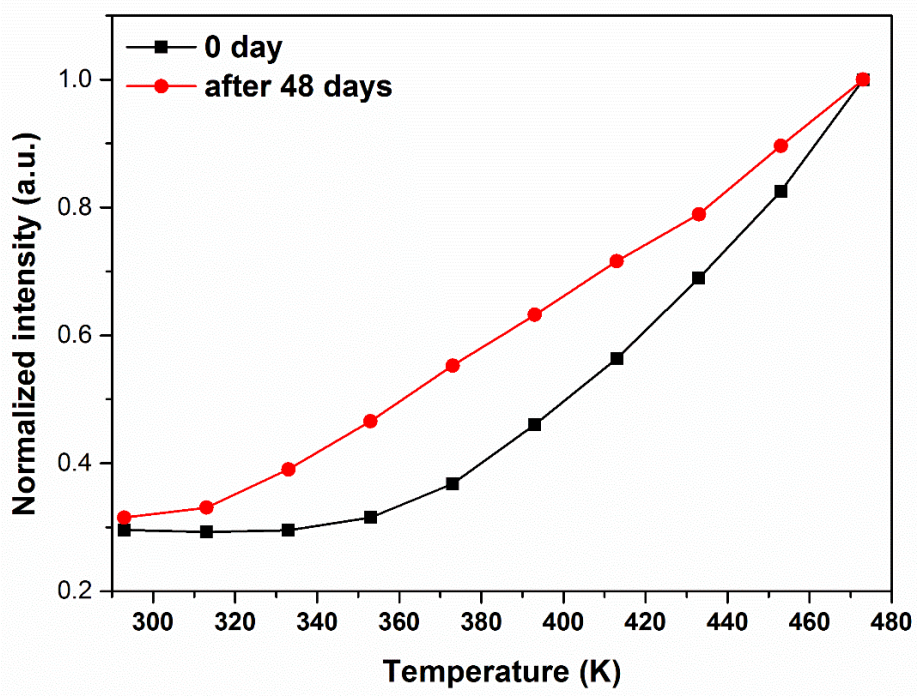

Figure 4.6 Temperature-dependent UCL intensities of Gd_2O_2S:20%Yb,1%Tm@$NaYF_4$ core/shell UCNPs measured at different times (day 0 and day 48).

3.2 Heating induced the change of fluorescence ratio

Apart from the UCL enhancement, interestingly, it was found that the intensity ratio of I_{652}/I_{540} was changed as a function of temperature for Gd_2O_2S:20%Yb,2%Er@$NaYF_4$ core/shell UCNPs. Figure 4.7 shows that the ratio first increases linearly from 293 K to 423 K, then keeps almost stable from 423 K to 463 K, and finally drops at 473 K. The ratio at 423 K is 165% higher than that at 293 K.

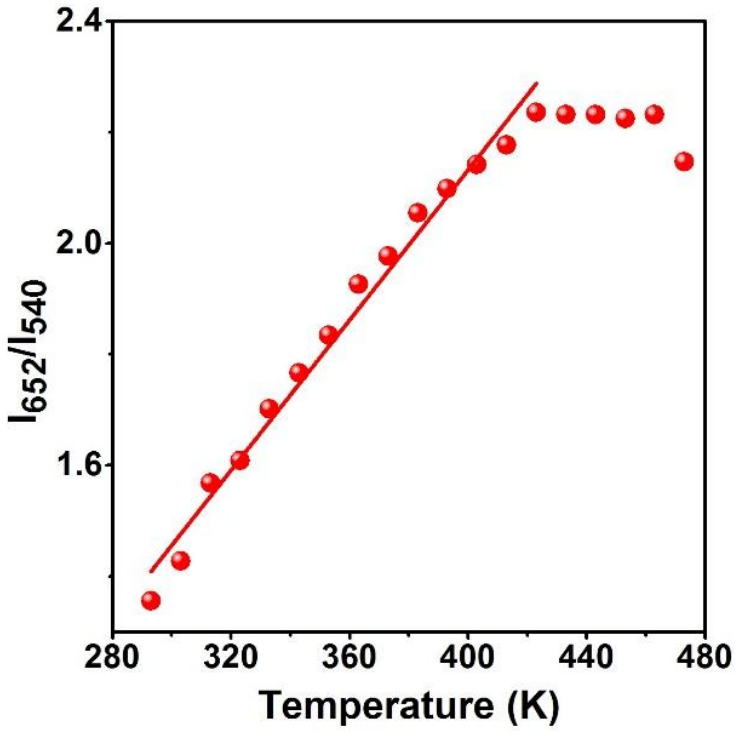

Figure 4.7 Temperature dependent red/green emission intensity ratios (I_{652}/I_{540}) of Gd_2O_2S:20%Yb,2%Er@$NaYF_4$ core/shell UCNPs. The red straight line is plotted by linear fitting in the temperature range of 293~423 K.

As we know, the variation of $^4S_{3/2} \rightarrow {}^4F_{9/2}$ non-radiative relaxation will influence the I_{652}/I_{540} ratios. Here two factors should be taken into account: heating and differential lattice expansion. Increasing temperature can enhance $^4S_{3/2} \rightarrow {}^4F_{9/2}$ non-radiative relaxation, leading to an increase of I_{652}/I_{540} ratio. This can explain the change in the first temperature range from 293 K to 423 K, but is not applicable for the rest of the temperature range. As the temperature continues to rise, the I_{652}/I_{540} ratio nearly keeps

constant and even drops at 473 K. Hence, the influence of lattice expansion in our nanoparticle has to be involved.

To validate the influence of lattice expansion, we first carried out in-situ XRD measurements at different temperatures (from 323 K to 573 K) for both core and core/shell UCNPs. To ensure the reversibility of the lattice constants after heating process, the XRD patterns of the UCNPs were measured twice at 323 K. Note the control Gd_2O_2S:Yb,Tm core UCNPs were synthesized by a solid state method for avoiding surface ligands and used as a reference[161], the surface ligands of Gd_2O_2S:Yb,Tm@$NaYF_4$ core/shell UCNPs were removed by an acid treatment method. Figure 4.8 shows the in-situ XRD patterns of Gd_2O_2S:Yb,Tm core UCNPs under different temperatures. It can be seen that the peak of (101) lattice plane shifts very little to the left with rising temperature. Comparatively, Figure 4.9 shows the in-situ XRD patterns of Gd_2O_2S:Yb,Tm@$NaYF_4$ core/shell UCNPs from 323 to 573 K. Apparently, the peak of (110) lattice plane shifts to the left a lot with temperature rising, indicating a large lattice expansion for the UCNPs.

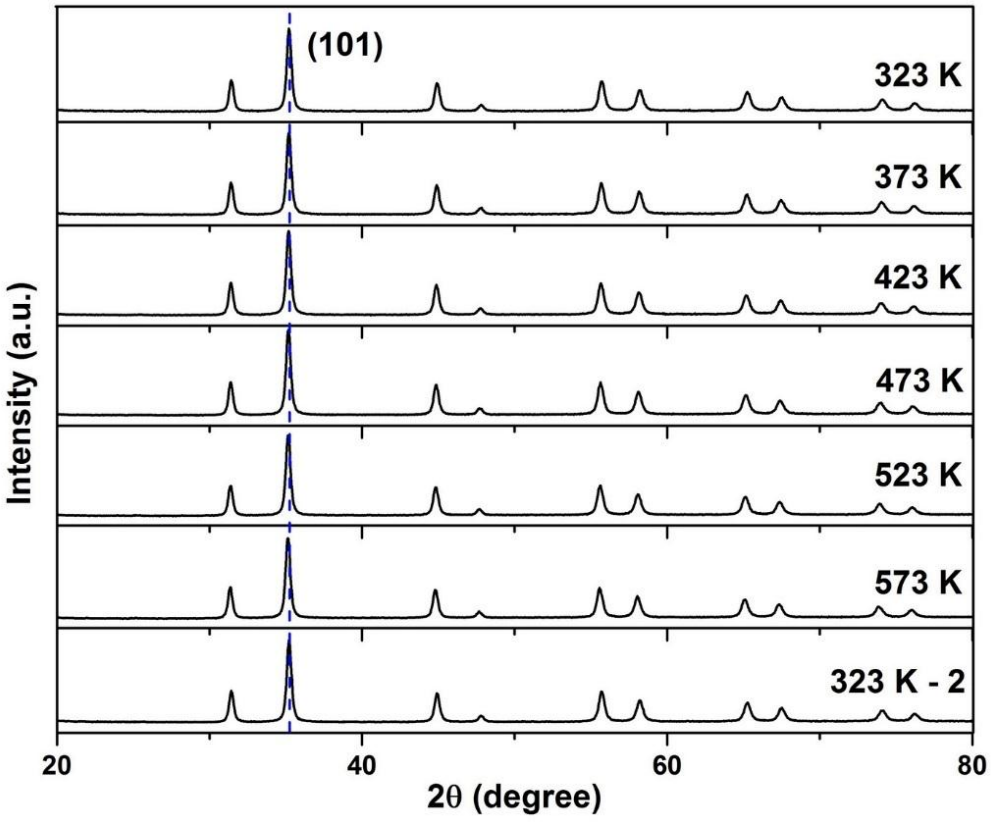

Figure 4.8 In-situ XRD study of Gd_2O_2S:Yb,Tm UCNPs at different temperatures from 323 K to 573 K. 323 K - 2 means the XRD pattern was measured again at 323 K after the heating process. It shows that the (101) lattice plane shifts to the left.

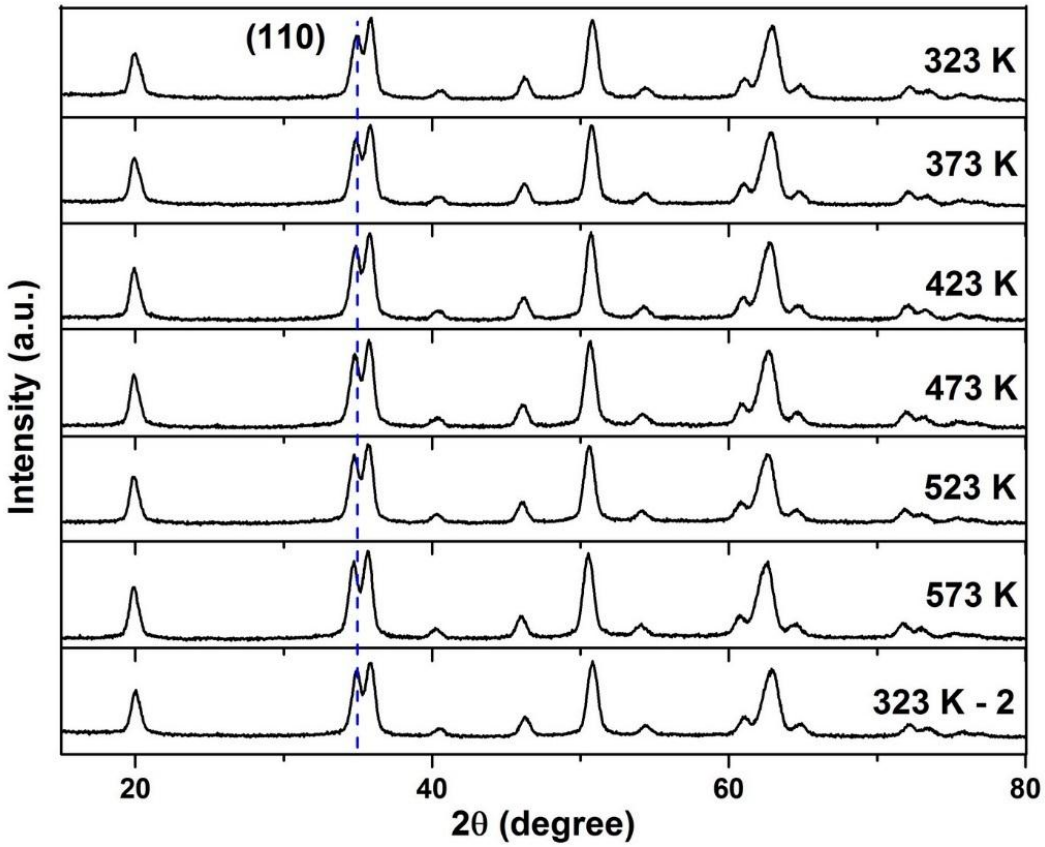

Figure 4.9 In-situ XRD study of Gd_2O_2S:Yb,Tm@$NaYF_4$ core/shell UCNPs at different temperatures from 323 K to 573 K. 323 K - 2 means the XRD pattern was measured again at 323 K after the heating process. The obvious shifting to the left of (110) lattice plane with varying temperature from low to high.

In order to quantify the lattice expansion, we examined the lattice constants of both core and core/shell UCNPs. The lattice constants (a and c) were first determined by fitting with the Pawley method[311], then the cell volumes at different temperatures were obtained in Table 4.1 and 4.2 for the core and core/shell UCNPs, respectively.

Table 4.1 Cell edges in Gd_2O_2S:8%Yb,1%Tm by XRD define.

Temperature (K)	a (Å)	c (Å)	Volume (Å^3)

323	3.8520	6.6685	257.0724
373	3.8541	6.6731	257.5247
423	3.8554	6.6753	257.7821
473	3.8567	6.6785	258.0833
523	3.8584	6.6816	258.4334
573	3.8602	6.6855	258.8291
323 (after heating)	3.8526	6.6701	257.2122

Table 4.2 Cell edges in Gd_2O_2S:20%Yb,1%Tm@$NaYF_4$ by XRD define.

Temperature (K)	**a (Å)**	**c (Å)**	**Volume (Å^3)**
323	6.0099	3.5399	332.1870
373	6.0158	3.5420	333.0386
423	6.0201	3.5431	333.6148
473	6.0275	3.5466	334.7659
523	6.0318	3.5497	335.5294
573	6.0386	3.5543	336.7227
323 (after heating)	6.0006	3.5358	330.7712

To obtain the thermal expansion coefficient, we first plotted the cell volume as a function of temperature for both core and core/shell UCNPs, as shown in Figure 4.10. Then the linear fitting of cell volume versus temperature plots revealed the thermal volume expansion rates of 0.007 Å^3/K and 0.021 Å^3/K for the Gd_2O_2S:Yb,Tm core and the Gd_2O_2S:Yb,Tm@$NaYF_4$ core/shell, respectively. As we can see, the thermal

expansion coefficient of Gd_2O_2S:Yb,Tm@$NaYF_4$ core/shell is much higher than that of Gd_2O_2S:Yb,Tm core in the same temperature range.

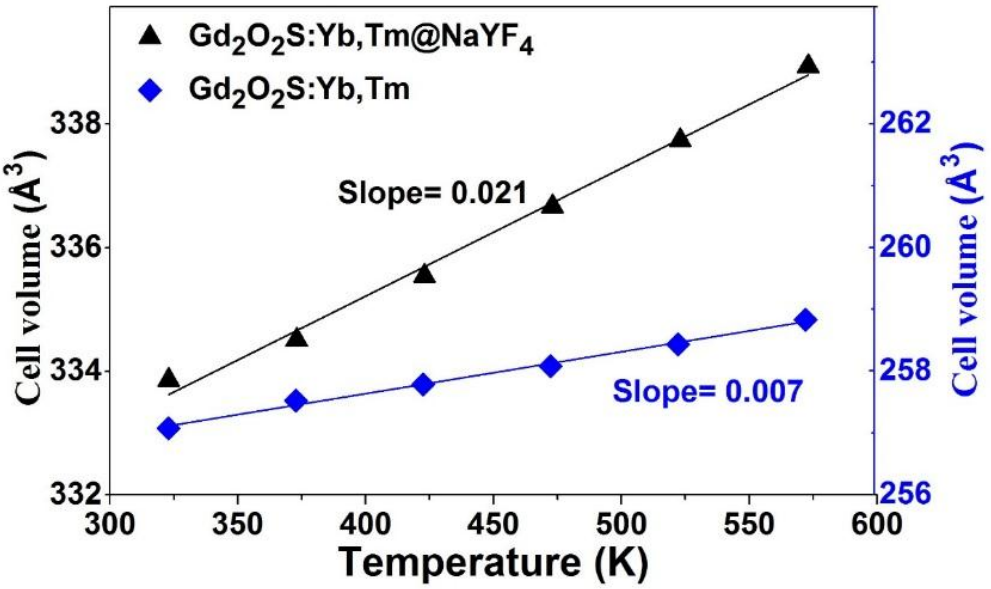

Figure 4.10 Cell volume as a function of temperature plots for both core and core/shell compositions. The thermal volume expansion rates can be determined by linear fitting the respective data points.

Based on the previous XRD patterns and HRTEM analyses in chapter III, it has been determined that the related crystal plane spacing of $NaYF_4$ is smaller than that of Gd_2O_2S at ambient temperature, indicating the core is coated a tensile shell. Therefore, we are able to determine the variation of the interface lattice distortion with elevating temperature as illustrated in Figure 4.11, in which it visually indicates that the lattice distortion will decrease with elevating temperature because of large difference of expanding rate between core and shell (shell expansion rate is 300% higher than core) and reach a kind of equilibrium. This process has been reported as lattice self-adaptation by Wu et al.,[310] recently. It is inferred that further increasing temperature would generate new compressive strain at the interface. Note the interface area can reach up to several atom layers, thus significantly affect the optical properties of heterostructures.

Applying the variation of lattice distortion, we can readily re-explain for the change of the I_{652}/I_{540} ratios. Firstly, the decrease of tensile strain would promote $^4S_{3/2} \rightarrow {}^4F_{9/2}$ nonradiative transition and improve the I_{652}/I_{540} ratio as a function of temperature in the range of 293~423 K, which is in a good agreement with investigations of Er^{3+} emission of other $NaYF_4$ based heterostructures under heating[309] and mechanical forces[312, 313]. Then, the I_{652}/I_{540} ratio will keep nearly constant in the range of 423~463 K due to constant strain under equilibrium state. Finally, the inverse compressive strain will decrease the I_{652}/I_{540} ratio at 473 K. Importantly, when lattice strain at the interface has a strong influence on the population of thermally-coupled emissive states, it can be harnessed to enhance the sensitivity to temperature.[309, 310, 312]

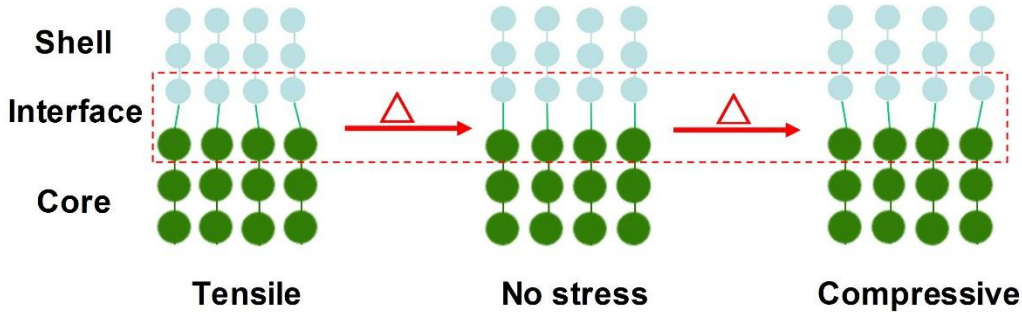

Figure 4.11 Schematic illustration of lattice distortion variation with increasing temperature. It shows that the lattice distortion varies from tensile strain to compressive strain due to large difference of thermal expansion rates of plane spacings between core and shell.

3.3 Thermal sensitivity study

In this section, we demonstrated a high response of UCL luminescence to temperature change using our custom-designed Ln^{3+} doped Gd_2O_2S@$NaREF_4$ heterostructures. Since 980 nm excited $^3F_{2,3} \rightarrow {}^3H_6$ (I_{690}) and $^3H_4 \rightarrow {}^3H_6$ (I_{803}) of Tm^{3+}, $^2H_{11/2} \rightarrow {}^4I_{15/2}$ (I_{520}) and $^4S_{3/2} \rightarrow {}^4I_{15/2}$ (I_{540}) of Er^{3+} upconversion emissions (arising from their respective thermally coupled energy levels) comply with Boltzmann distribution theory[244, 245], therefore the fluorescence intensity ratio (FIR) can be expressed following the equation:

$$FIR = \frac{I_2}{I_1} = Cexp^{(-\Delta E/kT)} \quad (4\text{-}1)$$

where I_2 and I_1 corresponds to the integrated fluorescent intensities of high-energy level and low-energy level, respectively; C is a constant; ΔE is the energy gap; k is the Boltzmann constant and T is the absolute temperature. The obtained FIR or Ln(FIR) values were well fitted with the Eq. (4-1) for Yb^{3+}/Tm^{3+} or Yb^{3+}/Er^{3+} doped Gd_2O_2S@$NaYF_4$ UCNPs, as shown in Figures 4.12a and 4.12d. The fitting results were expressed as $FIR(I_{690}/I_{803}) = 3.45 \times exp^{\left(\frac{-3330}{T}\right)} + 0.0016$ for Yb^{3+}/Tm^{3+} doped Gd_2O_2S@$NaYF_4$ UCNPs and $Ln(FIR\left(\frac{I_{520}}{I_{540}}\right)) = \frac{-967}{T} + 1.96$ for Yb^{3+}/Er^{3+} doped Gd_2O_2S@$NaYF_4$ UCNPs, where ΔE values were determined to be 3330 cm^{-1} and 967 cm^{-1} for Yb^{3+}/Tm^{3+} and Yb^{3+}/Er^{3+}, respectively.

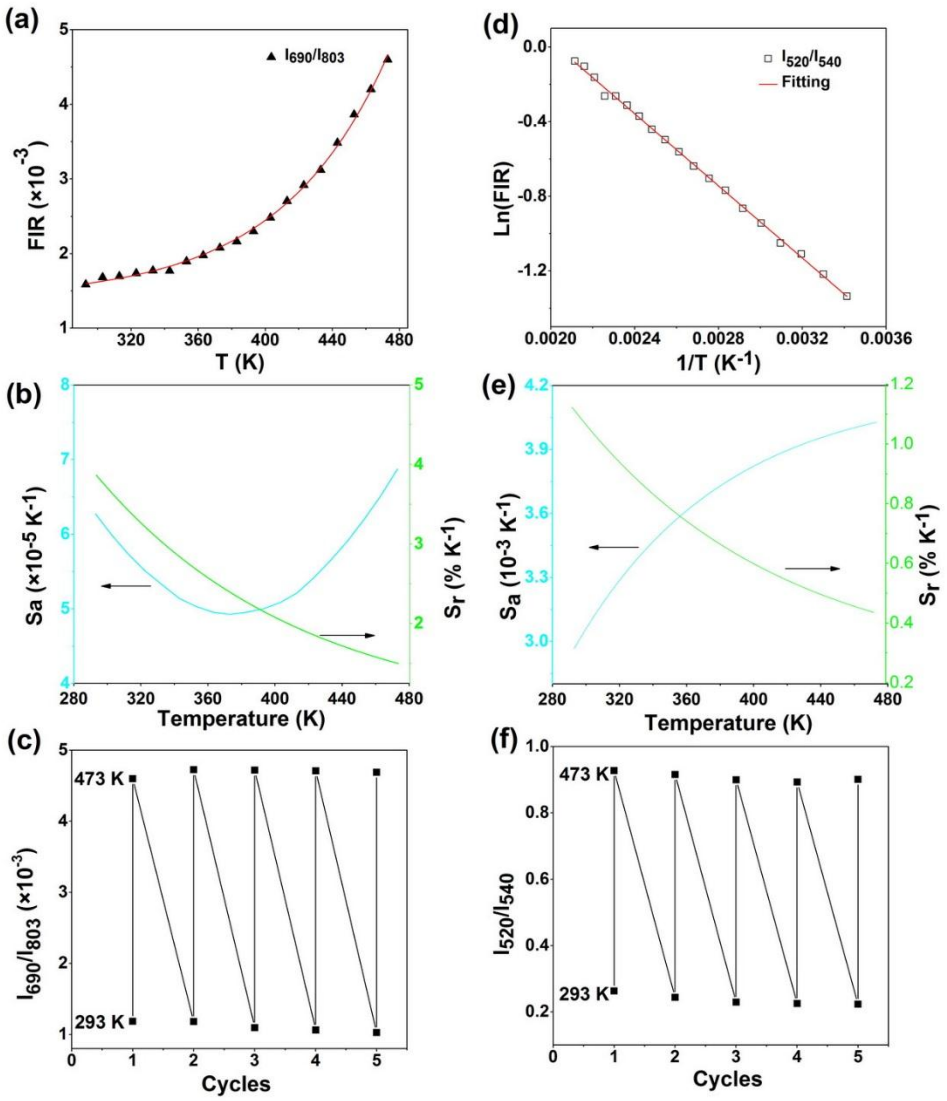

Figure 4.12 (a) FIR vs T, (b) dependence of absolute (S_a) and relative (S_r) thermal sensitivity on temperature, and (c) heating-cooling cycles for I_{690}/I_{803} of Gd_2O_2S:20%Yb,1%Tm@$NaYF_4$ core/shell UCNPs. (d) Ln(FIR) vs 1/T, (e) dependence of S_a and relative S_r on temperature, and (f) heating-cooling cycles for I_{520}/I_{540} of Gd_2O_2S:20%Yb,2%Er@$NaYF_4$ core/shell UCNPs.

To further evaluate temperature sensing behavior of our UCNPs, the absolute thermal sensitivity (S_a) and relative temperature sensitivity (S_r) were calculated using the following equations[244, 245]:

$$S_a = \frac{\partial FIR}{\partial T} = FIR\left(\frac{\Delta E}{kT^2}\right) \quad (4\text{-}2)$$

$$S_r = \frac{1}{FIR}\frac{\partial FIR}{\partial T} = \left(\frac{\Delta E}{kT^2}\right) \quad (4\text{-}3)$$

The S_a and S_r values for both Yb^{3+}/Tm^{3+} and Yb^{3+}/Er^{3+} doped UCNPs have been presented in Figures 4.12b and 4.12e. As can be seen, the Yb^{3+}/Tm^{3+} doped UCNPs exhibit the maximum S_a at 473 K with 0.0069% K^{-1} and S_r at 293 K with 3.9% K^{-1}; the Yb^{3+}/Er^{3+} doped UCNPs exhibit the maximum S_a at 473 K with 0.4% K^{-1} and S_r at 293 K with 1.1% K^{-1}. To assess the stability of our luminescent nanoprobes, we performed 5 heating-cooling cycles for both Yb^{3+}/Tm^{3+} and Yb^{3+}/Er^{3+} doped UCNPs. According to the data in Figures 4.12c and 4.12f, the reproducibility value (R) was calculated to be higher than 95% by the method reported previously[314]. The maximum S_r values for both Yb^{3+}/Tm^{3+} and Yb^{3+}/Er^{3+} doped Gd_2O_2S@$NaYF_4$ UCNPs are quite high.

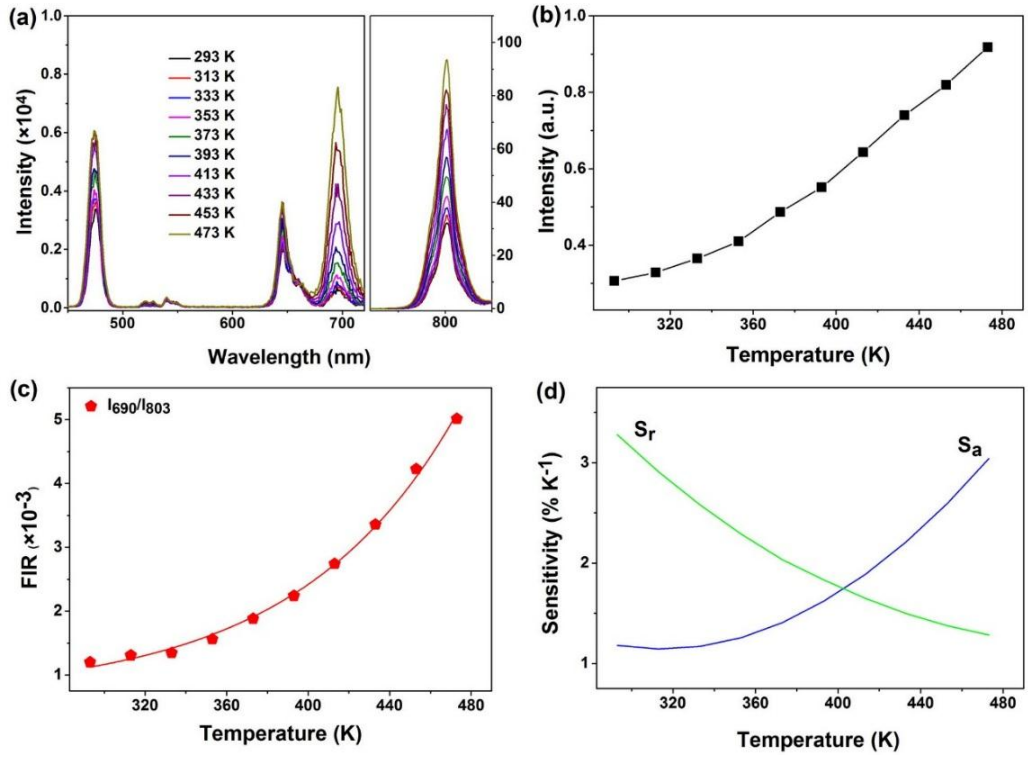

Figure 4.13 (a) Temperature-dependent UCL spectra, (b) enhancement of integrated intensity with increasing temperature, (c) plots of FIR vs T, and (d) dependence of absolute (S_a) and relative (S_r) thermal sensitivity on temperature, for I_{690}/I_{803} of Gd_2O_2S:20%Yb,1%Tm@$NaLuF_4$ core/shell UCNPs.

To verify the high thermal relative sensitivity values for our unique heterogeneous lanthanide doped Gd_2O_2S@$NaREF_4$ core/shell structure, we performed the same method to assess the temperature sensing capacity for Gd_2O_2S:20%Yb,1%Tm@$NaLuF_4$ UCNPs which owns a different shell matrix, as shown in Figure 4.13. The temperature-dependent UCL spectra and integrated intensity were recorded in Figures 4.13a and 4.13b. Figure 4.13c shows the plots of FIR(I_{690}/I_{803}) as a function of temperature T. The fitting results were expressed as $FIR(I_{690}/I_{803}) = 3.61 \times exp^{\left(\frac{-2837}{T}\right)} + 0.0011$, where the ΔE value was determined to be 2837 cm^{-1} for Gd_2O_2S:20%Yb,1%Tm@$NaLuF_4$ core/shell UCNPs. Figure 4.13d exhibits the S_a and S_r values as a function of temperature and the maximum S_a at 473 K with 3.0% K^{-1} and S_r at 293 K with 3.3% K^{-1} were obtained for the UCNPs.

Table 1. Comparison of the relative thermal sensitivities (S_r) of Yb/Tm or Yb/Er doped systems in the similar temperature range. Fluorescence intensity ratios (FIR) from the transitions $^3F_{2,3} \rightarrow {}^3H_6/{}^3H_4 \rightarrow {}^3H_6$ for Tm^{3+} and $^2H_{11/2} \rightarrow {}^4I_{15/2}/{}^4S_{3/2} \rightarrow {}^4I_{15/2}$ for Er^{3+} under 980 nm laser excitation.

Material	T-range (K)	FIR	S_r ($\%K^{-1}$)	Ref.
Gd_2O_2S:Yb,Tm@$NaYF_4$	293-473	I_{690}/I_{803}	3.9 at 293 K	This work
Gd_2O_2S:Yb,Tm@$NaLuF_4$	293-473	I_{690}/I_{803}	3.3 at 293 K	This work
$GdYO_4$:Yb,Tm@SiO_2	298-333	I_{700}/I_{800}	3.3 at 298 K	[315]
$LiNbO_3$:Yb,Tm	323-773	I_{700}/I_{800}	3.0 at 323 K	[316]
$NaYbF_4$:Tm	298-778	I_{697}/I_{803}	1.9# at 298 K	[141]
$NaBiF_4$:Yb,Tm	303-443	I_{697}/I_{800}	2.7# at 303 K	[307]
$KLuF_4$:Yb,Tm	303-503	I_{690}/I_{795}	1.4# at 303 K	[317]
Gd_2O_2S:Yb,Er@$NaYF_4$	293-473	I_{520}/I_{540}	1.1 at 293 K	This work
$(NaGdF_4$:Er/$NaYF_4)_n$	298-348	I_{520}/I_{539}	3.2 at 298 K	[310]
$NaLuF_4$:Yb,Er,Ho	298-503	I_{524}/I_{547}	0.74 at 298K	[318]
β-$NaYF_4$:Yb,Er@SiO_2	299-337	I_{525}/I_{545}	1.3 at 299 K	[319]
Gd_2O_3:Yb,Er	300-900	I_{523}/I_{548}	0.8# at 300 K	[320]
$NaYF_4$:Yb,Er	293-333	I_{525}/I_{545}	1.2# at 293 K	[321]

Values determined by us for this study, according to the data published by the authors in the original literature.

In order to compare the S_r values of our nanoprobes with that of other materials reported previously, we investigated some of reported S_r values. Table 1 lists the sensitivities obtained from other previously reported material systems using the same intensity ratios of Tm^{3+} and Er^{3+} for comparison. It can be found that the maximum S_r of Gd_2O_2S:20%Yb,1%Tm@$NaYF_4$ UCNPs is the highest among Yb^{3+}/Tm^{3+} doped systems in the similar temperature range, and even the $NaLuF_4$-coating UCNPs have a greater S_r value than previously reported Lu-based materials in the same temperature range in the literature. Meanwhile, the Yb^{3+}/Er^{3+} doped Gd_2O_2S@$NaYF_4$ UCNPs also

has an excellent maximum S_r value which is superior to most other systems. The better performance of thermal sensitivity of our UCNPs may be associated with interfacial lattice strain that has been demonstrated to be able to enhance temperature sensitivity. Note that all the compositions of our NPs in this study are still not optimized towards temperature sensitivity, which shows that the Ln^{3+} doped RE_2O_2S@$NaREF_4$ as a new kind of luminescence probe has a great potential for nano thermometry application.

4 Conclusions

In this chapter, we carefully analyze temperature-dependent UCL spectra for lanthanide-doped Gd_2O_2S@$NaREF_4$ core/shell UCNPs. Based on those spectra, we discuss the possible mechanism of thermal UCL enhancement. Then the variation of ratio I_{652}/I_{540} of Yb^{3+}/Er^{3+} doped Gd_2O_2S@$NaREF_4$ core/shell UCNPs with increasing temperature is found and explained by comparing the thermal expansion coefficient of core and core/shell UCNPs. Finally, we demonstrate the relative high response capacity for Yb^{3+}/Tm^{3+} and Yb^{3+}/Er^{3+} doped Gd_2O_2S@$NaREF_4$ core/shell UCNPs, showing the great potential nano-thermometry application for our nanoprobes.

In section 3.1, we first record temperature-dependent UCL spectra for Gd_2O_2S:20%Yb,1%Tm@$NaYF_4$ and Gd_2O_2S:20%Yb,2%Er@$NaYF_4$ core/shell UCNPs. Both of these two samples show abnormal UCL enhancement with increasing temperature from 293 K to 473 K. The heating-cooling cycle measurements confirm that water molecules play a vital role for the thermal enhancement.

In section 3.2, the variation of I_{652}/I_{540} as a function of temperature for Gd_2O_2S:20%Yb,2%Er@$NaYF_4$ core/shell UCNPs is investigated. It is found that the ratio first increases linearly from 293 K to 423 K, then keeps almost stable from 423 K to 463 K, and finally drops at 473 K. To understand the relationship between lattice expansion and change of fluorescence ratio, we analyzed the lattice expansion rates of Gd_2O_2S:Yb,Tm core and Gd_2O_2S:Yb,Tm@$NaYF_4$ core/shell. By using in-situ XRD, the thermal expansion coefficients are determined to be 0.007 $Å^3$/K and 0.021 $Å^3$/K in the same temperature range for Gd_2O_2S:Yb,Tm core and Gd_2O_2S:Yb,Tm@$NaYF_4$

core/shell, respectively, which displays 3 folds difference of thermal expansion rates between core and shell. Therefore, we prosed a mechanism for explanation of the variation of I_{652}/I_{540}, which is the lattice mismatch between core and shell produces tensile stress and the tensile stress would linearly decline with rising temperature, thus leading the linear increase of the ratio I_{652}/I_{540} in the temperature range of 293~423 K; as the temperature further elevates, the tensile stress disappears due to the higher lattice expansion rate of shell than core, hence no change of the ratio is observed. Finally, the fluorescence declines as temperature continues increasing which is ascribed to the appearance of compressive stress.

In section 3.3, we study the thermal sensitivities of lanthanide doped Gd_2O_2S@$NaREF_4$ core/shell UCNPs. The maximum S_r values are calculated to be 3.88 $\%K^{-1}$ and 3.30 $\%K^{-1}$ for Yb/Tm doped Gd_2O_2S@$NaYF_4$ and Gd_2O_2S@$NaLuF_4$, respectively, and 1.13 $\%K^{-1}$ for Yb/Er doped Gd_2O_2S@$NaYF_4$. These S_r values are quite high as compared to the Sr of other systems, showing a great potential nano-thermometry application for the lanthanide doped Gd_2O_2S@$NaREF_4$ core/shell UCNPs.

Chapter V: Core/multi-shell luminescent nanoparticles for asynchronous excitation and detection at ~800 nm

1 Introduction

Fluorescent probes for biological imaging have been widely studied and described in the literature for many years.[322] Yet one of the remaining challenges for in vivo imaging is the development of sufficiently efficient probes for biological tissue deep exploration. Due to biological medium absorption properties, a certain wavelength range is favoured, in the near infra-red. Between 650 and 1000 nm, biological tissues are considered as relatively transparent with however a range between 800 and 850 nm deemed as optimal.[251]

Lanthanide (Ln^{3+})-doped upconversion nanoparticles (UCNPs), as one of the fluorescent probes with excellent physical and chemical properties, have attracted a great deal of interest in the field of bioimaging. Currently, 980 and 808 nm lasers are generally selected as excitation light sources because their wavelengths overlap with the absorption bands of the sensitizers Yb^{3+} and Nd^{3+}, respectively.[323] Excitation at 980 nm using Yb^{3+} as a sensitizer is efficient. However, one major drawback is the strong absorption of water at this wavelength which can lead to (over)heating effects. This characteristic puts an upper limit on the excitation power that can be used to avoid heating effects particularly in cell and animal imaging studies. Water, which represents the major component of the biological medium, has an extinction coefficient 20 times lower at 800 nm (maximum transparency of the biological medium) than at 980 nm. Thus, it would be very beneficial to be able to excite the UCNP probes around 800 nm. Nd^{3+}, is commonly doped in $Y_3Al_5O_{12}$ crystal as the well-known Nd:YAG solid-state lasers, yet it is also used as an absorber since Nd^{3+} has a local absorption maximum at ~800 nm. Tm^{3+} ion is the best-known emitter for upconversion luminescence (UCL) at ~800 nm. $NaYF_4$ is regarded as the best candidate host for UCL due to its low phonon energy.

Therefore, the objective of this chapter is to develop strategies to shift both the excitation wavelength and the emission wavelength of UCNP family based on the host material $NaYF_4$ to this biological tissue transparency window (~800 nm). However,

there is a challenge using the excitation wavelength and the emission wavelength at nearly the same wavelength for bioimaging. Time-gated technique based on adjustable pulse width excitation seems to be able to resolve the issue. Therefore, we aim to establish a new time-gated luminescence technology, employing pulsed excitation (~808 nm) and time-delayed detection (~802 nm) to eliminate short-lived background from autofluorescence.

A candidate activator for bioimaging for our project is Tm^{3+} that has an emission band at ~802 nm ($^3H_4 \rightarrow {}^3H_6$), amongst others. Combining the Nd^{3+}/Yb^{3+} pair can improve the absorption at ~808 nm, therefore, energy transfer process can be described as $Nd^{3+} \rightarrow Yb^{3+} \rightarrow Tm^{3+}$ (Figure 5.1). To acquire a high luminescence efficiency, core/shell/shell architecture engineering (Figure 1, left) where Yb^{3+} is located / doped in the inner shell and the Nd^{3+}/Yb^{3+} pair doped in the outer shell, is expected to overcome back energy transfer from Yb^{3+} to Nd^{3+} and luminescence quenching. So, we will first synthesize Yb^{3+}/Tm^{3+} co-doped $NaYF_4$ core UCNPs with size no more than 20 nm, then $NaYF_4$:Yb^{3+} and $NaYF_4$:Nd^{3+}/Yb^{3+} shells will be then used for the coating of the cores. In this case, Nd^{3+} is only doped in the outer shell for harvesting the excitation energy; Yb^{3+} is doped in every shell layer and core for energy transfer; Tm^{3+} is only doped in core as the emitter. The first shell layer is designed for preventing cross relaxation between Nd^{3+} and Tm^{3+}.

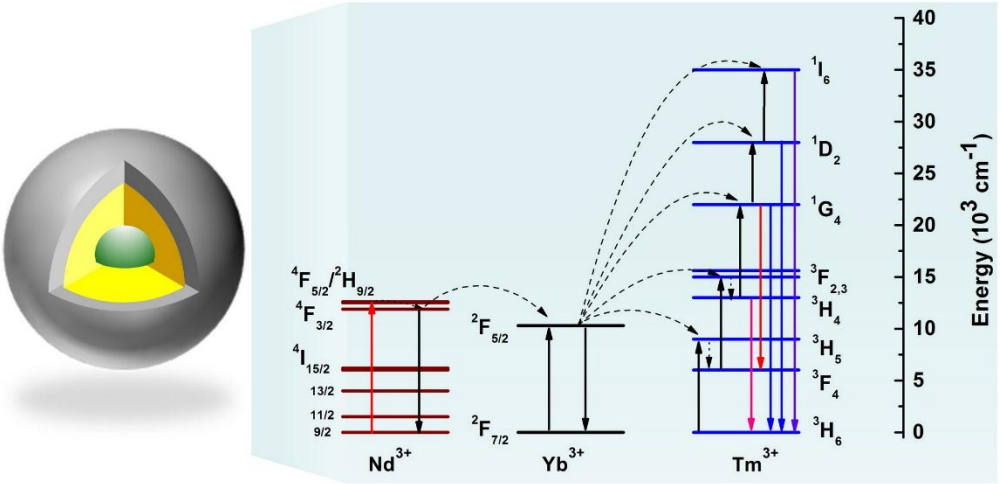

Figure 5.1 Illustration of the core/shell/shell nanostructure shifting the excitation and detection wavelength at ~800 nm.

2 Experimental

2.1 Materials

NaOH, ammonium fluoride (NH_4F), polyvinylpyrrolidone (PVP, MW= 10000), acetic acid, ethanol, methanol, and cyclohexane were purchased from Sigma-Aldrich. Oleic acid (OA) and 1-Octadecene (ODE) were purchased from TCI. All rare earth oxides (RE_2O_3, RE = Y, Gd, Tm and Yb) were purchased from Rone Poulenc. The $RE(CH_3COO)_3 \cdot 4H_2O$ were prepared by firstly dissolving moderate amount of the RE_2O_3 in excess acetic acid solution at 90 °C, then filtering and evaporating the solution, finally drying the resultant slurry in the oven at 70 °C. All chemicals were used as received without further purification.

2.2 Synthesis of $NaYF_4$:40%Gd,20%Yb,x%Tm core UCNPs

The $NaYF_4$:40%Gd,20%Yb,x%Tm core NPs were synthesized through a high-temperature co-precipitate method. In a typical synthesis, a mixture of 1 mmol of $RE(CH_3COO)_3 \cdot 4H_2O$ with a RE ratio of Y : Gd : Yb : Tm = (40-x) : 40 : 20 : x in mol, 6 mL of OA and 15 mL of ODE was heated at 160 °C for 30 min. When the temperature was cooled down to temperature, 10 mL methanol solution containing 4 mmol of NH_4F and 2.5 mmol of NaOH was added in above solution. The resulting mixture was stirred for 60 min at 60 °C to completely remove methanol, then, the temperature was elevated to 300 °C and kept for 1 h. After that, the solution was cooled down to temperature naturally. 20 mL ethanol was added to precipitate the NPs. Finally, the products were purified through washing with a mixture of ethanol and cyclohexane 2~3 times, and re-dispersed in cyclohexane for further characterizations and core/shell synthesis.

2.3 Synthesis of $NaYF_4$:40%Gd,20%Yb,1%Tm@$NaYF_4$:10%Yb core/shell UCNPs

The $NaYF_4$:40%Gd,20%Yb,1%Tm@$NaYF_4$:10%Yb core/shell UCNPs were

synthesized with the as-prepared $NaYF_4$:40%Gd,20%Yb,1%Tm as core NPs. Briefly, a mixture of 0.4 mmol of $Y(CH_3COO)_3 \cdot 4H_2O$, 0.1 mmol of $Yb(CH_3COO)_3 \cdot 4H_2O$, 6 mL of OA, and 15 mL of ODE was heated at 160 °C for 30 min. After cooling down, 10 ml of cyclohexane dispersion of 0.5 mmol $NaYF_4$:40%Gd,20%Yb,1%Tm core NPs was added, followed with addition of 5 mL methanol solution containing 2 mmol of NH_4F and 1.25 mmol of NaOH. After moderate stirring for 60 min at 60 °C to remove cyclohexane and methanol, the solution was heated to 300 °C for 1 h, and then cooled down to room temperature naturally. The products were precipitated, purified and re-dispersed cyclohexane.

2.4 Synthesis of $NaYF_4$:40%Gd,20%Yb,1%Tm@$NaYF_4$:10%Yb@$NaYF_4$:10%Yb,20%Nd core/shell/shell UCNPs

The $NaYF_4$:40%Gd,20%Yb,1%Tm@$NaYF_4$:10%Yb@$NaYF_4$:10%Yb,20%Nd core/shell/shell UCNPs were synthesized with the as-prepared $NaYF_4$:40%Gd,20%Yb,1%Tm@$NaYF_4$:10%Yb as seeds. Briefly, a mixture of 0.2 mmol of $Y(CH_3COO)_3 \cdot 4H_2O$, 0.1 mmol of $Yb(CH_3COO)_3 \cdot 4H_2O$, 0.2 mmol of $Nd(CH_3COO)_3 \cdot 4H_2O$, 6 mL of OA, and 15 mL of ODE was heated at 160 °C for 30 min. After cooling down, 10 ml of cyclohexane dispersion of 0.25 mmol $NaYF_4$:40%Gd,20%Yb,1%Tm@$NaYF_4$:10%Yb core NPs was added, followed with addition of 5 mL methanol solution containing 2 mmol of NH_4F and 1.25 mmol of NaOH. After moderate stirring for 60 min at 60 °C to remove cyclohexane and methanol, the solution was heated to 300 °C for 1 h, and then cooled down to room temperature naturally. The products were precipitated, purified and re-dispersed cyclohexane.

2.5 Synthesis of PVP-coated $NaYF_4$:40%Gd,20%Yb,1%Tm@$NaYF_4$:10%Yb@$NaYF_4$:10%Yb,20%Nd core/shell/shell UCNPs

The OA-free $NaYF_4$:40%Gd,20%Yb,1%Tm@$NaYF_4$:10%Yb@$NaYF_4$:10%Yb,20%Nd core/shell/shell UCNPs were first prepared through a ligand exchange method as reported previously[207]. Typical, 4 mL of nanocrystal dispersion in cyclohexane (~10 mg/mL) mixed with 4 mL of DMF solution of $NOBF_4$ (40 mg) to form a two-phase mixture at room temperature. The resulting mixture was gently shaken for 10 min. After removing the upper supernatant, 20 mL of chloroform was added to precipitate the nanocrystals, then centrifuging and washing the nanocrystals with DMF and chloroform for 3 times. The final OA-free NPs were re-dispersed in DMF.

To further coat PVP on the OA-free NPs, 1.2 g of PVP was added in 3 mL of DMF dispersion (5 mg/mL). The mixture was stirred for 6 hours, then, 20 mL of acetone was added to precipitate the NPs. The obtained NPs were washed several times with DMF and acetone and finally dispersed in 1 mL of water. The solution was stored in fridge under 4 °C for further use.

2.6 Cell labelling

HCT-116 cells were grown on round glass-coverslip coated gelatin and placed into 24-well plates. Then the cells were first incubated with Hoechst for 48 h and further incubated with PVP-coated $NaYF_4$:40%Gd,20%Yb,1%Tm@$NaYF_4$:10%Yb@$NaYF_4$:10%Yb,20%Nd core/shell/shell UCNPs for 6 hours at a concentration of 10 µg/mL. Finally, the coverslip was removed from the wells and flipped onto a glass slide with mounting medium in order to stick the coverslip to the glass. These experiments were carried out by Dr. Laure G. at IMRCP.

2.7 TEM measurements

Size, morphology, and structure analyses were carried out *via* on a transmission electron microscope, Phillips CM20, 200 kV.

2.8 UCL spectra measurements

Room-temperature UCL spectra were recorded on a Jobin-Yvon Model Fluorolog FL3-22 spectrometer that was combined with a 980 nm diode laser (MDL-III-980-5W, Changchun New Industries Optoelectronics Tech Co., Ltd) as excitation source, at CEMES, Toulouse, France.

2.9 Time-gated luminescence spectra and lifetime measurements

The time-gated luminescence spectra measurements were carried out on the time-gated spectroscopic system which is equipped with a pulse laser (980 nm or 808 nm, 2 mJ, 5 ns, 20 Hz, and linear polarization) with focused beam size of ~500 µm. Intensified CCD gated camera (256 × 1024 pixels – pix. size = 26 × 26 µm, "dead time" of 26 ns after laser pulse, time gates from 200 ns to 5 µs) is equipped and connected with a spectrometer (grating: 300 grooves/mm, bandpass: 10 nm). The decays of the UCNPs were recorded on a spectrometer equipped with a Nd:YAG laser (Continuum Surelite II, 976 nm, 2 Hz, pulse width 7-8 ns, 1 mJ) coupled to an Optical Parametric Oscillator (Continuum Panther Ex OPO) and SH05 shutter (Thorlabs). All the time-gated luminescence spectra and decays were recorded at LASIRE of University of Lille, Lille, France.

2.10 Confocal cell imaging

The cell imaging experiments were carried out on a two-photon confocal microscope upon excitations of 980 nm (detection range below 750 nm) and 405 nm (detection range of 415~750 nm).

3 Results and discussion

3.1 Characterizations of $NaYF_4$:40%Gd,20%Yb,x%Tm UCNPs

To first examine the influence of Tm doping concentration on the size and optical

properties of the final obtained NPs, a series of $NaYF_4$:40%Gd,20%Yb,x%Tm NPs (x = 0.1, 0.3, 0.5, 0.7, 1, 1.2, and 1.5) were synthesized through a high-temperature co-precipitation approach. It should be noted that the 40%Gd dopants of the composition are attempted to reduce the size of NPs. As shown in Figure 5.2, the TEM images show good dispersity and spherical shape of all NPs with different Tm concentrations, which means the different Tm doping does not affect the morphology or dispersity.

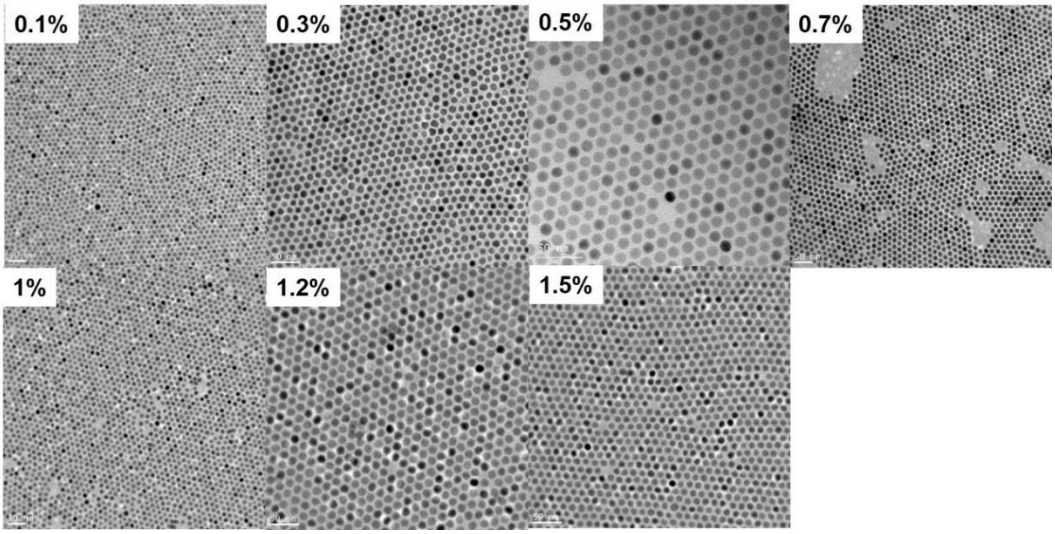

Figure 5.2 TEM images of $NaYF_4$:40%Gd,20%Yb,x%Tm NPs (x = 0.1, 0.3, 0.5, 0.7, 1, 1.2, and 1.5).

We further examine the influence on the size by calculating the average size of the NPs with different doping levels. Figure 5.3 shows the size distributions of the core NPs. It is clear that the size ranges from 9.8 ± 1.1 nm to 14.6 ± 0.9 nm with a size difference of ~5 nm. The large size difference could arise from not only variation of Tm doping concentrations on the one hand, but also the synthesis from batch to batch on the other hand which is normal and hard to avoid in the synthesis of nanomaterials.

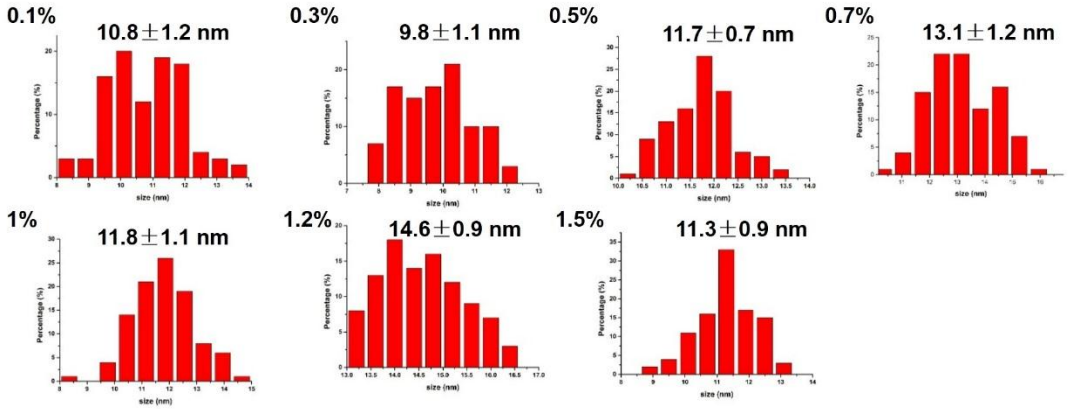

Figure 5.3 Histograms of size distributions of $NaYF_4$:40%Gd,20%Yb,x%Tm NPs with varying concentration from 0.1% to 1.5%.

3.2 UCL property of $NaYF_4$:40%Gd,20%Yb,x%Tm UCNPs

Subsequently, UCL spectra of $NaYF_4$:40%Gd,20%Yb,x%Tm (x = 0.1, 0.3, 0.5, 0.7, 1, 1.2, and 1.5) NPs were measured under 980 nm continuous wavelength (CW) laser excitation. Figure 5.4 exhibits the 3 identical emission peaks at 455 nm, 475 nm, and 800 nm which are corresponding to the transitions of $^1D_2 \rightarrow {}^3F_4$, $^1G_4 \rightarrow {}^3H_6$, and $^3H_4 \rightarrow {}^3H_6$. It is obvious that 800 nm emission is the most intense peak (more than 1 order higher than 475 nm) in the whole spectrum due to a higher probability population of lower $^3H_4$ energy level (two photon process) compared to other energy levels (three or more photon process). As it can be seen that the 1.2%Tm doped sample has the most intense UCL. To better compare the optical property of those samples, we integrated the luminescence intensity in the range of 770~840 nm of $^3H_4 \rightarrow {}^3H_6$ transition of Tm^{3+} for all samples, as shown in Figure 5.5a. Besides, the mean size values of the samples are plotted in Figure 5.5a as well. As a result, it apparently indicates that the UCL intensity is capable of a strong dependence on the mean size of UCNPs, as shown in Figure 5.5b. Generally speaking, as the size increases or decreases, the UCL intensity rises or declines as well. It seems the variation of Tm concentration plays a negligible role in our study. Herein, we consider 3 reasons that might be involved. First, the NPs are small and owing large surface to volume ratios so that the surface quenching is dominant; second, the real Tm concentration in the NPs should be checked to confirm

the variation; third, to eliminate the effects of surface quenching, a shell with the same thickness should be coated on those cores. In fact, since we don't have routine quantum yield (QY) measurements so we rely on brightness measurements on the spectrometer, otherwise, it could be interesting to compare the QYs of these series samples.

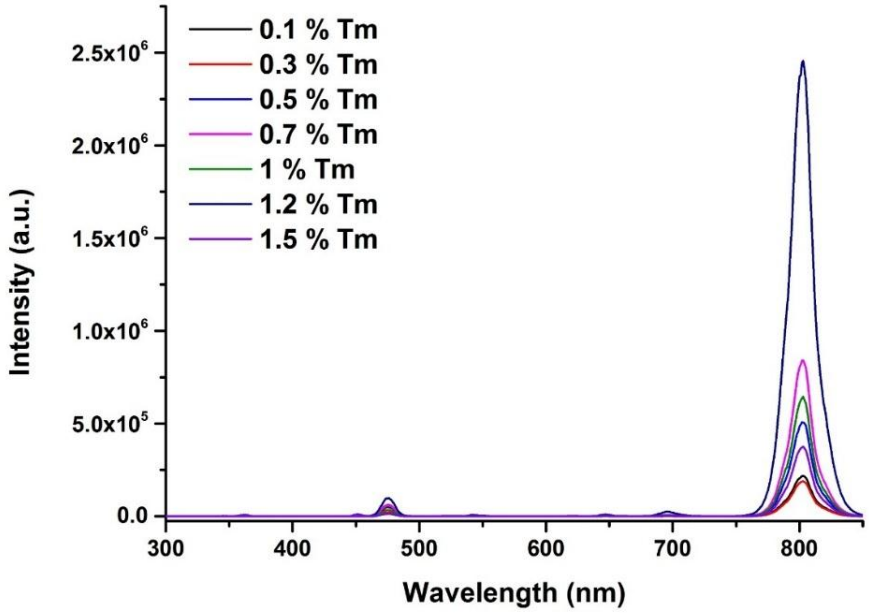

Figure 5.4 UCL spectra of $NaYF_4$:40%Gd,20%Yb,x%Tm core NPs (x = 0.1, 0.3, 0.5, 0.7, 1, 1.2, and 1.5) upon 980 nm CW laser irradiation. The concentration of all samples is 10 mg/mL in cyclohexane.

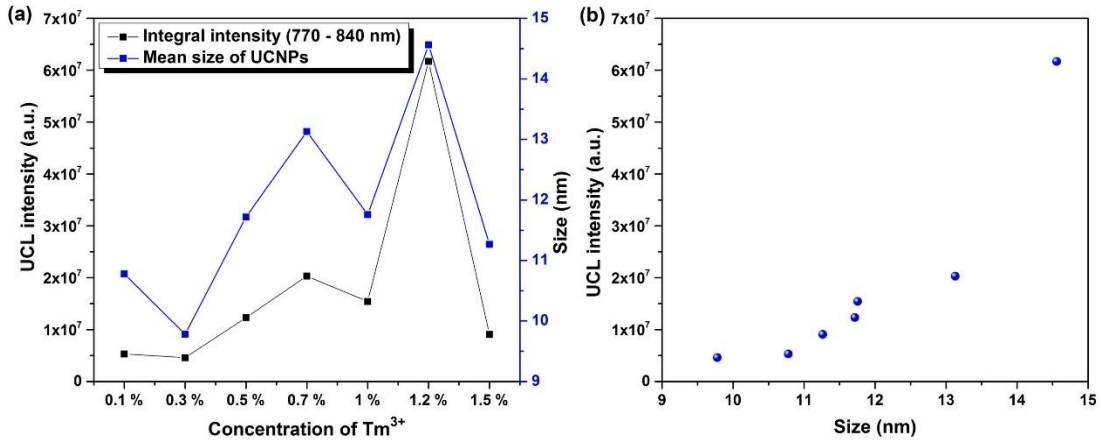

Figure 5.5 (a) Plots of integrated UCL intensities and mean sizes as a function of Tm doping concentration. (b) Plots of UCL intensities as a function of size.

3.3 Construction of core/shell/shell UCNPs

For the sake of construction of $NaYF_4$:40%Gd,20%Yb,1%Tm@$NaYF_4$:10%Yb@$NaYF_4$:10%Yb,20%Nd core/shell/shell UCNPs for time-gated bioimaging application, the $NaYF_4$:40%Gd,20%Yb,1%Tm core NPs were fist synthesized via a high-temperature co-precipitation method, then the first shell $NaYF_4$:10%Yb and the second shell $NaYF_4$:10%Yb,20%Nd were successively synthesized via a heating up strategy, as described in the experimental section (note the doping concentrations were taken from literatures). Figure 5.6a shows the size and morphology changes of the core (C), core/shell (CS), and core/shell/shell UCNPs. All the samples exhibit good dispersity in cyclohexane. The mean sizes were determined to be 16.9 ± 0.8 nm, 21.9 ± 1.2 nm, and 31.3 ± 1.0 nm for core, core/shell, and core/shell/shell UCNPs, respectively. Moreover, the shell thicknesses of the first layer of core/shell and the second layer of core/shell/shell UCNPs were measured to be 2.5 nm and 4.7 nm, respectively. The two layers not only protect the core from surface quenching but also act as bridges for energy transfer by doping Yb^{3+} and Nd^{3+}/Yb^{3+} in these two layers.

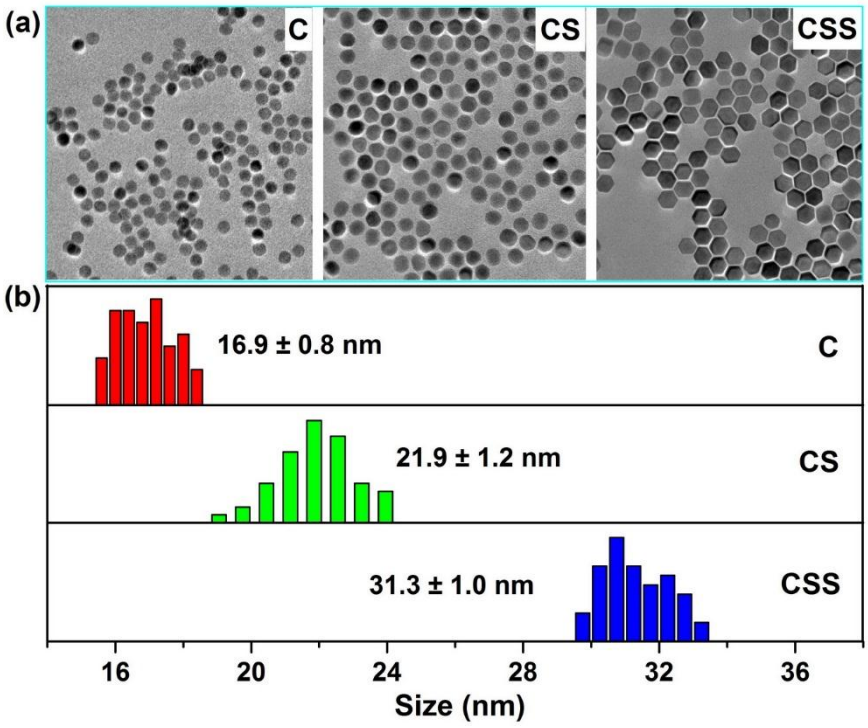

Figure 5.6 (a) TEM images and (b) size distributions of $NaYF_4$:40%Gd,20%Yb,1%Tm (C), $NaYF_4$:40%Gd,20%Yb,1%Tm@$NaYF_4$:10%Yb (CS), and $NaYF_4$:40%Gd,20%Yb,1%Tm@$NaYF_4$:10%Yb@$NaYF_4$:10%Yb,20%Nd (CSS) UCNPs

3.4 Typical upconversion properties

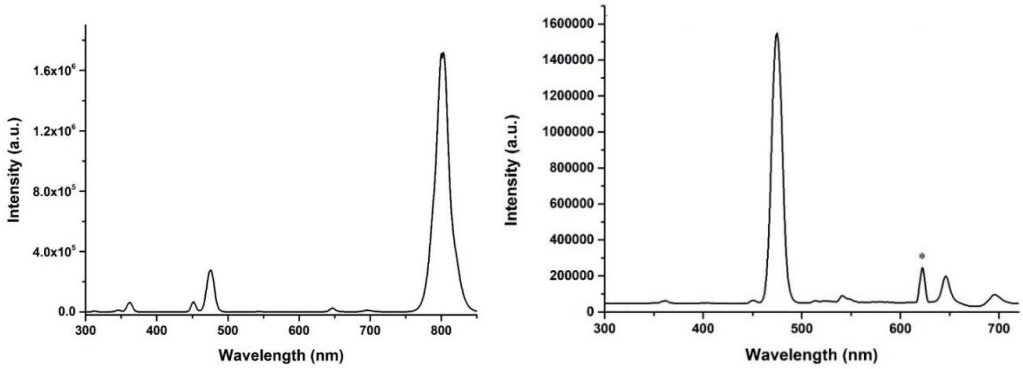

Figure 5.7 UCL spectrum of $NaYF_4$:40%Gd,20%Yb,1%Tm@$NaYF_4$:10%Yb@$NaYF_4$:10%Yb,20%Nd core/shell/shell UCNPs upon 980 nm (left) or 808 nm (right) laser excitation. The peak marked star in the right Figure possibly is ascribed to the impurity scattering light from the laser.

To evaluate the UCL properties of the as-prepared core/shell/shell UCNPs, the UCL spectra were measured upon 980 nm and 808 nm laser excitation. As shown in Figure 5.7, under 980 nm or 808 nm excitation, the Yb^{3+} or Nd^{3+} ions are able to absorb energy, then transfer to the emitter of Tm^{3+} ions, finally the UCNPs display intense luminescence of Tm^{3+}. However, the luminescence intensity ratios (I_{451}/I_{475}) of Tm^{3+} obviously changed because of two different energy transfer processes induced by two different excitation models.

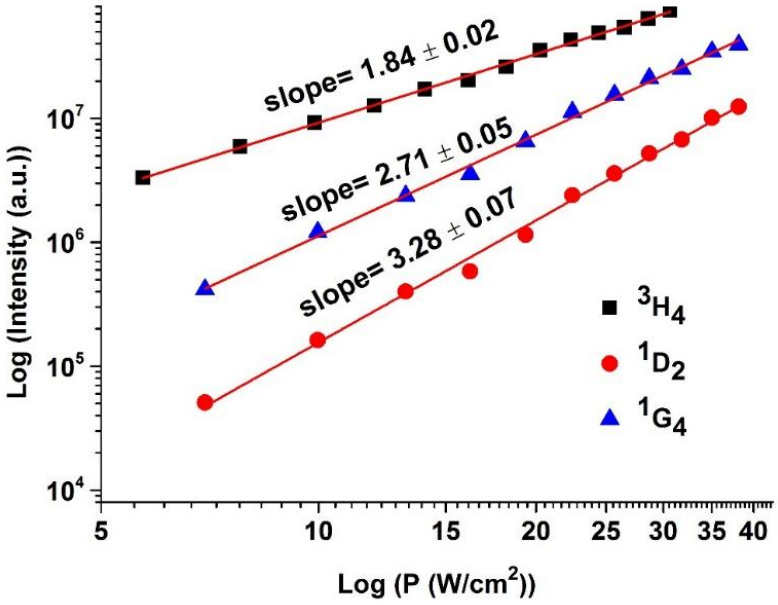

Figure 5.8 Log-log plots of the integrated UCL intensity versus 980 nm laser excitation power density (W/cm^2) for $^1D_2 \rightarrow {}^3F_4$, $^1G_4 \rightarrow {}^3H_6$, and $^3H_4 \rightarrow {}^3H_6$ transitions of Tm^{3+} in $NaYF_4$:40%Gd,20%Yb,1%Tm@$NaYF_4$:10%Yb@$NaYF_4$:10%Yb,20%Nd UCNPs.

In order to further understand the UCL processes, we measured the integrated UCL intensity as a function of power density of 980 nm laser excitation for $^1D_2 \rightarrow {}^3F_4$, $^1G_4 \rightarrow {}^3H_6$, and $^3H_4 \rightarrow {}^3H_6$ transitions of Tm^{3+}. According to the relationship $I \propto P^{(n)}$, where I, P, and n represent luminescence intensity, power density, and pump photons, respectively, the obtained log-log plots in Figure 5.8 were linearly fitted. And the slopes, namely, numbers of pump photons n, were determined to be 1.84 ± 0.02, 2.71 ± 0.05, and 3.28 ± 0.07 which are responsible for the UC emissions ascribed to $^3H_4 \rightarrow {}^3H_6$, $^1G_4 \rightarrow {}^3H_6$, and $^1D_2 \rightarrow {}^3F_4$ transitions of Tm^{3+}, respectively. Therefore, the UC emissions from $^3H_4$, $^1G_4$, and $^1D_2$ are confirmed to be 2, 3, and 4 -photon UC process, respectively. The deviation from the theoretically predicted photon number for the population of $^3H_4$ (2), $^1G_4$ (3), and $^1D_2$ (4) is most probably due to the UC saturation caused by the middle-to-high pump power density regime we employed.[101]

Finally, the UCL decay time curves of emission bands at 475 nm and 800 nm in $NaYF_4$:40%Gd,20%Yb,1%Tm core and $NaYF_4$:40%Gd,20%Yb,1%Tm@$NaYF_4$:10%Yb@$NaYF_4$:10%Yb,20%Nd

core/shell/shell UCNPs were measured as shown in Figure 5.9, by using an OPO pulsed 980 nm laser (pulse width of 5 ns, power of 2 mJ, and frequency of 20 Hz). As those decay curves can be fitted by single-exponential method, so, UCL lifetimes were determined by the single exponential function:

$$I(t) = I_0 \exp(-t/\tau) \quad (5\text{-}1)$$

where *I(t)* denotes the UCL intensity as a function of time *t*, and I_0 represents the the UCL intensity at $t = 0$ and τ represents the lifetime. After the calculations, the UCL lifetimes of 475 nm and 800 nm of Tm^{3+} were determined to increase from 324 ± 3 μs and 338 ± 4 μs in core UCNPs to 568 ± 4 μs and 995 ± 16 μs in core/shell/shell UCNPs, respectively. The prolongation of lifetimes of core/shell/shell UCNPs demonstrates the effective protection of shell from surface quenching.

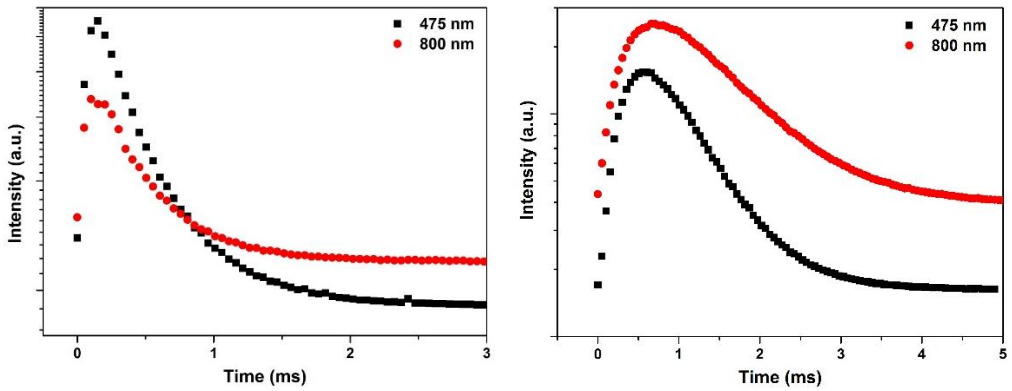

Figure 5.9 UCL lifetimes of emission bands at 475 nm and 800 nm in $NaYF_4$:40%Gd,20%Yb,1%Tm core (left) and $NaYF_4$:40%Gd,20%Yb,1%Tm@$NaYF_4$:10%Yb@$NaYF_4$:10%Yb,20%Nd (right) core/shell/shell UCNPs upon 980 nm pulse laser excitation.

3.5 Time-gated luminescence spectra

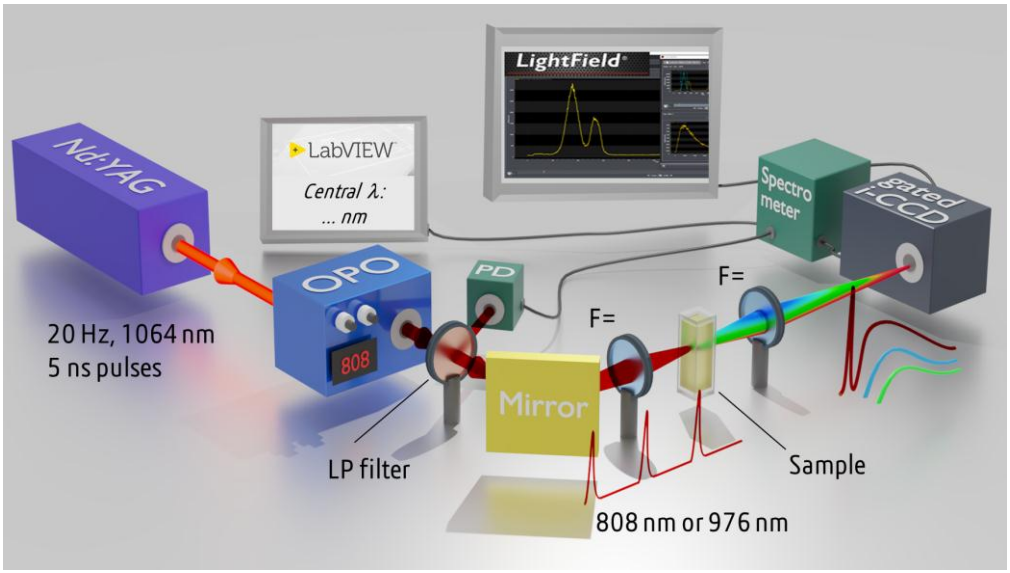

Figure 5.10 Illustration of advanced spectroscopic system in Lille. Nd:YAG: Nd:$Y_3Al_5O_{12}$ crystal. OPO: optical parametric oscillator.

By taking advantage of the established spectroscopic system at LASIRE, University of Lille, we were able to measure time-gated spectrum and lifetimes for the as-prepared $NaYF_4$:40%Gd,20%Yb,1%Tm@$NaYF_4$:10%Yb@$NaYF_4$:10%Yb,20%Nd core/shell/shell UCNPs. Figure 5.10 displays the set-up of the system where 1064 nm pulse laser is first pumped from Nd:YAG laser crystal, then 980 nm or 808 nm pulse laser can be output from OPO. After exciting the UCNPs in suspension, all the lights including laser and emissions from UCNPs are collected by the i-CCD camera, however, with controlling the gate time, the very short pulsed laser (several ns) can be eliminated and the long-lived emission (hundreds μs) from the UCNPs can be detected. Finally, we are able to obtain a time-gated spectrum where the emission range (700~1050 nm) covers the excitation wavelength without any interference.

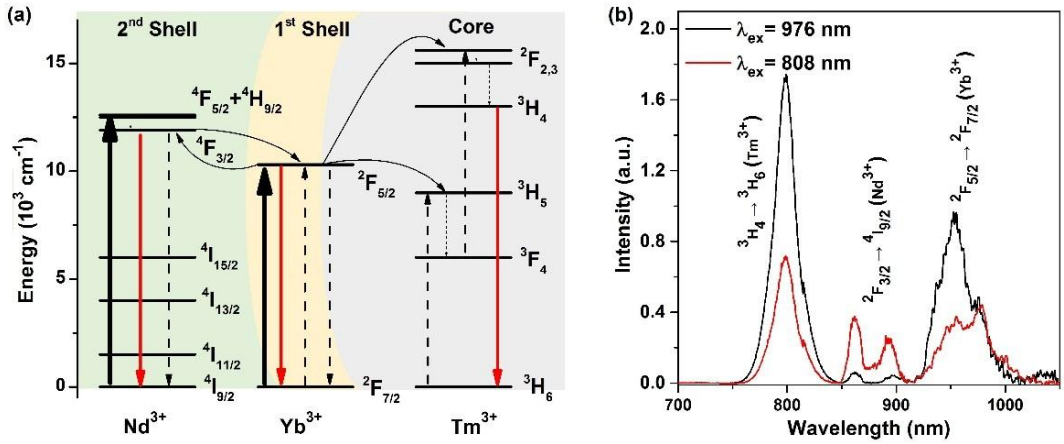

Figure 5.11 UCL (a) scheme and (b) spectra of $NaYF_4$:40%Gd,20%Yb,1%Tm@$NaYF_4$:10%Yb@$NaYF_4$:10%Yb,20%Nd core/shell/shell UCNPs under 980 nm or 808 nm irradiation.

Following that, we measured the time-gated spectra for the $NaYF_4$:40%Gd,20%Yb,1%Tm@$NaYF_4$:10%Yb@$NaYF_4$:10%Yb,20%Nd core/shell/shell UCNPs on the time-gated spectroscopic system. The UCL spectrum with a range of 700~1050 nm was collected upon 980 nm or 808 nm laser irradiation (Figure 5.11b). 3 main emission bands at 800 nm, 864 nm, and 951 nm can be ascribed to $^3H_4 \rightarrow {}^3H_6$ (Tm^{3+}), $^2F_{3/2} \rightarrow {}^4I_{9/2}$ (Nd^{3+}), and $^2F_{5/2} \rightarrow {}^2F_{7/2}$ (Yb^{3+}) transition, respectively. The detailed luminescence process is shown in Figure 5.11a, typically, when 980 nm laser is used, the Yb^{3+} sensitizer absorbs energy and is excited to $^2F_{5/2}$; the energy of excited Yb^{3+} then is transferred to an adjacent Tm^{3+}; once Tm^{3+} is excited to $^3H_5$ through ground state absorption (GSA), the population of $^3F_4$ occurs through non-radiative relaxation from $^3H_5$; $^3F_4$ can be further excited to higher energy level $^2F_{2,3}$ through absorption of another pump photon from Yb^{3+} (excited state absorption, ESA), thus enabling the population of $^3H_4$ through non-radiative relaxation and its near infrared emission at ~800 nm.

Meanwhile, in the second shell, $^4F_{3/2}$ of Nd^{3+} can be excited through phonon-assisted back energy transfer (BET) from excited Yb^{3+} thus leading to the radiative transition of $^4F_{3/2} \rightarrow {}^4I_{9/2}$.[324] Besides, the excited Yb^{3+} can directly emit single photon by transition

of $^2F_{5/2} \rightarrow {}^2F_{7/2}$.

Differently, when the 808 nm laser is utilized as excitation source, the ground $^4F_{5/2}$ state of Nd^{3+} is firstly excited, thus, enabling the population of $^4F_{3/2}$ of Nd^{3+} through non-radiative relaxation; the energy of excited Nd^{3+} is transferred to an adjacent Yb^{3+} in the second shell and further transferred to the Yb^{3+} in the first shell and core through energy migration (EM) process, finally to Tm^{3+}. The process has to be repeated at least once to enable 800 nm emission, and several times for other emissions from Tm^{3+}.

3.6 Lifetimes

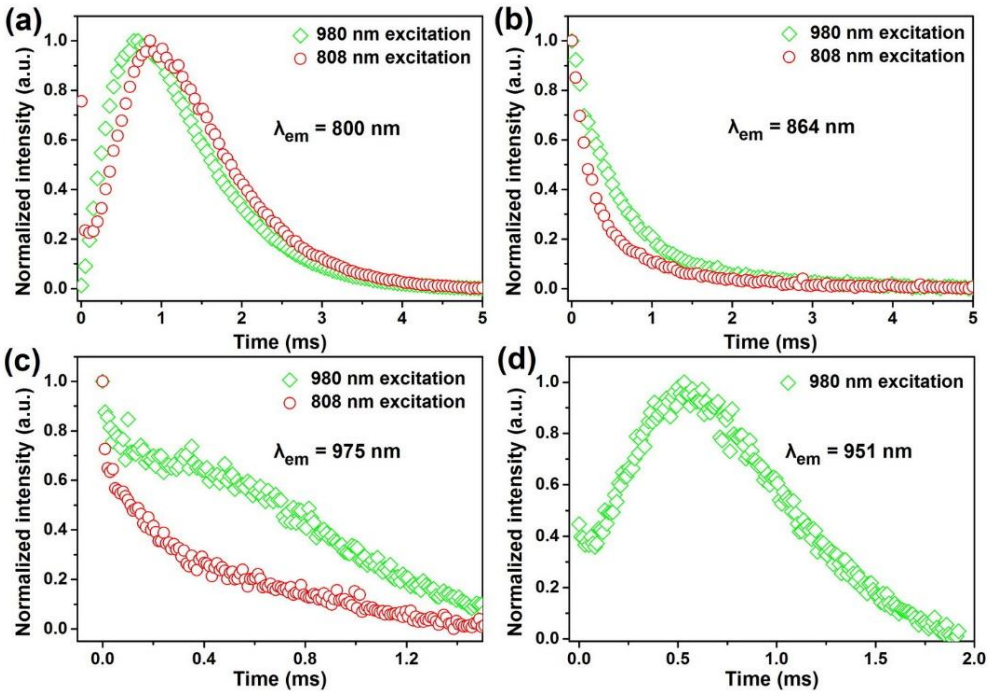

Figure 5.12 Decays of (a) $^3H_4$ of Tm^{3+}, (b) $^2F_{3/2}$ of Nd^{3+}, and (c, d) $^2F_{5/2}$ of Yb^{3+} in $NaYF_4$:40%Gd,20%Yb,1%Tm@$NaYF_4$:10%Yb@$NaYF_4$:10%Yb,20%Nd core/shell/shell UCNPs under 980 nm or 808 nm pulse laser irradiation.

For further investigation on the NIR luminescence of the core/shell/shell UCNPs, the emission decays of Tm^{3+}, Nd^{3+}, and Yb^{3+} upon 980 nm or 808 nm laser excitation were recorded and depicted in Figure 5.12. Upon fitting all of the decay curves by a single exponential function as described above, lifetimes values of Tm^{3+}, Nd^{3+}, and Yb^{3+} emitting states were calculated. The lifetime values of $^3H_4$ state of Tm^{3+} upon 980 nm

and 808 nm laser excitation were determined to be 995 ± 16 μs and 1047 ± 35 μs, respectively. Similarly, the lifetimes were determined to be 647 ± 6 μs and 512 ± 13 μs of $^2F_{3/2}$ of Nd^{3+}, 1147 ± 78 μs and 336 ± 32 μs of $^2F_{3/2}$ of Yb^{3+}, upon 980 nm and 808 nm laser excitation, respectively. Additionally, by monitoring the emission peak of 951 nm, its lifetime was determined to be 1063 ± 87 μs which is very close to the lifetime of 975 nm since these two emission bands originate from the same $^2F_{3/2}$ energy level of Yb^{3+}.

Interestingly, it is found that the lifetime of $^3H_4$ state of Tm^{3+} upon 980 nm laser excitation is slightly longer than that upon 808 nm laser excitation. This result indicates the high energy transfer efficiency of path $Nd^{3+} \rightarrow Yb^{3+} \rightarrow Tm^{3+}$. In fact, the absorption cross section at 808 nm of Nd^{3+} (2×10^{-20} cm^2) [264] is about 7 times larger than that of Yb^{3+} at 980 nm (0.3×10^{-20} cm^2)[264, 325] in $LiYF_4$ crystal, as a reference; on the other hand, the $Nd^{3+} \rightarrow Yb^{3+}$ energy transfer efficiency (calculation is based on the Nd^{3+} luminescence decays in the case of single- or co- doping in the host) is very high up to 95% in Ba-Al-metaphosphate glasses[326], as an example. Moreover, the addition of inner shell (1st shell in Figure 5.11a) prevents the cross relaxation between Nd^{3+} and Tm^{3+}. Taken together, the lifetimes of $^3H_4$ state of Tm^{3+} upon both 980 nm and 808 nm excitation have very small difference although there are more energy transfer steps and longer distance of the path $Nd^{3+} \rightarrow Yb^{3+} \rightarrow Tm^{3+}$ than the path $Yb^{3+} \rightarrow Tm^{3+}$. Additionally, the lifetime of $^2F_{3/2}$ of Yb^{3+} upon 808 nm is shorter than upon 980 nm excitation, which is because the lifetime of Yb^{3+} is associated with the short lifetime of $^2F_{3/2}$ of Nd^{3+}.

In a word, the long lifetime of $^3H_4$ state of Tm^{3+} upon 808 nm excitation enables a great advantage of the promising time-gated imaging application in our concept.

3.7 Confocal bioimaging

In order to prove the bioimaging application for our $NaYF_4$:40%Gd,20%Yb,1%Tm@$NaYF_4$:10%Yb@$NaYF_4$:10%Yb,20%Nd core/shell/shell UCNPs, we implemented the cell in-vivo imaging experiments through

confocal imaging microscope. To render the core/shell/shell UCNPs hydrophilic, the oleic acid molecules of the UCNPs' surface were first replaced by BF^- through ligand exchange method, then, PVP was coated on the OA-free UCNPs. The as-prepared PVP-coated UCNPs were dispersed in water for future use.

HCT-116 cells were incubated with organic dye Hoechst for 48 h, then further incubated with PVP-coated UCNPs (10 μg/mL) for 6 h. Finally, the cells were fixed on the slides and mounted. As shown in Figure 5.13a, upon 980 nm pulse laser irradiation, we were able to detect intense visible light (blue colour) which was originated from emission of Tm^{3+} in the UCNPs. In addition, upon 405 nm irradiation, the luminescence (red colour) of Hoechst dye from all the cells was detected (Figure 5.13b) as the Hoechst dye was able to stain the cell nucleus. By merging those two photos, we can clearly see the resulting visible light of UCNPs under 980 nm laser is from inside of the cells, which implies the successful incubation with UCNPs.

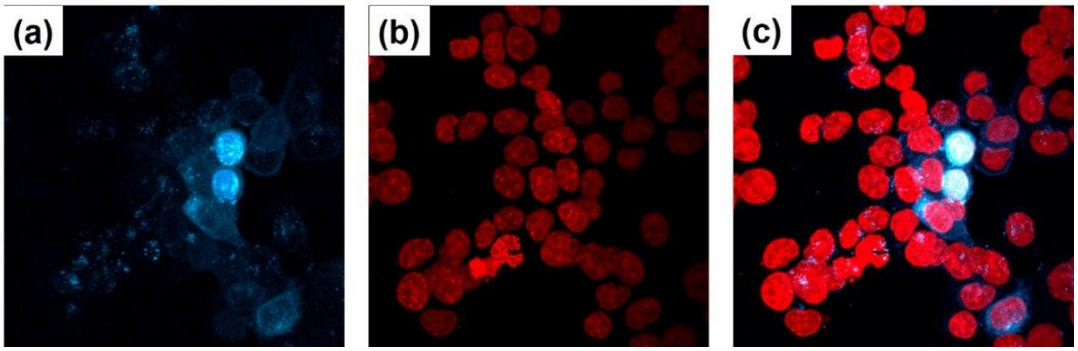

Figure 5.13 Images of cells under confocal microscope. (a) upon 980 nm femtosecond-pulsed, MHz, laser irradiation with a detection range below 750 nm; (b) upon 405 nm excitation with a detection range of 415~730 nm; (c) overlapping of (a) and (b).

To conclude, the as-prepared cells on the slides have been demonstrated successful incubation with UCNPs and can be further used for time-gated bioimaging. However, by lack of time and well-established set-up as well as our collaborators are ready, we are unable to realise the observation of this complex same wavelength excitation and emission scheme. It should be happening in the next few months but it is untimely for this thesis.

4 Conclusions

In this chapter, we first present the synthesis and characterizations of $NaYF_4$:40%Gd,20%Yb,x%Tm (x = 0.1, 0.3, 0.5, 0.7, 1, 1.2, and 1.5) UCNPs with different Tm concentration in sections 3.1 and 3.2. TEM results show that those UCNPs are monodisperse and spherical with size from 9.8 ± 1.1 nm to 14.6 ± 0.9 nm with a size difference of ~5 nm. The UCL spectra of those UCNPs show the UCL intensity is positively associated with nanoparticle size, however, not associated with Tm concentration. These results demonstrate that we should be careful when comparing a series samples with different concentrations of doping elements. The effect of the size is an important factor and cannot be ignored as well, especially when the size of nanoparticle is in nanoscale.

In sections 3.3 and 3.4, ~31 nm of $NaYF_4$:40%Gd,20%Yb,1%Tm@$NaYF_4$:10%Yb@$NaYF_4$:10%Yb,20%Nd core/shell/shell UCNPs are synthesized through high-temperature co-precipitation method. Under 980 nm or 800 nm CW laser irradiation, the core/shell/shell UCNPs exhibits intense emission of Tm^{3+}. The UC emissions from $^3H_4$, $^1G_4$, and $^1D_2$ are confirmed to be 2, 3, and 4 -photon UC process by the power-dependent UCL spectra. The UCL lifetimes of 475 nm and 800 nm of Tm^{3+} were determined to increase from 324 ± 3 μs and 338 ± 4 μs in core UCNPs to 568 ± 4 μs and 995 ± 16 μs in core/shell/shell UCNPs, respectively, dedicating effective shell protection from surface quenching.

In section 3.5, the time-gated spectra are measured for the as-prepared core/shell/shell UCNPs upon 980 nm and 808 nm pulse laser excitation. The emission processes of Tm^{3+}, Nd^{3+}, and Yb^{3+} in the NIR range of 700~1050 nm, are discussed carefully.

Furthermore, in section 3.6, the lifetimes of Tm^{3+}, Nd^{3+}, and Yb^{3+} in the NIR range of 700~1050 nm are recorded. Either upon 980 nm or 808 nm excitation, the lifetime of $^3H_4$ of Tm^{3+} keeps almost the same, enabling a great advantage of the promising

time-gated imaging application in our concept.

In section 3.7, the PVP-coated core/shell/shell UCNPs are prepared and incubated with HCT-116 cells. Then, via confocal microscope, we obtain images of cells under 980 nm and 405 nm irradiation, which shows the successful incubation with our UCNPs. These fixed cells on the slide can be further used for time-gated imaging when our home-made time-gated set up is completely established.

Chapter VI: Conclusions and perspectives

The objective of this thesis is to synthesize small-sized and highly efficient lanthanide-doped luminescent nanoparticles (NPs) for bioimaging applications.

In chapter 2, we demonstrate a versatile strategy for synthesizing 15 kinds of ultrasmall rare-earth oxysulfide (RE_2O_2S) NPs with size from 3 to 11 nm. In this strategy, a new compound named DPTU is for the first time used as sulphur source and LiOH is used as an additive to synthesize RE_2O_2S. Various reaction conditions including solvent ratio, amount of DPTU, reaction temperature and time, are carefully optimized to synthesize monodisperse and crystalized Gd_2O_2S NPs. However, the size of Gd_2O_2S NPs can be only tuned in a small range, which could be attributed to the fast growth process of the NPs originating from the high-speed consumption of sulphur source. Hence, the further step of preparing larger NPs will focus on how to precisely control the decomposition speed of DPTU.

To acquire multi modalities (NIR-II luminescence, magnetic, computed tomography, and photoacoustic performances), we further synthesize a series of Nd-doped Gd_2O_2S NPs with varying concentration. Under 808 nm laser irradiation, the sample Gd_2O_2S:60%Nd performs the highest NIR-II luminescence intensity. The hydrophilic PVP-coated Gd_2O_2S:60%Nd NPs high yields, and an excellent water solubility are further prepared by a facile ligand exchange method. Cytotoxicity study shows very low toxicity of as-prepared PVP-coated Gd_2O_2S:60%Nd NPs. We believe this method can be also extended to synthesis of other hydrophilic RE_2O_2S NPs.

Using these PVP-coated Gd_2O_2S:60%Nd NPs, we perform multimodal imaging experiments. NIR-II luminescence imaging experiments demonstrate that an optical penetration of 2.4 mm is determined for the NPs. Besides, the NPs show ability of both T_1 and T_2 weighted magnetic resonance imaging (MRI). CT-imaging experiments show the NPs have effective absorption ability of X-ray, which confirms the promising application of CT contrast agents. The clear contrast can be detected beyond ~2 mg/mL of NPs concentration. Photoacoustic imaging experiments demonstrate that the NPs can be used as ultrasound reagents. The future experiments would be applying the NPs for

vivo multimodal imaging for instance in cells, tissues, or live animals.

In chapter 3, we successfully construct a new class of heterogeneous RE_2O_2S@$NaREF_4$ core/shell nanoparticle. ~4 nm $NaYF_4$ shell is deposited on the ~6 nm Gd_2O_2S:20%Yb,1%Tm core nanoparticle. By HRTEM, HAADF, EELS, and element mapping analyses, we confirm the core/shell structure of Gd_2O_2S:20%Yb,1%Tm@$NaYF_4$. Importantly, other 14 kinds of Gd_2O_2S:20%Yb,1%Tm@$NaREF_4$ (RE = La, Ce, Pr, Nd, Sm, Eu, Gd, Tb, Dy, Ho, Er, Tm, Yb, and Lu) with size ranging from 11 nm to 27 nm are prepared by the same synthesis approach with optimal conditions. It demonstrates versatility of this method for synthesis of RE_2O_2S@$NaREF_4$. When we consider the 15 kinds of RE_2O_2S we have already obtained from chapter 2, it seems possible to construct 225 kinds of RE_2O_2S@$NaREF_4$ core/shell NPs in total.

By monitoring and analysing the size and phase evolution as a function of reaction time, we propose the growth mechanism for RE_2O_2S@$NaREF_4$ core/shell NPs. The formation processes include 3 stages: in the first stage, cation exchange process leads to the migration of rare earth elements between the solid core NPs and liquid solution, forming an amorphous layer on the core NPs; in the second stage, with rising temperature, α-$NaYF_4$ phase appears at 250 °C; finally, the α-$NaYF_4$ phase quickly disappears and β-$NaYF_4$ phase occurs, consequently, β-$NaYF_4$ deposits on the core NPs due to small lattice mismatch. This mechanism helps us understand the formation processes, still, the basic growth dynamics need to be explored.

The optical properties for the lanthanide doped core and core/shell UCNPs are systematically evaluated. For example, 836 and 4922 -fold enhancement for UCL intensities of Gd_2O_2S:20%Yb,1%Tm@$NaYF_4$ and Gd_2O_2S:20%Yb,2%Er@$NaYF_4$ are obtained compared to that of their corresponding cores. It is recorded that the lifetimes of 469 nm and 803 nm are increased from 8 μs and 5 μs of Gd_2O_2S:20%Yb,1%Tm core to 919 μs and 997 μs of Gd_2O_2S:20%Yb,1%Tm@$NaYF_4$ core/shell, respectively. The lifetimes of 520 nm, 540 nm, and 652 nm of Gd_2O_2S:20%Yb,2%Er@$NaYF_4$ are

determined to be 305 μs, 316 μs, and 351 μs, respectively. Finally, the power dependent UCQYs are measured for Gd_2O_2S:20%Yb,1%Tm@$NaYF_4$, Gd_2O_2S:20%Yb,2%Er@$NaYF_4$, and Gd_2O_2S:20%Yb,2%Er@$NaGdF_4$. The maximum UCQYs value with ~0.76% for Gd_2O_2S:20%Yb,1%Tm@$NaYF_4$ is recorded at a power density of 155 W/cm^2. These UCL properties of the core/shell UCNPs compete with those of other reported UCNPs with similar size, showing efficient UCL of the core/shell UCNPs for further applications.

Besides, we systematically investigate the UCL properties of Gd_2O_2S:20%Yb,x%Er@$NaYF_4$ (x = 1, 2, 5, 10, and 15) UCNPs. By analysing TEM images of Gd_2O_2S:20%Yb,x%Er core and Gd_2O_2S:20%Yb,x%Er@$NaYF_4$ core/shell UCNPs, we compare the size and the shell thickness of core/shell UCNPs. ICP-OES measurements reveal the composition of the core/shell UCNPs. The UCL spectra show the 2% Er sample has the most intense luminescence. The lifetimes of the core/shell UCNPs at 540 nm display that the lifetime declines as the Er concentration increases. UCQYs show that the 1% Er sample has the highest UCQYs values when the power density is below 57 W/cm^2, whereas, in the range of 83~155 W/cm^2, it has lower UCQYs values than the 2% Er sample at the same power density.

At the end of this chapter, a two-step surface modification is applied for Gd_2O_2S:20%Yb,2%Er@$NaYF_4$ core/shell UCNPs. In terms of that, we prepare PVP and alendronate -coated UCNPs. TEM images and DLS results show the good dispersity and size. On the one hand, these results are still preliminary that we need to further optimize the parameters in the process to obtain monodisperse hydrophilic NPs; on the other hand, we need characterize the optical properties for these hydrophilic NPs before using them for applications. And most importantly, the NPs for future applications such as bioimaging have to be carried out.

In Chapter 4, we carefully analyse temperature-dependent UCL spectra for lanthanide-doped Gd_2O_2S@$NaREF_4$ core/shell UCNPs. Based on those spectra, we discuss the possible mechanism based on water desorption process at elevated

temperatures accounting for the thermal UCL enhancement phenomenon of lanthanide-doped Gd_2O_2S@$NaREF_4$ core/shell UCNPs. Then the variation of ratio I_{652}/I_{540} of Yb^{3+}/Er^{3+} doped Gd_2O_2S@$NaREF_4$ core/shell UCNPs with increasing temperature is found and explained by comparing the thermal expansion coefficient of core and core/shell UCNPs. Firstly, the lattice mismatch between core and shell produces tensile stress and the tensile stress would linearly decline with rising temperature, thus leading the linear increase of the ratio I_{652}/I_{540} in the temperature range of 293~423 K; as the temperature further elevates, the tensile stress disappears due to the higher lattice expansion rate of shell than core, hence no change of the ratio is observed. Finally, the fluorescence declines as temperature continues increasing which is ascribed to the appearance of compressive stress. Although this mechanism seems to explain the variation of ratio I_{652}/I_{540} of Yb^{3+}/Er^{3+} doped Gd_2O_2S@$NaREF_4$ core/shell UCNPs, further confirmation of this mechanism in other similar core/shell structures is required.

Based on the temperature-dependent UCL spectra, we study the thermal sensitivities of lanthanide doped Gd_2O_2S@$NaREF_4$ core/shell UCNPs. The maximum S_r values are calculated to be 3.9 $\%K^{-1}$ and 3.3 $\%K^{-1}$ for Yb/Tm doped Gd_2O_2S@$NaYF_4$ and Gd_2O_2S@$NaLuF_4$, respectively, and 1.13 $\%K^{-1}$ for Yb/Er doped Gd_2O_2S@$NaYF_4$. These S_r values are quite high as compared to the Sr of other systems, showing a great potential nano-thermometry application for the lanthanide doped Gd_2O_2S@$NaREF_4$ core/shell UCNPs.

In Chapter 5, we synthesize a series of $NaYF_4$:40%Gd,20%Yb,x%Tm (x = 0.1, 0.3, 0.5, 0.7, 1, 1.2, and 1.5) UCNPs with size from 9.8 ± 1.1 nm to 14.6 ± 0.9 nm with a wide size distribution of ~5 nm. The UCL spectra of those UCNPs show the UCL intensity is positively associated with nanoparticle size, however, not associated with Tm concentration. These results demonstrate that we should be careful when comparing a series samples with different concentrations of doping elements. The effect of the size is an important factor and cannot be ignored as well, especially when the size of nanoparticle is in nanoscale.

Using the obtained $NaYF_4$:40%Gd,20%Yb,1%Tm as core, ~31 nm of $NaYF_4$:40%Gd,20%Yb,1%Tm@$NaYF_4$:10%Yb@$NaYF_4$:10%Yb,20%Nd core/shell/shell UCNPs are synthesized through high-temperature co-precipitation method. Under 980 nm or 800 nm CW laser irradiation, the core/shell/shell UCNPs exhibits intense emission of Tm^{3+}. The UC emissions from $^3H_4$, $^1G_4$, and $^1D_2$ are confirmed to be 2, 3, and 4 -photon UC process by the power-dependent UCL spectra. The UCL lifetimes of 475 nm and 800 nm of Tm^{3+} were determined to increase from 324 ± 3 μs and 338 ± 4 μs in core UCNPs to 568 ± 4 μs and 995 ± 16 μs in core/shell/shell UCNPs, respectively, dedicating effective shell protection from surface quenching. Then, upon 980 nm and 808 nm pulse laser excitation, the time-gated spectra are measured for the as-prepared core/shell/shell UCNPs. The emission processes of Tm^{3+}, Nd^{3+}, and Yb^{3+} in the NIR range of 700~1050 nm, are discussed carefully. Furthermore, the lifetimes of Tm^{3+}, Nd^{3+}, and Yb^{3+} in the NIR range of 700~1050 nm are recorded. Either upon 980 nm or 808 nm excitation, the lifetime of $^3H_4$ of Tm^{3+} keeps almost the same, enabling a great advantage of the promising time-gated imaging application in our concept.

Following, the PVP-coated core/shell/shell UCNPs are prepared and incubated with HCT-116 cells. Through confocal microscope, we obtain images of cells under 980 nm and 405 nm irradiation, which shows the successful incubation with our UCNPs. These fixed cells on the slide can be further used for time-gated imaging. However, because of the limitation of the unestablished time-gated small animal imaging system, in my project, we have no chance to complete the time-gated imaging experiments for the UCNPs.

In conclusion, in this thesis, we describe a general method for synthesis of rare-earth oxysulfide and rare-earth oxysulfide@sodium rare-earth fluoride NPs, respectively. Their optical, magnetic, and photoacoustic properties are widely characterized. Effective surface modification methods are successfully adopted for the NPs. The proof concept applications such as multimodal imaging and temperature sensing are

completed for the as-prepared NPs.

Bibliography

1. Khan, I.; Saeed, K.; Khan, I., Nanoparticles: Properties, applications and toxicities. *Arab. J. Chem.* **2019,** *12*, 908-931.

2. Heuer-Jungemann, A.; Feliu, N.; Bakaimi, I.; Hamaly, M.; Alkilany, A.; Chakraborty, I.; Masood, A.; Casula, M. F.; Kostopoulou, A.; Oh, E.; Susumu, K.; Stewart, M. H.; Medintz, I. L.; Stratakis, E.; Parak, W. J.; Kanaras, A. G., The Role of Ligands in the Chemical Synthesis and Applications of Inorganic Nanoparticles. *Chem. Rev.* **2019,** *119*, 4819-4880.

3. Steckiewicz, K. P.; Inkielewicz-Stepniak, I., Modified Nanoparticles as Potential Agents in Bone Diseases: Cancer and Implant-Related Complications. *Nanomaterials* **2020,** *10*, 658.

4. Houshmand, M.; Garello, F.; Circosta, P.; Stefania, R.; Aime, S.; Saglio, G.; Giachino, C., Nanocarriers as Magic Bullets in the Treatment of Leukemia. *Nanomaterials* **2020,** *10*, 276.

5. Benyettou, F.; Motte, L., Nanomedicine: Towards the "Magic Bullet" Science. *J. Bioanal. Biomed.* **2016,** *8* (2), 1000e137.

6. Y., T. S.; S., G., Paul Ehrlich (1854-1915): man with the magic bullet. *Singapore Med J* **2010,** *51 (11)*.

7. Kreuter, J., Nanoparticles—a historical perspective. *Int. J. Pharm.* **2007,** *331*, 1-10.

8. Standardization, I. O. f., Nanotechnologies — Vocabulary In *Part 2: Nano-objects*, 2015.

9. Union, C. o. t. E., COMMISSION RECOMMENDATION of 18 October 2011 on the definition of nanomaterial. Official Journal of the European Union: Brussels, 2011; pp L 275/38-40.

10. Bleeker, E. A. J.; Cassee, F. R.; Geertsma, R. E.; Jong, W. H. d.; Heugens, E. H. W.; Koers-Jacquemijns, M.; Meent, D. v. d.; Oomen, A. G.; Popma, J.; Rietveld, A. G.; Wijnhoven, S. W. P., Interpretation and implications of the European Commission Recommendation on the definition of nanomaterial. *RIVM Letter report* **2012**.

11. Nam, J.; Won, N.; Bang, J.; Jin, H.; Park, J.; Jung, S.; Jung, S.; Park, Y.; Kim, S., Surface engineering of inorganic nanoparticles for imaging and therapy. *Adv. Drug Del. Rev.*

2013, *65*, 622-648.

12. Jeong, U.; Teng, X.; Wang, Y.; Yang, H.; Xia, Y., Superparamagnetic Colloids: Controlled Synthesis and Niche Applications. *Adv. Mater.* **2007,** *19*, 33-60.

13. Sun, S.; Murray, C. B., Synthesis of monodisperse cobalt nanocrystals and their assembly into magnetic superlattices (invited). *J. Appl. Phys.* **1999,** *85*, 4325-4330.

14. Hyeon, T.; Lee, S. S.; Park, J.; Chung, Y.; Na, H. B., Synthesis of Highly Crystalline and Monodisperse Maghemite Nanocrystallites without a Size-Selection Process. *J. Am. Chem. Soc.* **2001,** *123*, 12798-12801.

15. Dumestre, F.; Chaudret, B.; Amiens, C.; Renaud, P.; Fejes, P., Superlattices of Iron Nanocubes Synthesized from $Fe[N(SiMe_3)_2]_2$. *Science* **2004,** *303*, 821-823.

16. Chen, M.; Liu, J. P.; Sun, S., One-Step Synthesis of FePt Nanoparticles with Tunable Size. *J. Am. Chem. Soc.* **2004,** *126*, 8394-8395.

17. Chena, M.; Nikles, D. E., Synthesis of spherical FePd and CoPt nanoparticles. *J. Appl. Phys.* **2002,** *91*, 8477-8479.

18. Shevchenko, E. V.; Talapin, D. V.; Schnablegger, H.; Kornowski, A.; Festin, O.; Svedlindh, P.; Haase, M.; Weller, H., Study of Nucleation and Growth in the Organometallic Synthesis of Magnetic Alloy Nanocrystals: The Role of Nucleation Rate in Size Control of $CoPt_3$ Nanocrystals. *J. Am. Chem. Soc.* **2003,** *125*, 9090-9101.

19. Shankar, S. S.; Deka, S., Metal Nanocrystals and Their Applications in Biomedical Systems. *Sci. Adv. Mater.* **2011,** *3*, 169-195.

20. Jain, P. K.; Huang, X.; El-Sayed, I. H.; El-Sayed, M. A., Noble Metals on the Nanoscale: Optical and Photothermal Properties and Some Applications in Imaging, Sensing, Biology, and Medicine. *Acc. Chem. Res.* **2008,** *41*.

21. Jain, P. K.; Lee, K. S.; El-Sayed, I. H.; El-Sayed, M. A., Calculated Absorption and Scattering Properties of Gold Nanoparticles of Different Size, Shape, and Composition: Applications in Biological Imaging and Biomedicine. *J. Phys. Chem. B* **2006,** *110*, 7238-7248.

22. Schultz, S.; Smith, D. R.; Mock, J. J.; Schultz, D. A., Single-target molecule detection with nonbleaching multicolor optical immunolabels. *PNAS* **2000,** *97*, 996-1001.

23. Pache, C.; Bocchio, N. L.; Bouwens, A.; Villiger, M.; Berclaz, C.; Goulley, J.; Gibson, M. I.; Santschi, C.; Lasser, T., Fast three-dimensional imaging of gold nanoparticles in living cells with photothermal optical lock-in Optical Coherence Microscopy. *Opt. Exp.* **2012,** *20*, 21385-21399.

24. Yang, X.; Skrabalak, S. E.; Li, Z.-Y.; Xia, Y.; Wang, L. V., Photoacoustic Tomography of a Rat Cerebral Cortex in vivo with Au Nanocages as an Optical Contrast Agent. *Nano Lett.* **2007,** *7*, 3798-3802.

25. Kim, D.; Park, S.; Lee, J. H.; Jeong, Y. Y.; Jon, S., Antibiofouling Polymer-Coated Gold Nanoparticles as a Contrast Agent for in Vivo X-ray Computed Tomography Imaging. *J. Am. Chem. Soc.* **2007,** *129*, 7661-7665.

26. Chavali, M. S.; Nikolova, M. P., Metal oxide nanoparticles and their applications in nanotechnology. *SN Appl. Sci.* **2019,** *1*, 607.

27. Nikolova, M. P.; Chavali, M. S., Metal Oxide Nanoparticles as Biomedical Materials. *Biomimetics* **2020,** *5*, 27.

28. Zheng, Z.; Huang, B.; Wang, Z.; Guo, M.; Qin, X.; Zhang, X.; Wang, P.; Dai, Y., Crystal Faces of Cu_2O and Their Stabilities in Photocatalytic Reactions. *J. Phys. Chem. C* **2009,** *113*, 14448-14453.

29. Pal, J.; Pal, T., Faceted metal and metal oxide nanoparticles: design, fabrication and catalysis. *Nanoscale* **2015,** *7*, 14159-14190.

30. An-Hui; Lu, E. L. S.; Schuth, F., Magnetic Nanoparticles: Synthesis, Protection, Functionalization, and Application. *Angew. Chem. Int. Ed.* **2007,** *46*, 1222-1244.

31. Verelst, M.; Ely, T. O.; Amiens, C.; Snoeck, E.; Lecante, P.; Mosset, A.; Respaud, M.; Broto, J. M.; Chaudret, B., Synthesis and Characterization of CoO, Co_3O_4, and Mixed Co/CoO Nanoparticules. *Chem. Mater.* **1999,** *11*, 2702-2708.

32. Carnes, C. L.; Stipp, J.; Klabunde, K. J., Synthesis, Characterization, and Adsorption Studies of Nanocrystalline Copper Oxide and Nickel Oxide. *Langmuir* **2002,** *18*, 1352-1359.

33. Lee, G. H.; Huh, S. H.; Jeong, J. W.; Choi, B. J.; Kim, S. H.; Ri, H.-C., Anomalous Magnetic Properties of MnO Nanoclusters. *J. Am. Chem. Soc.* **2002,** *124*, 12094-12095.

34. Lee, J.-H.; Huh, Y.-M.; Jun, Y.-w.; Seo, J.-w.; Jang, J.-t.; Song, H.-T.; Kim, S.; Cho, E.-J.; Yoon, H.-G.; Suh, J.-S.; Cheon, J., Artificially engineered magnetic nanoparticles for ultra-sensitive molecular imaging. *Nat. Med.* **2007,** *13*, 96-99.

35. Lee, J.-H.; Jang, J.-t.; Kim, J.-G.; Kim, I.-S.; Choi, J.-s.; Park, K. I.; Moon, S. H.; Noh, S.-h.; Cheon, J., Exchange-coupled magnetic nanoparticles for efficient heat induction. *Nat. Nanotechnol.* **2011,** *6*, 418-422.

36. Mansur, H. S., Quantum dots and nanocomposites. *WIREs Nanomed. Nanobiotechnol.* **2010,** *2*.

37. Mukai, K., Semiconductor Quantum Dots for Future Optical Applications. *J. Nanosci. Nanotechnol.* **2014,** *14*, 2148-2156.

38. Kagan, C. R.; Lifshitz, E.; Sargent, E. H.; Talapin, D. V., Building devices from colloidal quantum dots. *Science* **2016,** *353*, 885.

39. Wen, L.; Qiu, L.; Wu, Y.; Hu, X.; Zhang, X., Aptamer-Modified Semiconductor Quantum Dots for Biosensing Applications. *Sensors* **2017,** *17*, 1736.

40. Jovin, T. M., Quantum dots finally come of age. *Nat. Biotechnol.* **2003,** *21* (1), 32-33.

41. Gao, J.; Xu, B., Applications of nanomaterials inside cells. *Nano Today* **2009,** *4*, 37-51.

42. E., K., Biologists join the dots. *Nature* **2001,** *413*, 450-452.

43. Michalet, X.; Pinaud, F.; Dahan, M.; Bruchez, M. P.; Lacoste, T. D.; Alivisatos, A. P.; Weiss, S., Properties of Fluorescent Semiconductor Nanocrystals and their Application to Biological Labeling. *Single Mol.* **2001,** *4*, 261-276.

44. Erathodiyil, N.; Ying, J. Y., Functionalization of Inorganic Nanoparticles for Bioimaging Applications. *Acc. Chem. Res.* **2011,** *44*, 925-935.

45. Kokorina, A. A.; Ermakov, A. V.; Abramova, A. M.; Goryacheva, I. Y.; Sukhorukov, G. B., Carbon Nanoparticles and Materials on Their Basis. *Colloids Interfaces* **2020,** *4*, 42.

46. Patel, K. D.; Singh, R. K.; Kim, H.-W., Carbon-based nanomaterials as an emerging platform for theranostics. *Mater. Horiz.* **2019,** *6*, 434-469.

47. Maiti, D.; Tong, X.; Mou, X.; Yang, K., Carbon-Based Nanomaterials for Biomedical Applications: A Recent Study. *Front. Pharmacol.* **2019,** *9*, 1401.

48. Yin, L.; Zhou, H.; Lian, L.; Yan, S.; Song, W., Effects of C_{60} on the Photochemical Formation of Reactive Oxygen Species from Natural Organic Matter. *Environ. Sci. Technol.* **2016,** *50*, 11742-11751.

49. Lucky, S. S.; Soo, K. C.; Zhang, Y., Nanoparticles in Photodynamic Therapy. *Chem. Rev.* **2015,** *115*, 1990-2042.

50. Fan, Y.; Liu, H.; Han, R.; Huang, L.; Shi, H.; Sha, Y.; Jiang, Y., Extremely High Brightness from Polymer-Encapsulated Quantum Dots for Two-photon Cellular and Deep-tissue Imaging. *Sci. Rep.* **2015,** *5*, 9908.

51. Li, C.; Chou, T.-W., Elastic moduli of multi-walled carbon nanotubes and the effect of van der Waals forces. *Compos. Sci. Technol.* **2003,** *63*, 1517-1524.

52. Zhbanov, A. I.; Pogorelov, E. G.; Chang, Y.-C., Van der Waals Interaction between Two Crossed Carbon Nanotubes. *ACS Nano* **2010,** *10*, 5937-5945.

53. Niyogi, S.; Hamon, M. A.; Hu, H.; Zhao, B.; Bhowmik, P.; Sen, R.; Itkis, M. E.; Haddon, R. C., Chemistry of Single-Walled Carbon Nanotubes. *Acc. Chem. Res.* **2002,** *35*, 1105-1113.

54. Star, A.; Stoddart, F.; Steuerman, D.; Diehl, M.; Boukai, A.; Wong, E. W.; Yang, X.; Chung, S.-W.; Choi, H.; Heath, J. R., Preparation and Properties of PolymerWrapped Single-Walled Carbon Nanotubes. *Angew. Chem. Int. Ed.* **2001,** *40*, 1721-1725.

55. Meng, L.; Fu, C.; Lu, Q., Advanced technology for functionalization of carbon nanotubes. *Prog. Nat. Sci.* **2009,** *19*, 801-810.

56. Liu, J.-H.; Cao, L.; LeCroy, G. E.; Wang, P.; Meziani, M. J.; Dong, Y.; Liu, Y.; Luo, P. G.; Sun, Y.-P., Carbon "Quantum" Dots for Fluorescence Labeling of Cells. *ACS Appl. Mater. Interfaces* **2015,** *7*, 19439-19445.

57. Xiao, D.; Yuan, D.; He, H.; Lu, J., Microwave-assisted one-step green synthesis of amino-functionalized fluorescent carbon nitride dots from chitosan. *Luminescence* **2013,** *28*, 612-615.

58. Liang, Q.; Ma, W.; Shi, Y.; Li, Z.; Yang, X., Easy synthesis of highly fluorescent

carbon quantum dots from gelatin and their luminescent properties and applications. *Carbon* **2013,** *60*, 421-428.

59. Zhou, J.; Sheng, Z.; Han, H.; Zou, M.; Li, C., Facile synthesis of fluorescent carbon dots using watermelon peel as a carbon source. *Mater. Lett.* **2012,** *6*, 222–224.

60. Sachdeva, A.; Gopinath, P., Green synthesis of multifunctional carbon dots from coriander leaves and their potential application as antioxidants, sensors and bioimaging agents. *Analyst* **2015,** *140*, 4260-4269.

61. Sun, Y.-P.; Zhou, B.; Lin, Y.; Wang, W.; Fernando, K. A. S.; Pathak, P.; Meziani, M. J.; Harruff, B. A.; Wang, X.; Wang, H.; Luo, P. G.; Yang, H.; Kose, M. E.; Chen, B.; Veca, L. M.; Xie, S.-Y., Quantum-Sized Carbon Dots for Bright and Colorful Photoluminescence. *J. Am. Chem. Soc.* **2006,** *128*, 7756-7757.

62. Zhai, X.; Zhang, P.; Liu, C.; Bai, T.; Li, W.; Dai, L.; Liu, W., Highly luminescent carbon nanodots by microwave-assisted pyrolysis. *Chem. Commun.* **2012,** *48*, 7955-7957.

63. Qiao, Z.-A.; Wang, Y.; Gao, Y.; Li, H.; Dai, T.; Liua, Y.; Huo, Q., Commercially activated carbon as the source for producing multicolor photoluminescent carbon dots by chemical oxidation. *Chem. Commun.* **2010,** *46*, 8812-8814.

64. Zhang, Z.; Hao, J.; Zhang, J.; Zhang, B.; Tang, J., Protein as the source for synthesizing fluorescent carbon dots by a one-pot hydrothermal route. *RSC Adv.* **2012,** *2*, 8599-8601.

65. Protesescu, L.; Yakunin, S.; Bodnarchuk, M. I.; Krieg, F.; Caputo, R.; Hendon, C. H.; Yang, R. X.; Walsh, A.; Kovalenko, M. V., Nanocrystals of Cesium Lead Halide Perovskites ($CsPbX_3$, X = Cl, Br, and I): Novel Optoelectronic Materials Showing Bright Emission with Wide Color Gamut. *Nano Lett.* **2015,** *15* (6), 3692-3696.

66. Chen, Y.; Yi, H. T.; Wu, X.; Haroldson, R.; Gartstein, Y. N.; Rodionov, Y. I.; Tikhonov, K. S.; Zakhidov, A.; Zhu, X. Y.; Podzorov, V., Extended carrier lifetimes and diffusion in hybrid perovskites revealed by Hall effect and photoconductivity measurements. *Nat. Comm.* **2016,** *7* (1), 12253.

67. Galkowski, K.; Mitioglu, A.; Miyata, A.; Plochocka, P.; Portugall, O.; Eperon, G.

E.; Wang, J. T.-W.; Stergiopoulos, T.; Stranks, S. D.; Snaith, H. J.; Nicholas, R. J., Determination of the exciton binding energy and effective masses for methylammonium and formamidinium lead tri-halide perovskite semiconductors. *Energy Environ. Sci.* **2016,** *9* (3), 962-970.

68. Akkerman, Q. A.; Rainò, G.; Kovalenko, M. V.; Manna, L., Genesis, challenges and opportunities for colloidal lead halide perovskite nanocrystals. *Nat. Mater.* **2018,** *17* (5), 394-405.

69. Yuan, J.; Hazarika, A.; Zhao, Q.; Ling, X.; Moot, T.; Ma, W.; Luther, J. M., Metal Halide Perovskites in Quantum Dot Solar Cells: Progress and Prospects. *Joule* **2020,** *4* (6), 1160-1185.

70. Stranks, S. D.; Eperon, G. E.; Grancini, G.; Menelaou, C.; Alcocer, M. J. P.; Leijtens, T.; Herz, L. M.; Petrozza, A.; Snaith, H. J., Electron-Hole Diffusion Lengths Exceeding 1 Micrometer in an Organometal Trihalide Perovskite Absorber. *Science* **2013,** *342* (6156), 341-344.

71. Wang, Y.; Dar, M. I.; Ono, L. K.; Zhang, T.; Kan, M.; Li, Y.; Zhang, L.; Wang, X.; Yang, Y.; Gao, X.; Qi, Y.; Grätzel, M.; Zhao, Y., Thermodynamically stabilized β-$CsPbI_3$-based perovskite solar cells with efficiencies >18%. *Science* **2019,** *365* (6453), 591-595.

72. Song, J.; Li, J.; Li, X.; Xu, L.; Dong, Y.; Zeng, H., Quantum Dot Light-Emitting Diodes Based on Inorganic Perovskite Cesium Lead Halides ($CsPbX_3$). *Adv. Mater.* **2015,** *27* (44), 7162-7167.

73. Liang, J.; Chen, D.; Yao, X.; Zhang, K.; Qu, F.; Qin, L.; Huang, Y.; Li, J., Recent Progress and Development in Inorganic Halide Perovskite Quantum Dots for Photoelectrochemical Applications. *Small* **2020,** *16*, 1903398.

74. Xu, L.; Yuan, S.; Ma, L.; Zhang, B.; Fang, T.; Li, X.; Song, J., All-inorganic perovskite quantum dots as lightharvesting, interfacial, and light-converting layers toward solar cells. *J. Mater. Chem. A* **2021,** *9*, 18947.

75. Tian, J.; Xue, Q.; Yao, Q.; Li, N.; Brabec, C. J.; Yip, H.-L., Inorganic Halide Perovskite Solar Cells: Progress and Challenges. *Adv. Energy Mater.* **2010,** *10*, 2000183.

76. Zhang, Q.; Yin, Y., All-Inorganic Metal Halide Perovskite Nanocrystals: Opportunities and Challenges. *ACS Cent. Sci.* **2018,** *4*, 668−679.

77. Bünzli, J.-C. G.; Eliseeva, S. V., Basics of Lanthanide Photophysics. In *Lanthanide Luminescence: Photophysical, Analytical and Biological Aspects*, Hänninen, P.; Härmä, H., Eds. Springer Berlin Heidelberg: Berlin, Heidelberg, 2011; pp 1-45.

78. GabrielleAMandl; DanielRCooper; Hirsch, T.; Seuntjens, J.; Capobianco, J. A., Perspective: lanthanide-doped upconverting nanoparticles. *Methods Appl. Fluoresc.* **2019,** *7*, 012004.

79. Hyde, K. E., Methods for obtaining Russell-Saunders term symbols from electronic configurations. *J. Chem. Educ.* **1975,** *52* (2), 87.

80. Gorman, M., Rules for writing ground state Russell-Saunders symbols. *J. Chem. Educ.* **1973,** *50* (3), 189.

81. Dieke, G. H.; Crosswhite, H. M., The Spectra of the Doubly and Triply Ionized Rare Earths. *Appl. Opt.* **1963,** *2* (7), 675-686.

82. Hehlen, M. P.; Brik, M. G.; Krämer, K. W., 50th anniversary of the Judd–Ofelt theory: An experimentalist's view of the formalism and its application. *J. Lumin.* **2013,** *136*, 221-239.

83. Judd, B. R., Optical Absorption Intensities of Rare-Earth Ions. *Phys. Rev.* **1962,** *127* (3), 750-761.

84. Hovhannesyan, G.; Boudon, V.; Lepers, M., Transition intensities of trivalent lanthanide ions in solids: Extending the Judd-Ofelt theory. *J. Lumin.* **2022,** *241*, 118456.

85. Ofelt, G. S., Intensities of Crystal Spectra of Rare-Earth Ions. *J. Chem. Phys.* **1962,** *37* (3), 511-520.

86. Teo, R. D.; Termini, J.; Gray, H. B., Lanthanides: Applications in Cancer Diagnosis and Therapy. *J. Med. Chem.* **2016,** *59* (13), 6012-6024.

87. Bünzli, J.-C. G., Benefiting from the Unique Properties of Lanthanide Ions. *Acc. Chem. Res.* **2006,** *39* (1), 53-61.

88. Tanner, P. A., Lanthanide Luminescence in Solids. In *Lanthanide Luminescence: Photophysical, Analytical and Biological Aspects*, Hänninen, P.; Härmä, H., Eds. Springer

Berlin Heidelberg: Berlin, Heidelberg, 2011; pp 183-233.

89. Werts, M. H. V., Making sense of Lanthanide Luminescence. *Sci. Prog.* **2005,** *88* (2), 101-131.

90. Bünzli, J.-C. G.; Comby, S.; Chauvin, A.-S.; Vandevyver, C. D. B., New Opportunities for Lanthanide Luminescence. *J. Rare Earths* **2007,** *25* (3), 257-274.

91. Auzel, F., History of upconversion discovery and its evolution. *J. Lumin.* **2020,** *223*.

92. Auzel, F., Upconversion and anti-Stokes processes with f and d ions in solids. *Chem. Rev.* **2004,** *104*, 139−173.

93. Zou, X.; Izumitani, T., Spectroscopic properties and mechanisms of excited state absorption and energy transfer upconversion for Er^{3+}-doped glasses. *J. Non-Cryst. Solids* **1993,** *162* (1), 68-80.

94. Liu, Y.; Luo, W.; Zhu, H.; Chen, X., Optical spectroscopy of lanthanides doped in wide band-gap semiconductor nanocrystals. *J. Lumin.* **2011,** *131* (3), 415-422.

95. Chivian, J. S.; Case, W. E.; Eden, D. D., The photon avalanche: A new phenomenon in Pr^{3+}-based infrared quantum counters. *Appl. Phys. Lett.* **1979,** *35* (2), 124-125.

96. Joubert, M.-F., Photon avalanche upconversion in rare earth laser materials. *Opt. Mater.* **1999,** *11* (2), 181-203.

97. Lee, C.; Xu, E. Z.; Liu, Y.; Teitelboim, A.; Yao, K.; Fernandez-Bravo, A.; Kotulska, A. M.; Nam, S. H.; Suh, Y. D.; Bednarkiewicz, A.; Cohen, B. E.; Chan, E. M.; Schuck, P. J., Giant nonlinear optical responses from photon-avalanching nanoparticles. *Nature* **2021,** *589* (7841), 230-235.

98. Dexter, D. L., Possibility of Luminescent Quantum Yields Greater than Unity. *Phys. Rev.* **1957,** *108* (3), 630-633.

99. Maciel, G. S.; Biswas, A.; Kapoor, R.; Prasad, P. N., Blue cooperative upconversion in Yb^{3+}-doped multicomponent sol-gel-processed silica glass for three-dimensional display. *Appl. Phys. Lett.* **2000,** *76* (15), 1978-1980.

100. Zheng, W.; Huang, P.; Tu, D.; Ma, E.; Zhu, H.; Chen, X., Lanthanide-doped upconversion nano-bioprobes: electronic structures, optical properties, and biodetection. *Chem.*

Soc. Rev. **2015,** *44* (6), 1379-1415.

101. Zou, Q.; Huang, P.; Zheng, W.; You, W.; Li, R.; Tu, D.; Xu, J.; Chen, X., Cooperative and non-cooperative sensitization upconversion in lanthanide-doped $LiYbF_4$ nanoparticles. *Nanoscale* **2017,** *9* (19), 6521-6528.

102. Wang, F.; Deng, R.; Wang, J.; Wang, Q.; Han, Y.; Zhu, H.; Chen, X.; Liu, X., Tuning upconversion through energy migration in core–shell nanoparticles. *Nat. Mater.* **2011,** *10* (12), 968-973.

103. Chen, X.; Jin, L.; Kong, W.; Sun, T.; Zhang, W.; Liu, X.; Fan, J.; Yu, S. F.; Wang, F., Confining energy migration in upconversion nanoparticles towards deep ultraviolet lasing. *Nat. Comm.* **2016,** *7* (1), 10304.

104. Zhou, B.; Yan, L.; Huang, J.; Liu, X.; Tao, L.; Zhang, Q., NIR II-responsive photon upconversion through energy migration in an ytterbium sublattice. *Nat. Photonics* **2020,** *14* (12), 760-766.

105. Chen, X.; Jin, L.; Sun, T.; Kong, W.; Yu, S. F.; Wang, F., Energy Migration Upconversion in Ce(III)-Doped Heterogeneous Core−Shell−Shell Nanoparticles. *Small* **2017,** *13* (43), 1701479.

106. Tu, L.; Liu, X.; Wu, F.; Zhang, H., Excitation energy migration dynamics in upconversion nanomaterials. *Chem. Soc. Rev.* **2015,** *44* (6), 1331-1345.

107. Aebischer, A.; Gumy, F.; Bünzli, J.-C. G., Intrinsic quantum yields and radiative lifetimes of lanthanide tris(dipicolinates). *Phys. Chem. Chem. Phys.* **2009,** *11* (9), 1346-1353.

108. Huang, P.; Zheng, W.; Zhou, S.; Tu, D.; Chen, Z.; Zhu, H.; Li, R.; Ma, E.; Huang, M.; Chen, X., Lanthanide-Doped $LiLuF_4$ Upconversion Nanoprobes for the Detection of Disease Biomarkers. *Angew. Chem. Int. Ed.* **2014,** *53* (5), 1252-1257.

109. Boyer, J.-C.; van Veggel, F. C. J. M., Absolute quantum yield measurements of colloidal $NaYF_4$: Er^{3+}, Yb^{3+} upconverting nanoparticles. *Nanoscale* **2010,** *2* (8), 1417-1419.

110. Würth, C.; Kaiser, M.; Wilhelm, S.; Grauel, B.; Hirsch, T.; Resch-Genger, U., Excitation power dependent population pathways and absolute quantum yields of upconversion nanoparticles in different solvents. *Nanoscale* **2017,** *9* (12), 4283-4294.

111. Würth, C.; Grabolle, M.; Pauli, J.; Spieles, M.; Resch-Genger, U., Relative and absolute determination of fluorescence quantum yields of transparent samples. *Nat. Protoc.* **2013,** *8* (8), 1535-1550.

112. Würth, C.; Fischer, S.; Grauel, B.; Alivisatos, A. P.; Resch-Genger, U., Quantum Yields, Surface Quenching, and Passivation Efficiency for Ultrasmall Core/Shell Upconverting Nanoparticles. *J. Am. Chem. Soc.* **2018,** *140* (14), 4922-4928.

113. de Mello, J. C.; Wittmann, H. F.; Friend, R. H., An improved experimental determination of external photoluminescence quantum efficiency. *Adv. Mater.* **1997,** *9* (3), 230-232.

114. Pokhrel, M.; Kumar, G. A.; Sardar, D. K., Highly efficient NIR to NIR and VIS upconversion in Er^{3+} and Yb^{3+} doped in M_2O_2S (M = Gd, La, Y). *J. Mater. Chem. A* **2013,** *1* (38), 11595-11606.

115.Homann, C.; Krukewitt, L.; Frenzel, F.; Grauel, B.; Würth, C.; Resch-Genger, U.; Haase, M., $NaYF_4$:Yb,Er/$NaYF_4$ Core/Shell Nanocrystals with High Upconversion Luminescence Quantum Yield. *Angew. Chem. Int. Ed.* **2018,** *57*, 8765 –8769.

116. Kaiser, M.; Wurth, C.; Kraft, M.; Hyppanen, I.; Soukka, T.; Resch-Genger, U., Power-dependent upconversion quantum yield of $NaYF_4$:Yb^{3+},Er^{3+} nano- and micrometer-sized particles - measurements and simulations. *Nanoscale* **2017,** *9* (28), 10051-10058.

117. Chen, B.; Wang, F., Combating Concentration Quenching in Upconversion Nanoparticles. *Acc. Chem. Res.* **2020,** *53* (2), 358-367.

118. Wang, X.; Valiev, R. R.; Ohulchanskyy, T. Y.; Ågren, H.; Yang, C.; Chen, G., Dye-sensitized lanthanide-doped upconversion nanoparticles. *Chem. Soc. Rev.* **2017,** *46* (14), 4150-4167.

119. Wu, D. M.; García-Etxarri, A.; Salleo, A.; Dionne, J. A., Plasmon-Enhanced Upconversion. *J. Phys. Chem. Lett.* **2014,** *5* (22), 4020-4031.

120. Li, X.; Zhang, F.; Zhao, D., Highly efficient lanthanide upconverting nanomaterials: Progresses and challenges. *Nano Today* **2013,** *8* (6), 643-676.

121. Xu, W.; Chen, X.; Song, H., Upconversion manipulation by local electromagnetic field. *Nano Today* **2017,** *17*, 54-78.

122. Das, A.; Bae, K.; Park, W., Enhancement of upconversion luminescence using photonic nanostructures. *Nanophotonics* **2020,** *9* (6), 1359-1371.

123. Wen, S.; Zhou, J.; Zheng, K.; Bednarkiewicz, A.; Liu, X.; Jin, D., Advances in highly doped upconversion nanoparticles. *Nat. Comm.* **2018,** *9* (1), 2415.

124. Zhou, B.; Shi, B.; Jin, D.; Liu, X., Controlling upconversion nanocrystals for emerging applications. *Nat. Nanotechnol.* **2015,** *10* (11), 924-936.

125. Wen, S.; Zhou, J.; Schuck, P. J.; Suh, Y. D.; Schmidt, T. W.; Jin, D., Future and challenges for hybrid upconversion nanosystems. *Nat. Photonics* **2019,** *13* (12), 828-838.

126. Dong, J.; Gao, W.; Han, Q.; Wang, Y.; Qi, J.; Yan, X.; Sun, M., Plasmon-enhanced upconversion photoluminescence: Mechanism and application. *Rev. Phys.* **2019,** *4*, 100026.

127. Larquet, C.; Carenco, S., Metal Oxysulfides: From Bulk Compounds to Nanomaterials. *Front. Chem.* **2020,** *8*, 179.

128. Wang, X.; Sun, X. M.; Yu, D.; Zou, B. S.; Li, Y., Rare Earth Compound Nanotubes. *Adv. Mater.* **2003,** *15* (17), 1442-1445.

129. Heer, S.; Lehmann, O.; Haase, M.; Güdel, H.-U., Blue, Green, and Red Upconversion Emission from Lanthanide-Doped $LuPO_4$ and $YbPO_4$ Nanocrystals in a Transparent Colloidal Solution. *Angew. Chem. Int. Ed.* **2003,** *42* (27), 3179-3182.

130. Patra, A.; Friend, C. S.; Kapoor, R.; Prasad, P. N., Effect of crystal nature on upconversion luminescence in Er^{3+}:ZrO_2 nanocrystals. *Appl. Phys. Lett.* **2003,** *83* (2), 284-286.

131. Polizzi, S.; Bucella, S.; Speghini, A.; Vetrone, F.; Naccache, R.; Boyer, J. C.; Capobianco, J. A., Nanostructured Lanthanide-Doped Lu_2O_3 Obtained by Propellant Synthesis. *Chem. Mater.* **2004,** *16* (7), 1330-1335.

132. Sun, Y.; Liu, H.; Wang, X.; Kong, X.; Zhang, H., Optical Spectroscopy and Visible Upconversion Studies of YVO_4:Er^{3+} Nanocrystals Synthesized by a Hydrothermal Process. *Chem. Mater.* **2006,** *18* (11), 2726-2732.

133. Vetrone, F.; Boyer, J.-C.; Capobianco, J. A.; Speghini, A.; Bettinelli, M., Luminescence Spectroscopy and Near-Infrared to Visible Upconversion of Nanocrystalline

$Gd_3Ga_5O_{12}:Er^{3+}$. *J. Phys. Chem. B* **2003,** *107* (39), 10747-10752.

134. Ghosh, P.; Patra, A., Understanding the influence of nanoenvironment on luminescence of rare-earth ions. *Pramana* **2005,** *65* (5), 901-907.

135. Chen, X.; Ma, E.; Liu, G., Energy Levels and Optical Spectroscopy of Er^{3+} in Gd_2O_3 Nanocrystals. *J. Phys. Chem. C* **2007,** *111* (28), 10404-10411.

136. Guo, H.; Dong, N.; Yin, M.; Zhang, W.; Lou, L.; Xia, S., Visible Upconversion in Rare Earth Ion-Doped Gd_2O_3 Nanocrystals. *J. Phys. Chem. B* **2004,** *108* (50), 19205-19209.

137. Gruber, J. B.; Krupke, W. F.; Poindexter, J. M., Crystal-Field Splitting of Trivalent Thulium and Erbium J Levels in Yttrium Oxide. *J. Chem. Phys.* **1964,** *41* (11), 3363-3377.

138. Guo, H.; Zhang, W.; Lou, L.; Brioude, A.; Mugnier, J., Structure and optical properties of rare earth doped Y_2O_3 waveguide films derived by sol–gel process. *Thin Solid Films* **2004,** *458* (1), 274-280.

139. Muñoz-Santiuste, J. E.; Lavín, V.; Rodríguez-Mendoza, U. R.; Ferrer-Roca, C.; Errandonea, D.; Martínez-García, D.; Rodríguez-Hernández, P.; Muñoz, A.; Bettinelli, M., Experimental and theoretical study on the optical properties of $LaVO_4$ crystals under pressure. *Physi. Chem. Chem. Phys.* **2018,** *20* (43), 27314-27328.

140. Zharkov, D. K.; Shmelev, A. G.; Leontyev, A. V.; Nikiforov, V. G.; Lobkov, V. S.; Alkahtani, M. H.; Hemmer, P. R.; Samartsev, V. V., Light converting Yb^{3+}/Er^{3+} doped YVO_4 nanoparticles for biological applications. *Laser Phys. Lett.* **2020,** *17* (7), 075901.

141. Lei, L.; Zhang, S.; Xia, H.; Tian, Y.; Zhang, J.; Xua, S., Controlled synthesis of lanthanide-doped Gd_2O_2S nanocrystals with a novel excitation-dependent multicolor emissions. *Nanoscale* **2017,** *9*, 5718-5724.

142. Yuanbin, C.; Shenxin, L.; Qiuping, W.; Lizhong, W., Effect of pressure on electron state of Eu^{3+} in Gd_2O_2S. *Physica B Condens. Matter* **1998,** *245* (3), 293-300.

143. Stedman, G. E.; Newman, D. J., Crystal field in rare-earth fluorides, II parameters for Er^{3+} and Nd^{3+} in LaF_3. *J. Phys. Chem. Sollides* **1971,** *32* (1), 109-114.

144. Diamente, P. R.; Raudsepp, M.; van Veggel, F. C. J. M., Dispersible Tm^{3+}-Doped Nanoparticles that Exhibit Strong 1.47 μm Photoluminescence. *Advanced Functional Materials*

2007, *17* (3), 363-368.

145. Gruber, J. B.; Leavitt, R. P.; Morrison, C. A., Absorption spectrum, energy levels, and crystal-field parameters of Tm^{3+}:$LaCl_3$. *J. Chem. Phys.* **1981,** *74* (5), 2705-2709.

146. Chen, X.; Luo, Z., Group-chain scheme analysis of the energy levels and magnetic properties of Er^{3+} in the $LiYF_4$ crystal. *J. Condens. Matter Phys.* **1996,** *8* (15), 2571-2583.

147. Renfro, G. M.; Windscheif, J. C.; Sibley, W. A.; Belt, R. F., Optical transitions of Pr^{3+} and Er^{3+} ions in $LiYF_4$. *J. Lumin.* **1980,** *22* (1), 51-68.

148. Tu, D.; Liu, Y.; Zhu, H.; Li, R.; Liu, L.; Chen, X., Breakdown of Crystallographic Site Symmetry in Lanthanide-Doped $NaYF_4$ Crystals. *Angew. Chem. Int. Ed.* **2013,** *52* (4), 1128-1133.

149. Ivaturi, A.; MacDougall, S. K. W.; Martín-Rodríguez, R.; Quintanilla, M.; Marques-Hueso, J.; Krämer, K. W.; Meijerink, A.; Richards, B. S., Optimizing infrared to near infrared upconversion quantum yield of β-$NaYF_4$:Er^{3+} in fluoropolymer matrix for photovoltaic devices. *J. Appl. Phys.* **2013,** *114* (1), 013505.

150. Aarts, L.; van der Ende, B. M.; Meijerink, A., Downconversion for solar cells in $NaYF_4$:Er,Yb. *J. Appl. Phys.* **2009,** *106* (2), 023522.

151. Heer, S.; Kömpe, K.; Güdel, H. U.; Haase, M., Highly Efficient Multicolour Upconversion Emission in Transparent Colloids of Lanthanide-Doped $NaYF_4$ Nanocrystals. *Adv. Mater.* **2004,** *16* (23-24), 2102-2105.

152. Haase, M.; Schäfer, H., Upconverting Nanoparticles. *Angew. Chem. Int. Ed.* **2011,** *50* (26), 5808-5829.

153. Beeby, A.; M. Clarkson, I.; S. Dickins, R.; Faulkner, S.; Parker, D.; Royle, L.; S. de Sousa, A.; A. Gareth Williams, J.; Woods, M., Non-radiative deactivation of the excited states of europium, terbium and ytterbium complexes by proximate energy-matched OH, NH and CH oscillators: an improved luminescence method for establishing solution hydration states. *J. Chem. Soc. Perkin Trans 2* **1999,** (3), 493-504.

154. Layne, C. B.; Weber, M. J., Multiphonon relaxation of rare-earth ions in beryllium-fluoride glass. *Phys. Rev. B* **1977,** *16* (7), 3259-3261.

155. Reed, E. D.; Moos, H. W., Nonthermalization and Large Variation in Multiphonon Relaxation Rate among Rare-Earth-Ion Stark Levels. *Phys. Rev. B* **1973,** *8* (3), 988-992.

156. Krämer, K. W.; Biner, D.; Frei, G.; Güdel, H. U.; Hehlen, M. P.; Lüthi, S. R., Hexagonal Sodium Yttrium Fluoride Based Green and Blue Emitting Upconversion Phosphors. *Chem. Mater.* **2004,** *16* (7), 1244-1251.

157. Aebischer, A.; Hostettler, M.; Hauser, J.; Krämer, K.; Weber, T.; Güdel, H. U.; Bürgi, H.-B., Structural and Spectroscopic Characterization of Active Sites in a Family of Light-Emitting Sodium Lanthanide Tetrafluorides. *Angew. Chem. Int. Ed.* **2006,** *45* (17), 2802-2806.

158. Wang, J.; Deng, R.; MacDonald, M. A.; Chen, B.; Yuan, J.; Wang, F.; Chi, D.; Andy Hor, T. S.; Zhang, P.; Liu, G.; Han, Y.; Liu, X., Enhancing multiphoton upconversion through energy clustering at sublattice level. *Nat. Mater.* **2014,** *13* (2), 157-162.

159. Martín-Rodríguez, R.; Fischer, S.; Ivaturi, A.; Froehlich, B.; Krämer, K. W.; Goldschmidt, J. C.; Richards, B. S.; Meijerink, A., Highly Efficient IR to NIR Upconversion in Gd_2O_2S: Er^{3+} for Photovoltaic Application. *Chem. Mater.* **2013,** *25*, 1912−1921.

160. Pokhrel, M.; Kumar, G. A.; Sardar, D. K., Highly efficient NIR to NIR and VIS upconversion in Er^{3+} and Yb^{3+} doped in M_2O_2S(M = Gd, La, Y). *J. Mater. Chem. A* **2013,** *1*, 11595–11606.

161. Osseni, S. A.; Lechevallier, S.; Verelst, M.; Perriat, P.; Dexpert-Ghys, J.; Neumeyer, D.; Garcia, R.; Mayer, F.; Djanashvili, K.; Peters, J. A.; Magdeleine, E.; Gros-Dagnac, H.; Celsis, P.; Mauricot, R., Gadolinium oxysulfide nanoparticles as multimodal imaging agents for T_2-weighted MR, X-ray tomography and photoluminescence. *Nanoscale* **2014,** *6*, 555–564.

162. Santelli, J.; Lepoix, C.; Lechevallier, S.; Martinez, C.; Calise, D.; Zou, Q.; Moyano, S.; Cussac, D.; Verelst, M.; Mauricot, R., Custom NIR Imaging of New Up-Conversion Multimodal Gadolinium Oxysulfide Nanoparticles. *Part. Part. Syst. Charact.* **2021,** *38*, 2000216.

163. Santelli, J.; Lechevallier, S.; Baaziz, H.; Vincent, M.; Martinez, C.; Mauricot, R.;

Parini, A.; Verelst, M.; Cussac, D., Multimodal gadolinium oxysulfide nanoparticles a versatile contrast agent for mesenchymal stem cell labeling. *Nanoscale* **2018,** *10*, 16775-16786.

164. Santelli, J.; Lechevallier, S.; Calise, D.; Marsal, D.; Siegfriedb, A.; Vincent, M.; Martinez, C.; Cussac, D.; Mauricot, R.; Verelst, M., Multimodal gadolinium oxysulfide nanoparticles for bioimaging: A comprehensive biodistribution, elimination and toxicological study. *Acta Biomater.* **2020,** *108*, 261–272.

165. Zhang, P.; Liang, L.; Liu, X., Lanthanide-doped nanoparticles in photovoltaics – more than just upconversion. *J. Mater. Chem. C* **2021**, doi: 10.1039/D1TC02441H.

166. Yang, D.; Kang, X.; Ma, P. a.; Dai, Y.; Hou, Z.; Cheng, Z.; Li, C.; Lin, J., Hollow structured upconversion luminescent $NaYF_4$:Yb^{3+}, Er^{3+} nanospheres for cell imaging and targeted anti-cancer drug delivery. *Biomaterials* **2013,** *34* (5), 1601-1612.

167. Yang, D.; Dai, Y.; Ma, P.; Kang, X.; Cheng, Z.; Li, C.; Lin, J., One-Step Synthesis of Small-Sized and Water-Soluble $NaREF_4$ Upconversion Nanoparticles for In Vitro Cell Imaging and Drug Delivery. *Chem. Eur. J.* **2013,** *19* (8), 2685-2694.

168. Ju, Q.; Tu, D.; Liu, Y.; Li, R.; Zhu, H.; Chen, J.; Chen, Z.; Huang, M.; Chen, X., Amine-Functionalized Lanthanide-Doped $KGdF_4$ Nanocrystals as Potential Optical/Magnetic Multimodal Bioprobes. *J. Am. Chem. Soc.* **2012,** *134* (2), 1323-1330.

169. Qiu, H.; Chen, G.; Sun, L.; Hao, S.; Han, G.; Yang, C., Ethylenediaminetetraacetic acid (EDTA)-controlled synthesis of multicolor lanthanide doped $BaYF_5$ upconversion nanocrystals. *J. Mater. Chem.* **2011,** *21* (43), 17202-17208.

170. Zhang, F.; Wan, Y.; Yu, T.; Zhang, F.; Shi, Y.; Xie, S.; Li, Y.; Xu, L.; Tu, B.; Zhao, D., Uniform Nanostructured Arrays of Sodium Rare-Earth Fluorides for Highly Efficient Multicolor Upconversion Luminescence. *Angew. Chem. Int. Ed.* **2007,** *46* (42), 7976-7979.

171. Liu, L.; Chen, X., Energy levels, fluorescence lifetime and Judd–Ofelt parameters of Eu^{3+} in Gd_2O_3 nanocrystals. *Nanotechnology* **2007,** *18* (25), 255704.

172. Hu, H.; Chen, Z.; Cao, T.; Zhang, Q.; Yu, M.; Li, F.; Yi, T.; Huang, C., Hydrothermal synthesis of hexagonal lanthanide-doped LaF_3 nanoplates with bright upconversion luminescence. *Nanotechnology* **2008,** *19* (37), 375702.

173. Luo, W.; Li, R.; Liu, G.; Antonio, M. R.; Chen, X., Evidence of Trivalent Europium Incorporated in Anatase TiO_2 Nanocrystals with Multiple Sites. *J. Phys. Chem. C* **2008,** *112* (28), 10370-10377.

174. Vetrone, F.; Boyer, J.-C.; Capobianco, J. A.; Speghini, A.; Bettinelli, M., Significance of Yb^{3+} concentration on the upconversion mechanisms in codoped $Y_2O_3:Er^{3+}$, Yb^{3+} nanocrystals. *J. Appl. Phys.* **2004,** *96* (1), 661-667.

175. Wang, G.; Peng, Q.; Li, Y., Upconversion Luminescence of Monodisperse $CaF_2:Yb^{3+}/Er^{3+}$ Nanocrystals. *J. Am. Chem. Soc.* **2009,** *131* (40), 14200-14201.

176. Liu, Y.; Zhou, S.; Tu, D.; Chen, Z.; Huang, M.; Zhu, H.; Ma, E.; Chen, X., Amine-Functionalized Lanthanide-Doped Zirconia Nanoparticles: Optical Spectroscopy, Time-Resolved Fluorescence Resonance Energy Transfer Biodetection, and Targeted Imaging. *J. Am. Chem. Soc.* **2012,** *134* (36), 15083-15090.

177. Zeng, J. H.; Xie, T.; Li, Z. H.; Li, Y., Monodispersed Nanocrystalline Fluoroperovskite Up-Conversion Phosphors. *Cryst. Growth Des.* **2007,** *7* (12), 2774-2777.

178. Zeng, S.; Tsang, M.-K.; Chan, C.-F.; Wong, K.-L.; Hao, J., PEG modified $BaGdF_5$:Yb/Er nanoprobes for multi-modal upconversion fluorescent, in vivo X-ray computed tomography and biomagnetic imaging. *Biomaterials* **2012,** *33* (36), 9232-9238.

179. Zhang, Y.-W.; Sun, X.; Si, R.; You, L.-P.; Yan, C.-H., Single-Crystalline and Monodisperse LaF_3 Triangular Nanoplates from a Single-Source Precursor. *J. Am. Chem. Soc.* **2005,** *127* (10), 3260-3261.

180. Ye, X.; Collins, J. E.; Kang, Y.; Chen, J.; Chen, D. T. N.; Yodh, A. G.; Murray, C. B., Morphologically controlled synthesis of colloidal upconversion nanophosphors and their shape-directed self-assembly. *PNAS* **2010,** *107* (52), 22430.

181. Du, Y.-P.; Zhang, Y.-W.; Sun, L.-D.; Yan, C.-H., Luminescent Monodisperse Nanocrystals of Lanthanide Oxyfluorides Synthesized from Trifluoroacetate Precursors in High-Boiling Solvents. *J. Phys. Chem. C* **2008,** *112* (2), 405-415.

182. Mahalingam, V.; Vetrone, F.; Naccache, R.; Speghini, A.; Capobianco, J. A., Structural and optical investigation of colloidal Ln^{3+}/Yb^{3+} co-doped KY_3F_{10} nanocrystals. *J.*

Mater. Chem. **2009,** *19* (20), 3149-3152.

183. Vetrone, F.; Mahalingam, V.; Capobianco, J. A., Near-Infrared-to-Blue Upconversion in Colloidal $BaYF_5:Tm^{3+}$, Yb^{3+} Nanocrystals. *Chem. Mater.* **2009,** *21* (9), 1847-1851.

184. Sun, X.; Zhang, Y.-W.; Du, Y.-P.; Yan, Z.-G.; Si, R.; You, L.-P.; Yan, C.-H., From Trifluoroacetate Complex Precursors to Monodisperse Rare-Earth Fluoride and Oxyfluoride Nanocrystals with Diverse Shapes through Controlled Fluorination in Solution Phase. *Chem. Eur. J.* **2007,** *13* (8), 2320-2332.

185. Mahalingam, V.; Vetrone, F.; Naccache, R.; Speghini, A.; Capobianco, J. A., Colloidal Tm^{3+}/Yb^{3+}-Doped $LiYF_4$ Nanocrystals: Multiple Luminescence Spanning the UV to NIR Regions via Low-Energy Excitation. *Adv. Mater.* **2009,** *21* (40), 4025-4028.

186. Yi, G. S.; Chow, G. M., Synthesis of Hexagonal-Phase $NaYF_4$:Yb,Er and $NaYF_4$:Yb,Tm Nanocrystals with Efficient Up-Conversion Fluorescence. *Adv. Funct. Mater.* **2006,** *16* (18), 2324-2329.

187. Vetrone, F.; Naccache, R.; Mahalingam, V.; Morgan, C. G.; Capobianco, J. A., The Active-Core/Active-Shell Approach: A Strategy to Enhance the Upconversion Luminescence in Lanthanide-Doped Nanoparticles. *Adv. Funct. Mater.* **2009,** *19* (18), 2924-2929.

188. Wang, F.; Liu, X., Recent advances in the chemistry of lanthanide-doped upconversion nanocrystals. *Chem. Soc. Rev.* **2009,** *38* (4), 976-989.

189. Li, Z.; Zhang, Y.; Jiang, S., Multicolor Core/Shell-Structured Upconversion Fluorescent Nanoparticles. *Adv. Mater.* **2008,** *20* (24), 4765-4769.

190. Lezhnina, M. M.; Jüstel, T.; Kätker, H.; Wiechert, D. U.; Kynast, U. H., Efficient Luminescence from Rare-Earth Fluoride Nanoparticles with Optically Functional Shells. *Adv. Funct. Mater.* **2006,** *16* (7), 935-942.

191. Yi, G.-S.; Chow, G.-M., Water-Soluble $NaYF_4$:Yb,Er(Tm)/$NaYF_4$/Polymer Core/Shell/Shell Nanoparticles with Significant Enhancement of Upconversion Fluorescence. *Chem. Mater.* **2007,** *19* (3), 341-343.

192. Chen, G.; Shen, J.; Ohulchanskyy, T. Y.; Patel, N. J.; Kutikov, A.; Li, Z.; Song, J.; Pandey, R. K.; Ågren, H.; Prasad, P. N.; Han, G., (α-$NaYbF_4:Tm^{3+}$)/CaF_2 Core/Shell

Nanoparticles with Efficient Near-Infrared to Near-Infrared Upconversion for High-Contrast Deep Tissue Bioimaging. *ACS Nano* **2012,** *6* (9), 8280-8287.

193. Johnson, N. J. J.; Korinek, A.; Dong, C.; van Veggel, F. C. J. M., Self-Focusing by Ostwald Ripening: A Strategy for Layer-by-Layer Epitaxial Growth on Upconverting Nanocrystals. *J. Am. Chem. Soc.* **2012,** *134* (27), 11068-11071.

194. Li, X.; Shen, D.; Yang, J.; Yao, C.; Che, R.; Zhang, F.; Zhao, D., Successive Layer-by-Layer Strategy for Multi-Shell Epitaxial Growth: Shell Thickness and Doping Position Dependence in Upconverting Optical Properties. *Chem. Mater.* **2013,** *25* (1), 106-112.

195. Fan, Y.; Liu, L.; Zhang, F., Exploiting lanthanide-doped upconversion nanoparticles with core/shell structures. *Nano Today* **2019,** *25*, 68-84.

196. Dong, C.; van Veggel, F. C. J. M., Cation Exchange in Lanthanide Fluoride Nanoparticles. *ACS Nano* **2009,** *3* (1), 123-130.

197. Yan, C.; Dadvand, A.; Rosei, F.; Perepichka, D. F., Near-IR Photoresponse in New Up-Converting CdSe/$NaYF_4$:Yb,Er Nanoheterostructures. *J. Am. Chem. Soc.* **2010,** *132* (26), 8868-8869.

198. Li, X.; Zhou, L.; Wei, Y.; El-Toni, A. M.; Zhang, F.; Zhao, D., Anisotropic Growth-Induced Synthesis of Dual-Compartment Janus Mesoporous Silica Nanoparticles for Bimodal Triggered Drugs Delivery. *J. Am. Chem. Soc.* **2014,** *136* (42), 15086-15092.

199. Zhao, F.; Yuan, M.; Zhang, W.; Gao, S., Monodisperse Lanthanide Oxysulfide Nanocrystals. *J. Am. Chem. Soc.* **2006,** *128*, 11758-11759.

200. Larquet, C.; Carenco, S., Metal Oxysulfides: From Bulk Compounds to Nanomaterials. *Front. Chem.* **2020,** *8* (179).

201. Osseni, S. A.; Lechevallier, S.; Verelst, M.; Dujardin, C.; Dexpert-Ghys, J.; Neumeyer, D.; Leclercq, M.; Baaziz, H.; Cussac, D.; Santran, V.; Mauricot, R., New nanoplatform based on $Gd_2O_2S:Eu^{3+}$ core: synthesis, characterization and use for in vitro bio-labelling. *J. Mater. Chem.* **2011,** *21* (45), 18365-18372.

202. Liu, Y.; Tu, D.; Zhu, H.; Ma, E.; Chen, X., Lanthanide-doped luminescent nano-bioprobes: from fundamentals to biodetection. *Nanoscale* **2013,** *5* (4), 1369-1384.

203. Bogdan, N.; Vetrone, F.; Ozin, G. A.; Capobianco, J. A., Synthesis of Ligand-Free Colloidally Stable Water Dispersible Brightly Luminescent Lanthanide-Doped Upconverting Nanoparticles. *Nano Lett.* **2011,** *11* (2), 835-840.

204. Bogdan, N.; Rodríguez, E. M.; Sanz-Rodríguez, F.; Iglesias de la Cruz, M. a. C.; Juarranz, Á.; Jaque, D.; Solé, J. G.; Capobianco, J. A., Bio-functionalization of ligand-free upconverting lanthanide doped nanoparticles for bio-imaging and cell targeting. *Nanoscale* **2012,** *4* (12), 3647-3650.

205. Liu, J.; Bu, W.; Pan, L.; Zhang, S.; Chen, F.; Zhou, L.; Zhao, K.; Peng, W.; Shi, J., Simultaneous nuclear imaging and intranuclear drug delivery by nuclear-targeted multifunctional upconversion nanoprobes. *Biomaterials* **2012,** *33* (29), 7282-7290.

206. Zhang, T.; Ge, J.; Hu, Y.; Yin, Y., A General Approach for Transferring Hydrophobic Nanocrystals into Water. *Nano Lett.* **2007,** *7*, 3203-3207.

207. Dong, A.; Ye, X.; Chen, J.; Kang, Y.; Gordon, T.; Kikkawa, J. M.; Murray, C. B., A Generalized Ligand-Exchange Strategy Enabling Sequential Surface Functionalization of Colloidal Nanocrystals. *J. Am. Chem. Soc.* **2011,** *133*, 998–1006.

208. Nichkova, M.; Dosev, D.; Gee, S. J.; Hammock, B. D.; Kennedy, I. M., Microarray Immunoassay for Phenoxybenzoic Acid Using Polymer Encapsulated Eu:Gd_2O_3 Nanoparticles as Fluorescent Labels. *Anal. Chem.* **2005,** *77* (21), 6864-6873.

209. Cao, T.; Yang, Y.; Gao, Y.; Zhou, J.; Li, Z.; Li, F., High-quality water-soluble and surface-functionalized upconversion nanocrystals as luminescent probes for bioimaging. *Biomaterials* **2011,** *32* (11), 2959-2968.

210. Budijono, S. J.; Shan, J.; Yao, N.; Miura, Y.; Hoye, T.; Austin, R. H.; Ju, Y.; Prud'homme, R. K., Synthesis of Stable Block-Copolymer-Protected $NaYF_4$:Yb^{3+}, Er^{3+} Up-Converting Phosphor Nanoparticles. *Chem. Mater.* **2010,** *22* (2), 311-318.

211. Jiang, G.; Pichaandi, J.; Johnson, N. J. J.; Burke, R. D.; van Veggel, F. C. J. M., An Effective Polymer Cross-Linking Strategy To Obtain Stable Dispersions of Upconverting $NaYF_4$ Nanoparticles in Buffers and Biological Growth Media for Biolabeling Applications. *Langmuir* **2012,** *28* (6), 3239-3247.

212. Cheng, L.; Yang, K.; Zhang, S.; Shao, M.; Lee, S.; Liu, Z., Highly-sensitive multiplexed in vivo imaging using pegylated upconversion nanoparticles. *Nano Res.* **2010,** *3* (10), 722-732.

213. Ju, Q.; Liu, Y.; Tu, D.; Zhu, H.; Li, R.; Chen, X., Lanthanide-Doped Multicolor GdF3 Nanocrystals for Time-Resolved Photoluminescent Biodetection. *Chem. Eur. J* **2011,** *17* (31), 8549-8554.

214. Ye, Z.; Tan, M.; Wang, G.; Yuan, J., Preparation, Characterization, and Time-Resolved Fluorometric Application of Silica-Coated Terbium(III) Fluorescent Nanoparticles. *Anal. Chem.* **2004,** *76* (3), 513-518.

215. Hanaoka, K.; Kikuchi, K.; Kobayashi, S.; Nagano, T., Time-Resolved Long-Lived Luminescence Imaging Method Employing Luminescent Lanthanide Probes with a New Microscopy System. *J. Am. Chem. Soc.* **2007,** *129* (44), 13502-13509.

216. Tang, Y.; Pei, F.; Lu, X.; Fan, Q.; Huang, W., Recent Advances on Activatable NIR-II Fluorescence Probes for Biomedical Imaging. *Adv. Opt. Mater.* **2019,** *7* (21), 1900917.

217. Tao, Z.; Dang, X.; Huang, X.; Muzumdar, M. D.; Xu, E. S.; Bardhan, N. M.; Song, H.; Qi, R.; Yu, Y.; Li, T.; Wei, W.; Wyckoff, J.; Birrer, M. J.; Belcher, A. M.; Ghoroghchian, P. P., Early tumor detection afforded by in vivo imaging of near-infrared II fluorescence. *Biomaterials* **2017,** *134*, 202-215.

218. Yu, S.; Tu, D.; Lian, W.; Xu, J.; Chen, X., Lanthanide-doped near-infrared II luminescent nanoprobes for bioapplications. *Sci. China Mater.* **2019,** *62* (8), 1071-1086.

219. Li, Z.; Ding, X.; Cong, H.; Wang, S.; Yu, B.; Shen, Y., Recent advances on inorganic lanthanide-doped NIR-II fluorescence nanoprobes for bioapplication. *J. Lumin.* **2020,** *228*, 117627.

220. Wang, M.; Mi, C.-C.; Wang, W.-X.; Liu, C.-H.; Wu, Y.-F.; Xu, Z.-R.; Mao, C.-B.; Xu, S.-K., Immunolabeling and NIR-Excited Fluorescent Imaging of HeLa Cells by Using $NaYF_4$:Yb,Er Upconversion Nanoparticles. *ACS Nano* **2009,** *3* (6), 1580-1586.

221. Zhan, Q.; Qian, J.; Liang, H.; Somesfalean, G.; Wang, D.; He, S.; Zhang, Z.; Andersson-Engels, S., Using 915 nm Laser Excited $Tm^{3+}/Er^{3+}/Ho^{3+}$-Doped $NaYbF_4$

Upconversion Nanoparticles for in Vitro and Deeper in Vivo Bioimaging without Overheating Irradiation. *ACS Nano* **2011,** *5* (5), 3744-3757.

222. He, M.; Huang, P.; Zhang, C.; Hu, H.; Bao, C.; Gao, G.; He, R.; Cui, D., Dual Phase-Controlled Synthesis of Uniform Lanthanide-Doped $NaGdF_4$ Upconversion Nanocrystals Via an OA/Ionic Liquid Two-Phase System for In Vivo Dual-Modality Imaging. *Adv. Funct. Mater.* **2011,** *21* (23), 4470-4477.

223. Zhou, J.; Liu, Z.; Li, F., Upconversion nanophosphors for small-animal imaging. *Chem. Soc. Rev.* **2012,** *41* (3), 1323-1349.

224. Zijlmans, H. J. M. A. A.; Bonnet, J.; Burton, J.; Kardos, K.; Vail, T.; Niedbala, R. S.; Tanke, H. J., Detection of Cell and Tissue Surface Antigens Using Up-Converting Phosphors: A New Reporter Technology. *Anal. Biochem.* **1999,** *267* (1), 30-36.

225. Jin, J.; Gu, Y.-J.; Man, C. W.-Y.; Cheng, J.; Xu, Z.; Zhang, Y.; Wang, H.; Lee, V. H.-Y.; Cheng, S. H.; Wong, W.-T., Polymer-Coated $NaYF_4$:Yb^{3+}, Er^{3+} Upconversion Nanoparticles for Charge-Dependent Cellular Imaging. *ACS Nano* **2011,** *5* (10), 7838-7847.

226. Park, Y. I.; Kim, H. M.; Kim, J. H.; Moon, K. C.; Yoo, B.; Lee, K. T.; Lee, N.; Choi, Y.; Park, W.; Ling, D.; Na, K.; Moon, W. K.; Choi, S. H.; Park, H. S.; Yoon, S.-Y.; Suh, Y. D.; Lee, S. H.; Hyeon, T., Theranostic Probe Based on Lanthanide-Doped Nanoparticles for Simultaneous In Vivo Dual-Modal Imaging and Photodynamic Therapy. *Adv. Mater.* **2012,** *24* (42), 5755-5761.

227. Hilderbrand, S. A.; Shao, F.; Salthouse, C.; Mahmood, U.; Weissleder, R., Upconverting luminescent nanomaterials: application to in vivo bioimaging. *Chem. Commun.* **2009,** (28), 4188-4190.

228. Jin, D.; Piper, J. A., Time-Gated Luminescence Microscopy Allowing Direct Visual Inspection of Lanthanide-Stained Microorganisms in Background-Free Condition. *Anal. Chem.* **2011,** *83* (6), 2294-2300.

229. Liao, Z.; Tropiano, M.; Mantulnikovs, K.; Faulkner, S.; Vosch, T.; Just Sørensen, T., Spectrally resolved confocal microscopy using lanthanide centred near-IR emission. *Chem. Commun.* **2015,** *51* (12), 2372-2375.

230. Zheng, X.; Zhu, X.; Lu, Y.; Zhao, J.; Feng, W.; Jia, G.; Wang, F.; Li, F.; Jin, D., High-Contrast Visualization of Upconversion Luminescence in Mice Using Time-Gating Approach. *Anal. Chem.* **2016,** *88* (7), 3449-3454.

231. Wahsner, J.; Gale, E. M.; Rodríguez-Rodríguez, A.; Caravan, P., Chemistry of MRI Contrast Agents: Current Challenges and New Frontiers. *Chem. Rev.* **2019,** *119* (2), 957-1057.

232. Park, Y. I.; Lee, K. T.; Suh, Y. D.; Hyeon, T., Upconverting nanoparticles: a versatile platform for wide-field two-photon microscopy and multi-modal in vivo imaging. *Chem. Soc. Rev.* **2015,** *44* (6), 1302-1317.

233. Caravan, P.; Ellison, J. J.; McMurry, T. J.; Lauffer, R. B., Gadolinium(III) Chelates as MRI Contrast Agents: Structure, Dynamics, and Applications. *Chem. Rev.* **1999,** *99* (9), 2293-2352.

234. Lauffer, R. B., Paramagnetic metal complexes as water proton relaxation agents for NMR imaging: theory and design. *Chem. Rev.* **1987,** *87* (5), 901-927.

235. Zhou, Z.; Lu, Z.-R., Gadolinium-based contrast agents for magnetic resonance cancer imaging. *WIREs Nanomed. Nanobiotechnol.* **2013,** *5* (1), 1-18.

236. Liu, Q.; Sun, Y.; Li, C.; Zhou, J.; Li, C.; Yang, T.; Zhang, X.; Yi, T.; Wu, D.; Li, F., 18F-Labeled Magnetic-Upconversion Nanophosphors via Rare-Earth Cation-Assisted Ligand Assembly. *ACS Nano* **2011,** *5* (4), 3146-3157.

237. Liu, Y.; Ai, K.; Liu, J.; Yuan, Q.; He, Y.; Lu, L., A High-Performance Ytterbium-Based Nanoparticulate Contrast Agent for In Vivo X-Ray Computed Tomography Imaging. *Angew. Chem. Int. Ed.* **2012,** *51* (6), 1437-1442.

238. Zhu, X.; Zhou, J.; Chen, M.; Shi, M.; Feng, W.; Li, F., Core–shell Fe_3O_4@$NaLuF_4$:Yb,Er/Tm nanostructure for MRI, CT and upconversion luminescence tri-modality imaging. *Biomaterials* **2012,** *33* (18), 4618-4627.

239. Wang, Z.; Xing, B., Near-Infrared Multipurpose Lanthanide-Imaging Nanoprobes. *Chem. Asian J.* **2020,** *15* (14), 2076-2091.

240. Ferezou, I.; Bolea, S.; Petersen, C. C. H., Visualizing the Cortical Representation of Whisker Touch: Voltage-Sensitive Dye Imaging in Freely Moving Mice. *Neuron* **2006,** *50* (4),

617-629.

241. Maji, S. K.; Sreejith, S.; Joseph, J.; Lin, M.; He, T.; Tong, Y.; Sun, H.; Yu, S. W.-K.; Zhao, Y., Upconversion Nanoparticles as a Contrast Agent for Photoacoustic Imaging in Live Mice. *Adv. Mater.* **2014,** *26* (32), 5633-5638.

242. Lee, T.; Baac, H. W.; Li, Q.; Guo, L. J., Efficient Photoacoustic Conversion in Optical Nanomaterials and Composites. *Adv. Opt. Mater.* **2018,** *6* (24), 1800491.

243. Zhou, J.; del Rosal, B.; Jaque, D.; Uchiyama, S.; Jin, D., Advances and challenges for fluorescence nanothermometry. *Nat. Methods* **2020,** *17* (10), 967-980.

244. Wade, S. A.; Collins, S. F.; Baxter, G. W., Fluorescence intensity ratio technique for optical fiber point temperature sensing. *J. Appl. Phys.* **2003,** *94*, 4743-4756.

245. Bradac, C.; Lim, S. F.; Chang, H.-C.; Aharonovich, I., Optical Nanoscale Thermometry: From Fundamental Mechanisms to Emerging Practical Applications. *Adv. Opt. Mater.* **2020,** *8*, 2000183.

246. Vetrone, F.; Naccache, R.; Zamarrón, A.; Juarranz de la Fuente, A.; Sanz-Rodríguez, F.; Martinez Maestro, L.; Martín Rodriguez, E.; Jaque, D.; García Solé, J.; Capobianco, J. A., Temperature Sensing Using Fluorescent Nanothermometers. *ACS Nano* **2010,** *4* (6), 3254-3258.

247. Weissleder, R.; Pittet, M. J., Imaging in the era of molecular oncology. *Nature* **2008,** *452*, 580-589.

248. Dolmans, D. E. J. G. J.; Fukumura, D.; Jain, R. K., Photodynamic therapy for cancer. *Nat. Rev.* **2003,** *3*, 380-387.

249. Tsang, M.-K.; Wong, Y.-T.; Hao, J., Cutting-Edge Nanomaterials for Advanced Multimodal Bioimaging Applications. *Small Methods* **2018,** *2*, 1700265.

250. Sharma, P.; Brown, S.; Walter, G.; Santra, S.; Moudgil, B., Nanoparticles for bioimaging. *Adv. Colloid Interface Sci.* **2006,** *123–126*, 471–485.

251. Smith, A. M.; Mancini, M. C.; Nie, S., Bioimaging: second window for in vivo imaging. *Nat. Nanotechnol.* **2009,** *4* (11), 710-711.

252. Welsher, K.; Sherlock, S. P.; Dai, H., Deep-tissue anatomical imaging of mice using

carbon nanotube fluorophores in the second near-infrared window. *PNAS* **2011,** *108*, 8943–8948.

253. Hong, G.; Diao, S.; Chang, J.; Antaris, A. L.; Chen, C.; BoZhang; Zhao, S.; Atochin, D. N.; Huang, P. L.; Andreasson, K. I.; Kuo, C. J.; Dai, H., Through-skull fluorescence imaging of the brain in a new near-infrared window. *Nat. Photonics* **2014,** *8*, 723-730.

254. Diao, S.; Hong, G.; Antaris, A. L.; Blackburn, J. L.; Cheng, K.; Cheng, Z.; Dai, H., Biological imaging without autofluorescence in the second near-infrared region. *Nano Res.* **2015,** *8*, 3027-3034.

255. Xu, J.; Gulzar, A.; Yang, P.; Bi, H.; Yang, D.; Gai, S.; He, F.; Lin, J.; Xing, B.; Jin, D., Recent advances in near-infrared emitting lanthanide-doped nanoconstructs: Mechanism, design and application for bioimaging. *Coord. Chem. Rev.* **2019,** *381*, 104–134.

256. Dong, H.; Du, S.-R.; Zheng, X.-Y.; Lyu, G.-M.; Sun, L.-D.; Li, L.-D.; Zhang, P.-Z.; Zhang, C.; Yan, C.-H., Lanthanide Nanoparticles: From Design toward Bioimaging and Therapy. *Chem. Rev.* **2015,** *115*, 10725−10815.

257. Ding, Y.; Gu, J.; Ke, J.; Zhang, Y.-W.; Yan, C.-H., Sodium Doping Controlled Synthesis of Monodisperse Lanthanide Oxysulfide Ultrathin Nanoplates Guided by Density Functional Calculations. *Angew. Chem. Int. Ed.* **2011,** *50*, 12330 –12334.

258. Larquet, C.; Carriere, D.; Nguyen, A.-M.; Le, T. K.-C.; Frogneux-Plé, X.; Génois, I.; Griel, P. L.; Gauzzi, A.; Sanchez, C.; Carenco, S., Unraveling the Role of Alkali Cations in the growth Mechanism of Gd_2O_2S Nanoparticles. *Chem. Mater.* **2020,** *32* (3), 1131-1139.

259. Wang, T.; Yang, M.; Huang, J.; Zhao, Y.; Wang, H.; Leng, S.; Chen, J.; Sun, G.; Liu, J., NIR-to-NIR UCL/T1-weighted MR/CT multimodal imaging by $NaYbF_4$:Tm@$NaGdF_4$:Yb-PVP upconversion nanoparticles. *Sci. Bull.* **2017,** *62*, 903–912.

260. Machado, I. P.; Teixeira, V. C.; Pedroso, C. C. S.; Brito, H. F.; Rodrigues, L. C. V., X-ray scintillator $Gd_2O_2S:Tb^{3+}$ materials obtained by a rapid and cost-effective microwave-assisted solid-state synthesis. *J. Alloys Compd.* **2019,** *777*, 638-645.

261. Gao, Y.; Li, R.; Zheng, W.; Shang, X.; Zhang, M.; Xu, J.; You, W.; Chen, Z.; Chen, X., Broadband NIR photostimulated luminescence nanoprobes based on CaS:Eu^{2+},Sm^{3+} nanocrystals. *Chem. Sci.* **2019,** *10*, 5452–5460.

262. Zhang, T.; Gu, J.; Ding, Y.; Zhang, Y.-W.; Yan, C.-H., Experimental and Theoretical Studies on the Controlled Synthesis of Alkali-Metal-Doped Rare-Earth Oxysulfide Nanocrystals. *ChemPlusChem* **2013,** *78*, 515-521.

263. Larquet, C.; Hourlier, D.; Nguyen, A.-M.; Torres-Pardo, A.; Gauzzi, A.; Sanchez, C.; Carenco, S., Thermal stability of Oleate-Stabilized Gd2O2S Nanoplates in Inert and Oxidizing Atmospheres. *ChemNanoMat* **2019,** *5*, 539-546.

264. Ryan, J. R.; Beach, R., Optical absorption and stimulated emission of neodymium in yttrium lithium fluoride. *J. Opt. Soc. Am. B* **1992,** *9*, 1883-1887.

265. Kumar, K. U.; Babu, P.; Jang, K. H.; Seo, H. J.; Jayasankar, C. K.; Joshi, A. S., Spectroscopic and 1.06 μm laser properties of Nd^{3+}-doped K–Sr–Al phosphate and fluorophosphate glasses. *J. Alloys Compd.* **2008,** *458* (1), 509-516.

266. Ramachari, D.; Rama Moorthy, L.; Jayasankar, C. K., Optical absorption and emission properties of Nd^{3+}-doped oxyfluorosilicate glasses for solid state lasers. *Infrared Phys. Technol.* **2014,** *67*, 555-559.

267. Ryan, J. R.; Beach, R., Optical absorption and stimulated emission of neodymium in yttrium lithium fluoride. *J. Opt. Soc. Am. B* **1992,** *9* (10), 1883-1887.

268. Zhou, Z.; Lu, Z.-R., Gadolinium-based contrast agents for magnetic resonance cancer imaging. *WIREs Nanomed. Nanobiotechnol.* **2013,** *5*, 1-18.

269. Dong, N.-N.; Pedroni, M.; Piccinelli, F.; Conti, G.; Sbarbati, A.; Ramírez-Hernández, J. E.; Maestro, L. M.; Cruz, M. d. C. I. d. l.; Sanz-Rodríguez, F.; Juarranz, A.; Chen, F.; Vetrone, F.; Capobianco, J. A.; Solé, J. G.; Bettinelli, M.; Jaque, D.; Speghini, A., NIR-to-NIR Two-Photon Excited CaF_2: Tm^{3+},Yb^{3+} Nanoparticles: Multifunctional Nanoprobes for Highly Penetrating Fluorescence Bio-Imaging. *ACS Nano* **2011,** *5*, 8665–8671.

270. Wu, L.; Hu, J.; Zou, Q.; Lin, Y.; Huang, D.; Chen, D.; Lu, H.; Zhu, H.,

Synthesis and optical properties of a $Y_3(Al/Ga)_5O_{12}:Ce^{3+},Cr^{3+},Nd^{3+}$ persistent luminescence nanophosphor: a promising near-infrared-II nanoprobe for biological applications. *Nanoscale* **2020,** *12*, 14180–14187.

271. Rocha, U.; Kumar, K. U.; Jacinto, C.; Villa, I.; Sanz-Rodríguez, F.; Cruz, M. d. C. I. d. l.; Juarranz, A.; Carrasco, E.; Veggel, F. C. J. M. v.; Bovero, E.; Solé, J. G.; Jaque, D., Neodymium-Doped LaF_3 Nanoparticles for Fluorescence Bioimaging in the Second Biological Window. *Small* **2014,** *10*, 1141–1154.

272. Qin, Q.-S.; Zhang, P.-Z.; Sun, L.-D.; Shi, S.; Chen, N.-X.; Dong, H.; Zheng, X.-Y.; Li, L.-M.; Yan, C.-H., Ultralow-power near-infrared excited neodymium-doped nanoparticles for long-term in vivo bioimaging. *Nanocale* **2017,** *9*, 4660–4664.

273. Kwon, S. G.; Krylova, G.; Phillips, P. J.; Klie, R. F.; Chattopadhyay, S.; Shibata, T.; Bunel, E. E.; Liu, Y.; Prakapenka, V. B.; Lee, B.; Shevchenko, E. V., Heterogeneous nucleation and shape transformation of multicomponent metallic nanostructures. *Nat. Mater.* **2015,** *14*, 215-223.

274. Jang, Y.; Shapiro, A.; Isarov, M.; Rubin-Brusilovski, A.; Safran, A.; Budniak, A. K.; Horani, F.; Dehnel, J.; Sashchiuk, A.; Lifshitz, E., Interface control of electronic and optical properties in IV–VI and II–VI core/shell colloidal quantum dots: a review. *Chem. Commun.* **2017,** *53*, 1002-1024.

275. Zheng, K.; Loh, K. Y.; Wang, Y.; Chen, Q.; Fan, J.; Jung, T.; Nam, S. H.; Suh, Y. D.; Liu, X., Recent advances in upconversion nanocrystals: Expanding the kaleidoscopic toolbox for emerging applications. *Nano Today* **2019,** *29*.

276. Su, Q.; Han, S.; Xie, X.; Zhu, H.; Chen, H.; Chen, C.-K.; Liu, R.-S.; Chen, X.; Wang, F.; Liu, X., The Effect of Surface Coating on Energy Migration-Mediated Upconversion. *J. Am. Chem. Soc.* **2012,** *134* (51), 20849-20857.

277. Zhou, B.; Yan, L.; Huang, J.; Liu, X.; Tao, L.; Zhang, Q., NIR II-responsive photon upconversion through energy migration in an ytterbium sublattice. *Nat. Photonics* **2020,** *14*, 760-766.

278. Swabeck, J. K.; Fischer, S.; Bronstein, N. D.; Alivisatos, A. P., Broadband

Sensitization of Lanthanide Emission with Indium Phosphide Quantum Dots for Visible to Near-Infrared Downshifting. *J. Am. Chem. Soc.* **2018,** *140*, 9120−9126.

279. Ruan, L.; Zhang, Y., NIR-excitable heterostructured upconversion perovskite nanodots with improved stability. *Nat. Comm.* **2021,** *12*.

280. Würth, C.; Kaiser, M.; Wilhelm, S.; Grauel, B.; Hirsch, T.; Resch-Genger, U., Excitation power dependent population pathways and absolute quantum yields of upconversion nanoparticles in different solvents. *Nanoscale* **2017,** *9*, 4283-4294.

281. Würth, C.; Pauli, J.; Lochmann, C.; Spieles, M.; Resch-Genger, U., Integrating Sphere Setup for the Traceable Measurement of Absolute Photoluminescence Quantum Yields in the Near Infrared. *Anal. Chem.* **2012,** *84*, 1345−1352.

282. Ronny Costi; Saunders, A. E.; Banin, U., Colloidal Hybrid Nanostructures: A New Type of Functional Materials. *Angew. Chem. Int. Ed.* **2010,** *49*, 4878-4897.

283. Carbonea, L.; Cozzoli, D., Colloidal heterostructured nanocrystals: Synthesis and growth mechanisms. *Nano Today* **2010,** *5*, 449-493.

284. Zhang, J.; Tang, Y.; Lee, K.; Ouyang, M., Nonepitaxial Growth of Hybrid Core-Shell Nanostructures with Large Lattice Mismatches. *Science* **2010,** *327*, 1634-1638.

285. Chen, H.; Zhang, P.; Cui, H.; Qin, W.; Zhao, D., Synthesis and Luminescence Properties of Water Soluble α-$NaGdF_4$/β-$NaYF_4$:Yb,Er Core–Shell Nanoparticles. *Nanoscale Res. Lett.* **2017,** *12*, 548.

286. Shao, Q.; Yang, C.; Chen, X.; Zhang, H.; Feng, G.; Zhou, S., Core-mediated synthesis, growth mechanism and near-infrared luminescence enhancement of α-$NaGdF_4$@β-$NaLuF_4$:Nd^{3+} core–shell nanocrystals. *CrystEngComm* **2020,** *22*, 1359-1367.

287. Naccache, R.; Yu, Q.; Capobianco, J. A., The Fluoride Host: Nucleation, Growth, and Upconversion of Lanthanide-Doped Nanoparticles. *Adv. Opt. Mater.* **2015,** *3*, 482-509.

288. Peng, X.; Schlamp, M. C.; Kadavanich, A. V.; Alivisatos, A. P., Epitaxial Growth of Highly Luminescent CdSe/CdS Core/Shell Nanocrystals with Photostability and Electronic Accessibility. *J. Am. Chem. Soc.* **1997,** *119*, 7019-7029.

289. Peng, X.; Wickham, J.; Alivisatos, A. P., Kinetics of II-VI and III-V Colloidal

Semiconductor Nanocrystal Growth: "Focusing" of Size Distributions. *J. Am. Chem. Soc.* **1998,** *120*, 5343-5344.

290. Johnson, N. J. J.; Korinek, A.; Dong, C.; Veggel, F. C. J. M. v., Self-Focusing by Ostwald Ripening: A Strategy for Layer-by-Layer Epitaxial Growth on Upconverting Nanocrystals. *J. Am. Chem. Soc.* **2012,** *134*, 11068−11071.

291. Zhao, D.; Chen, H.; Zheng, K.; Chuai, X.; Yu, F.; Li, H.; Wu, C.; Qin, G.; Di, W.; Qin, W., Growth of hexagonal phase sodium rare earth tetrafluorides induced by heterogeneous cubic phase core. *RSC Adv.* **2014,** *4*, 13490–13494.

292. Chen, X.; Peng, D.; Ju, Q.; Wang, F., Photon upconversion in core–shell nanoparticles. *Chem. Soc. Rev.* **2015,** *44*, 1318-1330.

293. Zhao, Y.; Riemersma, C.; Pietra, F.; Koole, R.; de Mello Donegá, C.; Meijerink, A., High-Temperature Luminescence Quenching of Colloidal Quantum Dots. *ACS Nano* **2012,** *6* (10), 9058-9067.

294. Lin, Y.-C.; Bettinelli, M.; Karlsson, M., Unraveling the Mechanisms of Thermal Quenching of Luminescence in Ce^{3+}-Doped Garnet Phosphors. *Chem. Mater.* **2019,** *31* (11), 3851-3862.

295. Chen, B.; Wang, F., Emerging Frontiers of Upconversion Nanoparticles. *Trends Chem.* **2020,** *2* (5), 427-439.

296. Shi, R.; Martinez, E. D.; Brites, C. D. S.; Carlos, L. D., Thermal enhancement of upconversion emission in nanocrystals: a comprehensive summary. *Phys. Chem. Chem. Phys.* **2021,** *23*, 20-42.

297. Suyver, J. F.; Grimm, J.; Krämer, K. W.; Güdel, H. U., Highly efficient near-infrared to visible up-conversion process in $NaYF_4:Er^{3+},Yb^{3+}$. *J. Lumin.* **2005,** *114* (1), 53-59.

298. Li, D.; Shao, Q.; Dong, Y.; Jiang, J., Anomalous Temperature-Dependent Upconversion Luminescence of Small-Sized $NaYF_4:Yb^{3+}$, Er^{3+} Nanoparticles. *J. Phys. Chem. C* **2014,** *118* (39), 22807-22813.

299. Liu, G. K.; Chen, X. Y.; Zhuang, H. Z.; Li, S.; Niedbala, R. S., Confinement of electron–phonon interaction on luminescence dynamics in nanophosphors of $Er^{3+}:Y_2O_2S$ *J.*

Solid State Chem. **2003,** *171* (1-2), 123-132.

300. Zou, H.; Yang, X.; Chen, B.; Du, Y.; Ren, B.; Sun, X.; Qiao, X.; Zhang, Q.; Wang, F., Thermal Enhancement of Upconversion by Negative Lattice Expansion in Orthorhombic $Yb_2W_3O_{12}$. *Angew. Chem. Int. Ed.* **2019,** *58* (48), 17255-17259.

301. Hu, Y.; Shao, Q.; Dong, Y.; Jiang, J., Energy Loss Mechanism of Upconversion Core/Shell Nanocrystals. *J. Phys. Chem. C* **2019,** *123*.

302. Wang, Z.; Christiansen, J.; Wezendonk, D.; Xie, X.; van Huis, M. A.; Meijerink, A., Thermal enhancement and quenching of upconversion emission in nanocrystals. *Nanoscale* **2019,** *11* (25), 12188-12197.

303. Martínez, E. D.; Brites, C. D. S.; Carlos, L. D.; García-Flores, A. F.; Urbano, R. R.; Rettori, C., Electrochromic Switch Devices Mixing Small- and Large-Sized Upconverting Nanocrystals. *Adv. Funct. Mater.* **2019,** *29* (8), 1807758.

304. Cui, X.; Cheng, Y.; Lin, H.; Huang, F.; Wu, Q.; Wang, Y., Size-dependent abnormal thermo-enhanced luminescence of ytterbium-doped nanoparticles. *Nanoscale* **2017,** *9*, 13794–13799.

305. Zhou, J.; Wen, S.; Liao, J.; Clarke, C.; Tawfik, S. A.; Ren, W.; Mi, C.; Wang, F.; Jin, D., Activation of the surface dark-layer to enhance upconversion in a thermal field. *Nat. Photon.* **2018,** *12*, 154-158.

306. Brites, C. D. S.; Lima, P. P.; Silva, N. J. O.; Millán, A.; Amaral, V. S.; Palacio, F.; Carlos, L. D., A Luminescent Molecular Thermometer for Long-Term Absolute Temperature Measurements at the Nanoscale. *Adv. Mater.* **2010,** *22* (40), 4499-4504.

307. Tian, X.; Dou, H.; Wu, L., Photoluminescence and thermometry properties of upconversion phosphor NaBiF4: Yb^{3+}/Tm^{3+}. *Opt. Mater.* **2020,** *99*, 109544.

308. Bünzli, J.-C. G., On the design of highly luminescent lanthanide complexes. *Coord. Chem. Rev.* **2015,** *293-294*, 19-47.

309. Zhao, J.; Chen, X.; Chen, B.; Luo, X.; Sun, T.; Zhang, W.; Wang, C.; Lin, J.; Su, D.; Qiao, X.; Wang, F., Accurate Control of Core–Shell Upconversion Nanoparticles through Anisotropic Strain Engineering. *Adv. Funct. Mater.* **2019,** *1903295*.

310. Wu, X.; Zhan, S.; Han, J.; Liu, Y., Nanoscale Ultrasensitive Temperature Sensing Based on Upconversion Nanoparticles with Lattice Self-Adaptation. *Nano Lett.* **2021,** *21* (1), 272-278.

311. Pawley, G., Unit-cell refinement from powder diffraction scans. *J. Appl. Cryst.* **1981,** *14* (6), 357-361.

312. Lay, A.; Siefe, C.; Fischer, S.; Mehlenbacher, R. D.; Ke, F.; Mao, W. L.; Alivisatos, A. P.; Goodman, M. B.; Dionne, J. A., Bright, Mechanosensitive Upconversion with Cubic-Phase Heteroepitaxial Core−Shell Nanoparticles. *Nano Lett.* **2018,** *18*, 4454−4459.

313. Lay, A.; Wang, D. S.; Wisser, M. D.; Mehlenbacher, R. D.; Lin, Y.; Goodman, M. B.; Mao, W. L.; Dionne, J. A., Upconverting Nanoparticles as Optical Sensors of Nano- to MicroNewton Forces. *Nano Lett.* **2017,** *17*, 4172−4177.

314. Brites, C. D. S.; Balabhadra, S.; Carlos, L. D., Lanthanide-Based Thermometers: At the Cutting-Edge of Luminescence Thermometry. *Adv. Opt. Mater.* **2019,** *7*, 1801239.

315. Savchuk, O.; Marti, J. J. C.; Cascales, C.; Haro-Gonzalez, P.; Diaz, F.; Sanz-Rodríguez, F.; Aguilo, M., Bifunctional Tm^{3+},Yb^{3+}:$GdVO_4$@SiO_2 Core-Shell Nanoparticles in HeLa Cells: Upconversion Luminescence Nanothermometry in the First Biological Window and Biolabelling in the Visible. *Nanomaterials 2020, 10, 993* **2020,** *10*, 993.

316. Xing, L.; Xu, Y.; Wang, R.; Xu, W.; Zhang, Z., Highly sensitive optical thermometry based on upconversion emissions in Tm^{3+}/Yb^{3+} codoped $LiNbO_3$ single crystal. *Opt. Lett.* **2014,** *39*, 454-457.

317. Min, Q.; Bian, W.; Qi, Y.; Lu, W.; Yu, X.; Xu, X.; Zhou, D.; Qiu, J., Temperature sensing based on the up-conversion emission of Tm^{3+} in a single $KLuF_4$ microcrystal. *J. Alloys Compd.* **2017,** *728*, 1037-1042.

318. Runowskia, M.; Bartkowiaka, A.; Majewskaa, M.; Martínb, I. R.; Lisa, S., Upconverting lanthanide doped fluoride $NaLuF_4$:Yb^{3+}-Er^{3+}-Ho^{3+} - optical sensor for multi-range fluorescence intensity ratio (FIR) thermometry in visible and NIR regions. *J. Lumin.* **2018,** *201*, 104-109.

319. Runowski, M.; Stopikowska, N.; Szeremeta, D.; Goderski, S.; Skwierczyńska, M.;

Lis, S., Upconverting Lanthanide Fluoride Core@Shell Nanorods for Luminescent Thermometry in the First and Second Biological Windows: β-NaYF4:Yb^{3+} − Er^{3+}@SiO_2 Temperature Sensor. *ACS Appl. Mater. Interfaces* **2019,** *11*, 13389−13396.

320. Singh, S. K.; Kumar, K.; Rai, S. B., Er^{3+}/Yb^{3+} codoped Gd_2O_3 nano-phosphor for optical thermometry. *Sens. Actuators A Phys.* **2009,** *149*, 16-20.

321. Vetrone, F.; Naccache, R.; Zamarrón, A.; Fuente, A. J. d. l.; Sanz-Rodríguez, F.; Maestro, L. M.; Rodriguez, E. M.; Jaque, D.; Solé, J. G.; Capobianco, J. A., Temperature Sensing Using Fluorescent Nanothermometers. *ACS Nano* **2010,** *4*, 3254–3258.

322. Wolfbeis, O. S., An overview of nanoparticles commonly used in fluorescent bioimaging. *Chem. Soc. Rev.* **2015,** *44* (14), 4743-68.

323. Wiesholler, L. M.; Frenzel, F.; Grauel, B.; Würth, C.; Resch-Genger, U.; Hirsch, T., Yb,Nd,Er-doped upconversion nanoparticles: 980 nm versus 808 nm excitation. *Nanoscale* **2019,** *11*, 13440-13449.

324. Marciniak, Ł.; Bednarkiewicz, A.; Stefanski, M.; Tomala, R.; Hreniak, D.; Strek, W., Near infrared absorbing near infrared emitting highly-sensitive luminescent nanothermometer based on Nd^{3+} to Yb^{3+} energy transfer. *Phys. Chem. Chem. Phys.* **2015,** *17* (37), 24315-24321.

325. Demirbas, U.; Thesinga, J.; Kellert, M.; Kartner, F. X.; Pergament, M., Detailed investigation of absorption, emission and gain in Yb:YLF in the 78–300K range. *Opt. Mater. Exp.* **2021,** *11*, 250-272.

326. Sontakke, A. D.; Biswas, K.; Sen, R.; Annapurna, K., Efficient non-resonant energy transfer in Nd^{3+}-Yb^{3+} codoped BaAl-metaphosphate glasses. *J. Opt. Soc. Am. B* **2010,** *27*, 2750-2758.

Résumé de Thése

Les nanoparticules (NPs) sont des matériaux dans la plage de taille de 1 à 100 nm dans une dimension au moins, ont suscité un énorme intérêt en raison de leurs propriétés optiques, électroniques et magnétiques uniques qui découlent d'une combinaison de leurs caractéristiques intrinsèques telles que la taille, la forme, structure, la composition chimique et les types de molécules fonctionnalisées à la surface. Une variété de nanoparticules inorganiques ont été développées en tant que nanosondes pour l'imagerie, l'affichage, la thérapie et les applications optogénétiques ces dernières années. Leurs propriétés optiques, électroniques et magnétiques uniques peuvent être affinées en contrôlant la composition chimique, la taille, la morphologie, les groupes de surface et la structure des NPs, qui s'adaptent aux exigences de diverses utilisations.

Les NPs métalliques sont purement synthétisées à partir de précurseurs métalliques et peuvent posséder de nombreux types de propriétés qui sont déterminées par la composition, la taille, la forme et la structure. Deux propriétés caractéristiques des NPs métalliques sont le superparamagnétisme et la résonance plasmonique de surface (SPR).[1] Les nanoparticules d'oxyde métallique présentent une grande variété de tailles, de formes, de structures et de propriétés, ce qui les rend très attrayantes pour diverses applications.[2-3] On constate que les tailles, les formes et les structures peuvent affecter de manière significative les propriétés des NPs d'oxyde métallique.[1] Par exemple, les NPs de Cu_2O présentent des facettes possédant des propriétés catalytiques ainsi des faces 111 Cu_2O octaédriques montrent une réactivité plus élevée envers la réaction de couplage C-N que les faces cubiques 100.[4] Cependant, la faible réactivité du Cu_2O des faces cubiques 100 peut être améliorée par le processus de gravure assistée par O_2 qui fournit plus de sites actifs sur les nanocubes obtenus.[5] Les quantums dotes (QDs) semi-conducteurs sont de petits nanocristaux inorganiques qui, dans une plage de tailles allant de 1 à 10 nm de diamètre, présentent des effets de confinement quantique.[6] Un seul cristal QD contient plusieurs centaines à plusieurs milliers d'atomes. Ces QDs sont généralement composés de semi-conducteurs III-V, II-VI, IV et IV-VI.[7] Ils peuvent être

synthétisés par une technique de croissance épitaxiale bien établie, telle que le dépôt en phase vapeur organométallique et l'épitaxie par faisceau moléculaire, différemment, les QDs colloïdaux peuvent être obtenus par la méthode de chimie humide.[7] Les nanoparticules à base de carbone, notamment les fullerènes, les nanotubes de carbone, le graphène, l'oxyde de graphène, les nanodiamants et les quantums dotes à base de carbone, ont été largement étudiés en raison de leurs diverses propriétés chimiques et physiques telles que les performances thermiques, mécaniques, électriques, optiques et structurelles.[8-10] L'une des principales caractéristiques des fullerènes est qu'ils sont capables d'agir comme sensibilisateurs pour la production d'oxygène singulet ($^1O_2$) et d'autres espèces réactives de l'oxygène (ROS) sous excitation lumineuse. Par conséquent, ils sont utilisés pour la stérilisation du sang et la thérapie photodynamique du cancer.[11-12] Cependant, la faible dispersibilité des fullerènes dans l'eau limite leurs bio-applications bien que plusieurs méthodes concernant la fonctionnalisation hydrophile de surface des fullerènes aient été rapportées.[13] Les NP de pérovskite entièrement inorganique (AIP), y compris les QDs de faible dimension et les nanocristaux (NCs), en tant que nanomatériaux émergents, ont récemment attiré énormément d'attention en raison de leurs excellentes propriétés optoélectroniques, de leurs rendement quantique (QY) de photoluminescence élevés et de leur synthèse facile,[14-17] montrant une grande promesse dans l'utilisation des cellules solaires[18-20], diodes électroluminescentes[21], photoélectrochimie[22], et photodétecteurs[17]. La formule chimique générale de l'AIP est ABX_3 où A représente un cation monovalent tel que Cs^+ ou Rb^+, l'espèce B représente un cation métallique divalent tel que Pb^{2+}, Sn^{2+} ou Ge^{2+} et l'espèce X représente un anion halogénure monovalent tel que I^-, Br^-, ou Cl^-.[23]

Au cours des dernières décennies, les nanoparticules inorganiques dopées au lanthanide (Ln^{3+}) ont attiré beaucoup d'attention en raison de leurs avantages d'émissions à bande étroite, d'une longue durée de vie de fluorescence, d'importants décalages anti-Stokes, d'une résistance élevée au photoblanchiment, d'une faible toxicité et d'une large gamme de longueurs d'onde d'émission. Ils ont donc été appliqués

pour une large gamme d'applications telles que la bio-détection sans arrière-plan, l'administration de médicaments déclenchés par la lumière, la thérapie contre le cancer, la bio-imagerie multifonctionnelle, la mesure température, la récupération de l'énergie solaire et la microscopie à super-résolution[24-27]. Les ions Ln^{3+} ont une configuration électronique générale $[Xe]4f^N$ (N = 0-14) qui est la clé des propriétés chimiques et spectroscopiques des ions Ln^{3+}.[28] Parmi les ions Ln^{3+}, le cation La^{3+} n'a pas d'électrons 4f, tandis que Ln^{3+} a une sous-couche 4f remplie ou partiellement remplie. On voit que les électrons de valence dans les orbitales 4f des ions Ln^{3+} sont protégés, en particulier par les sous-couches $5s^2$ et $5p^6$ remplies, ce qui entraîne de faibles interactions des électrons de valence avec l'environnement, et des interactions de couplage électron-phonon minimales.[27] Pour cette raison, les transitions 4f-4f de la couche interne de Ln^{3+} présentent des pics fins et une identification facile dans les spectres d'émission.

Lorsque les ions Ln^{3+} dopants sont dans des matériaux appropriés, la luminescence peut être obtenue en utilisant diverses sources lumineuses d'excitation telles que les rayons X, les lampes UV-visible et les lasers. Lorsque la longueur d'onde incidente est plus courte que la longueur d'onde d'émission, le processus est appelé Stokes ou luminescence descendante (DSL). Au contraire, le processus de luminescence anti-Stokes nécessite que la longueur d'onde incidente soit plus grande que la longueur d'onde d'émission, ce qui est connu sous le nom de luminescence de conversion ascendante (UCL). Les NPs dopées aux ions Eu^{3+}, Tb^{3+}, Dy^{3+}, Sm^{3+}, Er^{3+}, Nd^{3+} présentant une DSL intense avec des pics fins et de longues durées de vie, sont largement utilisées pour la biodétection in vitro, le biomarquage multicolore et la détection de PL résolue en temps (TR).

La conversion ascendante est un processus optique non linéaire qui convertit deux ou plusieurs photons de faible énergie (généralement situés dans la région NIR) en un photon émis d'énergie plus élevée allant de l'UV au NIR. Ce phénomène a été prédit en 1959 par Bloembergen et observé indépendamment par Auzel, Ovsyankin et Feofilov au milieu des années 1960. Jusqu'à présent, cinq types de mécanismes populaires ont

été proposés pour expliquer le processus UC: absorption à l'état fondamental/absorption à l'état excité (GSA/ESA), transfert d'énergie (ETU), avalanche de photons (PA), upconversion de sensibilisation coopérative (CSU), et la migration d'énergie UC (EMU), comme le montre la Figure R-1.

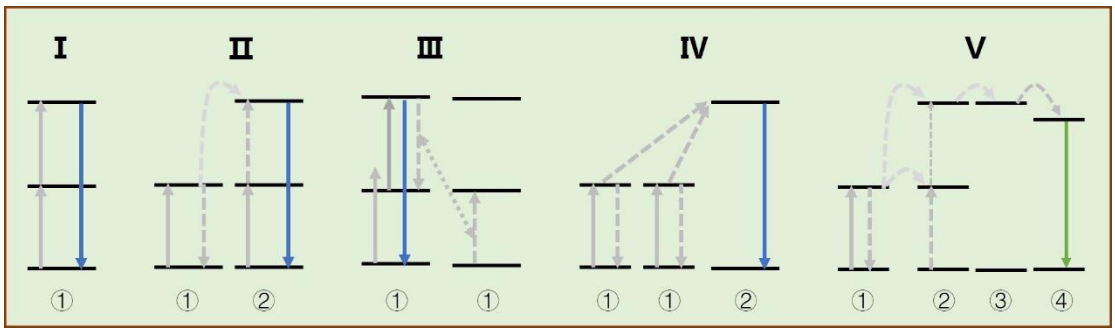

Figure R-1 Cinq diagrammes de niveau d'énergie simplifiés décrivant les mécanismes UC rapportés. I: GSA/ESA, II: ETU, III: PA, IV: CSU, et V: EMU.

Pour obtenir une UCL efficace, des matériaux hôtes appropriés avec une faible énergie de phonons et une faible symétrie de site sont très importants. Le candidat hôte populaire est $NaYF_4$ pour UCL en raison de son rendement quantique UC le plus élevé (UCQY). Par exemple, les valeurs UCQY les plus élevées de 9 % et 10 % ont été signalées à une densité de puissance similaire de 20 W/cm^2 pour des NPs de type 45 $NaYF_4$:Yb^{3+},Er^{3+}@$NaYF_4$ coeur/coquille[29] ayant 45 nm de taille et pour des matériaux de type $NaYF_4$:Yb^{3+},Er^{3+} matériau en vrac[30] de 3 µm de taille.

Parmi les hôtes, La famille de matériaux de type RE_2O_2S par ex. les Gd_2O_2S de phase hexagonale avec une structure trigonale (groupe d'espace *P-3m1*) ont été largement étudiés pour leur UCL depuis de nombreuses années en raison de leur faible énergie de phonons (Gd_2O_2S, 520 cm^{-1}). En 2013, Martín-Rodriguez et al. ont rapporté les valeurs UCQY de 12 ± 1% et 8,9 ± 0,7% pour Gd_2O_2S:10%Er et β-$NaYF_4$:25%Er optimisés, respectivement, montrant l'efficacité UCL plus élevée de Gd_2O_2S:10%Er que β-$NaYF_4$:25%Er sous excitation monochromatique vers 1500 nm à une puissance de 700 W/m^2.[31] La même année, Pokhrel et al. ont trouvé que l'UCQY dans les luminophores M_2O_2S:Yb^{3+}/Er^{3+} (M = Gd, Y, La) est 3 à 4 fois plus élevé que celui de

β-$NaYF_4$:20%Yb^{3+}/2%Er^{3+} à des densités de puissance d'excitation plus faibles.[32]

Classiquement, la poudre de RE_2O_2S peut être synthétisée par sulfuration partielle d'oxydes, oxydation de sulfures ou réduction de sulfates sous haute température et atmosphère spécifique.[33] Les grosses particules produites limitent leurs applications dans le milieu de la biomédecine. Plusieurs stratégies de synthèse des NPs RE_2O_2S ont également été démontrées. Par exemple, notre groupe a rapporté une nouvelle stratégie pour la synthèse des NPs Gd_2O_2S:Eu.[34] Dans cette stratégie, les nitrates de terres rares et l'urée ont été ajoutés dans un mélange eau/éthanol, suite à une dissolution, le précurseur hydroxycarbonate de terre rare s'est formé. Après purification, la poudre obtenue a d'abord été sulfurée par Ar/H_2S à 750 °C pendant 90 min, puis maintenue dans une atmosphère d'argon uniquement à 850 °C pendant 4 h. Les produits finaux étaient des NPs de Gd_2O_2S cristallines et sphériques après analyse par XRD et TEM. Il est important de noter que le diamètre des NPs peut être ajusté en ajustant le rapport eau/éthanol et le temps de réaction. Au cours des années suivantes, nous avons démontré que les NPs Gd_2O_2S dopées Ln^{3+} synthétisées par cette méthode ou avec une légère modification étaient utilisées avec succès pour diverses applications telles que le biomarquage, la fluorescence, la résonance magnétique (MR) et la bio-imagerie par tomodensitométrie (CT).[35-38] Cependant, il existe des inconvénients tels qu'une procédure de synthèse sophistiquée, des conditions de réaction rigoureuses, des agrégations évitables et une grande taille de NP résultantes, qui limitent encore les bioapplications étendues des NPs Gd_2O_2S.

Les autres stratégies basées sur un milieu organique pour la synthèse de RE_2O_2S, y compris les NPs Gd_2O_2S, ont été rapportées ces dernières années. Les NPs obtenues sont enrobées de ligands organiques, monodispersées, de petite taille (allant de 5 à 40 nm) et de multiples formes disponibles. Cependant, il y a encore quelques obstacles:

1) aucune méthode de synthèse générale n'a été signalée pour préparer des NPs de Gd_2O_2S de petite taille, hautement cristallisées, bien dispersées et à haut rendement ;

2) aucun autre exemple de construction de noyau/coquille n'a été signalé pour les

NPs de Gd_2O_2S;

3) aucune stratégie de modification de surface efficace n'a été signalée pour transférer le Gd_2O_2S revêtu de ligand organique hydrophobe à hydrophile.

Dans **le chapitre 2**, les NPs Gd_2O_2S ultrapetites ont d'abord été synthétisées par une méthode de décomposition à haute température améliorée avec la présence d'OA, d'OM et de TOA comme surfactant, de DPTU comme source de soufre et de LiOH comme minéralisateur (Figure R-2). En utilisant cette méthode, les conditions de réaction, y compris la quantité de DPTU, la composition du solvant, la température et le temps de réaction et la quantité de LiOH, ont été optimisées pour obtenir des NPs Gd_2O_2S hexagonales monodispersées, de petite taille et sphériques. La cristallinité élevée des NPs a été confirmée par des analyses XRD et TEM. La taille moyenne de 5,9 ± 0,8 nm a été enregistrée pour les conditions de synthèse optimisées. De manière frappante, nous avons obtenu 14 autres types de NPs RE_2O_2S (RE = Y, La, Ce, Pr, Nd, Sm, Eu, Tb, Dy, Ho, Er, Tm, Yb et Lu) avec une bonne dispersité et une cristallinité élevée, et les tailles moyennes vont de ~3 à ~10 nm, démontrant la polyvalence de la méthode de décomposition à haute température améliorée.

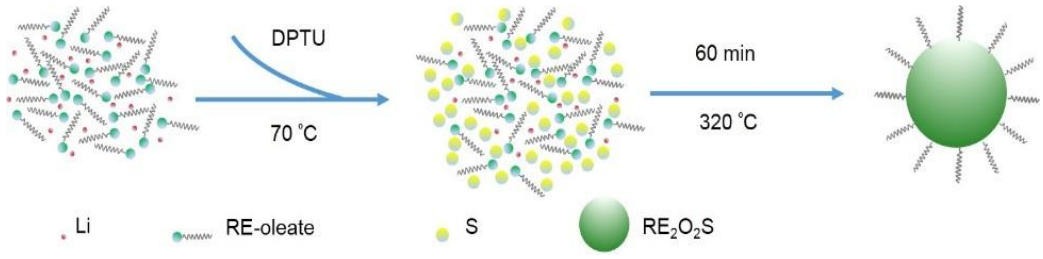

Figure R-2 Illustration schématique de la synthèse des NPs RE_2O_2S.

Pour acquérir des modalités multiples (luminescence NIR-II, performances photoacoustiques, ultrasonores, magnétiques et tomodensitométrie), nous avons en outre synthétisé une série de NPs Gd_2O_2S dopés au Nd avec une concentration variable. Les techniques de XRD et de TEM ont été utilisées pour étudier la variation de taille et de morphologie avec une concentration de Nd variable. Les spectres d'absorption UV-vis-NIR montrent par ailleurs que l'absorption est dépendante de la concentration d'ions Nd^{3+}. Avec des spectres d'absorption acquis, nous avons calculé la section efficace

d'absorption de Nd dans un petit cristal de Nd_2O_2S. Sous une irradiation laser de 808 nm, des spectres d'émission de photoluminescence de Gd_2O_2S:x%Nd (x = 10, 20, 40, 60 et 100) NPs ont été enregistrés, après quoi la concentration de Nd a été optimisée pour être de 60 % dans Gd_2O_2S.

Pour rendre les NPs hydrophiles, nous avons étudié 3 stratégies de modification de surface des NPs Gd_2O_2S:60%Nd. Le traitement à l'acide a donné un rendement extrêmement faible et une taille réduite des nanoparticules. L'échange de ligand avec la méthode $NOBF_4$ a donné une sévère agrégation des particules, bien que des conditions différentes aient été appliquées dans la préparation. Une étude plus approfondie sur l'interaction entre les ions de surface des nanoparticules et le groupe fonctionnel BF^- devrait être effectuée pour une meilleure compréhension des agrégations. Enfin, une méthode d'échange de ligand avec PVP a été proposée, où les PVP ont retiré la couche d'acide oléique hydrophobe de la surface des NPs de Gd_2O_2S:60%Nd. Les spectres FTIR ont confirmé le succès du processus d'échange de ligand. Cette méthode a fourni une procédure de préparation simple, un rendement élevé et une excellente solubilité dans l'eau (Figure R-3) et elle peut être étendue pour d'autres NPs RE_2O_2S obtenues par la méthode de décomposition thermique avec présence d'OA. L'étude de cytotoxicité des NPs Gd_2O_2S:60%Nd telles que préparées a montré une très faible toxicité de nos NPs.

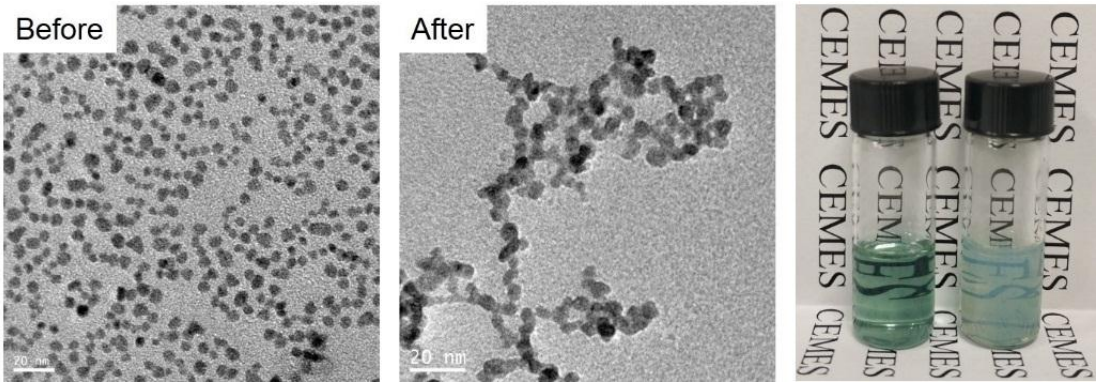

Figure R-3 Images TEM avant et après le processus d'échange de ligand PVP. La photo en médaillon montrant des NPs dispersées dans du chloroforme (à gauche) ou dans de l'eau (à droite) avec la même concentration de 10 mg/mL.

À l'aide de ces NPs Gd_2O_2S:60%Nd revêtues de PVP, nous avons effectué les expériences d'imagerie multimodale. Les NPs ont montré une capacité d'imagerie pondérée en T_1 et T_2, ce qui a été pour la première fois rapporté pour les NPs de Gd_2O_2S. Les valeurs de relaxivité longitudinale (r_1) et transversale (r_2) ont été calculées à 25 $(mM)^{-1}s^{-1}$ et 65 $(mM)^{-1}s^{-1}$ respectivement, selon l'ajustement linéaire des graphiques de la Figure R-4.

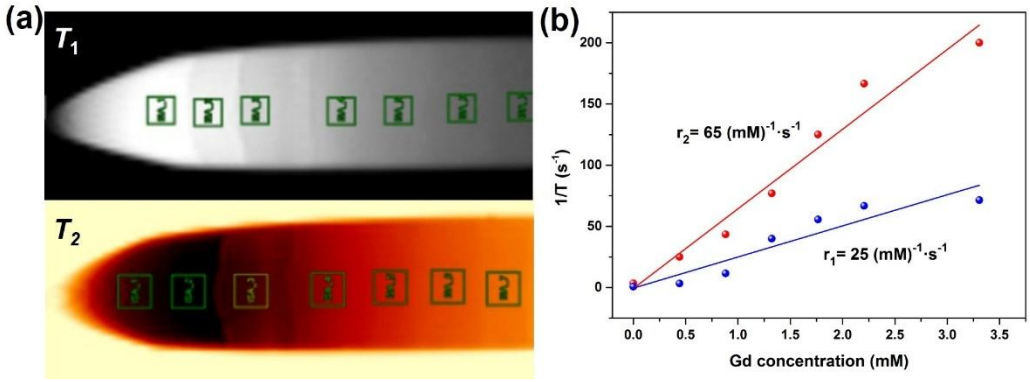

Figure R-4 (a) Images MRI pondérées en T_1 et T_2 de Gd_2O_2S:60%Nd NPs avec des concentrations (0, 0,2, 0,4, 0,6, 0,8, 1, 1,5 mg/mL) augmentant de gauche à droite. Temps de relaxivité T_1 et T_2 en fonction de la concentration en Gd de Gd_2O_2S:60%Nd NPs.

Des expériences d'imagerie CT ont montré que les NPs ont une capacité d'absorption efficace des rayons X, ce qui a confirmé l'application prometteuse des agents de contraste CT. Le contraste franc a pu être détecté au-delà de 2 mg/mL (Figure R-5).

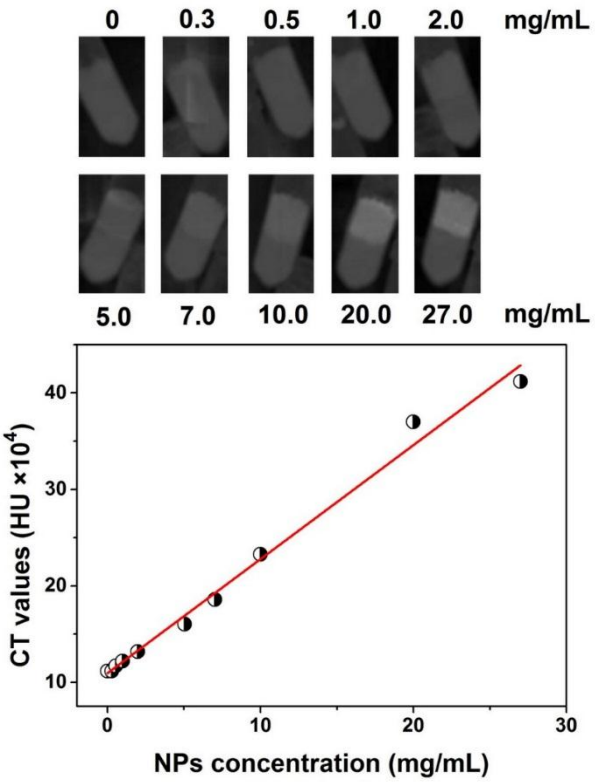

Figure R-5 (a) Images CT et (b) tracé de HU en fonction des concentrations de Gd_2O_2S:60 % Nd NPs.

Les résultats d'imagerie PA et US ont montré une bonne linéarité entre les signaux PA ou US et les concentrations des NPs. Le contraste a commencé sur l'image à partir d'une concentration autour de 5 mg/ml. Ces résultats ont ouvert la voie aux bio-applications des ultrapetites NPs RE_2O_2S. Les futurs travaux porteront sur la bio-imagerie multimodale in vivo sur cellules ou petits animaux avec des NPs RE_2O_2S. Des expériences d'imagerie par luminescence NIR-II ont démontré qu'une pénétration optique de 2,4 mm a été déterminée pour les NPs.

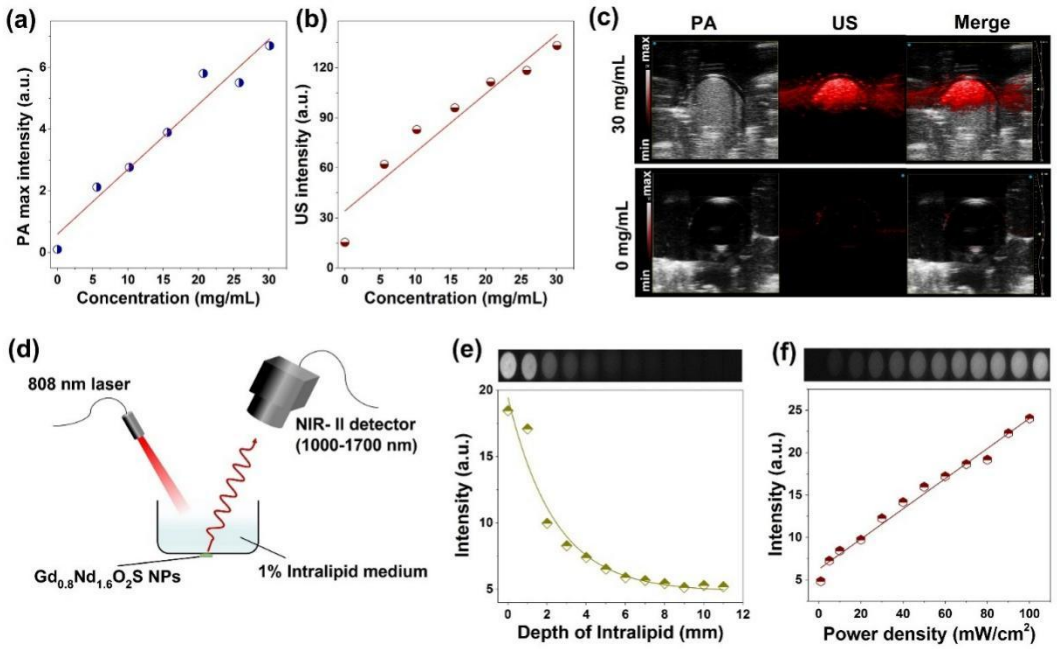

Figure R-4 Imagerie par luminescence PA, US et NIR-II des NPs Gd_2O_2S:60%Nd. Graphiques des intensités (a) PA et (b) US en fonction de la concentration en NPs de 0 à 30 mg/ml. (c) Images de comparaison obtenues sous PA, US et canaux de fusion pour les NP de concentrations 0 et 30 mg/mL. (d) Illustration schématique pour l'imagerie par luminescence NIR-II des NPs Gd_2O_2S:60%Nd recouvertes de 1% de milieu Intralipid. (e) Intensités de luminescence NIR-II obtenues pour les NPs par rapport à la profondeur d'immersion du milieu Intralipid sous excitation laser de 808 nm avec une densité de puissance de 50 mW/cm^2. (f) Tracé de l'intensité en fonction de la densité de puissance d'excitation laser avec une profondeur intralipide de 2 mm. Les photos en médaillon en (e) et (f) montrent les variations avec la profondeur Intralipid et la densité Et une accroissement progressif du contraste même avec un temps d'exposition de 75 ms pour toutes les images.

Dans **le chapitre 3**, nous avons construit avec succès une nouvelle classe de nanoparticules cœur/coquille hétérogènes RE_2O_2S@$NaREF_4$ dopées Ln^{3+}. Un grand lot des cœurs NPs Gd_2O_2S:20%Yb,1%Tm a d'abord été synthétisé. Ensuite, une coquille $NaYF_4$ d'environ 4 nm d'épaisseur a été déposée sur la nanoparticule centrale de ~ 6 nm Gd_2O_2S:20%Yb,1%Tm (Figure R-5). Par des analyses HRTEM, HAADF, EELS et

de cartographie d'éléments, nous avons confirmé la structure cœur/coquille de Gd_2O_2S:20%Yb,1%Tm@$NaYF_4$. Il est important de noter que 14 autres types de particules Gd_2O_2S:20%Yb,1%Tm@$NaREF_4$ (RE = La, Ce, Pr, Nd, Sm, Eu, Gd, Tb, Dy, Ho, Er, Tm, Yb et Lu) avec des tailles allant de 11 nm à 27 nm ont été préparées par la même approche de synthèse.

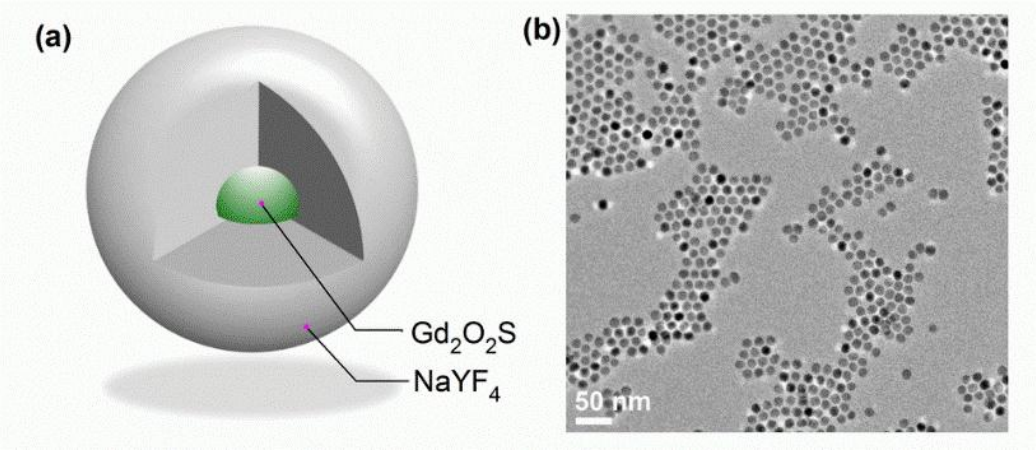

Figure R-5 (a) Concept de nanoarchitecture hétérogène Gd_2O_2S@$NaYF_4$. (b) Image TEM typique de Gd_2O_2S:20%Yb,1%Tm@$NaYF_4$ NPs hétérogènes.

Ensuite, nous avons étudié plus en détail la cinétique de croissance des NPs cœur/coquille Gd_2O_2S:20%Yb,1%Tm@$NaYF_4$. En surveillant l'évolution de la taille et de la phase au cours de l'ensemble de la synthèse, nous avons proposé le mécanisme de croissance qui comprend 3 étapes (Figure R-6): dans la première étape, le processus d'échange de cations conduit à la migration des éléments de terres rares entre les NPs du cœur solide et solution liquide, formant une couche amorphe sur les cœur NPs; dans la deuxième étape, avec la montée en température, la phase α-$NaYF_4$ apparaît à 250 °C ; enfin, la phase α-$NaYF_4$ disparaît rapidement et la phase β-$NaYF_4$ se produit, par conséquent, les dépôts de β-$NaYF_4$ sur les cœurs NPs en raison d'un petit décalage de réseau. En outre, les résultats SAXS ont également vérifié l'évolution de la taille au cours de la synthèse.

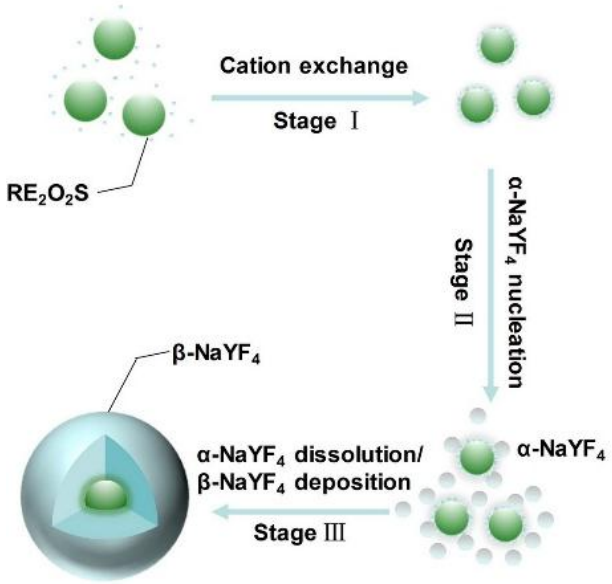

Figure R-6 Mécanisme de croissance proposé pour l'hétérostructure cœur/coquille RE_2O_2S@$NaYF_4$.

Les propriétés optiques des cœurs dopés aux lanthanides et des UCNPs coeur/coquille ont été systématiquement évaluées. Nous obtenons une amélioration de 836 et 4922 fois pour Gd_2O_2S:20%Yb,1%Tm@$NaYF_4$ et Gd_2O_2S:20%Yb,2%Er@$NaYF_4$, respectivement, par rapport à leurs cœur correspondants. Il a été enregistré que les durées de vie des raies d'émission à 469 nm et à 803 nm sont augmentées respectivement de 8 µs et 5 µs pour Gd_2O_2S:20%Yb,1%Tm cœur à 919 µs et 997 µs pour Gd_2O_2S:20%Yb,1%Tm@$NaYF_4$ cœur/coquille, respectivement. Les durées de vie de 520 nm, 540 nm et 652 nm de Gd_2O_2S:20%Yb,2%Er@$NaYF_4$ ont été déterminées à 305 µs, 316 µs et 351 µs, respectivement. Enfin, les UCQY dépendant de la puissance ont été mesurés pour Gd_2O_2S:20%Yb,1%Tm@$NaYF_4$, Gd_2O_2S:20%Yb,2%Er@$NaYF_4$ et Gd_2O_2S:20%Yb,2%Er@$NaGdF_4$ (Figure R-7). La valeur UCQY maximale était de ~0,76 % pour Gd_2O_2S:20%Yb,1%Tm@$NaYF_4$ à une densité de puissance de 155 W/cm^2.

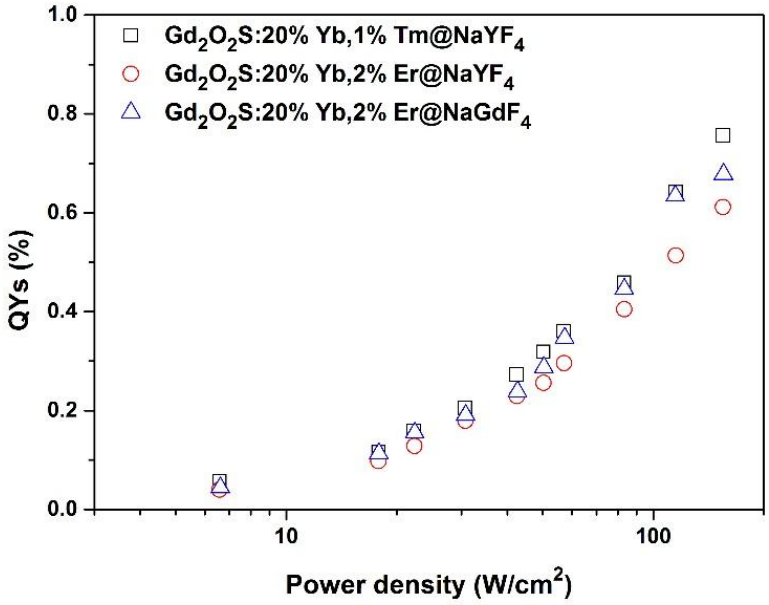

Figure R-7 UCQY dépendant de la puissance de Gd_2O_2S:20%Yb,1%Tm@$NaYF_4$, Gd_2O_2S:20%Yb,2%Er@$NaYF_4$ et Gd_2O_2S:20%Yb,2%Er@$NaGdF_4$ UCNPs coeur/coquille.

De plus, nous avons systématiquement étudié les propriétés UCL des UCNPs Gd_2O_2S:20%Yb,x%Er@$NaYF_4$ (x = 1, 2, 5, 10 et 15). En analysant les images TEM des UCNPs Gd_2O_2S:20%Yb,x%Er coeur et Gd_2O_2S:20%Yb,x%Er@$NaYF_4$ coeur/coquille, nous avons comparé la taille et l'épaisseur de la coquille des UCNPs coeur/coquille. Les mesures ICP-OES ont révélé la composition des UCNP coeur/coquille. Les spectres UCL ont montré que l'échantillon à 2% d'Er avait la luminescence la plus intense. Les durées de vie des UCNPs coeur/coquille à 540 nm ont montré que la durée de vie diminuait à mesure que la concentration en Er augmentait. Les UCQY ont montré que l'échantillon à 1% d'Er avait les valeurs d'UCQY les plus élevées lorsque la densité de puissance était inférieure à 57 W/cm^2, alors que, dans la plage de 83 à 155 W/cm^2, il avait des valeurs d'UCQY inférieures à celles de l'échantillon à 2% d'Er au même densité de puissance.

Enfin, dans ce chapitre, une modification de surface en deux étapes a été appliquée pour les UCNPs Gd_2O_2S:20%Yb,2%Er@$NaYF_4$ coeur/coquille. Ensuite, nous avons

préparé des UCNPs recouverts de PVP et d'alendronate. Les images TEM et les résultats DLS ont montré la bonne dispersité et la bonne taille. Ces résultats étaient encore préliminaires, d'une part, nous allons optimiser les paramètres du procédé pour obtenir des NPs hydrophiles monodisperses; d'autre part, nous caractériserons les propriétés optiques de ces NPs hydrophiles. Plus important encore, nous utiliserons les NPs pour des applications futures, telles que la bio-imagerie.

Dans **le chapitre 4**, les spectres UCL dépendant de la température ont été enregistrés pour la première fois pour les UCNPs Gd_2O_2S:20%Yb,1%Tm@$NaYF_4$ et Gd_2O_2S:20%Yb,2%Er@$NaYF_4$ coeur/coquille. Ces deux échantillons ont montré un accroissement anormal de l'UCL avec une augmentation de la température de 293 K à 473 K (Figure R-8). Les mesures du cycle de chauffage-refroidissement ont confirmé que les molécules d'eau jouaient un rôle vital pour l'amélioration thermique de la luminescence.

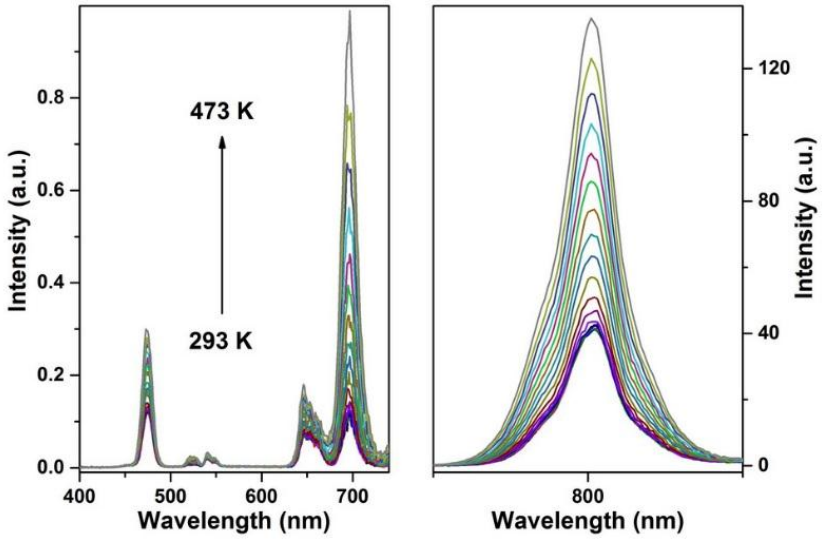

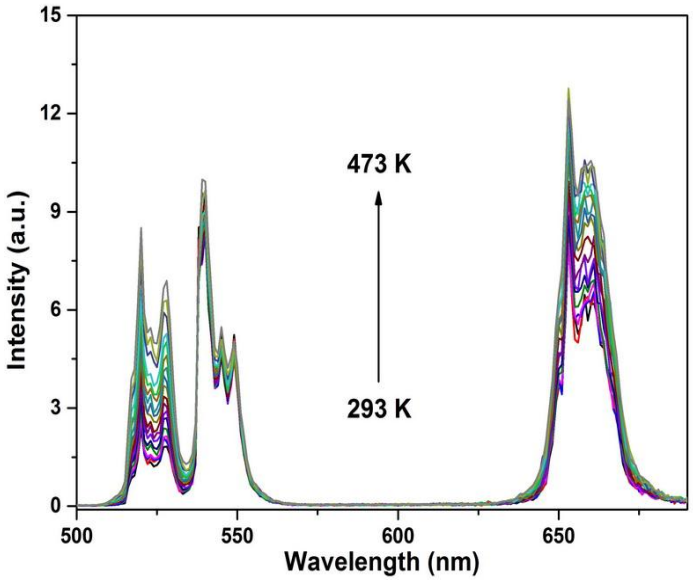

Figure R-8 Spectres UCL dépendant de la température de Gd_2O_2S:20%Yb,1%Tm@$NaYF_4$ (en haut) et Gd_2O_2S:20%Yb,2%Er@$NaYF_4$ (en bas) coeur/coquille UCNPs, sous excitation laser de 980 nm à une densité de puissance de 25 W/cm^2.

Ensuite, la variation de I_{652}/I_{540} en fonction de la température pour Gd_2O_2S:20%Yb,2%Er@$NaYF_4$ coeur/coquille UCNPs a été étudiée. Il a été constaté que le rapport a d'abord augmenté de manière linéaire de 293 K à 423 K, puis est resté presque stable de 423 K à 463 K, et a finalement chuté à 473 K (Figure R-9 en haut). Pour comprendre la relation entre l'expansion du réseau et le changement du rapport de fluorescence, nous avons analysé le taux d'expansion du réseau de Gd_2O_2S:Yb,Tm coeur et Gd_2O_2S:Yb,Tm@$NaYF_4$ coeur/coquille. En utilisant la XRD in-situ, les coefficients de dilatation thermique ont été déterminés à 0,007 Å^3/K et 0,021 Å^3/K dans la même plage de température pour Gd_2O_2S:Yb,Tm coeur et Gd_2O_2S:Yb,Tm@$NaYF_4$ coeur/coquille, respectivement, qui a affiché une différence de 3 fois les taux de dilatation thermique entre le coeur et la coquille. Par conséquent, nous avons proposé un mécanisme pour expliquer la variation de I_{652}/I_{540} (Figure R-9 en bas) qui était le décalage de réseau entre le coeur et la coquille produit une contrainte de traction et la contrainte de traction diminuerait linéairement avec l'augmentation de la température, entraînant ainsi l'augmentation linéaire du rapport I_{652}/I_{540} dans la plage

de température de 293 à 423 K; à mesure que la température augmentait davantage, la contrainte de traction disparaissait en raison du taux d'expansion du réseau plus élevé de la coquille que du coeur, par conséquent aucun changement du rapport n'a été observé. Enfin, la fluorescence diminuait à mesure que la température continuait d'augmenter, ce qui était attribué à l'apparition d'une contrainte de compression.

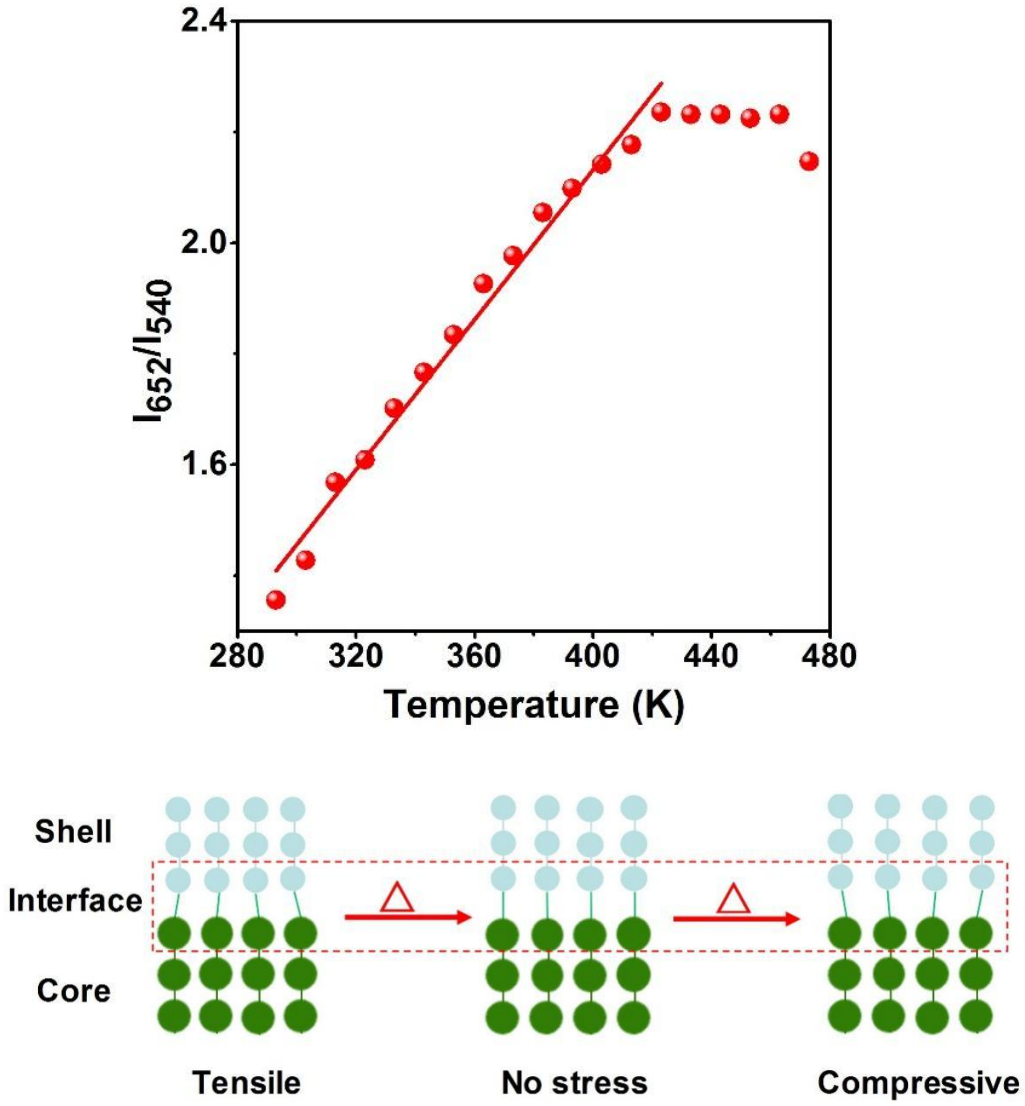

Figure R-9 Rapports d'intensité d'émission rouge/vert dépendant de la température (I_{652}/I_{540}) de Gd_2O_2S:20%Yb,2%Er@$NaYF_4$ coeur/coquille UCNPs (en haut). Illustration schématique de la variation de la distorsion du réseau avec l'augmentation de la température (en bas).

Sur la base des spectres UCL dépendants de la température, nous avons étudié les

sensibilités thermiques des UCNPs coeur/coquille dopés Ln^{3+} Gd_2O_2S@$NaREF_4$. Les valeurs maximales de Sr ont été calculées à 3,9 $\%K^{-1}$ et 3,3 $\%K^{-1}$ pour Gd_2O_2S@$NaYF_4$ dopé Yb/Tm et Gd_2O_2S@$NaLuF_4$, respectivement, et 1,1 $\%K^{-1}$ pour Gd_2O_2S@$NaYF_4$ dopé Yb/Er. Ces valeurs de Sr étaient assez élevées par rapport au Sr des autres systèmes, montrant un grand potentiel d'application de la nano-thermométrie pour les UCNPs coeur/coquille Gd_2O_2S@$NaREF_4$ dopés aux lanthanides.

Dans **le chapitre 5**, dans le but de concevoir des UCNP coeur/coquille pour des applications de bio-imagerie temporisée, nous avons d'abord présenté la synthèse et les caractérisations de $NaYF_4$:40%Gd,20%Yb,x%Tm (x = 0,1, 0,3, 0,5, 0,7, 1, 1,2 et 1,5) UCNPs avec différentes concentrations de Tm. Les résultats TEM ont montré que ces UCNPs étaient monodisperses et sphériques avec une taille de 9,8 ± 1,1 nm à 14,6 ± 0,9 nm avec une différence de taille d'environ 5 nm. Les spectres UCL de ces UCNPs ont montré que l'intensité de l'UCL était positivement associée à la taille des nanoparticules, mais non associée à la concentration de Tm. Ces résultats ont démontré que nous devons être prudents lorsque nous comparons une série d'échantillons avec différentes concentrations d'éléments dopants. L'effet de la taille était un facteur important et ne peut pas non plus être ignoré, en particulier lorsque la taille des nanoparticules est à l'échelle nanométrique.

Par la suite, des objets coeur/coquille/coquille de 31 nm de taille environ à conversion ascendante $NaYF_4$:40%Gd,20%Yb,1%Tm@$NaYF_4$:10%Yb@$NaYF_4$:20%Nd,10%Yb sont synthétisés par une méthode de co-précipitation (Figure R-10). Sous irradiation de laser continue CW de 980 nm ou 800 nm, les UCNPs coeur/coquille/coquille ont présenté une émission intense de l'ion Tm^{3+}. Les émissions UC de $^3H_4$, $^1G_4$ et $^1D_2$ ont été confirmées comme étant des processus UC à 2, 3 et 4 photons par les spectres UCL dépendants de la puissance. Il a été montré que les durées de vie UCL des émissions 475 nm et 800 nm de Tm^{3+} augmentaient respectivement à 324 ± 3 µs et 338 ± 4 µs dans les UCNP de base contre 568 ± 4 µs et 995 ± 16 µs dans les UCNPs de

coeur/coquille/coquille, respectivement, consacrant une efficacité de protection de la coque contre la trempe superficielle.

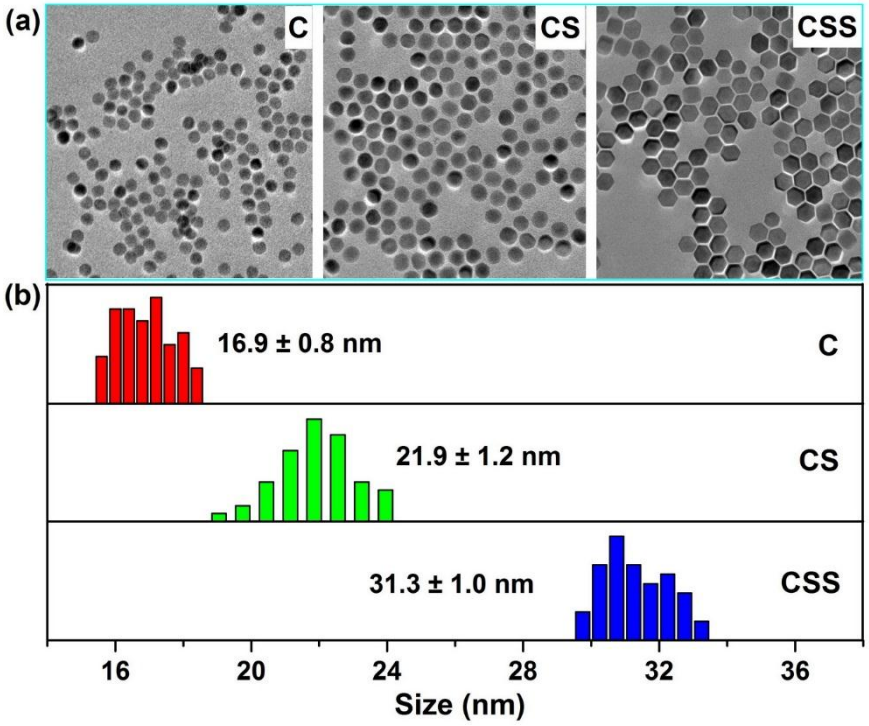

Figure R-10 (a) Images TEM et (b) distributions de taille de $NaYF_4$:40%Gd,20%Yb,1%Tm (C), $NaYF_4$:40%Gd,20%Yb,1%Tm@$NaYF_4$:10%Yb (CS) et $NaYF_4$:40%Gd,20%Yb,1%Tm@$NaYF_4$:10%Yb@$NaYF_4$:10%Yb,20%Nd (CSS) UCNPs.

Grâce à une plate-forme de spectroscopie optique avancée, les spectres temporels ont été mesurés pour les UCNPs coeur/coquille/coquille tels que préparés sous excitation laser pulsée de 980 nm et 808 nm. Les processus d'émission de Tm^{3+}, Nd^{3+} et Yb^{3+} dans la plage NIR de 700~1050 nm ont été discutés attentivement (Figure R-11). De plus, les durées de vie de Tm^{3+}, Nd^{3+} et Yb^{3+} dans la plage NIR de 700~1050 nm ont été enregistrées. Que ce soit après une excitation à 980 nm ou à 808 nm, la durée de vie de $^3H_4$ de Tm^{3+} est restée presque la même, ce qui a permis un grand avantage de l'application prometteuse d'imagerie temporelle dans notre concept.

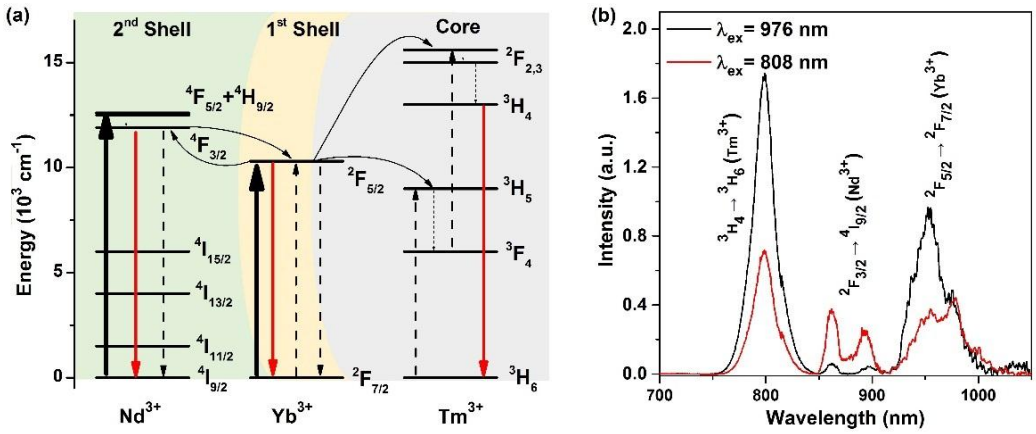

Figure R-11 Schéma UCL (a) et (b) spectres de $NaYF_4$:40%Gd,20%Yb,1%Tm@$NaYF_4$:10%Yb@$NaYF_4$:10%Yb,20%Nd coeur/coquille/coquille UCNPs sous irradiation de 980 nm ou 808 nm.

Les UCNPs coeur/coquille/coquille recouverts de PVP ont ensuite été préparés et incubés avec des cellules HCT-116. Ensuite, via un microscope confocal, nous avons obtenu des images de cellules sous irradiation de 980 nm et 405 nm, qui ont montré l'incubation réussie de nos UCNPs (Figure R-12). Ces cellules fixées sur une lame peuvent également être utilisées pour l'imagerie temporelle lorsque notre dispositif temporel maison sera complètement établie.

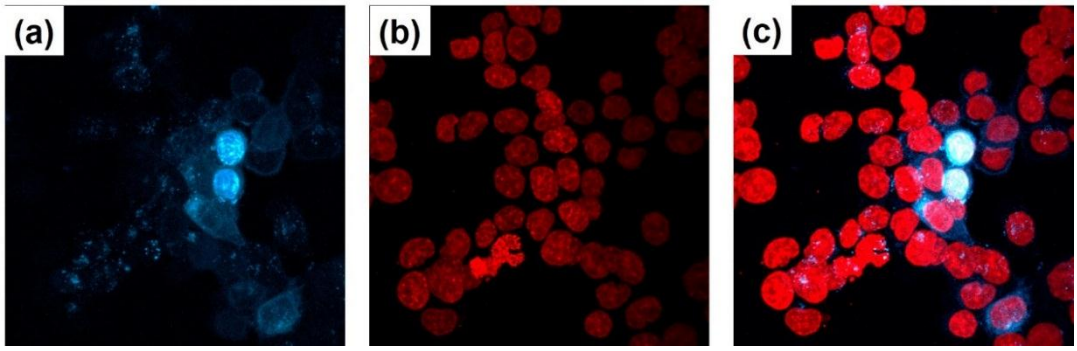

Figure R-12 Images de cellules sous microscope confocal. (a) Lors d'une irradiation laser à pulsation femtoseconde à 980 nm, MHz, avec une plage de détection inférieure à 750 nm ; (b) lors d'une excitation à 405 nm avec une plage de détection de 415 à 730 nm ; (c) chevauchement de (a) et (b).

Mots clés: nanoparticules dopées aux lanthanides, RE_2O_2S, $NaREF_4$, photoluminescence, imagerie multimodale, détection de température, temporisation.

Bibliographie

1. Nam, J.; Won, N.; Bang, J.; Jin, H.; Park, J.; Jung, S.; Jung, S.; Park, Y.; Kim, S., Surface engineering of inorganic nanoparticles for imaging and therapy. *Adv. Drug Del. Rev.* **2013,** *65*, 622-648.

2. Chavali, M. S.; Nikolova, M. P., Metal oxide nanoparticles and their applications in nanotechnology. *SN Appl. Sci.* **2019,** *1*, 607.

3. Nikolova, M. P.; Chavali, M. S., Metal Oxide Nanoparticles as Biomedical Materials. *Biomimetics* **2020,** *5*, 27.

4. Zheng, Z.; Huang, B.; Wang, Z.; Guo, M.; Qin, X.; Zhang, X.; Wang, P.; Dai, Y., Crystal Faces of Cu_2O and Their Stabilities in Photocatalytic Reactions. *J. Phys. Chem. C* **2009,** *113*, 14448-14453.

5. Pal, J.; Pal, T., Faceted metal and metal oxide nanoparticles: design, fabrication and catalysis. *Nanoscale* **2015,** *7*, 14159-14190.

6. Mansur, H. S., Quantum dots and nanocomposites. *WIREs Nanomed. Nanobiotechnol.* **2010,** *2*.

7. Mukai, K., Semiconductor Quantum Dots for Future Optical Applications. *J. Nanosci. Nanotechnol.* **2014,** *14*, 2148-2156.

8. Kokorina, A. A.; Ermakov, A. V.; Abramova, A. M.; Goryacheva, I. Y.; Sukhorukov, G. B., Carbon Nanoparticles and Materials on Their Basis. *Colloids Interfaces* **2020,** *4*, 42.

9. Patel, K. D.; Singh, R. K.; Kim, H.-W., Carbon-based nanomaterials as an emerging platform for theranostics. *Mater. Horiz.* **2019,** *6*, 434-469.

10. Maiti, D.; Tong, X.; Mou, X.; Yang, K., Carbon-Based Nanomaterials for Biomedical Applications: A Recent Study. *Front. Pharmacol.* **2019,** *9*, 1401.

11. Yin, L.; Zhou, H.; Lian, L.; Yan, S.; Song, W., Effects of C_{60} on the Photochemical Formation of Reactive Oxygen Species from Natural Organic Matter. *Environ. Sci. Technol.* **2016,** *50*, 11742-11751.

12. Lucky, S. S.; Soo, K. C.; Zhang, Y., Nanoparticles in Photodynamic Therapy. *Chem. Rev.* **2015,** *115*, 1990-2042.

13. Fan, Y.; Liu, H.; Han, R.; Huang, L.; Shi, H.; Sha, Y.; Jiang, Y., Extremely High Brightness from Polymer-Encapsulated Quantum Dots for Two-photon Cellular and Deep-tissue Imaging. *Sci. Rep.* **2015,** *5*, 9908.

14. Protesescu, L.; Yakunin, S.; Bodnarchuk, M. I.; Krieg, F.; Caputo, R.; Hendon, C. H.; Yang, R. X.; Walsh, A.; Kovalenko, M. V., Nanocrystals of Cesium Lead Halide Perovskites ($CsPbX_3$, X = Cl, Br, and I): Novel Optoelectronic Materials Showing Bright Emission with Wide Color Gamut. *Nano Lett.* **2015,** *15* (6), 3692-3696.

15. Chen, Y.; Yi, H. T.; Wu, X.; Haroldson, R.; Gartstein, Y. N.; Rodionov, Y. I.; Tikhonov, K. S.; Zakhidov, A.; Zhu, X. Y.; Podzorov, V., Extended carrier lifetimes and diffusion in hybrid perovskites revealed by Hall effect and photoconductivity measurements. *Nat. Comm.* **2016,** *7* (1), 12253.

16. Galkowski, K.; Mitioglu, A.; Miyata, A.; Plochocka, P.; Portugall, O.; Eperon, G. E.; Wang, J. T.-W.; Stergiopoulos, T.; Stranks, S. D.; Snaith, H. J.; Nicholas, R. J., Determination of the exciton binding energy and effective masses for methylammonium and formamidinium lead tri-halide perovskite semiconductors. *Energy Environ. Sci.* **2016,** *9* (3), 962-970.

17. Akkerman, Q. A.; Rainò, G.; Kovalenko, M. V.; Manna, L., Genesis, challenges and opportunities for colloidal lead halide perovskite nanocrystals. *Nat. Mater.* **2018,** *17* (5), 394-405.

18. Yuan, J.; Hazarika, A.; Zhao, Q.; Ling, X.; Moot, T.; Ma, W.; Luther, J. M., Metal Halide Perovskites in Quantum Dot Solar Cells: Progress and Prospects. *Joule* **2020,** *4* (6), 1160-1185.

19. Stranks, S. D.; Eperon, G. E.; Grancini, G.; Menelaou, C.; Alcocer, M. J. P.; Leijtens, T.; Herz, L. M.; Petrozza, A.; Snaith, H. J., Electron-Hole Diffusion Lengths Exceeding 1 Micrometer in an Organometal Trihalide Perovskite Absorber. *Science* **2013,** *342* (6156), 341-344.

20. Wang, Y.; Dar, M. I.; Ono, L. K.; Zhang, T.; Kan, M.; Li, Y.; Zhang, L.; Wang, X.; Yang, Y.; Gao, X.; Qi, Y.; Grätzel, M.; Zhao, Y., Thermodynamically stabilized β-$CsPbI_3$-based perovskite solar cells with efficiencies >18%. *Science* **2019,** *365* (6453), 591-595.

21. Song, J.; Li, J.; Li, X.; Xu, L.; Dong, Y.; Zeng, H., Quantum Dot Light-Emitting Diodes Based on Inorganic Perovskite Cesium Lead Halides ($CsPbX_3$). *Adv. Mater.* **2015,** *27* (44), 7162-7167.

22. Liang, J.; Chen, D.; Yao, X.; Zhang, K.; Qu, F.; Qin, L.; Huang, Y.; Li, J., Recent Progress and Development in Inorganic Halide Perovskite Quantum Dots for Photoelectrochemical Applications. *Small* **2020,** *16*, 1903398.

23. Xu, L.; Yuan, S.; Ma, L.; Zhang, B.; Fang, T.; Li, X.; Song, J., All-inorganic perovskite quantum dots as lightharvesting, interfacial, and light-converting layers toward solar cells. *J. Mater. Chem. A* **2021,** *9*, 18947.

24. Dong, H.; Du, S.-R.; Zheng, X.-Y.; Lyu, G.-M.; Sun, L.-D.; Li, L.-D.; Zhang, P.-Z.; Zhang, C.; Yan, C.-H., Lanthanide Nanoparticles: From Design toward Bioimaging and Therapy. *Chem. Rev.* **2015,** *115*, 10725−10815.

25. Zheng, W.; Huang, P.; Tu, D.; Ma, E.; Zhu, H.; Chen, X., Lanthanide-doped upconversion nano-bioprobes: electronic structures, optical properties, and biodetection. *Chem. Soc. Rev.* **2015,** *44* (6), 1379-1415.

26. Teo, R. D.; Termini, J.; Gray, H. B., Lanthanides: Applications in Cancer Diagnosis and Therapy. *J. Med. Chem.* **2016,** *59* (13), 6012-6024.

27. GabrielleAMandl; DanielRCooper; Hirsch, T.; Seuntjens, J.; Capobianco, J. A., Perspective: lanthanide-doped upconverting nanoparticles. *Methods Appl. Fluoresc.* **2019,** *7*, 012004.

28. Bünzli, J.-C. G.; Eliseeva, S. V., Basics of Lanthanide Photophysics. In *Lanthanide Luminescence: Photophysical, Analytical and Biological Aspects*, Hänninen, P.; Härmä, H., Eds. Springer Berlin Heidelberg: Berlin, Heidelberg, 2011; pp 1-45.

29. Homann, C.; Krukewitt, L.; Frenzel, F.; Grauel, B.; Würth, C.; Resch-Genger, U.;

Haase, M., $NaYF_4$:Yb,Er/$NaYF_4$ Core/ShellNanocrystals with High Upconversion Luminescence Quantum Yield. *Angew.Chem. Int.Ed.* **2018,** *57*, 8765 –8769.

30. Kaiser, M.; Wurth, C.; Kraft, M.; Hyppanen, I.; Soukka, T.; Resch-Genger, U., Power-dependent upconversion quantum yield of $NaYF_4$:Yb^{3+},Er^{3+} nano- and micrometer-sized particles - measurements and simulations. *Nanoscale* **2017,** *9* (28), 10051-10058.

31. Martín-Rodríguez, R.; Fischer, S.; Ivaturi, A.; Froehlich, B.; Krämer, K. W.; Goldschmidt, J. C.; Richards, B. S.; Meijerink, A., Highly Efficient IR to NIR Upconversion in Gd_2O_2S: Er^{3+} for Photovoltaic Application. *Chem. Mater.* **2013,** *25*, 1912−1921.

32. Pokhrel, M.; Kumar, G. A.; Sardar, D. K., Highly efficient NIR to NIR and VIS upconversion in Er^{3+} and Yb^{3+} doped in M_2O_2S(M = Gd, La, Y). *J. Mater. Chem. A* **2013,** *1*, 11595–11606.

33. Larquet, C.; Carenco, S., Metal Oxysulfides: From Bulk Compounds to Nanomaterials. *Front. Chem.* **2020,** *8* (179).

34. Osseni, S. A.; Lechevallier, S.; Verelst, M.; Dujardin, C.; Dexpert-Ghys, J.; Neumeyer, D.; Leclercq, M.; Baaziz, H.; Cussac, D.; Santran, V.; Mauricot, R., New nanoplatform based on Gd_2O_2S:Eu^{3+} core: synthesis, characterization and use for in vitro bio-labelling. *J. Mater. Chem.* **2011,** *21* (45), 18365-18372.

35. Santelli, J.; Lechevallier, S.; Calise, D.; Marsal, D.; Siegfriedb, A.; Vincent, M.; Martinez, C.; Cussac, D.; Mauricot, R.; Verelst, M., Multimodal gadolinium oxysulfide nanoparticles for bioimaging: A comprehensive biodistribution, elimination and toxicological study. *Acta Biomater.* **2020,** *108*, 261–272.

36. Osseni, S. A.; Lechevallier, S.; Verelst, M.; Perriat, P.; Dexpert-Ghys, J.; Neumeyer, D.; Garcia, R.; Mayer, F.; Djanashvili, K.; Peters, J. A.; Magdeleine, E.; Gros-Dagnac, H.; Celsis, P.; Mauricot, R., Gadolinium oxysulfide nanoparticles as multimodal imaging agents for T_2-weighted MR, X-ray tomography and photoluminescence. *Nanoscale* **2014,** *6*, 555–564.

37. Santelli, J.; Lechevallier, S.; Baaziz, H.; Vincent, M.; Martinez, C.; Mauricot, R.; Parini, A.; Verelst, M.; Cussac, D., Multimodal gadolinium oxysulfide nanoparticles a versatile contrast agent for mesenchymal stem cell labeling. *Nanoscale* **2018,** *10*, 16775-16786.

38. Santelli, J.; Lepoix, C.; Lechevallier, S.; Martinez, C.; Calise, D.; Zou, Q.; Moyano, S.; Cussac, D.; Verelst, M.; Mauricot, R., Custom NIR Imaging of New Up-Conversion Multimodal Gadolinium Oxysulfide Nanoparticles. *Part. Part. Syst. Charact.* **2021,** *38*, 2000216.